COMPUTATIONAL FLUID DYNAMICS (CFD) AND PHYSICAL MODELLING OF A METAL REFINING PROCESS

by

Suman Kumar

A thesis submitted in partial fulfilment of the requirements for the degree of

Doctor of Philosophy (PhD)

University of Greenwich, UK

This research work was sponsored by Britannia Refined Metals Ltd. (BRM), Northfleet, UK

June 2003

ABSTRACT

Impeller-stirred mixing is one of the most important processes employed throughout the chemical, metallurgical and allied industries. The research reported in this thesis is focused on impeller stirred mixing associated with the refining of lead bullion. The aim of this process is to sequentially remove contained impurities such as copper, antimony, silver and bismuth. This occurs in hemispherical vessels, called kettles, where reagents are initially added to the lead bath to form surface dross that contains both the required impurity and a large amount of lead oxide. This dross is then continuously mixed back into the bath to remove the lead oxide and capture more of the required impurity. A key requirement for this process is to obtain and remove dross that contains a high concentration of the impurity. Although this process has been in operation for many years, there is very little known on how the fluid dynamics associated with the mixing process affects final dross content.

The aim of this research is to fully investigate the lead refining process using scientific analysis methods that help understand the mixing process and provide design tools which can be used to optimise process conditions. The three methods of analysis used are: (1) Direct readings from a real kettle, (2) Physical modelling (using water), and finally (3) Computational Fluid Dynamics (CFD).

The use of physical modelling, exploiting the techniques of similitude, to predict vortex was also validated. An Acoustic Doppler Velocimeter (ADV) probe was used for the velocity measurement at various locations inside the water model and this gave valuable insight about the flow phenomena occurring inside the refining kettle. A particular important finding was that when fluid is stirred above certain rotational speed the vortex depth becomes independent of the Reynolds number of the operation.

With regards CFD technology, the Volume of Fluid (VOF) method was used to capture the free surface and the Lagrangian Particle Tracking (LPT) and Algebraic Slip Model (ASM) to simulate the dross phase. Appropriate methods were also used to represent the moving

impeller region. Validation of simulation results against experimental data was very encouraging. Computed vortex depth showed the similar trend as observed during the experiments on the physical model. A design strategy was developed that integrates results from both physical and computational modelling to allow optimal process conditions to be predicted at the kettle design stage.

The use of this integrated physical and computational modelling methodology successfully helped eliminate surface swirl by introducing baffles to the kettle. The design and introduction of these flow controllers was also validated to ensure that it optimised the dross mixing process and final impurity content in the dross.

ACKNOWLEDGMENTS

Firstly, I wish to express my sincere gratitude to my supervisors, Prof. Chris Bailey and Dr. Mayur Patel, for this research project. Throughout the course of this research, they continuously provided expert guidance, constructive criticism and many valuable suggestions.

I acknowledge the financial support by Britannia Refined Metals Ltd. (BRM), Northfleet, UK, for this project. Thanks to the people of BRM, particularly Dr. A. W. Piper, for his valuable contribution towards my understanding of the lead refining process. I also recognise the help and guidance given by Mr. R. Forsdick, Mr. S. Hance and Mr. M. Cowling for the experimental work.

I wish to express my sincere appreciation for the staff of university library, particularly to Mrs. G. Pinder in procuring numerous reference materials that were required for this work. In addition, my special thanks to the staff of university computing services for their support.

In one way or other, all my family members and friends contributed towards completion of this project. I would like to convey heartfelt thanks to my brother-in-law, Dr. B. N. Singh and sister, Mrs. Sudha Singh. Without their support, my dream of higher education would have never been fulfilled. My friend, Mr. Parthiban Swaminathan deserves special mention for his generous help and support. Finally, I extend my thanks to Mr. Gana Nathan for his timely help and most of all, for his friendship.

TABLE OF CONTENTS

Chapter 1

INTRODUCTION

1.1 Impeller-Stirred Mixing

Impeller-stirred mixing is one of the most widely used operations throughout the process industries. It is employed from pilot plant to full-scale production operation in a range of chemical and allied industries, namely, chemical, pharmaceutical, food processing, biotechnological, paper & pulp, mineral and metal processing industries, to name a few. Its crucial importance in the chemical industries can be highlighted by the fact that half of the $750 billion per year [1] output of the US chemical process industry involves process related to stirred tank reactors. The most common objectives for impeller-stirred mixing are:

- Blending a miscible liquid
- Dispersing an immiscible liquid
- Dispersing gas or solid in the liquid
- Mixing reactant for chemical reactions
- Heat transfer promotion.

Figure-1.1 gives a schematic representation of a typical impeller-stirred tank. Impeller rotation generates a complex three-dimensional re-circulating, most often turbulent, flow field. The rotating impeller interacts with its surroundings and introduces mechanical energy into the system. This energy in turn gives rise to the hydrodynamic motion of the fluid and hence, accelerates the associated transport processes. Obviously, the geometry of

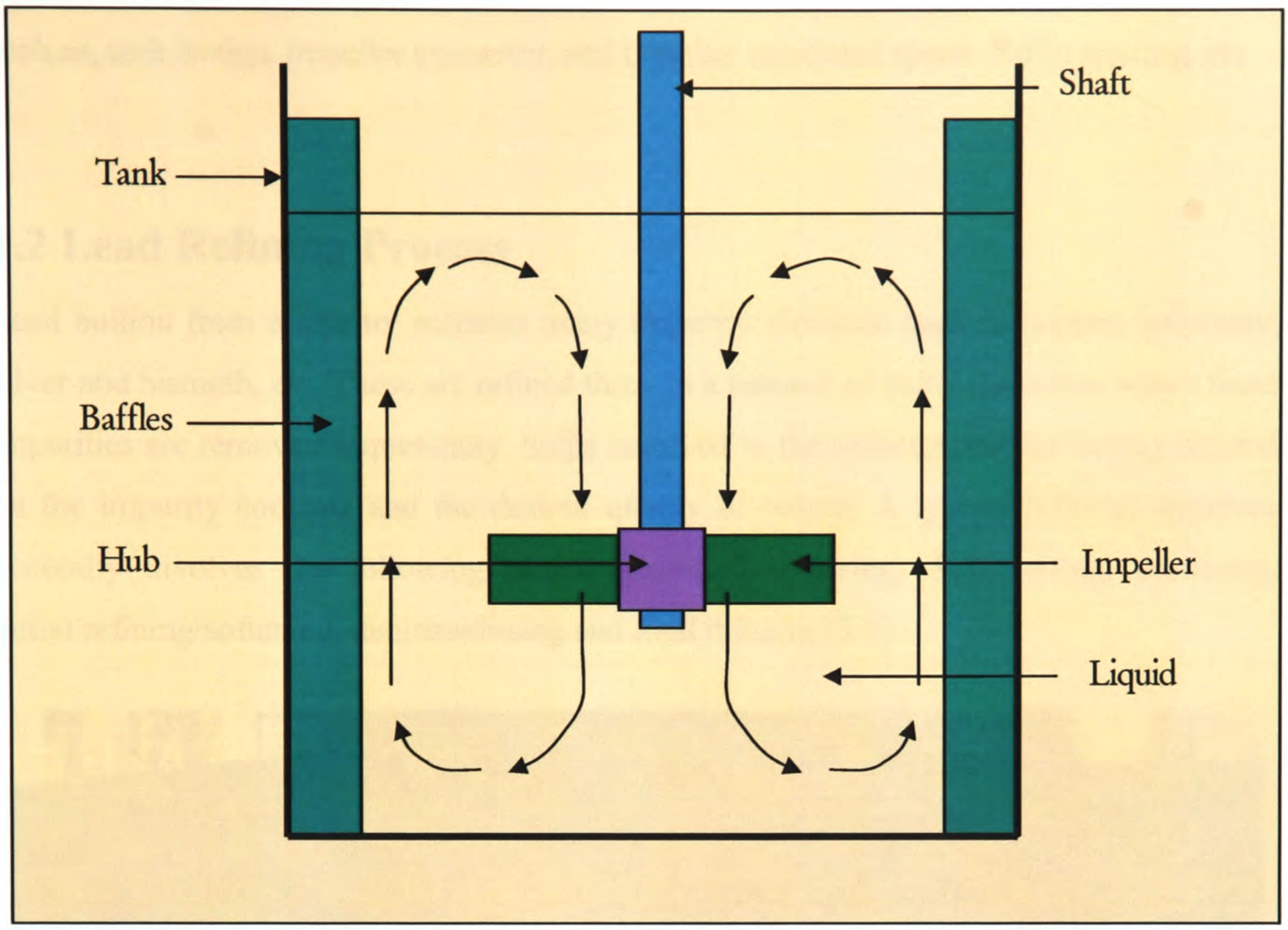

Figure 1.1: Schematic Diagram of an Impeller Stirred Tank

the impeller blades has a profound impact on the generated flow field (velocity/pressure distributions, and turbulent characteristics, etc.). Other design and operational parameters such as impeller clearance, proximity of tank walls, presence of baffles, and rotational speed of impeller also strongly affect the generated flow field [2].

Depending on the requirements of the process, design and operational variables for the impeller-stirred tank vary from one process to another. Desired nature of final products and optimisation of the process dictate the choice for these variables. For instance, in impeller-stirred chemical reactors, the yield and selectivity of the reaction are mainly determined by the flow pattern. Here, the major tasks with respect to optimisation are to avoid zones with high residence time and achieve high turbulence for good mixing. At the same time operating conditions should also ensure that the energy consumption and hence cost is low.

In most of the situations optimal performance is derived by varying the control parameters such as, tank design, impeller geometry, and impeller rotational speed, baffle spacing, etc.

1.2 Lead Refining Process

Lead bullion from a smelter contains many impurity elements such as copper, antimony, silver and bismuth, etc. These are refined through a number of batch processes where these impurities are removed sequentially. Steps involved in the refining process largely depend on the impurity contents and the desired quality of output. A typical refining sequence generally involves the following steps: melting/decoppering, desilverising, dezincing, initial refining/softening, debismuthising and final refining [3-5].

Figure 1.2: A Typical Lead Refining Kettle

The melting/decoppering is carried out in an open-top hemispherical iron vessel called a kettle, see Figure-1.2. The size of each kettle varies, depending on the volume of production, and a typical industrial kettle can hold anything between 80 to 250 tons of molten lead bullion. First of all, lead bullion is melted at very high temperature (600°C-

800°C) and then allowed to cool slowly. As their solubility decreases at the lower temperature (480°C), the impurities, including considerable portion of copper, rise to the bath surface forming a hard crust known as dross. The bath is then stirred using a mechanical impeller, which breaks the hard dross layer into smaller lumps and draws it back again into the melt and then throws out to the surface periodically, breaking it down further. The stirring action, which may last for a number of hours, finally converts the dross into fine powder that is then skimmed off using a mechanical shovel.

The next stage in the lead refining involves desilverising. At this stage, silver is removed from lead by adding zinc to the bath. The temperature of the kettle is raised above the melting point of zinc (410°C). With impeller added stirring of the bath, the molten zinc reacts with the silver and forms a compound that is lighter than the lead. On cooling, this compound turns into crust and floats to the bath surface, which is then skimmed off for further processing. After removing silver, the access of zinc from the lead is removed using a vacuum dezincing process. Under vacuum, the boiling point of zinc decreases below the operating temperature. In this condition, while the bath is stirred, zinc evaporates from the bath surface and condenses on the water-cooled kettle lid where it forms a layer of solid zinc crystal.

If the bismuth content is high then lead is debismuthised. This operation is very similar to the desilverising, except that a combination of calcium and magnesium metals are used as the reagents to form high-melting point intermetallic compounds with bismuth, which are skimmed off and treated for recovery of bismuth. The final stage of refining involves removal of antimony. This is achieved by impeller-stirred mixing of caustic soda into the bath. This reagent successfully removes antimony along with any other trace impurities and float to the bath surface as dross.

It is clear from the above that the impeller-stirred mixing is central to lead refining process. Figure-1.3 gives the schematic representation of the mixing process in the lead refining kettle. Generally, a 3–4 blade axial impeller with 45-degree blade angle is used for this purpose. A vortex formed during stirring provides a mechanism to break the hard crust of

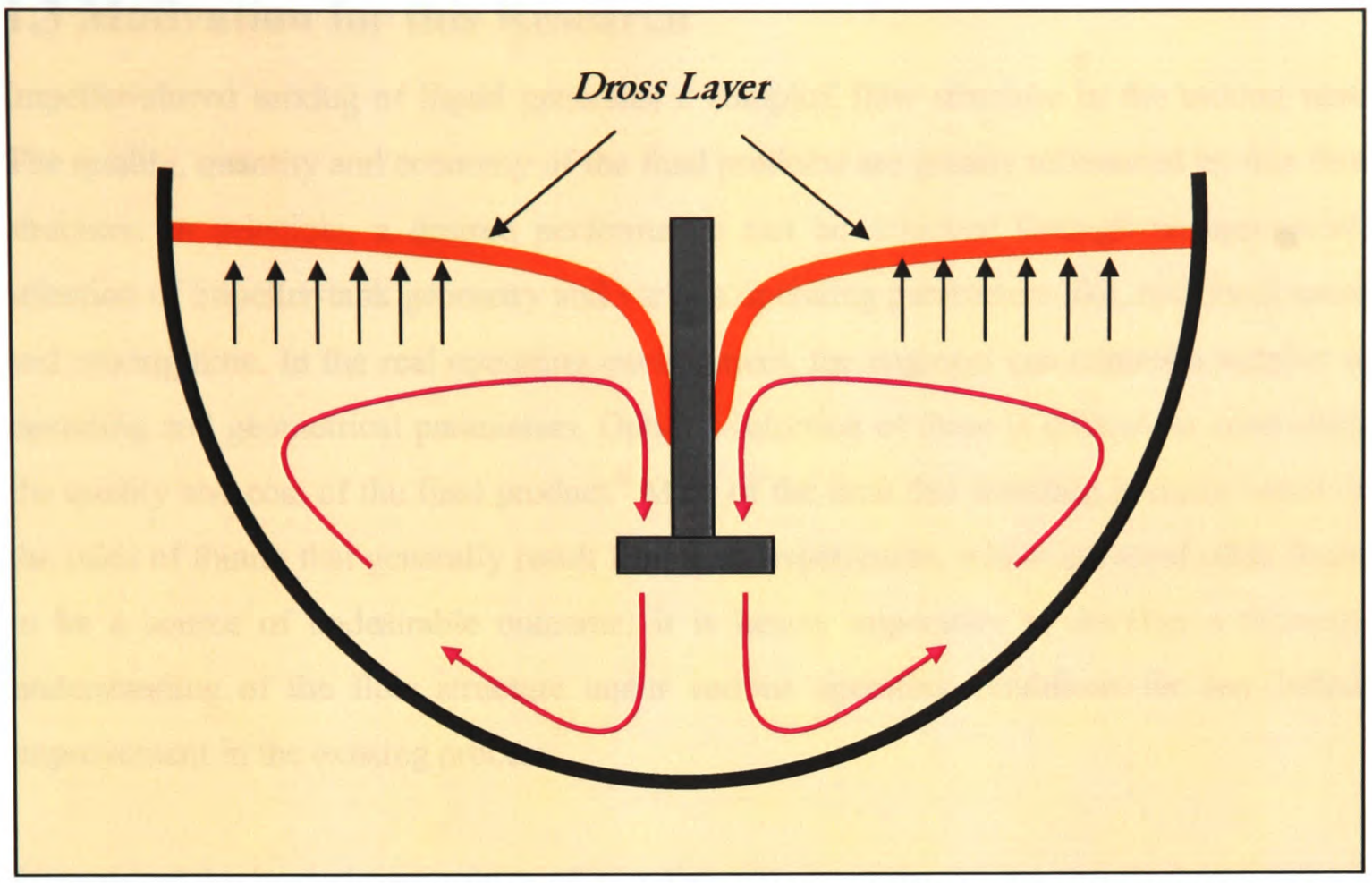

Figure 1.3: A Schematic Representation of Flow Profile in Lead Refining Kettle

dross into powder and/or mix reagent into the bath. At the earlier stage of mixing, the dross contains a large quantity of lead along with the required impurities. Continuous stirring of the lead bath, which may last for a number of hours, helps remove excess lead from the dross and hopefully capture more of the impurities still present in the bath.

Although a good vortex is required for the mixing, increasing the speed of impeller beyond a certain limit causes the vortex to break up and give rise to air entrapment within the bulk. This in turn leads to lead oxide formation in the dross and that lowers the content of required impurity. Furthermore, increasing stirring time can also cause undesired lead oxide formation due to prolonged exposure of the bath surface to air. Hence, it is important that the mixing is controlled to achieve the optimum bath condition and hence good dross grades.

During this refining process increasing the amount of impurities in the dross while keeping the lead oxide formation as low as possible and decreasing the mixing time will result in greater profits, energy saving and reduced environmental impact.

1.3 Motivation for this Research

Impeller-stirred mixing of liquid generates a complex flow structure in the mixing tank. The quality, quantity and economy of the final products are greatly influenced by this flow structure. In principle, a desired performance can be achieved through an appropriate selection of impeller-tank geometry and various operating parameters like, rotational speed and mixing time. In the real operating environment, the engineer can control a number of operating and geometrical parameters. Optimal selection of these is critical for controlling the quality and cost of the final product. Most of the time this selection is made based on the rules of thumb that generally result from past experiences, which are most often found to be a source of undesirable outcome. It is hence, imperative to develop a thorough understanding of the flow structure under various operating conditions for any further improvement in the existing process.

Because of the central importance of impeller-stirred mixing in the chemical industries a great deal of research has already been devoted to develop better understanding. It is still a rapidly evolving field of investigation where new tools and methods have constantly been employed. In spite of all this progress, the structure of the flow field and its effect of process efficiency are not completely understood. The criticality of this problem was pointed out [6] that the lack of fundamental understanding of the process associated with impeller-stirred tanks leads to losses of the order $ 10 billion per year for these industries.

In the lead refining process also, the impeller-stirred mixing plays a central role. However, there are two fundamental differences between the impeller-stirred mixing employed in the lead refining process from that of other chemical industries.

- In the majority of chemical industries impeller stirred mixing is employed for the off bottom suspension of particulate second phase which is heavier than the first phase. Whereas, in the lead refining process impeller stirred mixing is employed for the drawdown and dispersion of the lighter second phase (e.g. dross, reagents, etc.) that is floating on the bath surface.

- Unlike other chemical industries, where mixing is generally carried out in cylindrical shape vessels, lead refining process is carried out in hemispherical vessels.

Along with its own complexity, the problems typically associated with impeller-stirred mixing employed in the chemical industries are also faced in the lead refining process.

Although there is a considerable amount of information on the chemistry and the various metallurgical practices of lead refining, there is only limited published knowledge of the process engineering aspects. This is a little investigated area where design decisions are generally based on poorly established criteria resulting from ad-hoc mixing models. Geometry and operating conditions of the lead refining kettle form a very complex flow profile and without a quantitative knowledge of controlling parameters scale-up is a source of uncertainties and risk. It is very difficult to scale-up the dross-layer movement, vortex formation and other dynamical processes simultaneously, while maintaining all the flow features.

A comprehensive understanding of flow field, vortex formation, power consumption and surface movement of dross under various operating conditions is crucial in establishing criteria for optimum process control. Worldwide competition, stringent quality requirement and mounting environmental pressures have necessitated this research to bring improvement in the existing lead refining process in order to make it more efficient and cost effective.

1.4 Need for Modelling Technology

The most obvious option for investigating the flow field in the impeller stirred tank is to carry out experiments directly on a real lead refining kettle. But in majority of cases, limitation of measuring devices, hostile process environment, cost, time and labour involved in this exercise make this prohibitively difficult. Another possible option is to build a laboratory scale test unit for experimental measurements. However, it is a well

known fact that hydrodynamic behaviour of flow field changes with geometrical scale [7]. Hence, laboratory scale process cannot be treated as the true representation of production scale process. It is possible to scale up a small size setup to the production size setup through several carefully planned successive stages where each stage becoming larger than its successor by extrapolating data from the previous to the next stage. However, this can be a rather time consuming and cost intensive exercise. This clearly explains the need for an alternative approach of investigation which is speedier, cost effective and reliable.

In the situation like this modelling technology representing the impeller-stirred mixing process, based either on mathematical methods or on experimental techniques (physical modelling) is highly desirable. It is required that modelling technology provides opportunity to carry out detailed analysis, predict flow behaviour under various operating conditions, and help rapid prototyping for both existing and new plant processes. Clearly,

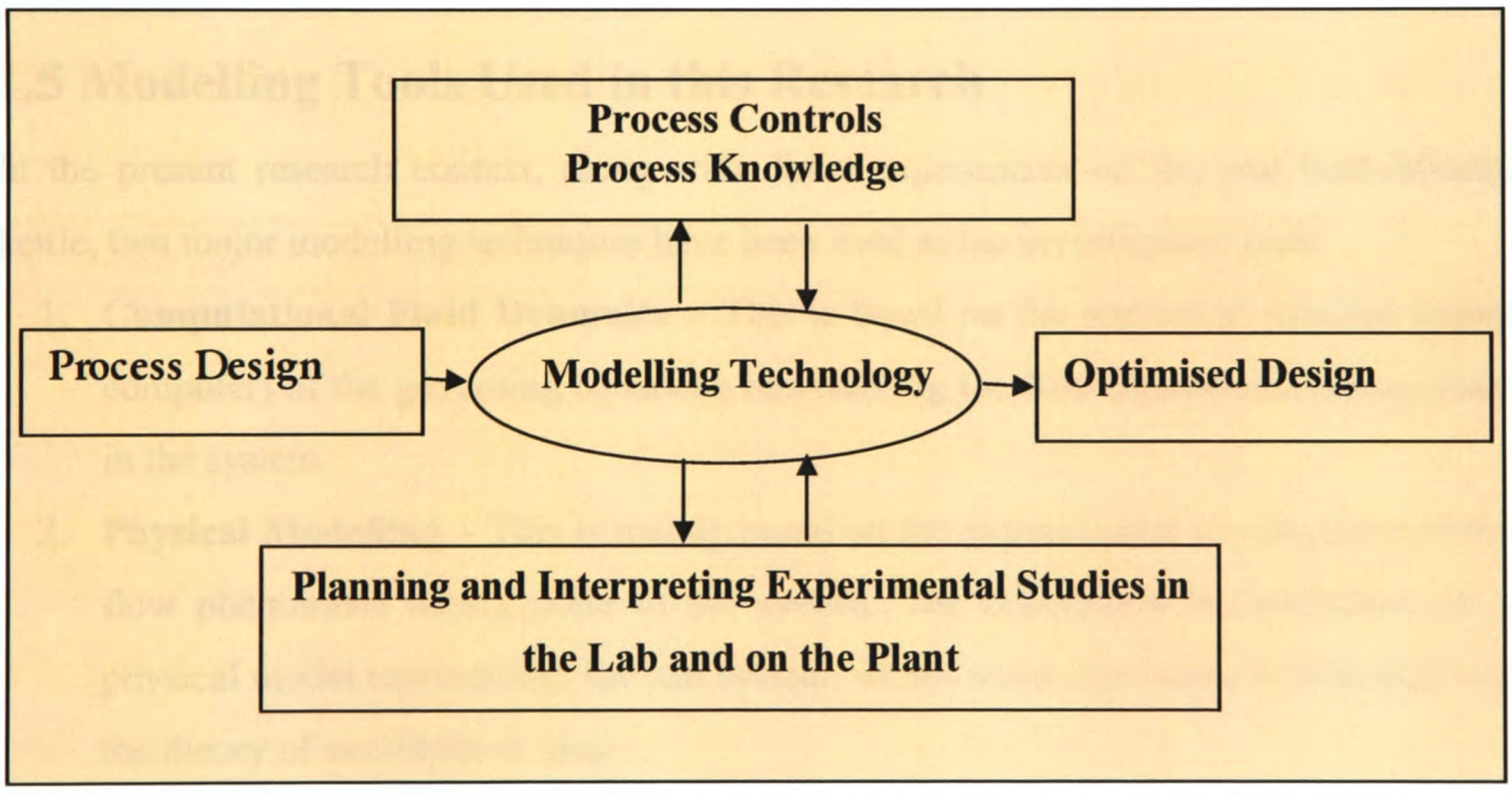

Figure 1.4: Role of Modelling Technology in Industrial Context

this can be a valuable aid in identifying defects and providing solutions for improvements. Figure-1.4 illustrates the expected role of modelling technology in an industrial setting.

It can be seen from Figure-1.5 that employing this kind of modelling tools at an early stage of design provides huge cost savings. It is much cheaper to rectify any defects at this stage than later once the plant is built [8].

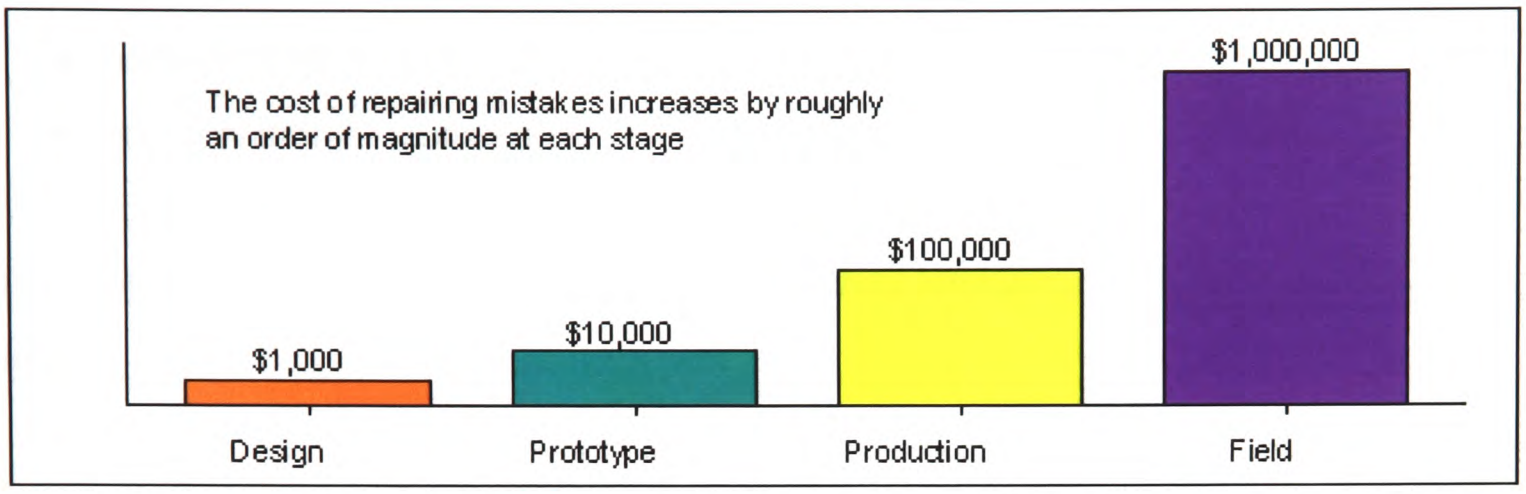

Figure 1.5: Cost of Repairing at Various Stages within Process Design [8]

1.5 Modelling Tools Used in this Research

In the present research context, along with direct experiments on the real lead-refining kettle, two major modelling techniques have been used as the investigation tools.

1. **Computational Fluid Dynamics** – This is based on the numerical solution (using computer) of the governing equations representing the flow phenomena taking place in the system.
2. **Physical Modelling** – This is mainly based on the experimental investigation of the flow phenomena taking place in the system. The experiment is undertaken on a physical model representing the real system, where water represents molten lead and the theory of similitude is used.

Both of these tools have been explained in further details in the next two sections. This is followed by a discussion on the interaction amongst the analysis techniques (experiment on the real lead refining kettle, physical modelling and Computational Fluid Dynamics) employed in this research.

1.5.1 Computational Fluid Dynamics (CFD)

The flow phenomena taking place in real life situation can accurately be expressed mathematically in the form of partial differential equations. These equations are derived from the fundamental laws of physics, namely:

- conservation of mass
- conservation of momentum
- conservation of energy

These represent various physical phenomena and their interactions taking place in the flow domain.

Exact solution of these equations can be achieved analytically only for some simple and idealized problems. However, most of the problems of practical importance are either nonlinear or involve complex geometry, or both, and remain intractable even for the sophisticated analytical techniques. Alternatively, numerical methods can be applied to find the solution. In this approach the governing equations are transformed into algebraic equations, and values of the dependent variables are determined at discrete intervals of space and/or time. However, any reasonable sized problem results in so many algebraic equations, which require solution by computers. Recent advances in computer technology along with the development of sophisticated and robust numerical algorithms have made it possible to solve these equations with sufficient accuracy and ease.

The accuracy of the solution improves with increasing the number of discrete points but in turn it also increases the cost of computation (in terms of computer memory and computation time). CFD is routinely applied to solve a wide range of industrial flow problems including impeller-stirred tanks.

A reliable CFD model that can adequately predict the complex hydrodynamics of impeller-stirred tank is a valuable tool. The design decision based on this can greatly reduce the cost of experiment and eliminates the problems of scale-up [9]. However, development of a

CFD model for stirred tanks involves considerable effort and expertise because of the complex interaction between flow and the moving impeller-tank geometry.

1.5.2 Physical Modelling

Physical model is a system constructed to give adequately close representation of the real world process. Most of the time it involves change in the scale of operation or/and change in the working materials. The theory of similitude (based on geometrical, kinematic and

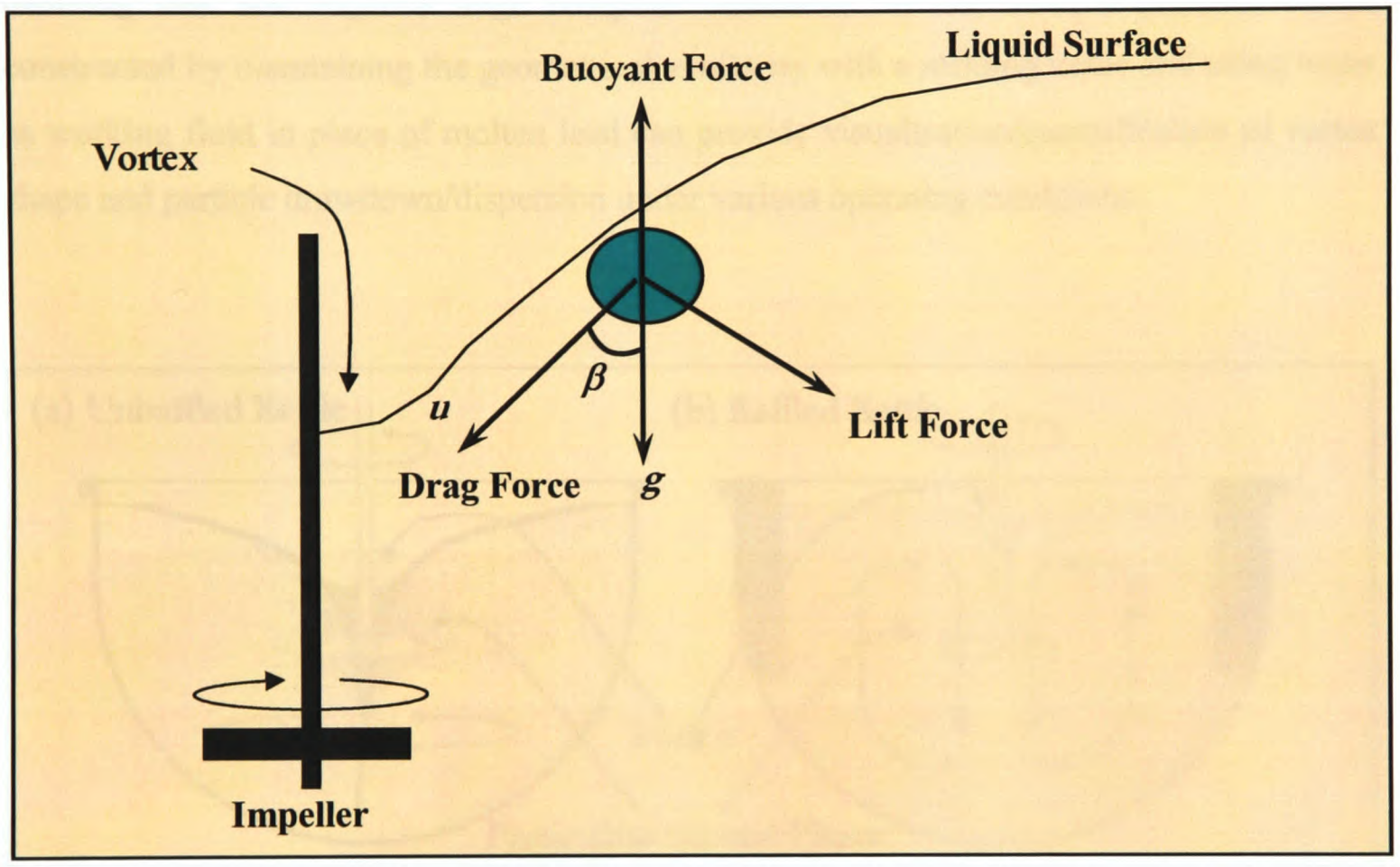

Figure 1.6: Drawdown of Floating Particles in the Impeller-Stirred Tank

dynamic similarities) [10] is used in its development. Ease of experimentation, flexibility in operation, and low set-up costs are the main motivating factors. Often it is not possible to reproduce all the phenomena of the real world process in the physical model. In that case we seek to reproduce the key phenomena (phenomena under investigation) as closely as possible.

A physical model can also be used to carry out experimental measurement (e.g. velocities at various locations, etc) for the validation of computational model. It can also provide valuable qualitative understanding (visualisation) of the phenomena that cannot easily be observed on production plant or cannot easily be simulated using computational model. For example, the drawdown and dispersion of floating dross greatly depends on the shape of the central vortex generated by the impeller-stirred mixing (Figure-1.6). It is impossible to observe/quantify the vortex shape and particle drawdown and dispersion within the real lead refining kettle. At the same time modelling of the multiphase process using CFD is a daunting task and requires huge computer resources. In this case, a physical model constructed by maintaining the geometrical similarity with a refining kettle and using water as working fluid in place of molten lead can provide visualisation/quantification of vortex shape and particle drawdown/dispersion under various operating conditions.

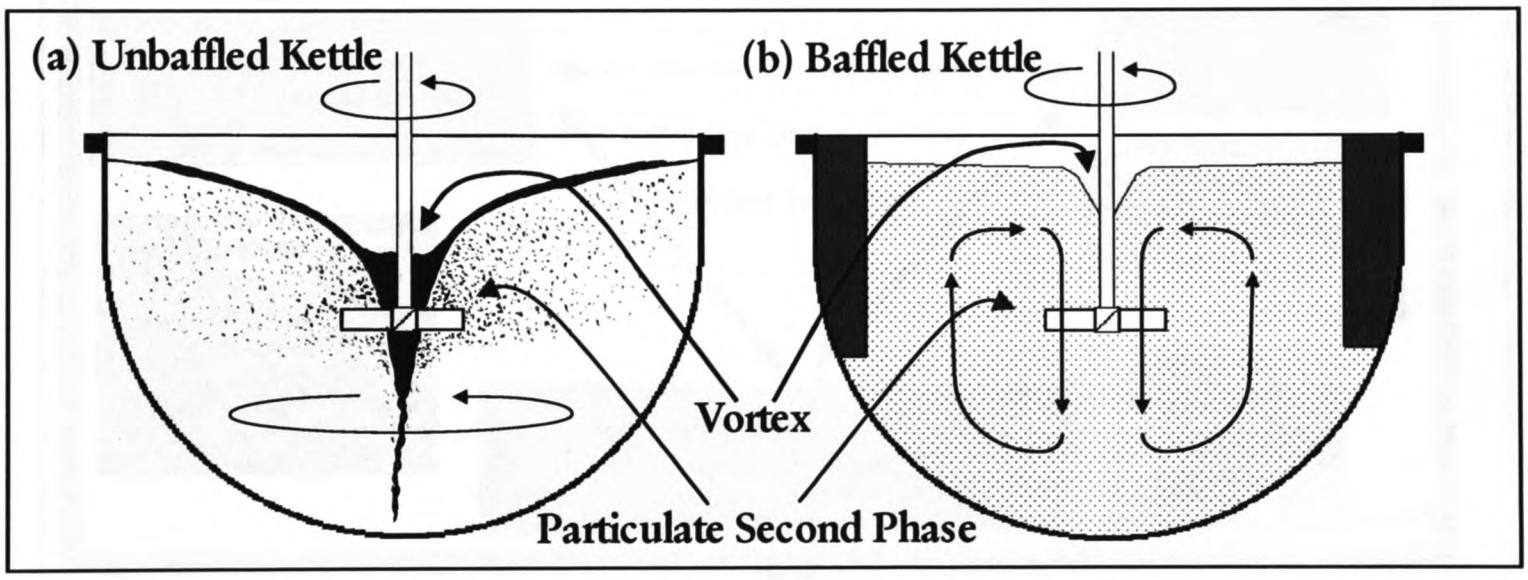

Figure 1.7: Vortex Shape and Distribution of Dispersed Particles in (a) Unbaffled and (b) Baffled Kettles Respectively

Figure-1.7 illustrates the vortex shape and particle distribution under two operating conditions namely unbaffled kettle and baffled kettles.

1.5.3 Interaction amongst the Modelling Tools

The present work is a part of a research effort aimed at developing and validating a predictive Computational Fluid Dynamics (CFD) based model that can simulate the complex hydrodynamics of the impeller-stirred lead refining kettle. The model will have capability of predicting vortex formation and drawdown and dispersion of the particulate second phase (in this case it is floating dross). To achieve this objective, three major techniques of investigations:

- Experiment on real lead refining kettle
- Physical modelling (using water as working fluid)
- CFD modelling

will be used as an integrated tool. As Figure-1.8 shows, information drawn from this will be used to optimise and scale-up the existing refining process.

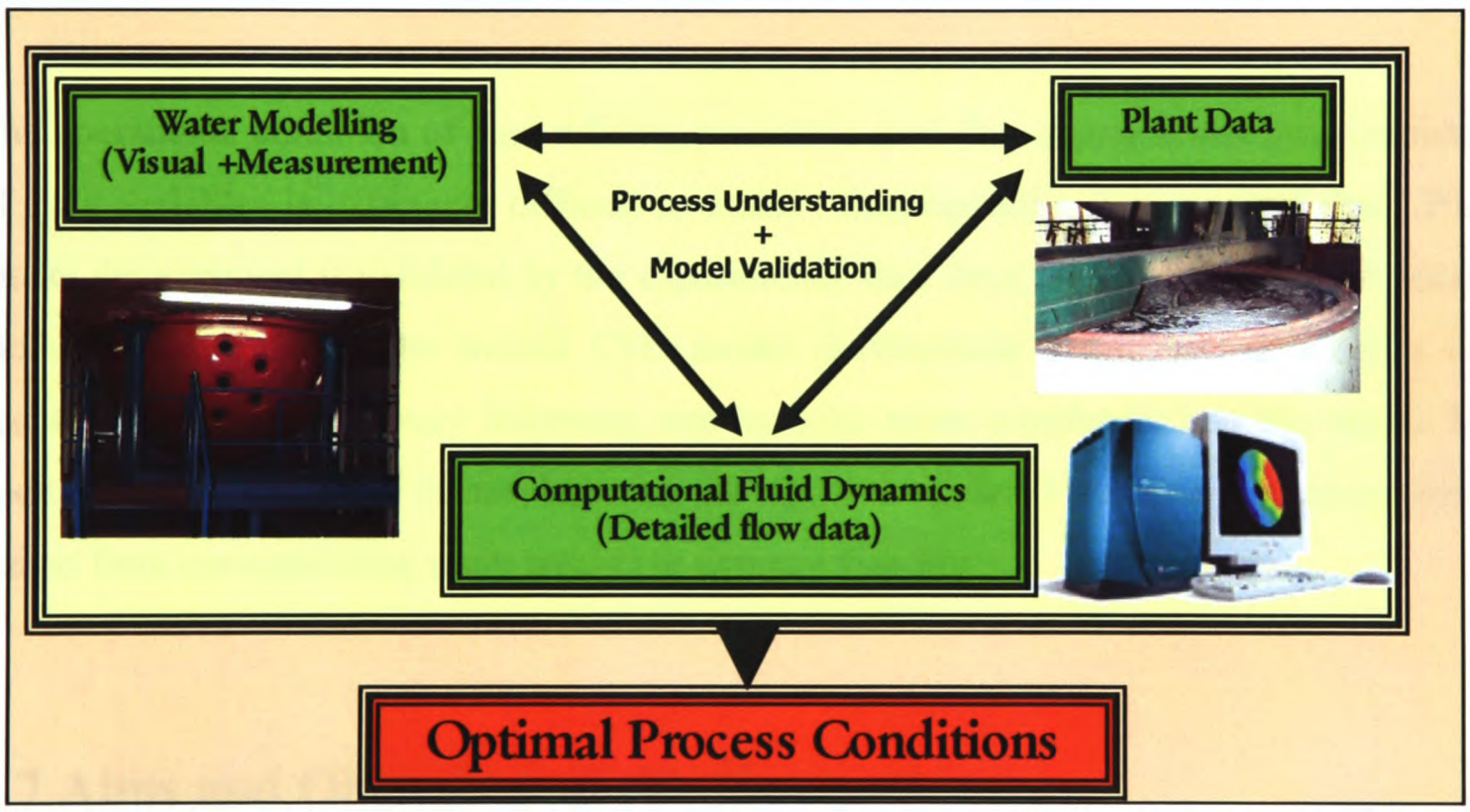

Figure 1.8: Interaction among Modelling, Lab Experiments and Plant Trials

1.6 Research Methodology

Application of CFD modelling into the lead refining process is a challenging task. Flow field in the refining kettle forms a highly interactive and complex pattern where the influence of many factors is not known before hand. Considering the very high density of molten lead with dross layer movement and rotating components; simultaneous implementation of three-dimensionality, unsteadiness, multiphase coupling, turbulence and vortex formation is a formidable task.

Despite all of the progress in computer technology and in numerical techniques, CFD technology cannot be used to model all these completely without making some simplifying assumptions. With these simplifications and limitations of numerical schemes, computational method can only approximate the real physical phenomena. It is hence, essential to validate the computed results against experimental data.

The operational condition of lead refining process is such that experimental measurement of flow variables is extremely difficult to make. Consequently, it is required that CFD model development is validated by the experimental data from the corresponding physical model (water model). The overall CFD model development is planned in a series of successive steps where every following step includes more complexity into the model. In addition, at every stage of its development, the model is validated against experimental data (taken from corresponding water model) to ensure reliability.

1.7 Aims and Objectives of this Research

The overall objective of this research project is to develop a novel predictive model to simulate the flow field generated by the impeller-stirred mixing in the lead refining kettle. Within the scope of this research, ideas and techniques from diverse areas have been brought together to lay a firm foundation for present and any future research. This involves a number of steps and that can be summed up as follows:

1. Carry out a literature survey to identify the state-of-the-art CFD modelling techniques for impeller-stirred mixing.
2. Bring together the fundamentals of physical modelling (the theory of similitude) that forms the basis for experiments on water model.
3. Where possible, carry out experiments to quantify the velocity of lead surface on a production scale lead refining kettle.
4. Carry out experiments of water model to quantify the vortex formation under various operating conditions. Also, monitor readings for power consumption under different operating conditions.
5. Use Acoustic Doppler Velocimeter (ADV) to measure velocities at various locations in the water model.
6. Investigate the capability of CFD modelling techniques to simulate the behaviour of molten lead in the refining kettle. Compare the simulation results with experimental data.
7. Develop a CFD modelling technique that can simulate the vortex formation in the refining kettle. Validate the simulation results with experimental data.
8. Extend the CFD modelling techniques by including the calculated vortex shape into the three-dimensional grid for kettle geometry. Further validate the simulation results with experimental data.
9. Extend the CFD model further to include the particulate second phase to model drawdown and dispersion of floating particles (i.e. dross).

1.8 Major Contributions

The accomplishments of this work are highlighted below in terms of the modelling techniques and its major findings.

1. In the open literature, this is perhaps the first systematic attempt to apply integrated physical models (water model) and CFD for predicting the flow pattern occurring inside the lead refining kettle.

2. Majority of published work on the modelling impeller-stirred vessels is mainly concerned with simple cylindrical shaped vessels. However, this work investigated the flow field in hemispherical shaped vessels (lead refining kettle) for various geometric (unbaffled, baffled, off-centred shaft, etc.) and operating (impeller rotational speed, impeller shaft depth, etc.) conditions.

3. A range of experiments on water model was carried out for various operating conditions. The data for power consumption (Section-4.4.1) and vortex depth (in terms of vortex factor) was presented (Section-4.5).

4. Based on the vortex depth data, it was assumed that vortex factor becomes independent of Reynolds number when impeller rotates above a limit (Section-4.5). This assumption enables us to use water model to approximately reproduce vortex phenomena taking place in the real lead refining kettle.

5. It is reported in the literature that drawdown and dispersion of the floating particulate second phase depends on the Froude number and the density ratio (the ratio of the density difference of fluid and particle to the density of fluid). Hence, by appropriate selection of particulate second phase the water model can be used to study the movement of dross particles of the lead refining kettle (Section-4.5.1).

6. For the velocity measurements at the various locations in the water model Acoustic Dopple Velocimeter (ADV) was used. This is the first time when ADV probe is used in the field of impeller-stirred mixing vessel.

7. Two sets of ADV measured velocity data from two-baffled water model for two different baffles positions are compared. It was found that fluid velocity field in the bulk region is largely axisymmetric. This fact can be used to simplify a time consuming three-dimensional CFD model to the two-dimensional axisymmetric CFD model (Section-4.7.1 & Section-6.4.1).

8. In order to develop understanding of the lead refining process some direct experiments were also carried out. A range of power consumption readings was taken. A novel technique was devised to measure the surface velocity in the lead refining kettle. The floating of a steel ball was monitored through a reference hole. The movement of the steel ball was video recorded and timed, which was then used to calculate the surface velocity (Section-4.8).

9. Feasibility of CFD modelling for the lead refining was established by comparing the results from simplified CFD models with that of experimental data and these found to be encouraging (Section-6.3.1).

10. Rest of the CFD model development was carried out in successive stages of increasing complexity where model development was mainly guided and validated by water model. These steps can be given as follow:
    - First set of CFD simulation used flat surface approximation for the top free surface at air water interface. The three geometrical configurations (unbaffled, baffled and off-centred shaft) were used and validated against corresponding experimental data. It was realised that flat surface approximation affects the accuracy of the simulation results (Section-6.3.2).
    - At next stage, a novel two-dimensional axisymmetric CFD model was developed that could calculate the vortex shape. The calculated vortex depth also exhibited the similar trend as that found in experiment (Section-6.4.1.1).
    - The calculated vortex shape was then used to develop a full three-dimensional CFD model. The simulation results from this model showed very good agreement with the experimental data (Section-6.4.2).

11. The above model was further extended to simulate the mixing behaviour, movement of particulate second phase and drawdown and dispersion of floating particles. The underlying techniques are given below:
    - Simulation for the blending of neutral tracer was used to visualise the mixing pattern and efficiency (Section-6.5).

- The particle tracking was used to identify the relative residence time distribution of particles under various operating conditions (Section-6.6.1).
- To simulate the drawdown and dispersion of particulate second phase a novel strategy developed. This used the three-dimensional geometry with vortex shape where the top layer was considered to be a mixture of particles and water. The simulation was carried out using multiphase CFD solver (Section-6.6.2).

Among all the above simulations, CFD modelling of the drawdown and dispersion of floating particulate is the most important because there is no published work available.

1.9 Outline of Thesis

The organisation of contents for this thesis is summarised as follow:

Chapter-2 presents the literature review on the computational modelling techniques for the impeller-stirred tank. The classification of the literature is largely based on the type of impeller modelling technique used.

Chapter-3 brings together the fundamentals of physical modelling that form the basis of experiments on water model. This also includes a review of previous physical modelling work done for the lead refining kettle. A detail of present water modelling setup and device used to measure the velocities at various locations in the water model is also covered.

Chapter-4 presents the experimental techniques used for measuring the various quantities on lead refining kettle and also for corresponding water model. The results are presented and analysed to identify the most significant factors that influence the flow field in the lead refining kettle.

Chapter-5 introduces the fundamentals of mathematical techniques used to develop the Computational Fluid Dynamics (CFD) algorithm. Here focus is on the finite-volume method, which is the main technique employed by most commercial CFD software.

Chapter-6 discusses the strategy and implementation of computational modelling. The simulation results obtained under various operating conditions are further analysed and discussed.

Chapter-7 finally summarises the main points and findings from the research. Also, this chapter presents the methodology for kettle design and gives recommendations for the future research.

Chapter 2

LITERATURE REVIEW - CFD MODELLING OF IMPELLER STIRRED VESSELS

2.1 Introduction

Impeller-stirred mixing is one of the most widely used processes throughout the chemical and allied industries. Its fundamental importance has led to a great deal of interest in exploiting the power of Computational Fluid Dynamics (CFD) to simulate the associated flow phenomena. As it can be seen from the available literature, for example [11-14], that over the past two decades a wide range of CFD modelling techniques have been developed to predict the associated flow profile in stirred tanks.

This chapter presents a detailed literature review on the CFD techniques that have been used for the prediction of impeller-stirred mixing. From the review of literature, it is clear that representation of a rotating impeller in the CFD modelling is the main challenge and for that, a number of techniques have been devised. The various modelling techniques, as given below, for impeller rotation have been used as the basis of presentation here.

- Experimental Boundary Conditions Based Model
- Blade-Element Theory Based Model
- Rotational Reference Frame Method
- Snapshot Method

- Inner-Outer Method
- Multiple Reference Frame Method
- Moving-Deforming Mesh Method
- Sliding-Mesh Method

2.1.1 Experimental Boundary Conditions Based Model

Flow field in an impeller-stirred tank is complex and inherently unsteady. Experimental determination of associated flow field would be very expensive and time consuming, whereas CFD model for this purpose is an economical option. However, the complex blade geometry and its motion relative to baffles pose considerable difficulties in developing a CFD model that can include the computation in the impeller region as well.

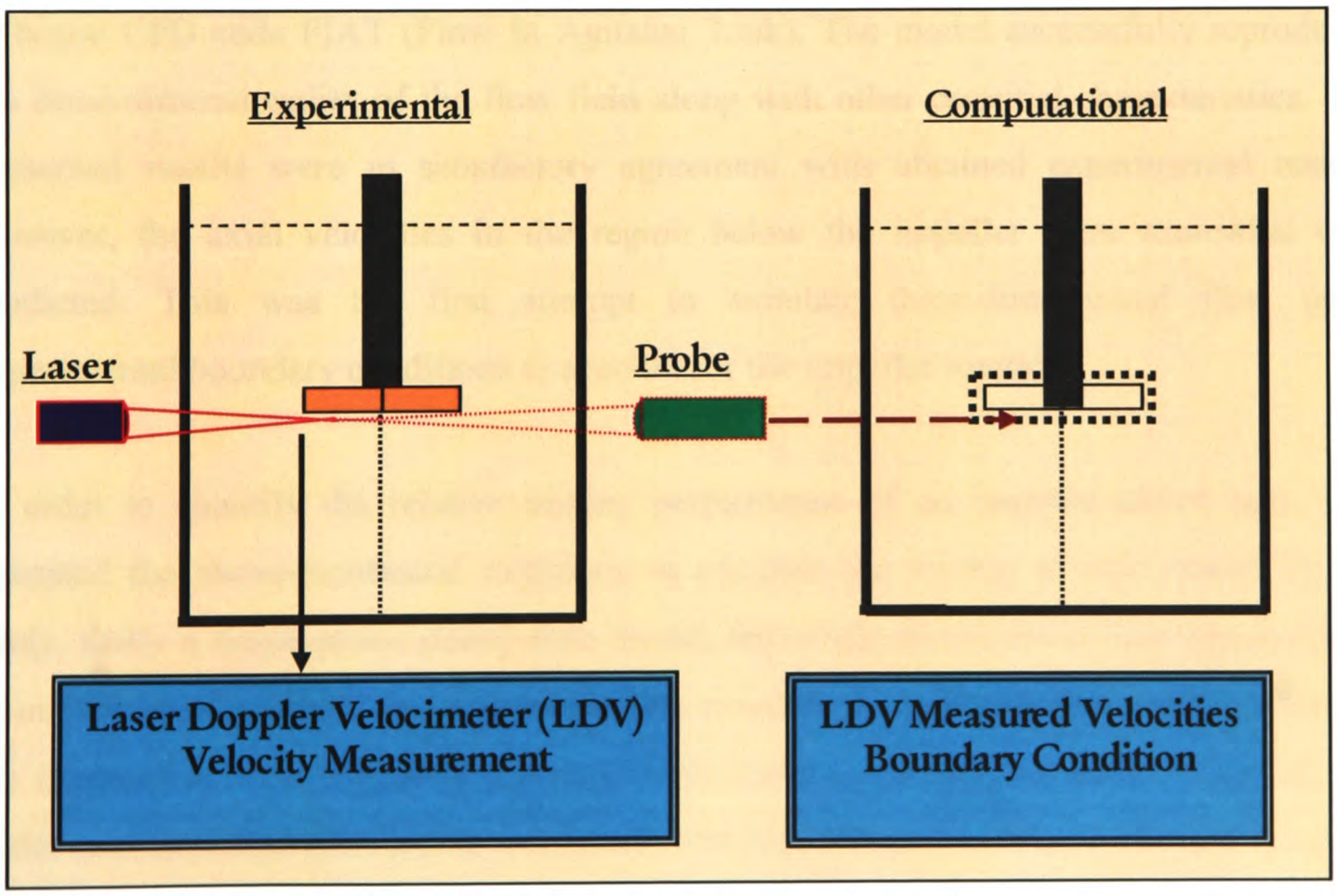

Figure 2.1: Experiment Based Impeller Model

One of the traditional approaches is to treat impeller swept region as a black box and exclude it from the computational domain. The representation of a rotating impeller is achieved by setting experimentally measured, using Laser Doppler Anemometer/Velocimeter (LDA/LDV) [15], velocities and turbulence on the surface of impeller swept region. Then computation is carried out for rest of the tank. Figure-2.1 shows this modelling strategy.

Another method similar to the above involves representing the impeller action as body forces through assigning experimentally measured, using LDA/LDV [15], momentum source distributed over the impeller region. The value, assigned for the impeller region, is treated as a stationary boundary condition for the rest of the computational domain.

An example of the above is the use of LDA for experimental investigation [15] and subsequent use of gathered data for CFD modelling [16]. In these simulations, boundary conditions were imposed at the bottom surface of impeller swept region and standard two-equation k-ε turbulence model was used. The computations were carried out using an in-house CFD code FIAT (Flow In Agitated Tank). The model successfully reproduced the three-dimensionality of the flow field along with other essential characteristics. The presented results were in satisfactory agreement with obtained experimental results; however, the axial velocities in the region below the impeller were somewhat over predicted. This was the first attempt to simulate three-dimensional flow using experimental boundary conditions to account for the impeller rotation.

In order to quantify the relative mixing performance of an impeller-stirred tank, [17] extended the above-mentioned technique to compute the mixing of inert tracer. In this study, firstly a single-phase steady-state model, for which experimental data was available from [15], was simulated and validated. This simulation result was then used to calculate the transient mixing of passive tracer. For the computation of this transient mixing, the initial condition was specified as zero tracer concentration everywhere in the tank except at the feed cell, where the concentration was set equal to the tracer input concentration. A zero flux boundary condition at the walls was used for mixing calculations. The simulated

mixing performance for the pitched blade turbine was in very good agreement with the experimental data.

The influence of different impeller configurations on the fluid field was reported in [18]. Here the flow fields generated by impellers with eight different geometric configurations were studied using Laser Doppler Anemometer. The measured flow data near the impeller was presented in a form suitable for specifying boundary conditions into a CFD model. It was observed that two-equation k-ε turbulence model adequately predicted the bulk flow profile in the case of all the impellers.

Based on the data presented in [18], a detailed study of the effect of different numerical schemes on the flow field prediction was carried out in [19]. Here six different impeller configurations were studied using two-dimensional CFD models. For these simulations, relative performance of three numerical schemes, namely, upwind scheme, hybrid scheme, and power-law scheme was evaluated. CFD simulations were run using the SIMPLE algorithm and the standard two-equation k-ε turbulence model. In these simulations the effects of grid distribution, initial guess, under-relaxation, internal iterations, etc., on the rate of convergence and solution qualities were investigated. It was found that predicted values were qualitatively in good agreement with the experimental data. The comparison of three numerical schemes showed that power-law scheme was more robust and accurate as compared to the hybrid, and upwind schemes. It was also observed that a suitable combination of initial guess value for flow variables and underrelaxation parameter enhanced the rate of convergence.

In order to carry out a detailed sensitivity analysis of the individual components of the boundary conditions on flow field in an impeller-stirred tank, [20] took a somewhat different approach to model the impeller. Here it was modelled as a thin disk with inlets on both the surfaces. The boundary conditions for velocities and turbulent quantities on both the upper and lower surfaces of the impeller discharge were specified through experimental data. CFD simulations were run, using SIMPLEC algorithm and hybrid discretisation scheme, and compared to two experimentally determined sets of data. It was observed that

there was almost no apparent interaction between the velocity and turbulence fields. The turbulent kinetic energy dissipation rate was at a maximum close to the impeller. Within this region, the average dissipation rate was five and half times greater that the average dissipation rate in the tank. In this study, it was concluded that a very accurate specification of boundary conditions at the impeller swept surface is crucial for correct prediction of flow profile.

In [21], the impeller was modelled as an empirically determined (LDA measured) body force by imposing distributed momentum source in impeller swept region. This was perhaps the first paper to present a three-dimensional computation of the flow in a turbine stirred tank. In this study, the calculated single-phase flow pattern was further used as a basis for predicting the chemical yield in the tank.

A series of computational models was presented in [22] for impeller stirred tank. These also included an empirically determined source term approach to model the presence of the impeller where the measured value for velocity components was set through the impeller swept volume. All other variables were solved for within that volume as for any other part of the flow. For these simulations, two different sets of boundary conditions were used. For the first set, all three velocity components were specified at the top and bottom surfaces of the impeller region, and the tangential velocities at the outer vertical cylindrical wall of the volume swept by impeller. For the second set, the radial velocities were specified at the outer vertical cylindrical wall of the volume swept by impeller. A detailed comparison of results was also carried out. Discussion on these results will be covered in later section.

2.1.2 Blade-Element Theory Based Model

Another method to model the impeller blade action on the surrounding fluid is to assign quadratic sources to the momentum for the impeller swept volume. Similarly, the presence of baffles is modelled by assigning quadratic sink to the momentum for the baffle region. This method requires blade element theory to calculate the momentum contributions arising from lift and drag terms. The values for lift and drag coefficients need to be obtained using experiment. Further details on this method can be found in APPENDIX-A.

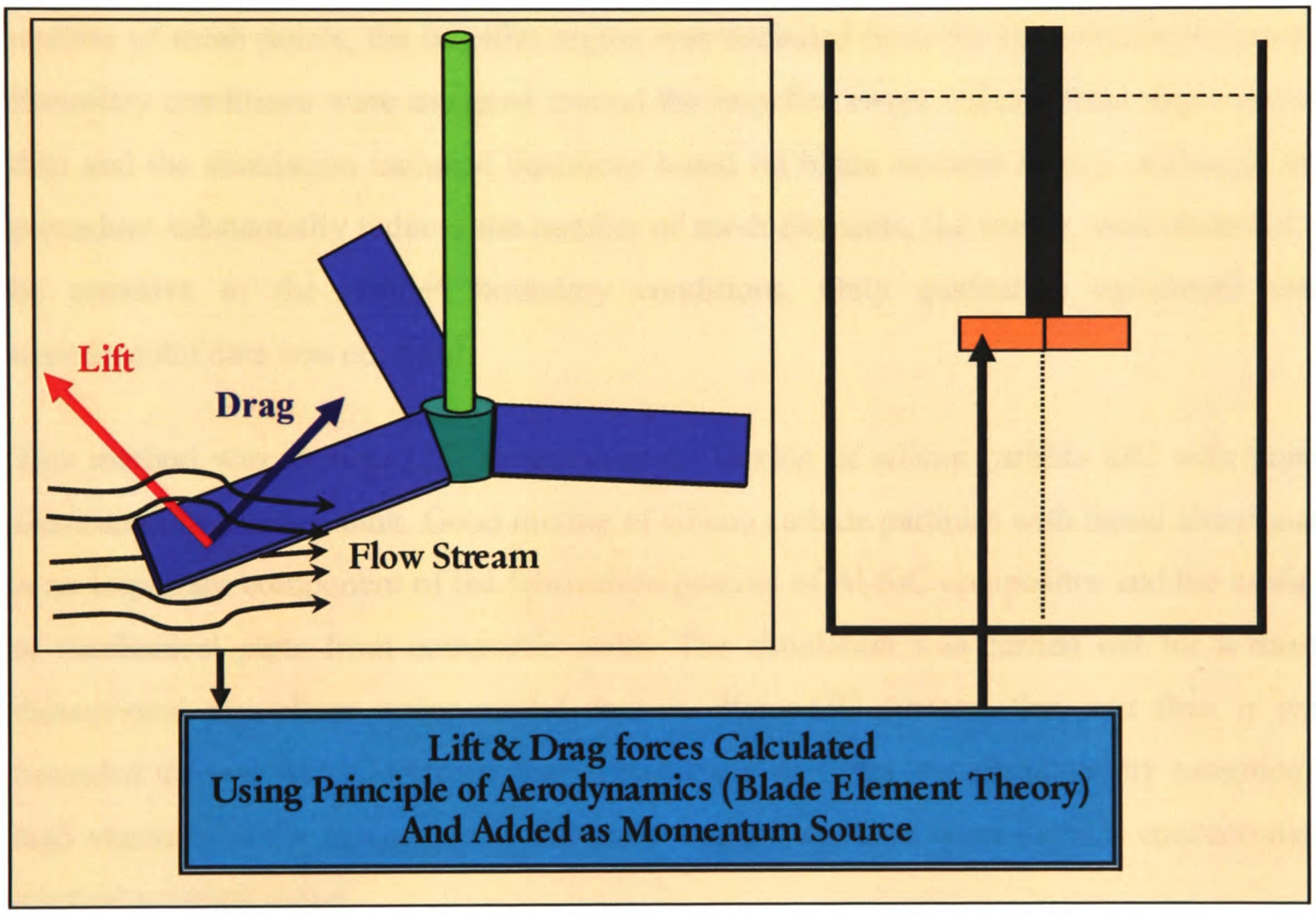

Figure 2.2: Blade-Element theory Based Impeller Modelling

The first effort to develop a model of impeller stirred vessel using blade-element theory was [23]. In order to model a chemical impeller-stirred reactor a two-dimensional axisymmetric approach was followed. In that the impeller and baffles were treated as time-averaged angular or axial momentum (or both depending on type) source/sink quantities incorporated in appropriate source term of Navier-Stokes equations describing flow field. The simulations were run using the CFD code PHOENICS, using various geometrical

features of impeller and vessel. The presence of oxidant in the reactor in the form of gas bubbles was also investigated to determine its distribution, which affected the rate of reaction, and also its effects on impeller performance. Dispersion of gas bubbles in mixture was modelled using Algebraic Slip Model (ASM). In general, the predicted results were in good agreement with available experimental data but some discrepancies were reported in the predicted turbulence quantities.

A combination of experimental data (LDV data) and blade element theory for three-dimensional model of an impeller-stirred vessel was used in [24]. In order to reduce the number of mesh points, the impeller region was excluded from the computational domain. Boundary conditions were assigned around the impeller swept volume from experimental data and the simulation included equations based on blade element theory. Although this procedure substantially reduces the number of mesh elements, the results were observed to be sensitive to the applied boundary conditions. Only qualitative agreement with experimental data was obtained.

This method was used in [25] to simulate the mixing of silicon carbide SiC with liquid aluminium in a stirred tank. Good mixing of silicon carbide particles with liquid aluminium is an important component of the fabrication process of Al-SiC composites and the casting of mechanical parts from composite melts. The simulation was carried out for a three-dimensional two-phase water model, that is Water-SiC system, first and then it was extended for real Al-SiC furnace. Sedimentation of particles was simulated by assigning a high viscosity to the second phase and removing gravity force when particle concentration reached a critical value.

In a similar effort [26], a one phase model was developed. In this model mixture was considered as one fluid, and the SiC flow was differentiated from the main mixture flow by a slip velocity, calculated from the balance of forces exerted on the particles. The advantage of the later modelling was that it took much less computing time and could accommodate a distribution of particle sizes instead of being limited to one size. The shape of the furnace for both of the above simulations was rectangular, it was equipped with three impellers, and simulations were run using the commercial code PHOENICS.

A similar parametric study to find out optimum geometrical design parameters and operating conditions which could give a homogeneous mixture and a high heat transfer efficiency [27]. In this work a number of three-dimensional simulations were carried out for two-phase Al-SiC medium in a holding tank with a truncated cone shape that was equipped with an off-centre impeller. Simulations were run using the commercial code FLOW3D. It was observed that increasing impeller size and impeller speed and decreasing melt height and cone angle improve the mixture homogeneity.

2.1.3 Rotating Reference Frame

In the absence of baffles a simpler method employing rotating frame of reference can be used, provided that tank walls are axially symmetrical and co-axial with the impeller shaft. Figure-3.3 shows an unbaffled tank with central shaft where rotating frame method can be

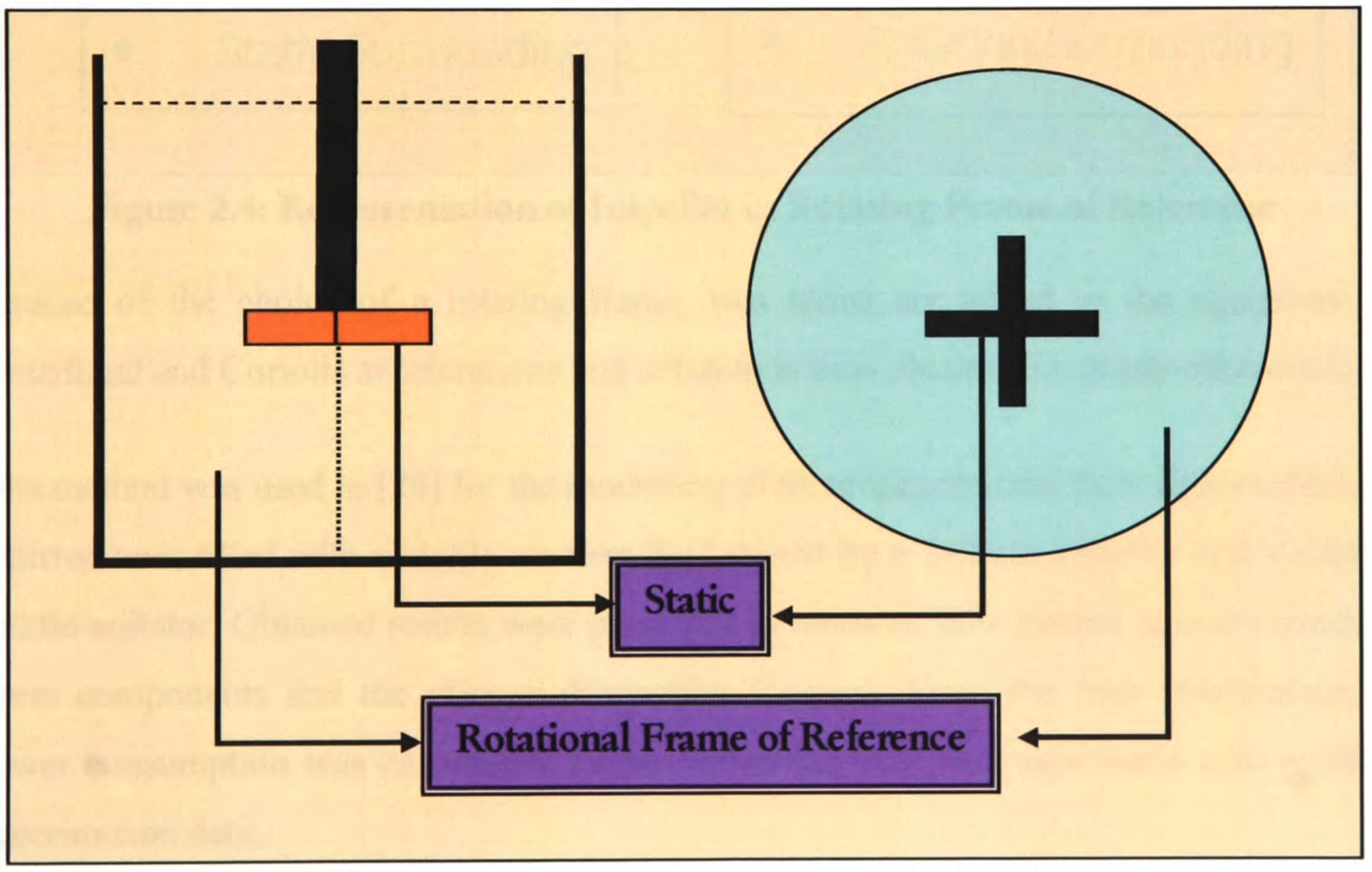

Figure 2.3: Unbaffled Tank Where Rotating Reference Frame is used

applied. In this approach, no experimental boundary conditions are required, only detailed geometry of impeller and surrounding region is required to be created. For the CFD

computation, the Navier-Stokes equations are written in a rotating coordinate system. The rotational direction of reference frame is considered to be opposite to the impeller rotation, and the impeller is considered to be static. This is illustrated in Figure-2.4. Furthermore,

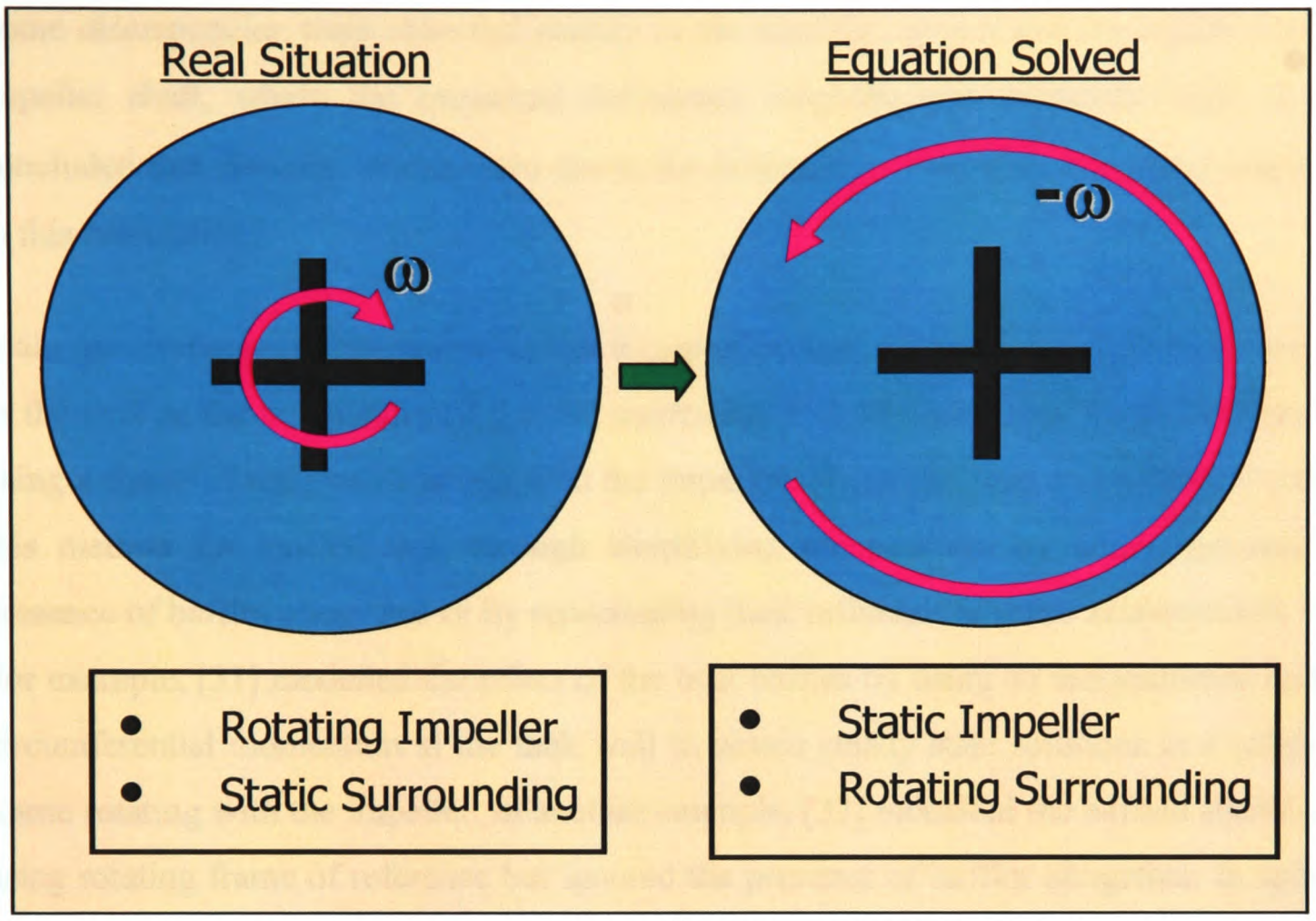

Figure 2.4: Representation of Impeller in Rotating Frame of Reference

because of the choice of a rotating frame, two terms are added to the equations: the centrifugal and Coriolis accelerations and solution is then obtained in steady-state mode.

This method was used in [28] for the modelling of three-dimensional flow characteristics of a stirred tank filled with a highly viscous fluid stirred by a 2-blade-impeller and a 2-blade-paddle-agitator. Obtained results were presented in terms of flow pattern at every point, the stress components and the viscous dissipation function. From the later information, the power consumption was calculated. These results showed good agreement with available experimental data.

A detailed experimental measurement of the flow for an unbaffled tank, stirred by an eight-bladed-flat-paddle impeller was carried out by [29]. Using geometry and results from this work, [30] reported a detailed simulation result. Simulations were run using the rotating

frame of reference technique using the commercial code FLUENT. The details of modelling were presented and the simulation results were compared with experimental data. Mean velocities and turbulent energy were in good agreement with experimental data. Some discrepancies were observed mainly in the impeller stream and the region near the impeller shaft, where the measured turbulence intensity was relatively high. It was concluded that these deviations were due to the limitations of standard k-ε model employed in this calculation.

Main disadvantage of this method is that it cannot be used directly when baffles are present in the tank as the computational domain associated with baffles cannot be immobilised by using a frame of reference rotating with the impeller. There has been some effort to extend this method for baffled tank through simplifying the problem by either ignoring the presence of baffles altogether or by representing their influence in some axisymmetric way. For example, [31] modelled the effect of the tank baffles by using an axisymmetric sink of circumferential momentum at the tank wall to obtain steady state solutions in a reference frame rotating with the impeller. In another example, [32] modelled the baffled stirred tank using rotating frame of reference but ignored the presence of baffles altogether. In spite of its simplicity, this approach can be used to obtain reliable results only where impeller-baffle interactions are very weak.

2.1.4 Snapshot Method

In real impeller-stirred vessel, impeller blades continuously rotate with respect to surrounding stationary vessel. Interaction creates a flow field inside the vessel that becomes periodically repeating after some time and hence taking a snapshot at any particular instant in time can give details of flow profile that represents the overall pattern.

Based on the above, a computational model called the snapshot method has been developed [33]. In this method, impeller blades are fixed at one particular position with respect to the baffles. In reality blades rotate at this particular time and cause displacement of fluid from the front face of blades and equivalent suction from the back face (as fluid rushes to fill the

gap caused by the movement of the blades). These phenomena of displacement and suction of fluid by rotating blade is simulated by snapshot method. In snapshot method, impeller is considered to be fixed at one position. In order to mimic the rotation, on front and back faces of the impeller blades mass source and sink are attached respectively. Furthermore, to ensure mass conservation appropriate source and sink terms (momentum, energy) need to

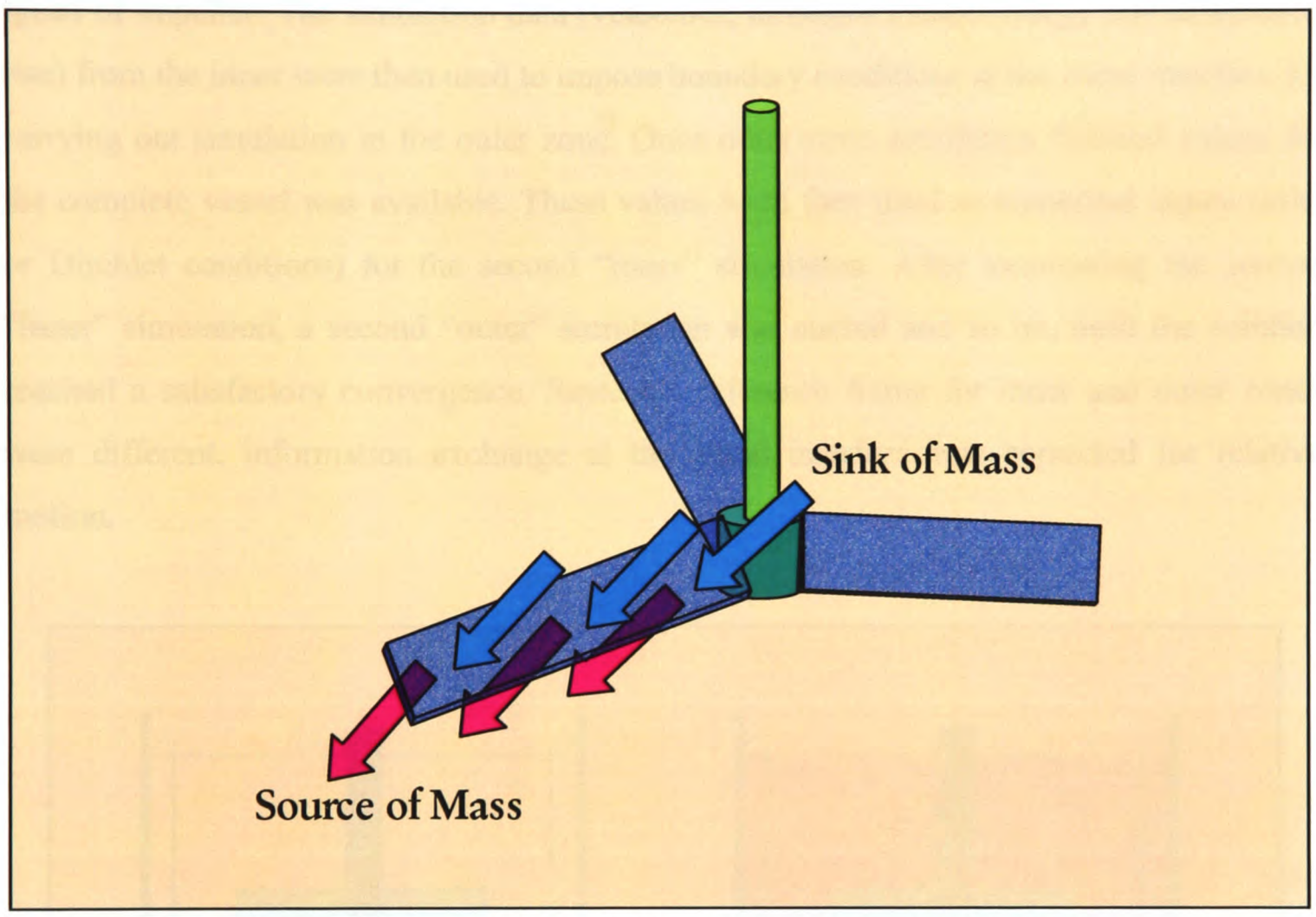

Figure 2.5: Impeller Modelling Using Snapshot Method

be defined for all the other variables as well. Periodic nature of the flow is used to reformulate the time derivative in terms of the spacial gradient and incorporated as a source term in the Navier-Stokes equation. This modelling strategy is illustrated in Figure-2.5.

2.1.5 Inner-Outer Method

A novel method was proposed by [34] to simulate the flow profile in an impeller-stirred vessel. In this, the whole vessel volume was divided into two concentric zones. Inner zone enclosed the impeller and the outer zone was attached with rest of the geometry. First trial simulation was carried out in inner zone using rotating frame of reference with rotational speed of impeller. The simulation data (velocities, turbulent kinetic energy and dissipation rate) from the inner were then used to impose boundary conditions at the zonal interface for carrying out simulation in the outer zone. Once outer zone simulation finished values for the complete vessel was available. These values were then used as numerical inputs (inlet or Dirchlet conditions) for the second "inner" simulation. After terminating the second "inner" simulation, a second "outer" simulation was started and so on, until the solution reached a satisfactory convergence. Since the reference frame for inner and outer zones were different, information exchange at the zonal interface was corrected for relative motion.

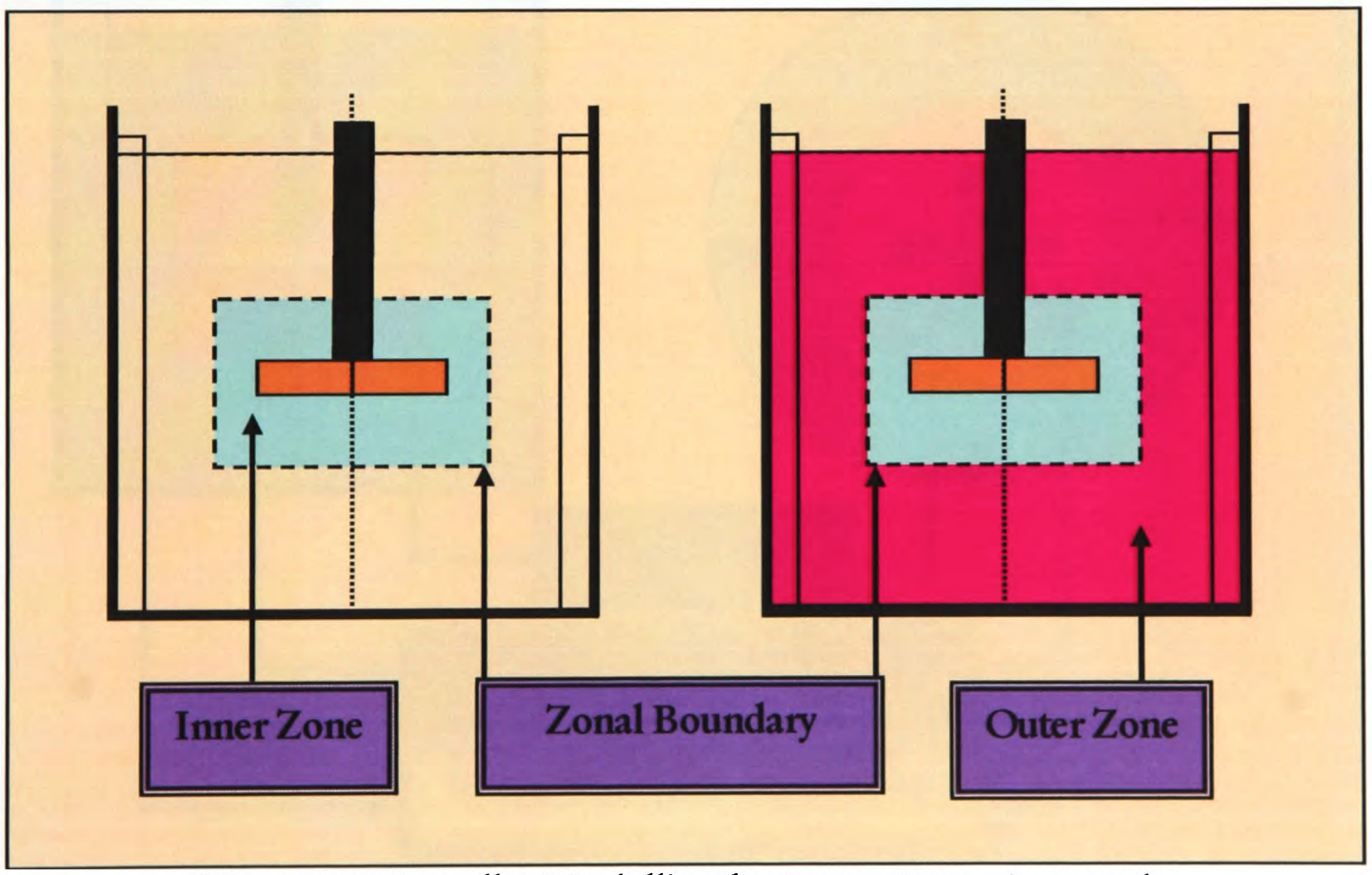

Figure 2.6: Impeller Modelling by Inner-Outer Approach

Figure-2.6 shows the two zones used in this modelling. Reported results were in satisfactory agreement with experimental observation. The paper reported a total of 16,000 iterations and a total CPU time of about one hundred hours on an IBM-3090 "main frame" or on a RISC workstation. Although this method doesn't require input from experiments, the simulation time is very high in comparison with experimental method of impeller modelling.

2.1.6 Multiple Reference Frame Method

A new steady-state computational approach was presented by [35] to predict the detailed flow field in the whole tank and the impeller region. The method uses two frames of reference. The first one rotates at the impeller speed and is used to compute the flow field within the impeller region in a steady-state manner; the second frame is stationary and is

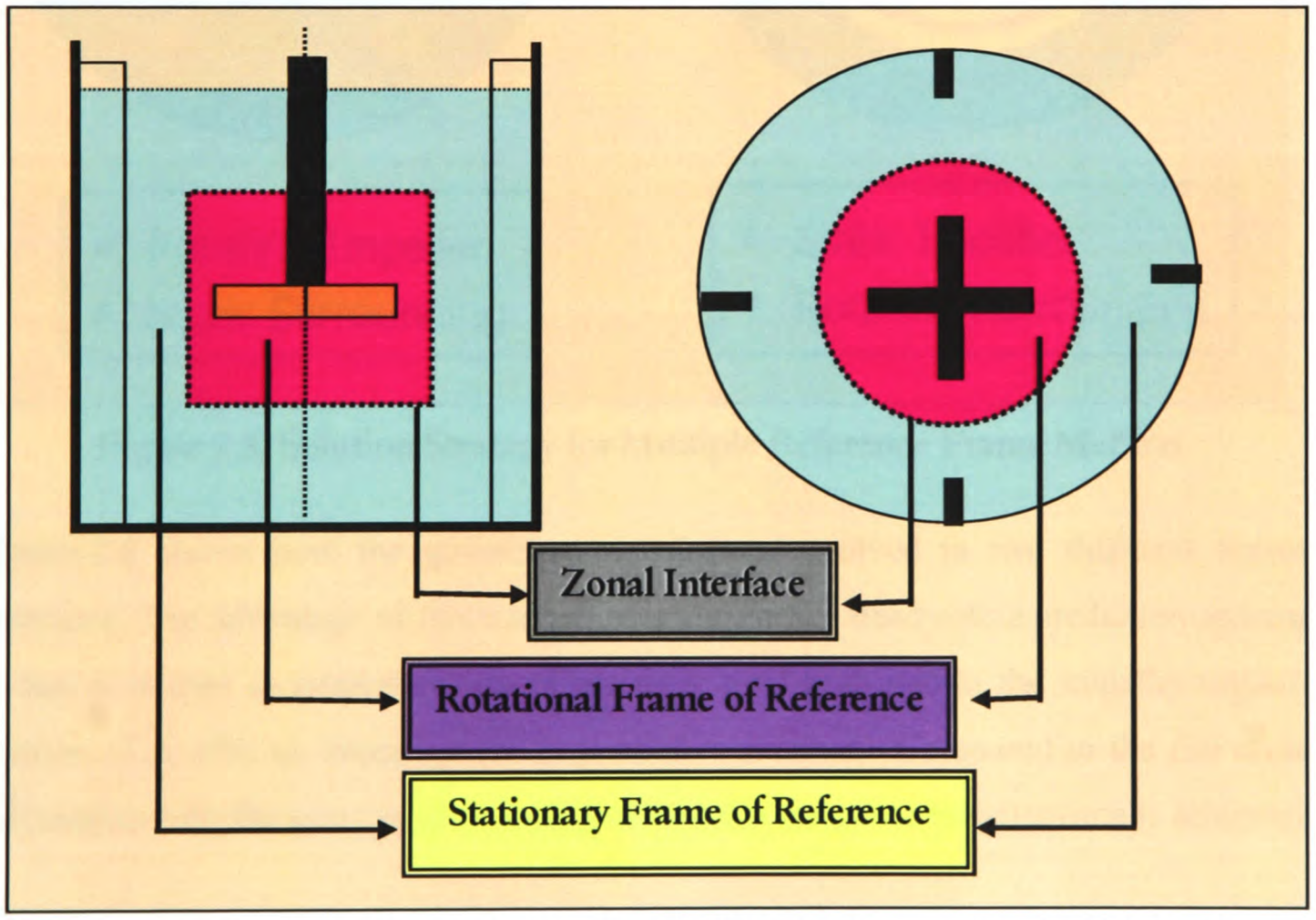

Figure 2.7: Impeller Modelling by Multiple Reference Frame Method

used to compute the flow away from the impeller region. The mesh fitted to the whole geometry always remains static. At the interface between the two computational regions that are placed on two different frames of reference, the two solutions are matched locally via the appropriate velocity transformations from one frame to the other in an implicit manner ensuring conservation. Figure-2.7 gives the schematic representation of this method.

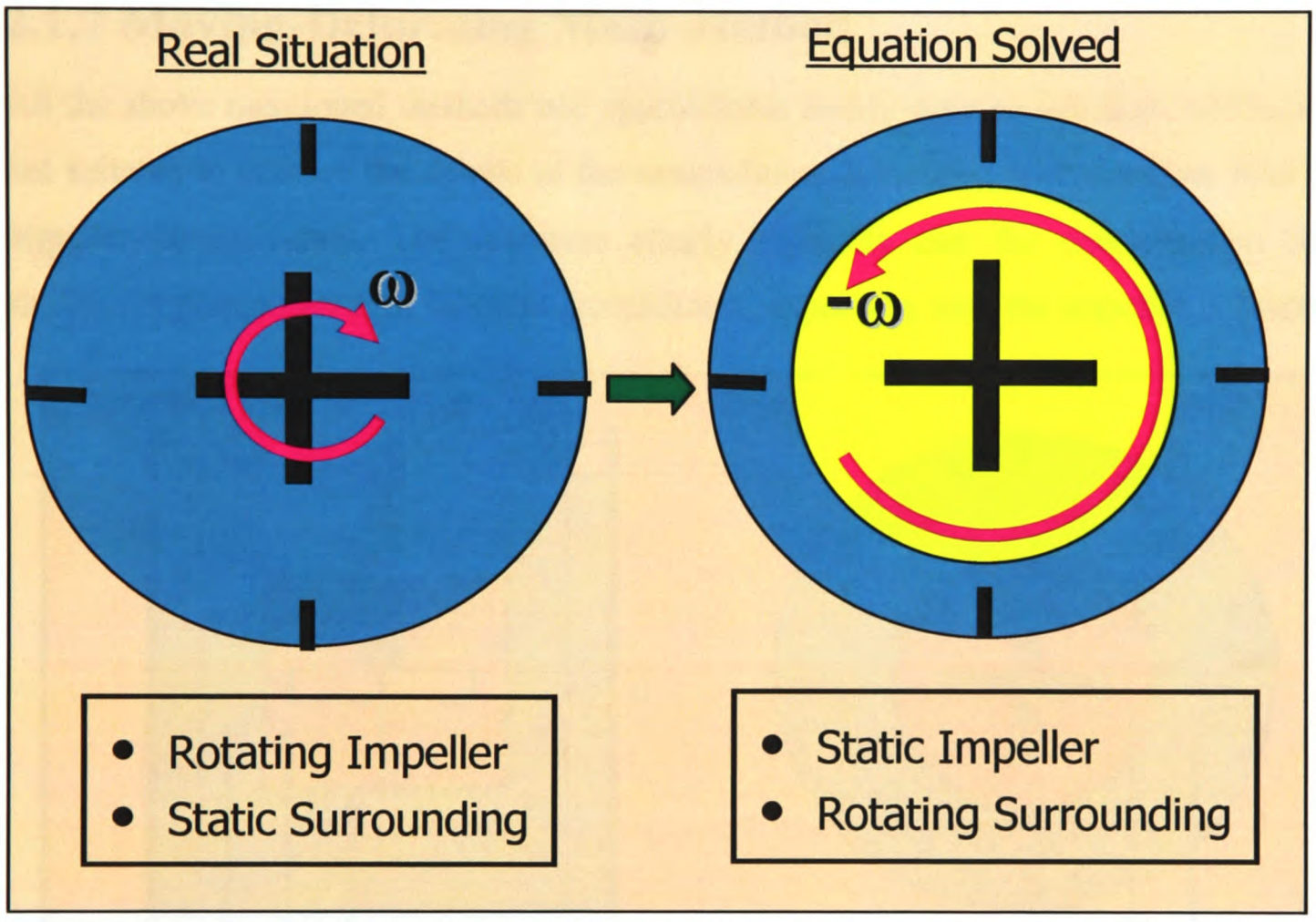

Figure 2.8: Solution Strategy for Multiple Reference Frame Method

Figure-2.8 shows how the governing equations are solved in two different frames of reference. The advantage of this method over the earlier steady-state prediction approaches is that it is able to predict details of the flow field both within the impeller region and outside of it, with an improvement in predictive accuracy. Compared to the full unsteady calculation with the same mesh, a saving of over ten times in computer time is achieved.

The main difference between inner-outer approach and multiple reference frame method is that the former simulation proceeds in successive stages; starting from inner domain to outer domain and so on and each zone providing boundary conditions data for other zone

till the desired convergence is reached. The later simulation proceeds simultaneously for both the domains and information exchange takes pace at the domain interface implicitly taking account of different reference frames for both domains and ensuring global mass conservation for each domain.

2.1.7 Moving-Deforming Mesh Method

All the above mentioned methods use approximate steady-state simulations, and hence are not suitable to capture the details of the unsteadiness associated with the flow field in the impeller-stirred vessel. The literature clearly indicates that the consideration of this significant phenomenon of inherent unsteadiness, especially near the impeller is essential if

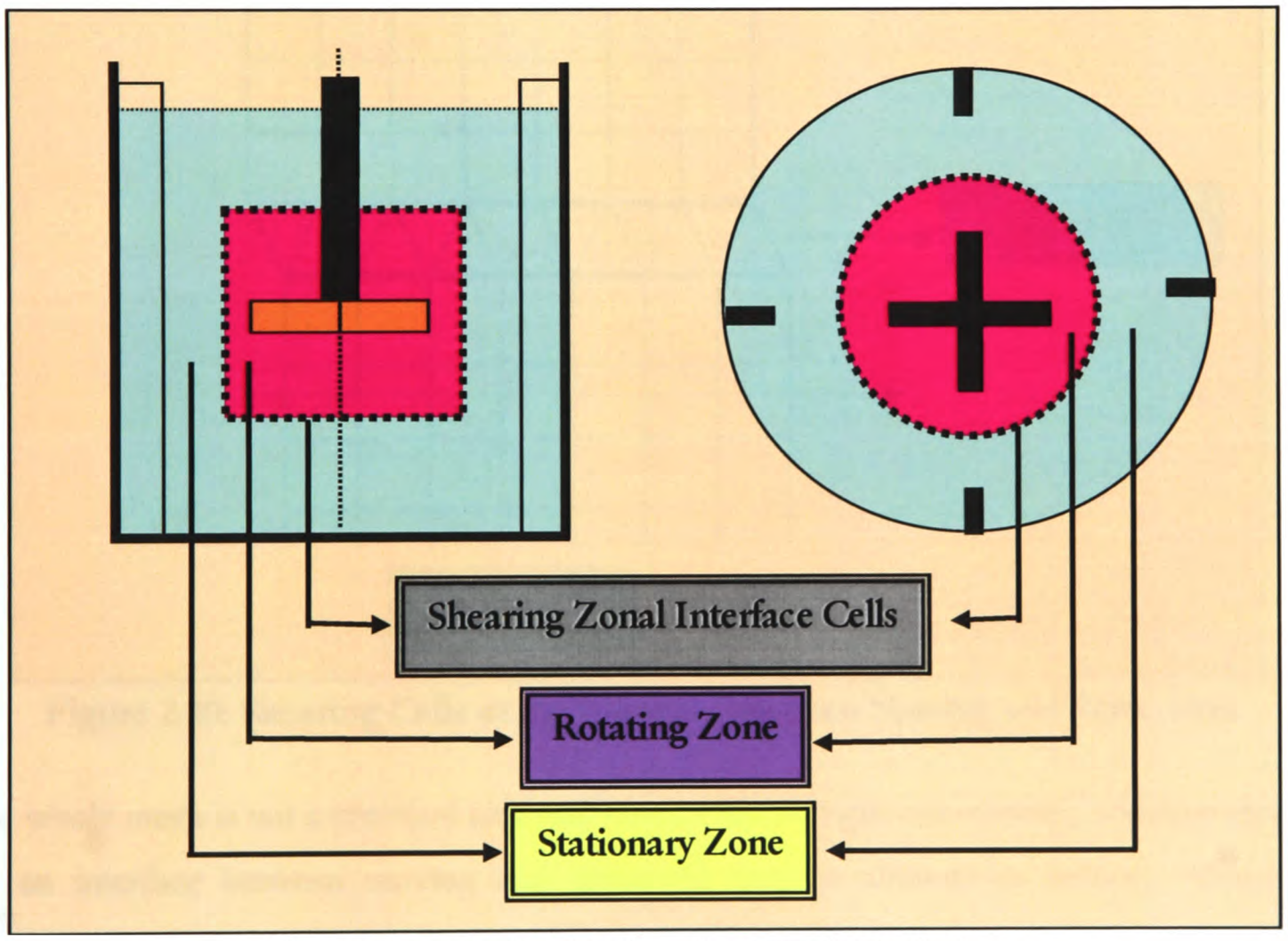

Figure 2.9: Moving Deforming Mesh Technique

accurate predictions are to be made [36]. Only recently have methods becomes available to calculate the flow around an impeller blade using the full time-dependent Navier-Stokes

formulation that can simulate the unsteadiness in sufficient detail. Moving-Deforming Mesh technique is an example of such developments. For this model only the geometry and mesh of the system is required to be created in detail, no experimental data is required for the boundary conditions. Simulations are run in full transient mode that also captures any unsteadiness present in the system. The Figure-2.9 illustrates the techniques involved in moving deforming mesh method.

A detail of moving-deforming mesh technique to simulate the flow in an impeller stirred vessel was presented in [37]. In this method a single grid is used to span both stationary and moving part and allows grid to deform with the moving part (see Figure-2.10). Deforming

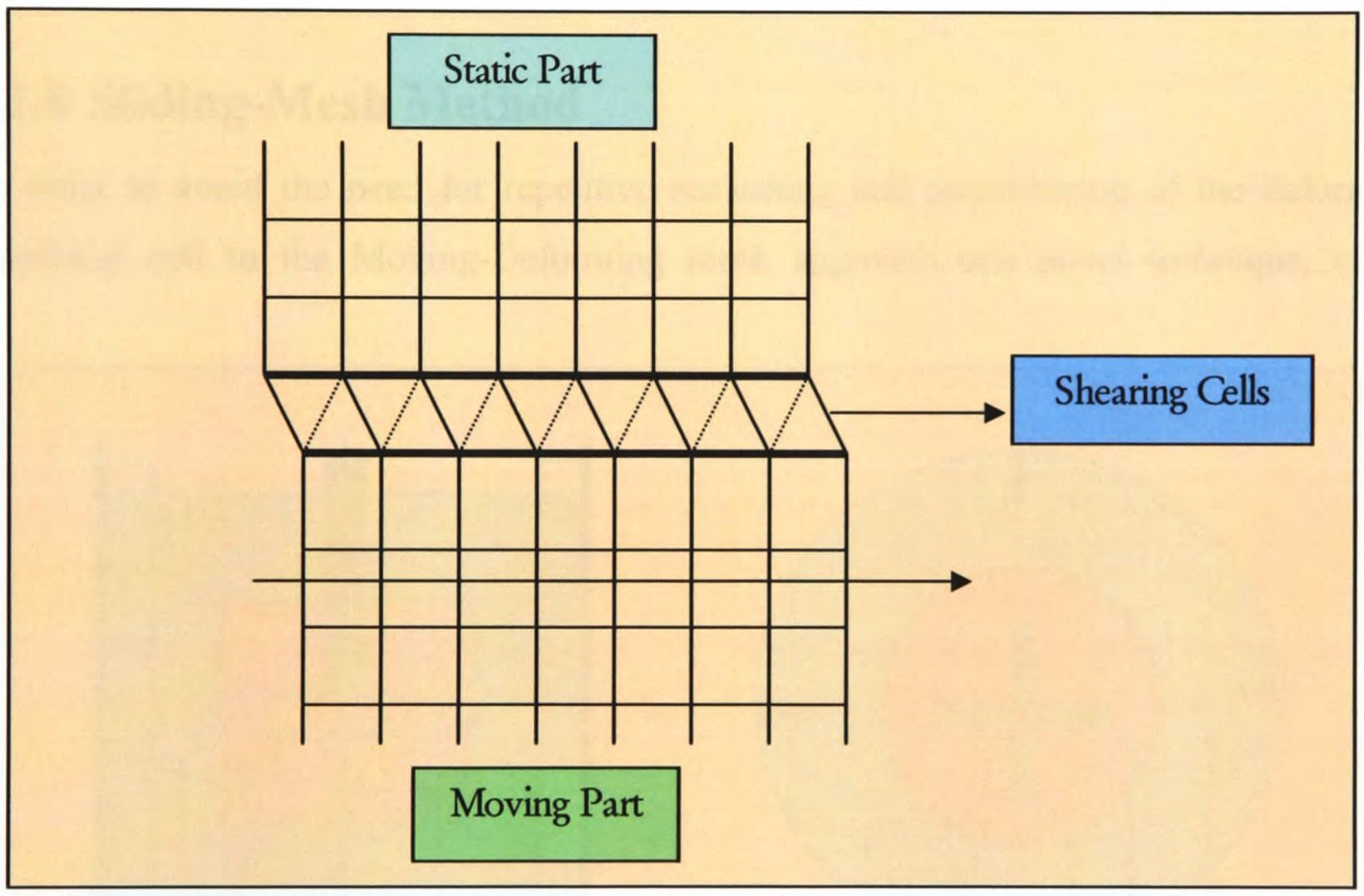

Figure 2.10: Shearing Cells at the Interface between Moving and Static Part

the whole mesh is not a practical idea and hence only a single row of cells, which is chosen as an interface between moving and stationary part, is allowed to deform. When the deformation of these interfacial cells reaches a pre-set limit, the grid is snapped back by one cell. As interfacial cells are allowed to skew with the movement of impeller, accuracy of solution may degenerate. To overcome this disadvantage shearing of the cells is kept low

by periodic snapping and selecting interfacial row in the region where variations of the flow variables are small. With this strategy, simulation is run in transient mode.

The use of this technique along with the sliding mesh technique (to be discussed later) have been discussed in [36] (also quoted earlier) but it is not clearly mentioned that which method has been used to run the simulations. The authors compared the obtained results with steady-state calculations, observed a large discrepancy in the results, and concluded that it was only because steady-state calculations ignored the effect of unsteadiness.

2.1.8 Sliding-Mesh Method

In order to avoid the need for repetitive remeshing and renumbering of the deforming interfacial cell in the Moving-Deforming mesh approach one novel technique, called

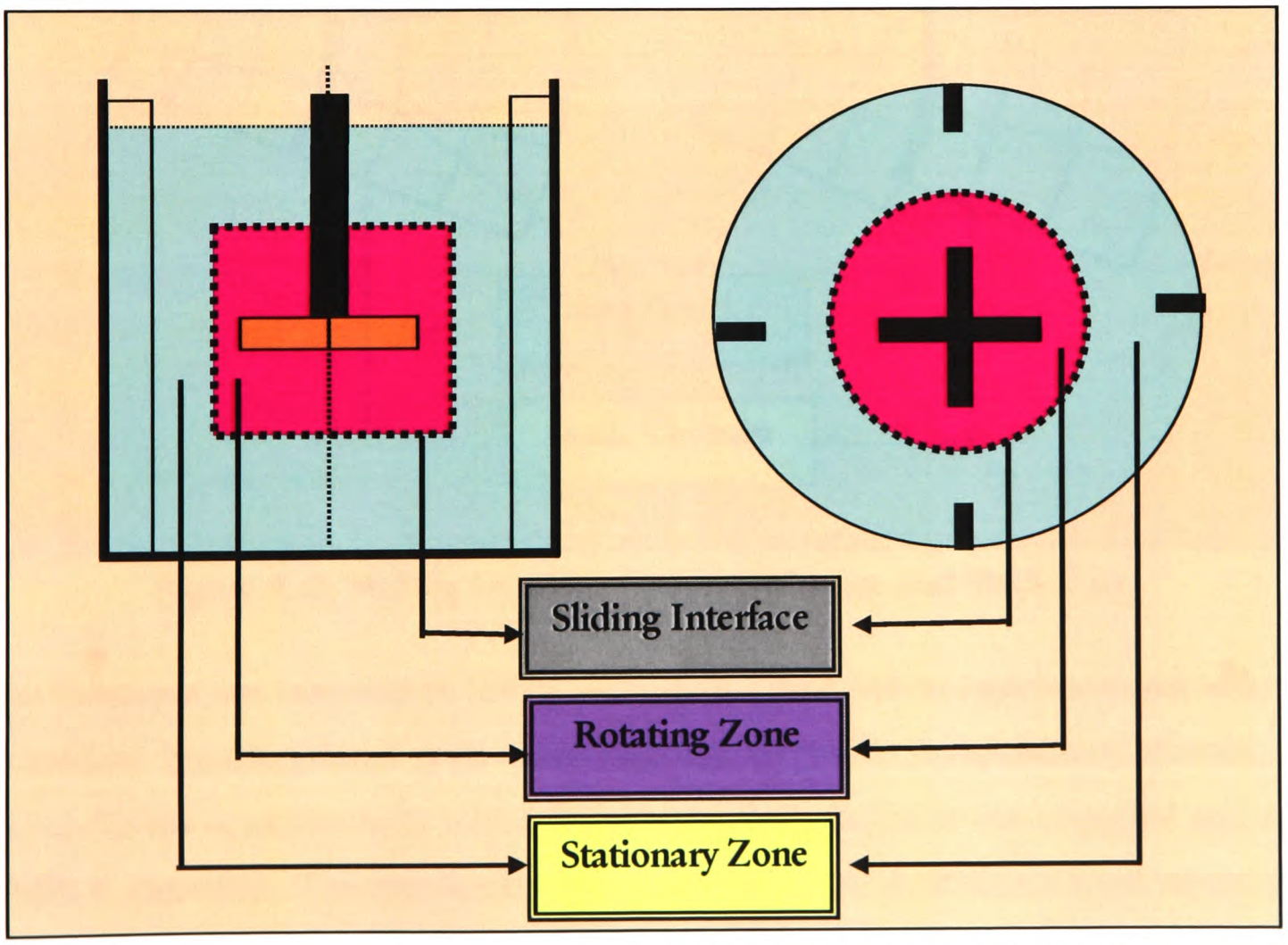

Figure 2.11: Modelling Technique Applied in Sliding Mesh Method

Sliding-Mesh method, has been developed. In this approach, two separate grids are used; one moves with the rotating part and the other fixed to the enclosing part. The two grids move relative to each other while slipping along a common interface. In the early phase of its development, [38] applied this method to carry out both Euler and Navier-Stokes simulations for rotor-stator interactions in turbomachinery. Here patched and/or overlaid grids were used in order to handle the conservative interpolation of flux transfer across the sliding interface and excellent results were obtained for two-dimensional cases.

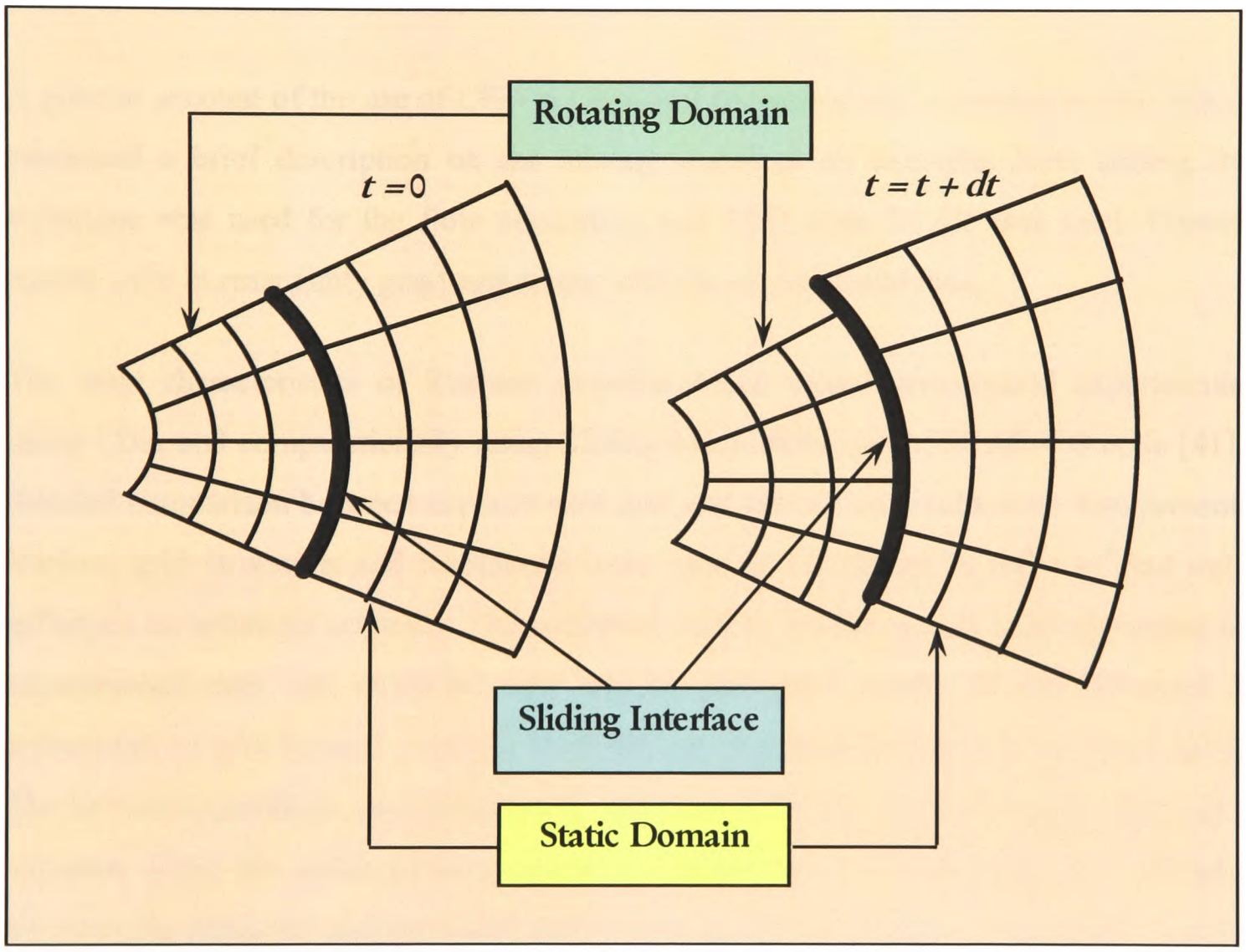

Figure 2.12: Sliding Interface between Moving and Static Part

This technique was extended by [39] to compute the flow field in impeller-stirred tank. The generalised boundary-fitted grids were used for the whole computational domain. The Navier-Stokes equations were solved for velocity and pressure in non-staggered grid using SIMPLE algorithm. The simulations for laminar two and three-dimensional model were

presented. Figure-2.11 and Figure-2.12 give overall scheme of this technique for impeller modelling.

This method along with the moving-deforming mesh technique has been outlined by [36] (also mentioned earlier); however, it was not indicated which method was used for the simulations. Here PISO method for the pressure and velocity coupling was used. A comparison of results from both steady and unsteady simulation runs against experimental data was given. The unsteady simulation results were in far better agreement with experimental data than the steady simulation results.

A general account of the use of CFD in Chemical Industries was presented in [40] that also contained a brief description on the mixing vessel as an example. Here sliding mesh technique was used for the flow simulation and CFD code STAR was used. Presented results were in reasonably good agreement with the experimental data.

The flow characteristics of Rushton impeller-stirred vessel investigated experimentally using LDA and computationally using Sliding-Mesh technique of STAR-CD code [41]. A detailed comparison between experimental data and simulation results were also presented. Various grid structures and resolutions were used in simulation in order to find out its influence on solutions accuracy. The predicted velocity profile was in good agreement with experimental data and exhibited very similar qualitative trends. It was observed that refinement of grid beyond a certain level did not significantly improve the result quality. The turbulent quantities were consistently under-predicted for all blade angles, although the variation along the radial position had been qualitatively well predicted. The differences between the measured and predicted results were greater at locations where high values for turbulence kinetic energy were measured. One of the significant finding of this work was "the choice of the location of the interface between the rotating and static volumes is entirely arbitrary and has no influence on the solution".

The applicability of this method to simulate the laminar flow in baffled stirred vessel with Rushton turbine impeller was demonstrated by [42]. Simulations were carried out using a commercial software package FLUENT. Validation was carried out against the LDA

experimental data for velocities and for power consumption. Quality of modelling results was assessed in terms of model/experimental error ratio. This ratio in this work was slightly above unity and hence, it was concluded that results were in good agreement with experimental data.

Both, Multiple-Reference-Frame and Sliding-Mesh method was used by [43] to investigate the flow generated by 6-blade Rushton turbine. Simulations were run using both techmiques for medium-resolution and high-resolution grid densities and results were validated against experimental data. It was found that Multiple-Reference-Mesh technique was very suitable for a large vessel with small impeller because it was computationally cheaper and fast and yielded reasonably good results. However, for a test case where blade-baffle gap was narrow, this method was inapplicable and Sliding-Mesh was the method of choice. The simulation, using Sliding-Mesh method, results generally agreed well with the experimental data when high-resolution grid was used. However, it somewhat overpredicted for tangential and radial components, particularly in the outer part of the tank. In this work vortex-structure around the impeller blades was studied using enstropy, which is the magnitude of the vorticity.

Commercial packages FLOW3D and CFX were used by [22] to perform simulations of the impeller-stirred vessel. Both the techniques experimental boundary conditions and Sliding Mesh methods were used to model the impeller and simulation results were compared. In this work, relative performance of four turbulence models, namely standard k-ε model, the RNG k-ε model, the Algebraic Reynolds stress model (ASM) and the Reynolds stress model (RSM) to predict flow field were investigated too. Based on comparison, it was concluded that the realistic description of the impeller region using the Sliding-Mesh model produced far better agreement with experimental data than experimental source term model. With RSM and ASM calculated normal Reynolds stress components were compared with the measured values. All these models produced lower values for normal stresses. However, the amount of experimental data was too small for reliable comparison between the results of turbulence models.

The Sliding-Mesh method was applied in [44] to model the Rushton turbine impeller-stirred tank with a single phase Newtonian fluid. The tank geometry and operating conditions were chosen to match those for experimental data available in the literature. In this work, simulations were carried out using commercial CFD code CFX4. A detailed comparison of the modelling results for the velocity components indicated reasonable agreement with experimental data. Validation was also carried out for global parameters such as the flow number and power number. The power number was calculated by two methods: (a) calculated from the torque on the impeller shaft and this was estimated from the pressure differential on the blades and the shear stress on the disc, (2) calculated by carrying out summation of turbulence energy dissipation rate over the whole tank. The power number calculated using the first approach was in close agreement with experiments but it was underpredicted from the second method.

Both, steady and unsteady computations for laminar flow in impeller-stirred tank were carried out by [45]. A method similar to Multiple-Reference-Frame was used for steady computations and Sliding-Mesh technique for unsteady computation. A comparative study of results from both methods of simulations was given and further validated them against the experimental data. A detailed account of grid generation and numerical method was covered in this paper. This work applied the zonal overlapping techniques, conservative interpolation at the interface of two domains (i.e. rotating and static domains), and time accurate artificial compressibility method for solving pressure- velocity coupling. It was concluded that for high Reynolds number turbulent flows in tanks the unsteady calculation, using Sliding-Mesh, is required to obtain realistic solutions.

A short paper [46] also presented Sliding-Mesh technique to simulate the laminar flow profile of impeller-stirred tank. Here commercial CFD package FLUENT was used for the simulations. A brief description of modelling was followed by qualitative comparison of velocity profile and quantitative comparison of impeller pumping number against experimental data. At low Reynolds number, the impeller created a radial flow pattern rather than axial, and the pumping number decreased with Reynolds number. The predicted results compared favourably with the experimental data.

2.2 Conclusions

From the above discussion, it is clear that a variety of techniques have been developed to model the impeller. Figure-2.13 summarises all the important impeller modelling techniques discussed so far. An impeller model based on empirically assigned boundary conditions relies heavily on LDV data that limits this model to the cases where

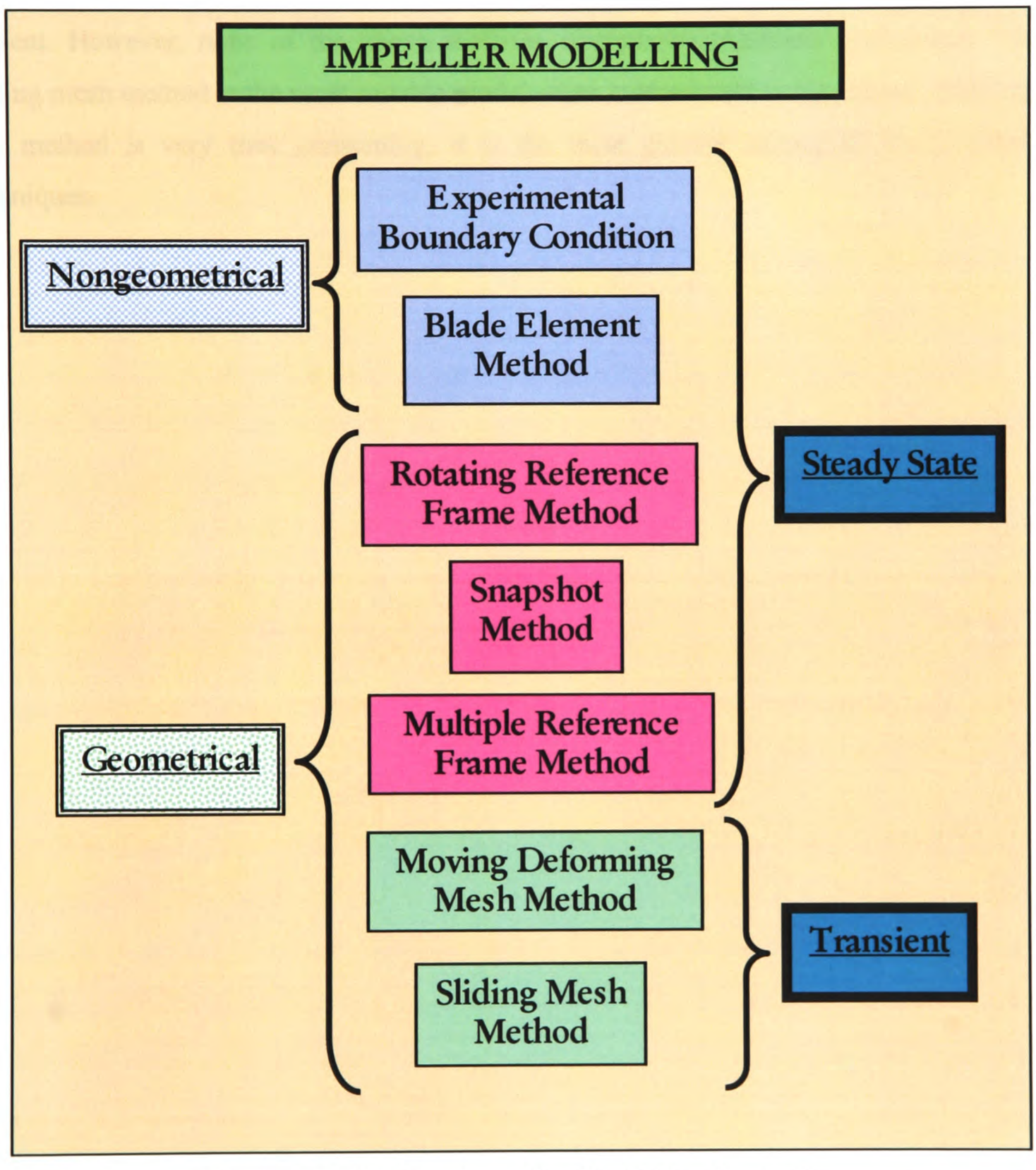

Figure 2.13: Various Impeller Modelling Strategies

experimental data are available. The impeller model based on blade element is somewhat wider in scope, but even this depends on experimentally determined lift and drag coefficients and these can be obtained only for some well known blade shapes. These methods cannot be regarded as general modelling techniques. The rotational reference frame method is wider in scope and the most suitable option when baffles are not present in the tank. The multiple reference frame method is the appropriate choice when baffles are present. However, none of the above methods incorporates unsteady phenomena. The sliding mesh method is the most suitable model when unsteadiness is significant. Although this method is very time consuming, it is the most general among all the available techniques.

Chapter 3

PHYSICAL MODELLING

3.1 Introduction

The techniques of physical modelling traditionally have played a very significant role in the development of the chemical, metallurgical and allied industries. Although rapid growth in the field of computer aided engineering has brought radical changes in the research methods, the importance of physical modelling is still significant. Combining both computer and physical modelling together opens up vast possibilities for new methods of research and development, which are not feasible by using either of the two alone. In this chapter we present some of the theoretical background of physical modelling techniques that are directly relevant to this research project.

3.2 Complexity of Problem

A fully predictive CFD model for lead refining process would be greatly beneficial as it can be used for repeated computer experiments to identify optimum process condition without any need for costly and time consuming experimental tests. This eliminates many of the intermediate steps of scale-up and can avoid the risk of potential failure. However, development of a computational model requires good understanding of the essential process variables and the laws that govern the interaction among them. At the same time, detailed information about boundary and initial conditions is also required to solve the governing equations.

The commercial scale operating conditions for the lead refining process are such that we have very limited access for the direct experiments and hence, qualitative and quantitative understanding of the various factors involved is very little. The flow field associated for this process is too complex and involves numerous phenomena, namely, unsteady flow, chemical reaction, phase change, dross formation, etc. The system of equations that would ultimately result from considering all these simultaneously would be too complex or too expensive to solve and that makes the computational modelling prohibitively difficult. In order to make the problem computationally manageable some simplifying conditions are applied, however, that may suppress some of the factors. On the other hand, every numerical algorithm has its own characteristic error pattern. It is clear that model building is based on approximations and assumptions that may cause the model to be removed somewhat from reality. So there is no guarantee with regard to the accuracy of a simulation results. Hence, it requires judicious validation against experimental data before it becomes reliable enough to influence design decisions.

The CFD simulation requires highly detailed information concerning the boundary conditions of the problem and generates a large volume of solution data. To validate these in a meaningful way it is necessary to produce experimental data of similar scope. The code validation is not the immediate objective of this project. However, we have taken an alternative approach to use a commercial code that has already been validated stringently and extensively for a wide range of applications in general and for impeller-stirred tanks. Our effort is to extend and apply it to the problem in hand and frequently checking it against the real process to determine its adequacy in making predictions that are accurate enough to be useful

.

3.3 Why We Need Physical Model

It is virtually impossible to obtain detailed experimental data from a lead refining kettle. For example, getting details of flow profile of molten lead within the real refining kettle is impossible. This environment is too hostile for the delicate laboratory equipment, at the

same time the construction of the lead refining system is such that it poses severe limitations on the easy access for direct measurements or/and observations. Under such conditions we have another very useful tool at our disposal: the construction of a more accessible physical model. Data gathered on a physical model can be used for validation of the computer model that would lead to the predictive model of the real refining system.

3.4 Physical Modelling

A physical model is an approximate representation of the real process where we seek to reproduce the behaviour of a real process or some particular aspect of it. Frequently it is achieved by changing the scale of operation or/and by changing the material involved. In developing a physical model, cost effectiveness and ease of measurement are the main guiding factors, while care is taken to ensure a realistic representation as adequately as possible. This whole objective can be summed up in words of J. Szekely, et. al. [10] "*The main objective of modelling is to achieve a realistic representation of a system using materials and equipment with which measurements may be made conveniently and in a cost-effective manner*". The key phrases in this statement are *realistic representation*, *convenient measurement* and *cost-effective*, concepts that reflect the necessity of making compromises in certain instances.

It has already been discussed that the flow field in the lead refining process is very complex and involves various interdependent phenomena. Representation of this process or some key aspect of it into a physical model requires careful planning. This needs a clear definition of the objective with a good level of awareness of the limitations. In this study, the following steps were undertaken in developing the physical model.

1. ***Study of the existing process:*** In order to get a good physical appreciation of the various factors affecting the flow field in the lead refining process thorough observations made on the existing plant. Some of the qualitative and quantitative readings were also taken. For example, readings for power consumption, measurements

of vortex depth, photographs of surface movement, etc. under various operating conditions.

2. ***Identify process need:*** The design of a physical model should start with a thorough examination of all the process needs of the existing plant. Lead bullion contains many impurities, different impurities are eliminated in sequence of different operations but stirring is the basic to most of the refining processes. Here our focus area is the copper de-drossing process. The main factor needed for this process is a good formation of vortex to convert hard dross into fine powder with minimum of air entrapment and in least possible time to avoid undesired lead oxide formation with less power consumption.

3. ***Identify key process parameters*:** In the physical model our objective is to reproduce a similar qualitative and quantitative correlation among various factors associated with the lead refining process. For this purpose, it is essential to identify the parameters associated with the real refining process. In this case, the main operational parameters can be classified under two broad categories. The first category is the independent parameters that can be controlled directly. These are: (a) kettle geometry, (b) impeller geometry, (c) impeller-depth, (d) impeller speed, (e) melt depth. Second category is the dependent variables. These are dependent on the first parameters and are: (a) dross layer thickness, (b) vortex depth, (b) reaction rate, (c) phase change, (d) volume fraction, (e) power consumption, etc. Through the physical model, we seek to study some or all of above said parameters and their interdependence.

4. ***Isolate key phenomena*:** It is not possible to reproduce all the phenomena of the lead refining process into a physical model. For example, practically it is not possible to reproduce chemical reactions and phase change in the physical model. These are very much affected by the profile of the flow field without imparting significant influence on the flow field. We have restricted our attention to the most dominating factors that can be reproduced. Here we are mainly interested in flow re-circulation pattern, turbulence, vortex formation and dispersion of solid phase when agitated by the impeller under various operating conditions.

5. ***Make assumptions*:** A physical model can only be an approximate representation of the real process. When developing a physical model, the complexity of the real system is reduced by making a number of assumptions. In this study we have made the following assumptions:
   - In the lead refining kettle concentration of solid phase and reactant are sufficiently low for the molten lead to behave as normal Newtonian fluid.
   - Phase change and chemical reactions do not affect the flow field.
   - Dross is assumed to behave as a single-phase solid material.

6. ***Choose model design*:** The geometry of the process has direct impact on the flow profile. Hence, the geometry should be selected so that it satisfies the criteria of geometric similarity as closely as possible. In this case, we have set up a physical model that satisfies all the criteria of geometric similarity. The physical model is an exact geometrical replica of lead refining kettle and its ratio to real system geometry is 0.75.

7. ***Choose model materials*:** It is not always possible to use the same materials as that of the real system. At the same time if scaled model is to satisfy all of the criteria of similarity, different material is required to mimic the material of the real system. For present physical model, water has been selected as the main working fluid to represent the molten lead and polystyrene granules to mimic the presence of dross. The reason for this selection is explained later in this chapter.

8. ***Test model*:** Final stage in the model development is its testing. Tests on the model give an insight into whether the physical model gives the true representation of key factors of the real process. Test on model can be qualitative observation in order to visualise the flow profile and/or it can be quantitative measurements. By comparing water model to the phenomena in the lead refining process, it has been observed that flow patterns in the water model are very similar to that of molten lead on the bath surface. Vortex

formation, circulation pattern and instability of surface under certain conditions are qualitatively similar for both the cases.

The following section explains some of the theoretical concepts and tools used in the development of a physical model.

3.4.1 Dimensional Analysis

An equation describing a physical system must dimensionally be consistent. In other words, the dimension of each term in the equation must be same. As an example consider an equation describing fluid motion of boundary layer [47]:

$$\frac{\partial u_x}{\partial t} + u_x \frac{\partial u_x}{\partial x} + u_y \frac{\partial u_y}{\partial y} + u_z \frac{\partial u_z}{\partial z} = -\frac{1}{\rho}\frac{\partial P}{\partial x} + \frac{\mu}{\rho}\left[\frac{\partial^2 u_x}{\partial x^2} + \frac{\partial^2 u_x}{\partial y^2}\right] + g_x \qquad (3.1)$$

From the above equation it can be seen that each term has the dimension L/t^2. If an equation has to be physically meaningful it is not permissible to add terms with different dimensions. If the whole equation is divided by any one of the terms, each remaining term in the equation becomes dimensionless. These dimensionless quantities are called *dimensionless numbers*. These have considerable use in developing a physical model where the functional relationships among various factors involved is expressed using them. Example of such dimensionless numbers is: Reynolds Number, Froude Number, etc.

3.4.2 Buckingham's π Theorem

For problem solving purposes the need for dimensional homogeneity can be generalised and expressed in the form of Buckingham's π theorem [47] as:

1. The solution of any dimensionally homogeneous equation representing physical quantities can be expressed in terms of a certain number of dimensionless groups, π, say,

$$f(\pi_1, \pi_2, \pi_3, ...) = 0 \tag{3.2}$$

2. If the quantities are independent, then the number of dimensionless groups needed to define the problem equals the number of individual variables minus the number of fundamental magnitudes (mass, length, time, etc.) needed to express these variables.

3.4.3 Concept of Similarity

In order to achieve the same flow profile in a physical model as that of the real refining system we need to consider a number of similarity criteria. There exists many states of similarity; however, we will confine our attention to the most important ones which are outlined as follows:

- Geometrical Similarity
- Kinematic Similarity
- Dynamic similarity

3.4.3.1 Geometrical Similarity

Geometrical similarity is the similarity of shape. Systems are geometrically similar when the ratio of any length in one system to the corresponding length in other system is everywhere the same. This ratio is usually termed the scale factor. While geometric similarity is one of the most obvious requirements in modelling, often it may not be possible to attain perfect geometric similarity. Under such conditions, certain critical dimensions of the model are scaled to the prototype while other dimensions are not. This procedure is called the use of distorted model. For the physical model, in this research we have ensured total geometrical similarity.

3.4.3.2 Kinematic Similarity

Kinematic similarity represents the similarity of motion. In essence, kinematic similarity is observed between two systems, if in addition to being geometrically similar the velocities at corresponding locations in the two systems are also in the fixed ratio.

3.4.3.3 Dynamic Similarity

Dynamic similarity represents the similarity of forces. The main forces to be considered, that are relevant to the impeller stirred system, in obtaining dynamic similarity are the following:

- Inertial Forces
- Pressure Forces
- Viscous Forces
- Gravity

The ratio of these forces gives rise to a number of dimensionless numbers. By ensuring that the numerical value of these dimensionless numbers is the same in the model and in the real process, one can ascertain that dynamic similarity is observed.

The inertial force acting on a fluid element is the mass of the element, multiplied by its acceleration. Thus, if the characteristic length is L, the characteristic velocity is U, and the density is ρ, we may write

$$Inertial\ Force \propto (\rho L^3) \times \left(U^2 / L\right)$$

$$Inertial\ Force \propto (\rho L^2 U^2) \tag{3.3}$$

The viscous force acting on the fluid is given by (shear stress)×(area), i.e. $(\mu du_x / dy)L^2$. Since $u_x \propto U$, $y \propto L$, we have

$$Viscous\ Force \propto (\mu UL) \tag{3.4}$$

By similar arguments we have

$$Gravity\ Force \propto (\rho L^3 g) \tag{3.5}$$

Choice of these similarity criteria is not arbitrary but can be derived rigorously by making the governing differential equations dimensionless. When considering a new system that has not been thoroughly investigated, it is highly desirable to obtain dimensionless form of the governing equations. Analysing these and its associate boundary conditions enable one to examine a problem in detail and thus to obtain a checklist so that no important parameter is overlooked. Next section illustrates the uses of dimensionless differential equations for fluid flow to obtain some of the interesting information of similarity requirements.

3.4.4 Dimensionless Fluid Flow Equations

The governing equations for fluid flow are given as follow

- *Continuity equation*

$$\nabla \cdot U = 0 \tag{3.6}$$

- *Equation of motion*

$$\frac{\mathrm{D}U}{\mathrm{D}t} = -\nabla P + \mu \nabla^2 U + \rho F \tag{3.7}$$

These equations are made dimensionless by selecting a characteristic length (L), a characteristic velocity (U) and a reference pressure (P_0). The choices of these are arbitrary but require careful specification. For the impeller-stirred vessel, L and U can be the diameter and velocity of impeller respectively while P_0 can be some convenient reference pressure. Let us define the following dimensionless parameters:

$$U^* = \frac{U}{U_0},\ x^* = \frac{x}{L},\ y^* = \frac{y}{L},\ z^* = \frac{z}{L},\ P^* = \frac{P - P_0}{\rho U_0^2},\ t^* = t\frac{L}{U_0} \tag{3.8}$$

that is $\nabla^* = L\nabla$, $(\nabla^*)^2 = L^2\nabla$, and so on. Substitution of these quantities into Equations (3.6) and (3.7) gives the dimensionless form of equations.

$$\nabla^* \cdot U^* = 0 \tag{3.9}$$

and

$$\frac{DU^*}{Dt^*} = -\nabla P^* + \left(\frac{\mu}{LU_0\rho}\right)\nabla^{*2} U^* + \left(\frac{gL}{U_0^2}\right)\frac{F}{g} \tag{3.10}$$

Note that in these dimensionless forms of the equations variables describing the over-all size and speed of the system and its physical properties are concentrated in two dimensionless groups. These can be used to represent the scale factors. These groups in inverted form are *Reynolds* and *Froude* numbers respectively.

$$Reynolds\ Number\ (Re) = \frac{LU_0\rho}{\mu} \tag{3.11}$$

$$Froude\ Number\ (Fr) = \frac{U_0^2}{gL} \tag{3.12}$$

***Analysis*:** If in two different systems the scale factors are such that the Froude and Reynolds numbers are the same for both, then both systems are described by identical dimensionless differential equations. If, in addition, the dimensionless initial and boundary conditions are same (this is possible only if the two different systems are geometrically similar), then the two systems are mathematically identical; that is, the dimensionless velocity distribution U*(x*, y*, z*, t*) and the dimensionless pressure distribution P*(x*, y*, z*, t*) are the same in each. Such systems are said to be "dynamically similar". In the scale-up of processes that are not well understood, it is often desirable to maintain dynamic similarity. Next section illustrates the use of this procedure in model development.

3.4.5 Prediction of Vortex Depth

For simple impeller-vessel geometry, for example, a cylindrical vessel equipped with a flat blade impeller, it is possible to predict the vortex shape analytically. The overview of this approach is presented in APPENDIX-B. The applicability of this method is very much limited to the simple vessel-impeller geometry. However, most of the impeller-stirred vessels of industrial interest have structure that is much more complex. Alternatively, vortex shape can be predicted using a laboratory scale physical model; provided physical

model satisfies the conditions of similitude. The use of physical model, using method of similitude, to predict vortex shape is presented next.

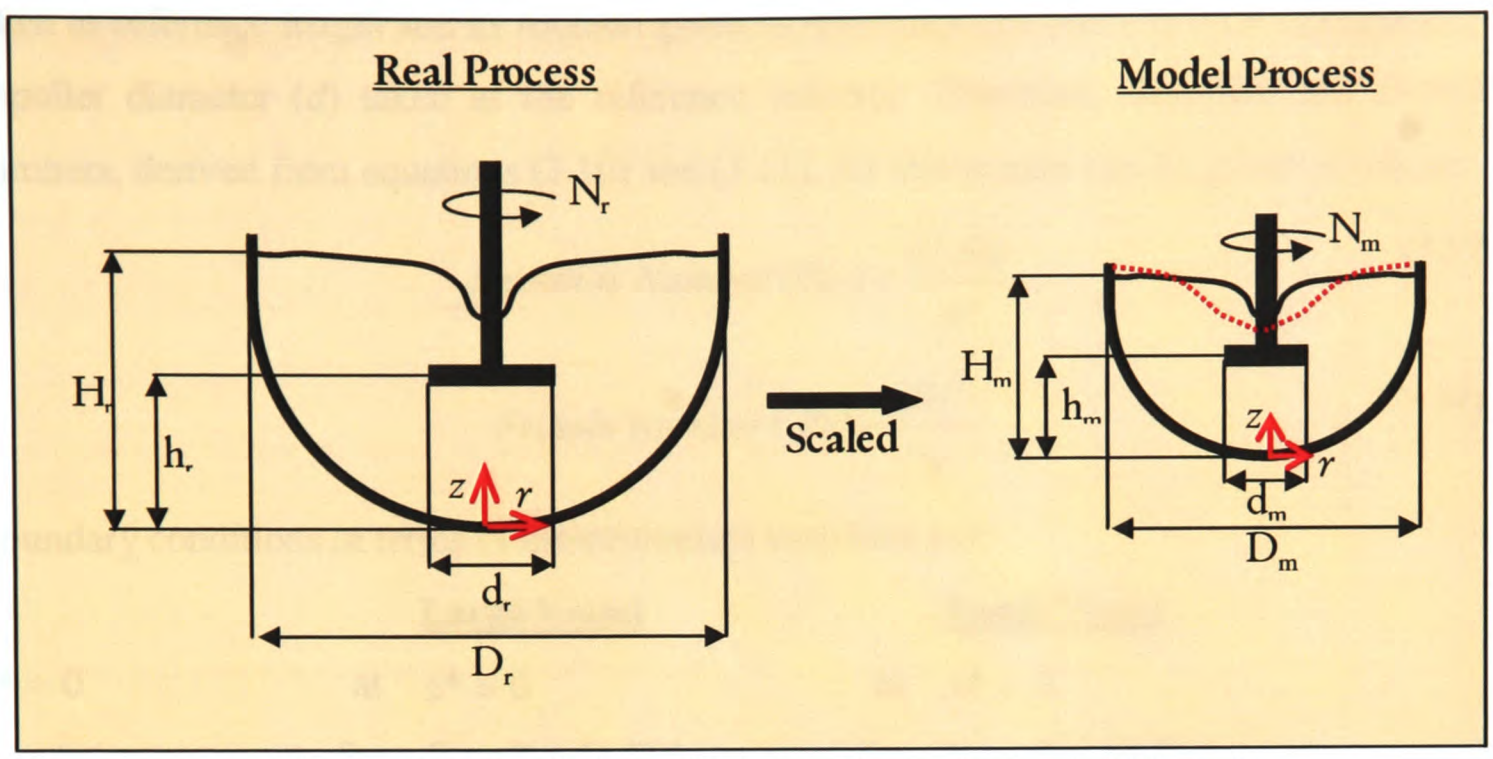

Figure 3.1: Prediction of Vortex Shape in Scaled Vessel

Suppose we need to predict vortex depth in a large industrial scale impeller-stirred kettle as a function of impeller speed. Here we can use the principles of similarity to find out what criteria we should meet in order to have similar vortex pattern in the small lab scale unit as that in the industrial scale unit [48]. We use subscripts r and m for the quantities used to represent the large unit (that is real industrial scale) and the small unit (that is lab scale model), respectively. We assume all the flows are steady-state. Then

		Large Vessel		**Small Vessel**
$v = 0$	at	$z = 0$	at	$z = 0$
	for	$0 < r < D_r/2$	for	$0 < r < D_m/2$
	at	$r = D_r/2$	at	$r = D_m/2$
	for	$0 < z < H_r$	for	$0 < z < H_m$
$p = p_0$	at	$S_r(r,z)$	at	$S_m(r,z)$

Here S_r and S_m are the vortex surfaces (defined in terms of parameters: distance from axis, r and surface height, z) in the large and small vessels, and p_0 is the atmospheric pressure. It is also possible to write all the velocities relative to the moving solid wall here but this is

not necessary for the following analysis. The operating condition is assumed to be steady-state here so that we do not require the initial condition of the system. Impeller diameter is taken as reference length and its rotation given in revolution per unit (N) time multiplied by impeller diameter (d) taken as the reference velocity. Therefore, *Reynolds* and *Froude* numbers, derived from equations (3.10) and (3.11), for this system can be given as follow:

$$Reynolds\ Number\ (Re) = \frac{d^2 N \rho}{\mu} \tag{3.13}$$

$$Froude\ Number\ (Fr) = \frac{dN^2}{g} \tag{3.14}$$

Boundary conditions in terms of dimensionless variables are:

		Large Vessel		**Small Vessel**
$v^* = 0$	at	$z^* = 0$	at	$z^* = 0$
	for	$0 < r^* < D_r/2d_r$	for	$0 < r^* < D_m/2d_m$
$v^* = 0$	at	$r = H_r/2d_r$	at	$r^* = H_m/2d_m$
	for	$0 < z^* < H_r/d_r$	for	$0 < z^* < H_m/d_m$
$p^* = 0$	at	$S_r * \left(\frac{r}{d_r}, \frac{z}{d_r}\right)$	at	$S_m * \left(\frac{r}{d_m}, \frac{z}{d_m}\right)$

It can be said that to have similar flow pattern in the two vessels the following equalities must exist:

Kettle Geometry
$$\frac{D_r}{d_r} = \frac{D_m}{d_m} \tag{3.15}$$

Kettle Geometry
$$\frac{H_r}{d_r} = \frac{H_m}{d_m} \tag{3.16}$$

Vortex Shape
$$S_r * \left(\frac{r}{d_r}, \frac{z}{d_r}\right) = S_m * \left(\frac{r}{d_m}, \frac{z}{d_m}\right) \tag{3.17}$$

Reynolds Number
$$\frac{d_r^2 N_r \rho_r}{\mu_r} = \frac{d_m^2 N_m \rho_m}{\mu_m} \tag{3.18}$$

Froude Number
$$\frac{d_r N_r^2}{g} = \frac{d_m N_m^2}{g} \tag{3.19}$$

Here Equations (3.15) and (3.16) are for geometric similarity between two vessels. However, all the geometric similarity requirements are satisfied only when two systems have similar vortex shape because dimensionless vortex shapes $S_r*\left(r/d_r, z/d_r\right)$ and $S_m*\left(r/d_m, z/d_m\right)$ contain the geometric quantities too. It is obvious that for more detailed description of this system requires that more conditions to be satisfied. Fortunately, for present analysis above mentioned conditions are enough. From Equations (3.15) and (3.16), we can calculate the scale factors for the similar vortex shape in two vessels. Now from Equation (3.19) we get:

$$\frac{N_m}{N_r} = \sqrt{\frac{d_r}{d_m}} \tag{3.20}$$

Substituting this into Equation (3.18) we get:

$$\frac{\mu_m}{\rho_m} = \frac{\mu_r}{\rho_r}\left(\frac{d_m}{d_r}\right)^{3/2} \tag{3.21}$$

***Analysis*:** From the above we can see that we cannot get similar vortex on two vessels of different scale by using same fluid. To achieve this we need to have two different working fluids, which are linked by Equation (3.21). For example if the model vessel has half the scaled dimension of the real size vessel then the kinematic viscosity of the working fluid used in the model must be $1/\sqrt{8}$ times that of fluid in the real vessel. If the same fluid were used in both and at the same Reynolds number, then the Froude number in the small tank would be greater and the vortex would be proportionately deeper. This is represented by dotted curve in the Figure-3.1.

Following a similar argument, if we were to model a similar vortex formation on the lead refining kettle by using water as working fluid in the physical model, then the model dimension must be $1/3$ of the real kettle. In the practical sense, it will be impossible to build a water model to represent the vortex formation phenomena for lead refining kettle that requires matching both Reynolds and Froude numbers. Fortunately, the vortex depth has the main significance in this process and this becomes independent of Reynolds number

beyond certain limit [49] and only dependent on the Froude number. Here also, using the experimental results (from this research) an assumption (as approximation) was made regarding the independence of vortex depth (see Chapter-4, Section-4.5). We can see from Equation (3.12) that the Froude number is not dependent on fluid properties like density and viscosity. It is only a function of geometry and impeller rotational speed. This means we can use a kettle of similar geometry for the water model and match the Froude number by matching impeller rotational speed. Also operating beyond Reynolds number 10^5 (as confirmed by experiment) we can get the same vortex depth as that of the lead kettle.

3.4.6 Power Consumption

Scale-up is also generally guided by the global parameters like power consumption. Generated flow profile is directly related with the power consumption and incorrect estimation of it can result in deviation in desired flow profile. From a practical point of view, power consumption is perhaps the most important parameter in the scale-up of stirred vessels. In this section using methods of dimensional analysis, we illustrate the method for developing correlation for power consumption.

Meaning of symbols for this section is as follows: D – vessel diameter, d – impeller diameter, H – liquid height in vessel, h – impeller clearance, β – pitch of impeller, l – length of impeller blades, w – width of impeller, ρ – liquid density, γ – kinematic viscosity of liquid, μ – dynamic viscosity of liquid, g – gravitational acceleration, N – rotational speed of impeller, P_w – power consumption, K – constant of proportionality.

To apply method of dimensional analysis we consider power consumption as a function of variables involved in an impeller-stirred vessel and expressed in a general equation as

$$P_w = f(D,d,H,h,\beta,l,w,\rho,\gamma,g,N) \tag{3.22}$$

To fulfil the requirement of dimensional consistency, dimensions of all the terms in right and left-hand sides must be equal. In order to apply the *Pi* theorem it is customary to write this equation in a convenient form as

$$0 = f(D,d,H,h,\beta,l,w,\rho,\gamma,g,N,P_w) \tag{3.23}$$

Now we apply Buckingham's Pi theorem. Twelve variables of this function can be redefined in terms of three fundamental units: mass, length, time. This reduces the function with nine dimensionless groups. However, for the dimensional analysis of impeller stirred system it is convenient to express these groups in terms of impeller diameter, impeller speed and the fluid density while maintaining the dimensional consistency. Hence each group is expressed with four variables of which three are impeller diameter, impeller speed and fluid density with some sort of power on them and fourth variable, which change from group to group, with an exponent of -1.

$$f'(\pi_1,\pi_2,\pi_3,\pi_4,\pi_5,\pi_6,\pi_7,\pi_8,\pi_9) = 0 \tag{3.24}$$

The values of the π terms can be determined

$$\pi_1(\text{for tank diameter } D) = d^x N^y \rho^z D^{-1} \tag{3.25}$$

Substitute dimensions:

$$0 = L^x \cdot (T^{-1})^y \cdot (ML^{-3})^z \cdot L^{-1} \tag{3.26}$$

Solve for x, y and z

$$\left.\begin{array}{lrl} L: & x-3z-1 & =0 \\ T: & -y & =0 \\ M: & z & =0 \end{array}\right\} \tag{3.27}$$

that gives

$$\left.\begin{array}{rcl} x & = & 1 \\ y & = & 0 \\ z & = & 0 \end{array}\right\} \tag{3.28}$$

and hence

$$\pi_1 = \frac{d}{D} \tag{3.29}$$

As the equations for dimensions of $\pi_2 - \pi_6$ will be similar to that for π_1, by inspection the values of these terms can be evaluated as:

$$\pi_2 = \frac{d}{H}, \quad \pi_3 = \frac{d}{h}, \quad \pi_4 = \frac{d}{\beta}, \quad \pi_5 = \frac{d}{l}, \quad \pi_6 = \frac{d}{w} \tag{3.30}$$

Now similarly we can evaluate other π's as follows:

The values of the π terms can be determined

$$\pi_7(\text{for } \gamma) = d^x N^y \rho^z \gamma^{-1} \tag{3.31}$$

Substitute dimensions:

$$0 = L^x \cdot (T^{-1})^y \cdot (ML^{-3})^z \cdot (L^2T^{-1})^{-1} \tag{3.32}$$

Solve for x, y and z

$$\left.\begin{array}{lrl} L: & x-3z-2 & =0 \\ T: & -y+1 & =0 \\ M: & z & =0 \end{array}\right\} \tag{3.33}$$

that gives

$$\left.\begin{array}{lcl} x & = & 2 \\ y & = & 1 \\ z & = & 0 \end{array}\right\} \tag{3.34}$$

and hence

$$\pi_7 = \frac{d^2 N}{\gamma} \tag{3.35}$$

Now

$$\pi_8(\text{for } g) = d^x N^y \rho^z g^{-1} \tag{3.36}$$

Substitute dimensions:

$$0 = L^x \cdot (T^{-1})^y \cdot (ML^{-3})^z \cdot (LT^{-2})^{-1} \tag{3.37}$$

Solve for x, y and z

$$\left.\begin{array}{lrl} L: & x-3z-1 & =0 \\ T: & -y+2 & =0 \\ M: & z & =0 \end{array}\right\} \tag{3.38}$$

that gives

$$\left.\begin{array}{lcl} x & = & 1 \\ y & = & 2 \\ z & = & 0 \end{array}\right\} \tag{3.39}$$

and hence

$$\pi_8 = \frac{dN^2}{g} \tag{3.40}$$

Now

$$\pi_9(\text{for } p_w) = d^x N^y \rho^z p_w^{-1} \tag{3.41}$$

Substitute dimensions:

$$0 = L^x \cdot (T^{-1})^y \cdot (ML^{-3})^z \cdot (ML^2T^{-3})^{-1} \tag{3.42}$$

Solve for x, y and z

$$\left.\begin{array}{rrl} L: & x-3z-2 & =0 \\ T: & -y+3 & =0 \\ M: & z-1 & =0 \end{array}\right\} \tag{3.43}$$

that gives

$$\left.\begin{array}{rcl} x & = & 5 \\ y & = & 3 \\ z & = & 1 \end{array}\right\} \tag{3.44}$$

and hence

$$\pi_9 = \frac{d^5 N^3 \rho}{P_w} \tag{3.45}$$

This is the most straightforward derivation where only most important factors have been taken into consideration. To have a complete description of system we may need to consider number of blades, blade thickness, number of baffles, dimensions of baffles, etc. and bringing an appropriate change to the Equation (3.24) for generality and carry out dimensional analysis. Suppose we carry out somewhat detailed analysis of an unbaffled system and hence, introduce number of impeller N_b as a new variable. In dimensionless form it may be written as N_b/N_0. In this N_0 is a reference number and selected conveniently. For a baffled kettle, the variable N_{bf}/N_0 can be used where N_{bf} is the number of baffles.

Recombining the π terms, the following can be written:

$$0 = f'\left(\frac{d}{D},\frac{d}{H},\frac{d}{h},\frac{d}{\beta},\frac{d}{l},\frac{d}{w},\frac{d^2N}{\gamma},\frac{dN^2}{g},\frac{d^5N^3\rho}{P_w},\frac{N_b}{N_0}\right) \tag{3.46}$$

In most general form this equation can be written as

$$0 = f'\left(\frac{d}{D},\frac{d}{H},\frac{d}{h},\frac{d}{\beta},\frac{d}{l},\frac{d}{w},\frac{d^2N}{\gamma},\frac{dN^2}{g},\frac{d^5N^3\rho}{P_w},\frac{N_b}{N_0},\cdots\right) \tag{3.47}$$

This equation includes all the requirements of similarity that is geometric, kinematic and dynamic similarity. Each term in this expression is dimensionless provided consistent units are used. The viscosity and gravity terms are expressed respectively as, the *Reynolds Number* (Re) and the *Froude Number* (*Fr*):

$$\mathrm{Re} = \frac{d^2N}{\gamma} \tag{3.48}$$

since kinematic viscosity, $\gamma = \mu/\rho$, Re can be written as:

$$\mathrm{Re} = \frac{d^2N\rho}{\mu} \tag{3.49}$$

and similarly Froude Number

$$Fr = \frac{dN^2}{g} \tag{3.50}$$

The term $d^5N^3\rho/p_w$ characterises the basic flow pattern and depends on the impeller-vessel configuration and the flow regime. In practice, this term is written in inverted form so that power term P_w appears in the numerator and is defined as the power number. Thus, power number

$$N_P = \frac{P_w}{\rho N^3 d^5} \tag{3.51}$$

Following the above arguments Equation (3.26) for power number can be expressed as:

$$N_P = K(\mathrm{Re})^m(Fr)^n(D/d)^u(H/h)^v(h/d)^i(\beta/d)^j(l/d)^q(w/d)^r(N_b/N_0)^t\cdots \tag{3.52}$$

This equation is the most general equation which relates the power consumption with other operating variables. If a set of experiments are to be carried out in steady state using the same geometric and boundary conditions (following similar arguments as that of Sections-3.4.1) Equation (3.52) can be reduced to:

$$N_P = K(\mathrm{Re})^m (Fr)^n \tag{3.53}$$

where K is the overall shape factor which depends upon the geometry of system. K, m and n local in nature as these depend on the impeller-vessel configuration and on the flow regime that is laminar, transient or turbulent, prevailing in the mixing vessel hence, must be determined experimentally. Equation (3.53) is often written [2] as

$$\phi = \frac{N_P}{(Fr)^n} = K(\mathrm{Re})^m \tag{3.54}$$

where this gives convenience when presenting the data in graphical form. Here ϕ is defined as the dimensionless power function.

3.4.7 Power Curves

A power curve is a plot of the power function ϕ or the power number N_P against the Reynolds number (Re) on log-log co-ordinates. Each geometrical configuration has its own power curve and since the plot involves dimensionless groups, it is independent of the tank size. Thus, a power curve can be used to correlate power data from a real operating unit to the model if their geometrical configurations are similar.

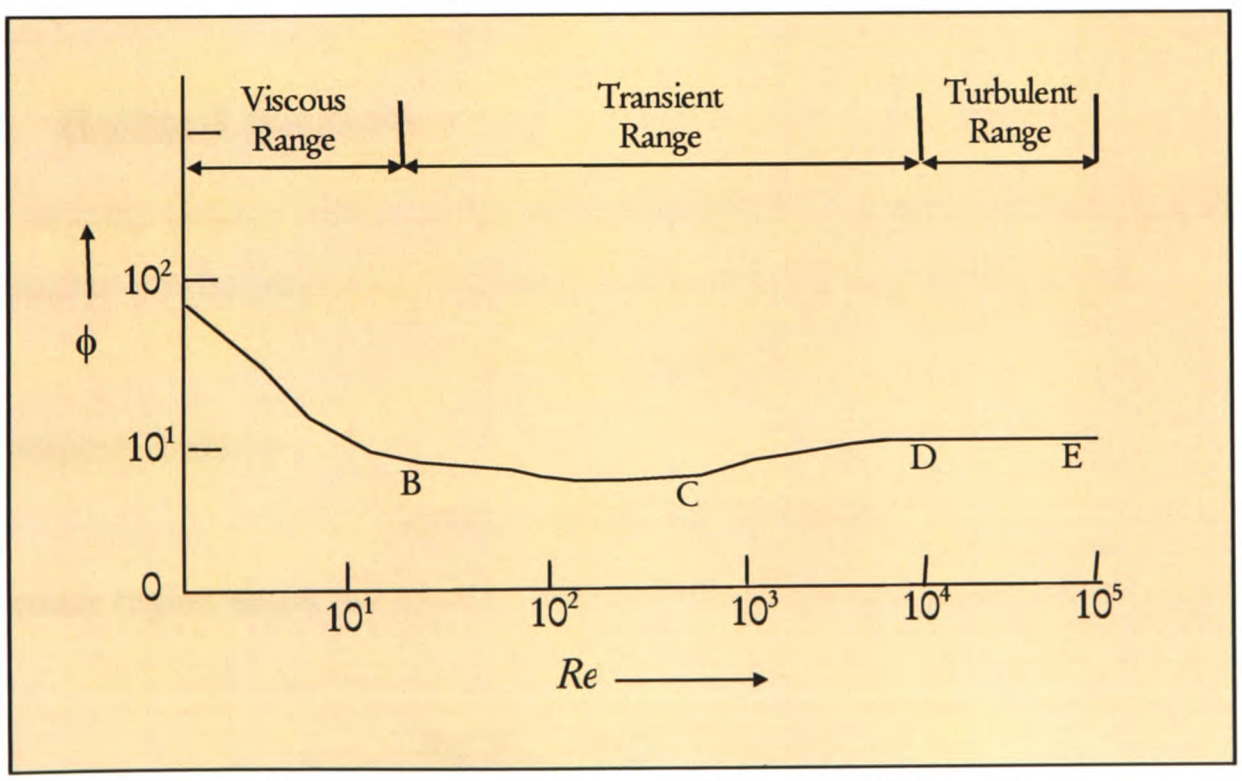

Figure 3.2: Power Curve for Baffled Vessel

Figure-3.2 and Figure-3.3 show the schematic power curve (see [2, 50-51] for details) for standard vessel-impeller configuration that is cylindrical, vertical axis, flat bottom vessel where these represent baffled and unbaffled vessels respectively. However, similar power curve can be obtained for different shape vessel as well, for example hemispherical shape lead refining kettle.

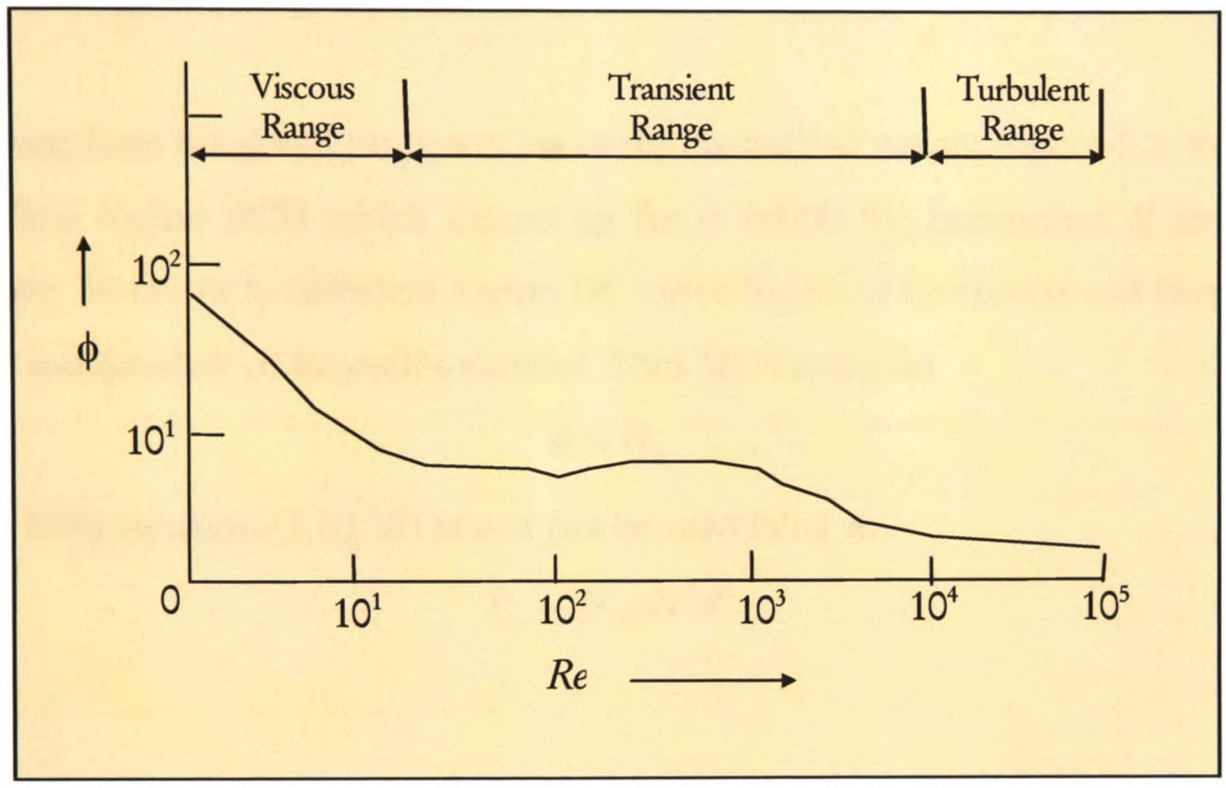

Figure 3.3: Power Curve for Unbaffled Vessel

3.4.7.1 Baffled System

In liquid mixing system where vortexing is negligible or suppressed by using baffles the Froude number can be neglected and hence equation (3.54) can be written as

$$\phi = N_P = K(\mathrm{Re})^m \tag{3.55}$$

or in logarithmic form as

$$\log N_P = \log K + m \cdot \log(\mathrm{Re}) \tag{3.56}$$

In the laminar region slope AB for Re < 10 is -1.0 and hence equation (3.56) can be written as

$$\log N_P = \log K - \log(\mathrm{Re}) \tag{3.57}$$

and hence

$$N_P = \frac{K}{\mathrm{Re}} \tag{3.58}$$

Now from equations (3.51) and (3.58) we can find the power

$$P_w = K\mu N^2 d^3 \tag{3.59}$$

As stated before K depends on the type of impeller-vessel arrangement. It is now obvious that in laminar region power is directly proportional to dynamic viscosity for a fixed speed.

It can be seen from the graph for power curve for the baffled vessel, Figure-3.2, that for the transient flow region BCD which extend up Re = 10000 the parameters K and m vary continuously. In the fully turbulent region DE curve becomes horizontal and hence power function is independent of Reynolds number. Thus for this region

$$\phi = N_p \tag{3.60}$$

and hence from equation (3.10.30) power can be calculated as

$$P_w = N_P \rho N^3 d^5 \tag{3.61}$$

3.4.7.2 Unbaffled System

On comparing both powers curves, it is clear that curve for unbaffled is similar to that of baffled system up to point C. That is to say effect of Froude number in this region is negligible. In fact for Re < 300, the effect of Froude number is absent and Equation (3.54) holds true. However, beyond this point Reynolds number increases and so the vortexing and power curve falls sharply. For this region Froude number comes into play. This can be expressed in equations as

$$\left.\begin{aligned} \phi &= N_P \quad \text{for} \quad \mathrm{Re} < 300 \\ \phi &= \frac{N_P}{(Fr)^n} \quad \text{for} \quad \mathrm{Re} > 300 \end{aligned}\right\} \tag{3.62}$$

In this case Equation (3.53) can be written in logarithmic form as

$$\log N_P = \log K + m \cdot \log(\mathrm{Re}) + n \cdot \log(Fr) \tag{3.63}$$

A plot of N_P against Re on log-log co-ordinates for the unbaffled system gives a family of curves at Re > 300. Each curve has a constant Froude number. A plot of N_P against Fr on

log-log co-ordinates is a straight line of slope m at a constant Reynolds number. A number of lines can be plotted for different values of Re. A plot of m against log(Re) is also a straight line. If the slope of line is $-1/b$ and the intercept at Re=1 is a/b then

$$n = \frac{a - \log(\mathrm{Re})}{b} \tag{3.64}$$

Substituting Equation (3.64) into Equation (3.63) gives

$$\phi = \frac{N_P}{(Fr)^{\{[a-\log(\mathrm{Re})]/b\}}} \tag{3.65}$$

If power curve is available for particular system geometry, it can used to calculate the power consumed by an impeller at various rotational speeds, liquid viscosities and densities. The method is as follows: calculate the Reynolds number; read the power number or power function and calculate power as

$$P_w = \phi \rho N^3 d^5 \left(\frac{N^2 d}{g}\right)^n \tag{3.66}$$

3.4.8 Scale-up

After identifying optimum combination of operational conditions for a desired result on the model, it is desirable to translate all these to the full-scale set-up. It is now clear that the principle of similarity together with the use of relevant dimensionless groups is essential for this purpose. However, for most of the practical situations conflicting demands of similarity crops up when simultaneously scaling-up for geometry, free surface and dynamic processes. Some times this conflict is resolved by deliberately suppressing the effect of certain dimensionless number in favour of others. For example, effect of Froude number can be eliminated through suppressing vortexing by using baffles. When it is not possible to exclude conflicts then results on small system must be extrapolated to dissimilar conditions on the large system. This type of extrapolation is made on the basis of extended principle of similarity that is expressed as

$$\pi_1 = K \pi_2^x \pi_3^y \cdots \tag{3.67}$$

where the dimensionless group π_1 is proportional to the dimensionless group π_2 to the xth power and the dimensionless group π_3 to the yth power and so on. K is the constant of proportionality that depends on the geometry of the system and consequently a shape factor, which must be determined experimentally.

3.4.9 Previous Work

There is a considerable amount of work done on the metallurgical aspect and on the chemistry of lead refining process. However, there is only very limited information available on the flow behaviour of molten lead and on the modelling of the mixing operation used in industrial lead refining process. Using theory of similarity, as discussed above, [52] analysed the flow behaviour of molten lead under various set-up of practical importance, namely, flow over weirs, through orifices, through pump and in mixing kettles. The authors presented a number of equations based on appropriate dimensionless groups to support their experimental findings. Corresponding water models for flow over weirs were also used to find the correlations. Results clearly showed that molten lead behaves like normal Newtonian fluid and a corresponding water model can be used to predict flow profile in a novel system. They deduce correlation for power consumption through a series of experimental data, for variety of impellers and on several kettle sizes, from the real refining plant. They established that power consumption for two or three blade impeller lie between $(0.014AN^3d^5)$ and $(0.023AN^3d^5)$ for unbaffled and fully baffled kettles, where A is a conversion factor and depends on the system of unit used.

Along the same line of work, [53] further extended the dimensional analysis to model heat and mass transfer in the refining kettle. Both works also discussed the chemistry of refining process, whereas the experimental work [54-56] were devoted to the water model analysis of the corresponding refining process. All of them basically analysed power consumption under various operating conditions, namely, different types of impellers, water depth, shaft depth, impeller speed and presence of simulating dross layer.

3.4.10 Present Physical Model Setup

The physical model for the lead real refining kettle has been developed by maintaining complete geometrical similarity. Water is used as a working fluid to represent molten lead and polystyrene granules are used to represent presence of dross. The dimensions of the kettle are equivalent to the dimensions of an 80ton real refining kettle. It is hemispherical in shape with 1.5m radius. It has a number of glass fitted circular windows to allow visual observation of the flow pattern. Figure-3.4 shows the side view of the water model where we can see the number of portholes available for viewing the inside.

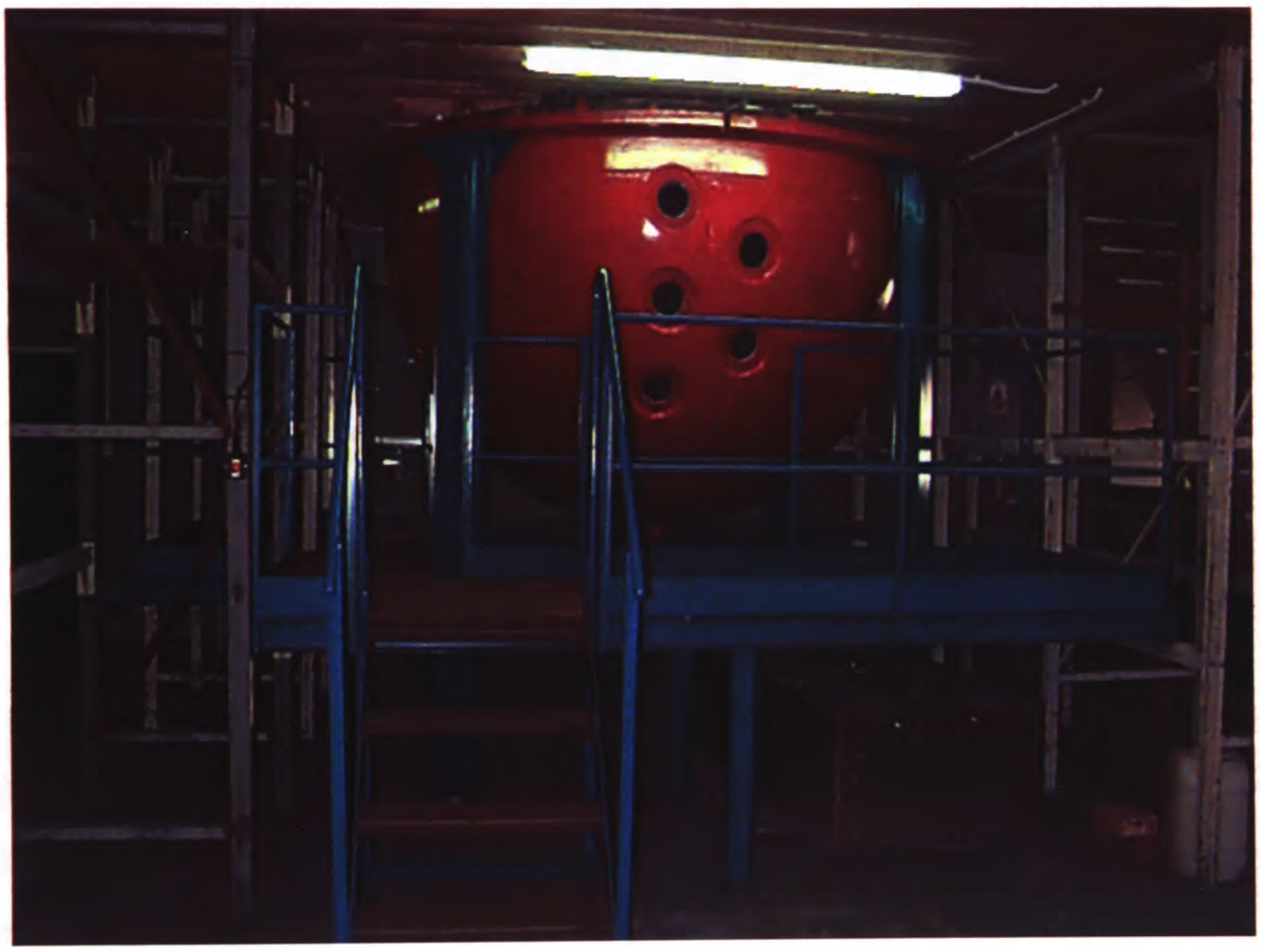

Figure 3.4: Water Model –Side View

A variable speed motor drives the shaft-impeller and this whole setting is mounted on a platform that is placed on rails. This arrangement allows us to adjust the shaft at desired positions with respect to the central axis. The shaft is erected through a hydraulic clamp that can be loosened or tightened in order to adjust shaft length, where a pulley system is provided to help lifting or lowering the shaft. To change the impeller conveniently, motor-shaft system is so constructed that it can be tilted on the platform by using a steering wheel.

Impeller consists of a square hub (that can be replaced by the hub of other shape when number of blades needs to be changed) and its each side faces has an adjustable blade.

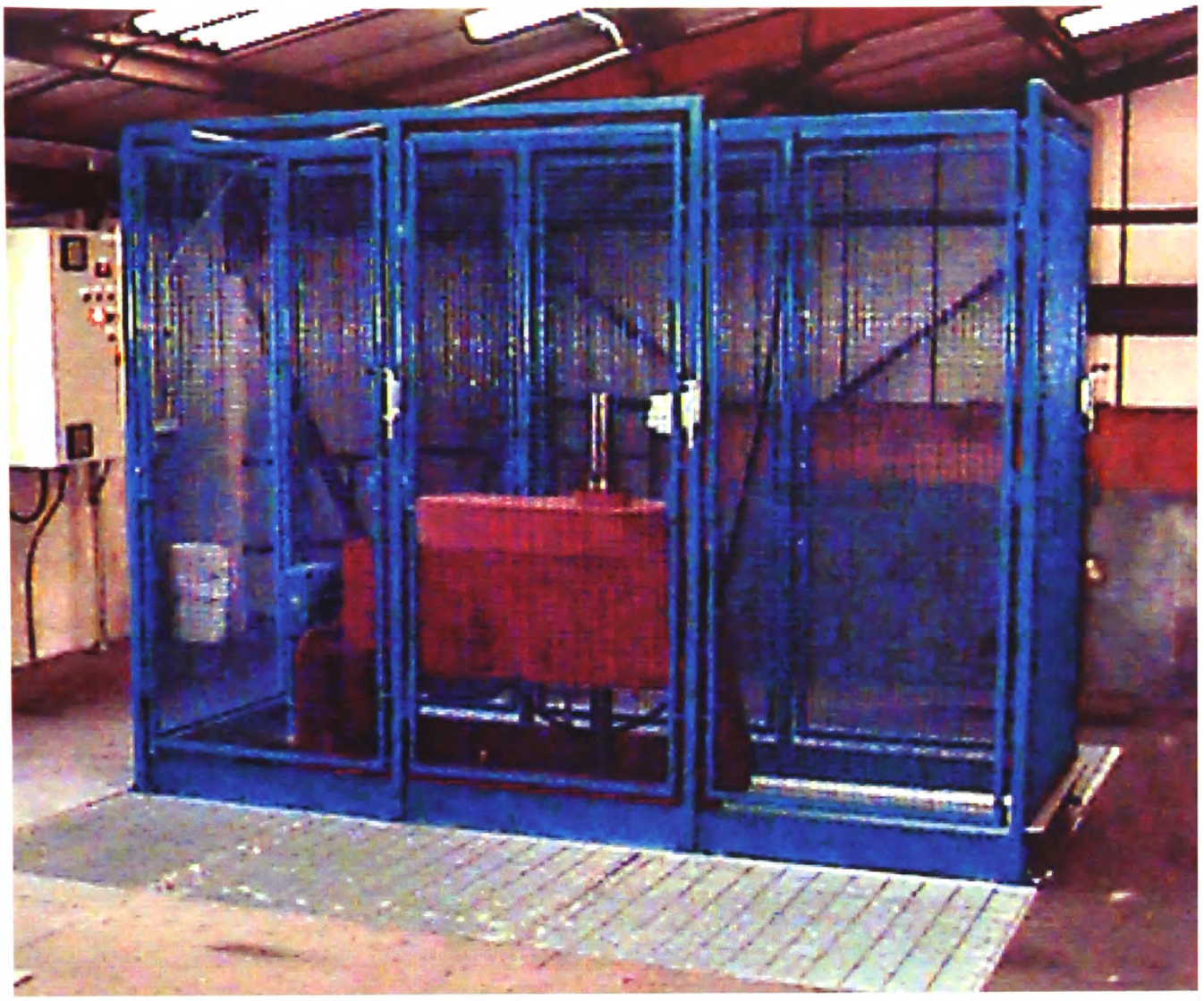

Figure 3.5: Upper Section of Water Model – Caged Rotor-Shaft Assembly

As for safety measure, we can see from Figure-3.5, the whole motor-shaft system is insulated in a cage. It has a number of doors that can be opened whenever the motor/shaft/impeller configuration required to be changed. However, for safety reasons it is required that they should be kept locked when motor is operational. Similarly, top of kettle is also covered by grill frame that has a number of access slots for ADV probe so that probe can be mounted for a number of axial and radial positions.

For the observation and measurement of various factors involved with the flow field of this physical model, a number of experiments were carried out for number of different operating conditions. The next chapter gives the details of experimental results.

3.5 Conclusions

Traditionally the techniques of physical modelling have played a central role in the development of chemical, metallurgical and allied industries. However, in recent years there is also a phenomenal growth in the computational modelling techniques applied in these industries. Despite all the progress in these two methods of investigation, both suffer from their own limitation when addressing the complexity involved in the impeller-stirred mixing process. It is realised that physical modelling or computational modelling techniques alone are not capable of representing the range of complexities associated with the refining of molten lead. However, combining physical modelling with the power of computational modelling, new possibilities for the research and development in the field of lead refining process can be explored.

Keeping the above in mind, the present chapter brought together the essential theoretical background for the techniques of physical modelling applied to the impeller-stirred mixing. First, the need for physical modelling was discussed in some detail. Then, steps required for identifying the essential features of the given problem were presented. Next, a mathematical framework for the principle of similitude was given. This was further illustrated by vortex shape and power consumption prediction. Then, a discussion on the previous work by other researchers was included. Finally, a detail overview of the present physical model (water model) was given.

Chapter 4

EXPERIMENTAL RESULTS

4.1 Introduction

The vast majority of experimental work related to impeller-stirred mixing has mainly been concerned with laboratory scale prototype with somewhat simple geometry, namely cylindrical shape. However, in the lead refining process hemispherical kettles are widely used and for this, there is a very little published experimental work. This chapter presents the results from the various types of experiments carried out on the physical model (water model), described in the previous chapter, and also on the real lead refining kettle under various operating conditions.

4.2 Contributions from this Research

This work is novel in the sense that for the first time systematic experimental work was undertaken on an industrial scale hemispherical water model representing the lead refining process. Apart from visualising the flow behaviour under various operating conditions a range of power consumption readings were also taken. The free surface deformation and vortex generated by the impeller stirring of fluid for industrial scale mixing vessel is one of the little investigated areas in the impeller stirred mixing process. The present experimental work also carried out readings for vortex depth using different impeller rotational speeds. The analysis of the vortex data successfully identified the independence of vortex depth from Reynolds number when operating beyond certain rotational speed. This is perhaps the first attempt to use Acoustic Doppler Velocimeter (ADV) [57] for velocity measurement in an impeller-stirred vessel (in this case, it is water model kettle).

4.3 Flow Visualisation

It is impossible to see the fluid movement of molten lead in the refining kettle. This type of observation could easily be performed using a water model which can facilitate our

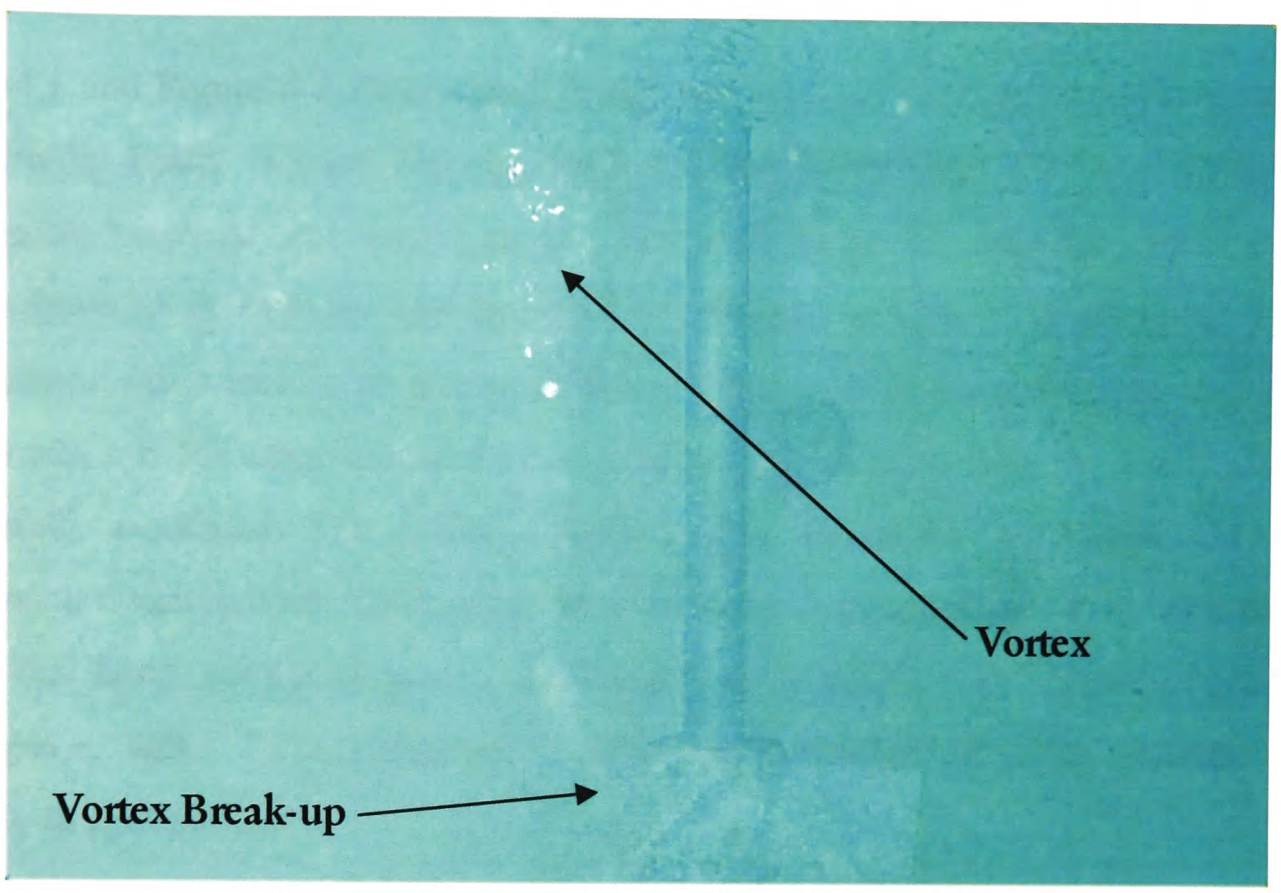

Figure 4.1: Vortex Formation and Breakup

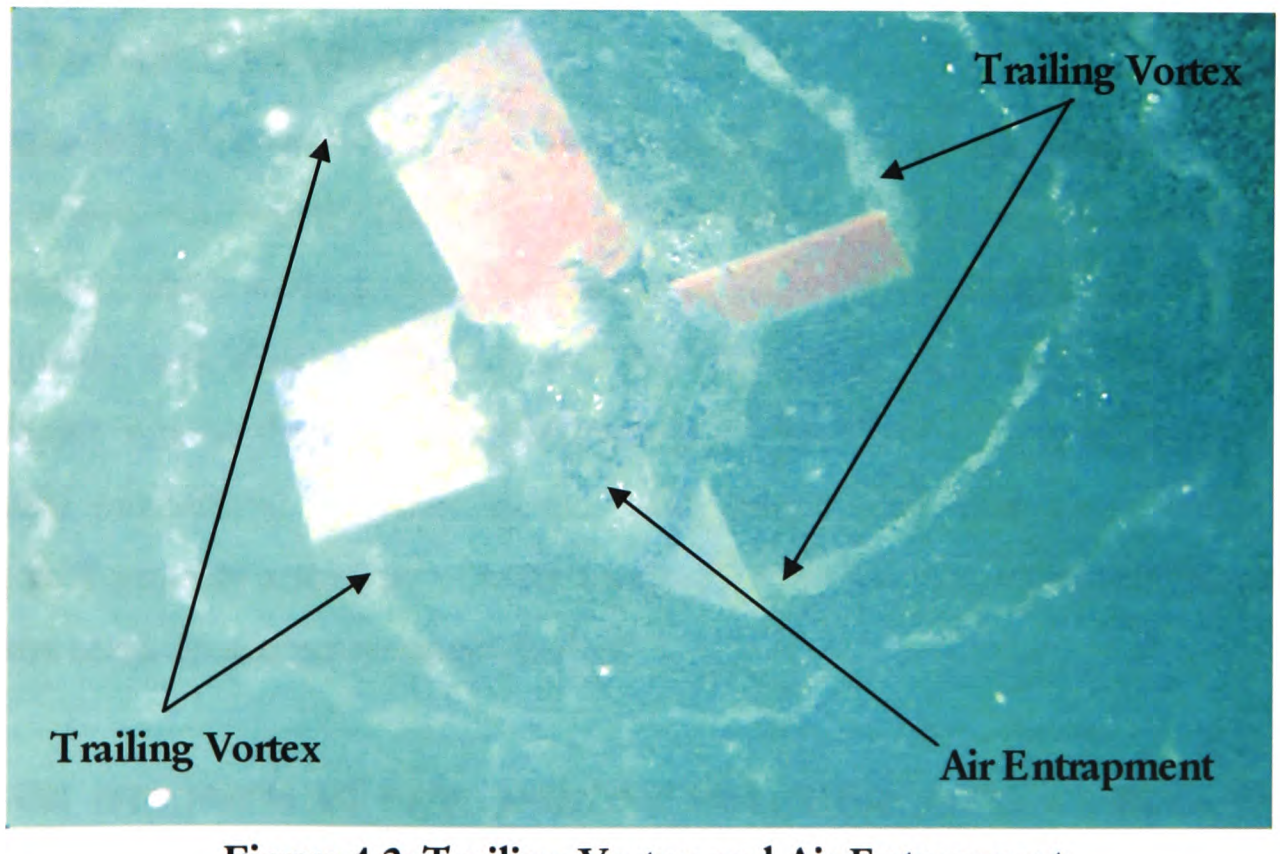

Figure 4.2: Trailing Vortex and Air Entrapment

understanding of impeller induced flow behaviour. Apart from direct observations and quantitative measurements of various aspects involved in this stirring process, the flow pattern was also video recorded.

Figure-4.1 and Figure-4.2 show details from typical video footage taken for an unbaffled water model kettle. As we can see from the Figure-4.1 that a central vortex, which periodically revolves and wraps around the impeller-shaft, extending from the water surface down to the impeller and intermittently breaks up with the rotating impeller. This phenomenon gives rise to air entrapment and dispersion in the fluid bulk. From Figure-4.2 we can see the structure of trailing vortex behind each impeller blade, which are tangentially spiralling. The trailing vortices, formed behind the blades, have a low-pressure core and provide mechanism for air bubble dispersion and cavity formation [58-59]. In this figure we can also see the entrapped air in the form of a cavity sticking below the impeller hub. This visualization helps understanding the flow pattern near the impeller in a stirred tank.

4.4 Power Consumption

The importance of power consumption for both the operation and modelling of impeller-stirred vessels was highlighted in the previous chapter. To quantify the pattern of power consumption under varying process conditions a number of readings were taken on the water model and also on the real lead refining kettle. The main objective of these experiments was to develop an understanding of the effect of process variables on the associated phenomena. Impeller speed, blade angle, shaft length, the shaft positions (centred/off-centred) and effect of baffles were the main factors investigated for their effect on vortex break up and power consumption.

In all the experiments on water model the four bladed standard impeller of 480mm diameter and 110mm blade height was used, whereas other operating conditions were changed from one case to another. It is interesting to note that the observed pattern of

power consumption, vortex break-up and fluid oscillations have been similar for both water model and real lead refining kettle.

4.4.1 Results for Water Model

Figure-4.3 shows the power required in producing a vortex break-up using a centrally positioned impeller-shaft with different blade angles and shaft depths. There is an increasing trend in power consumption with increasing the shaft depth and blade angle;

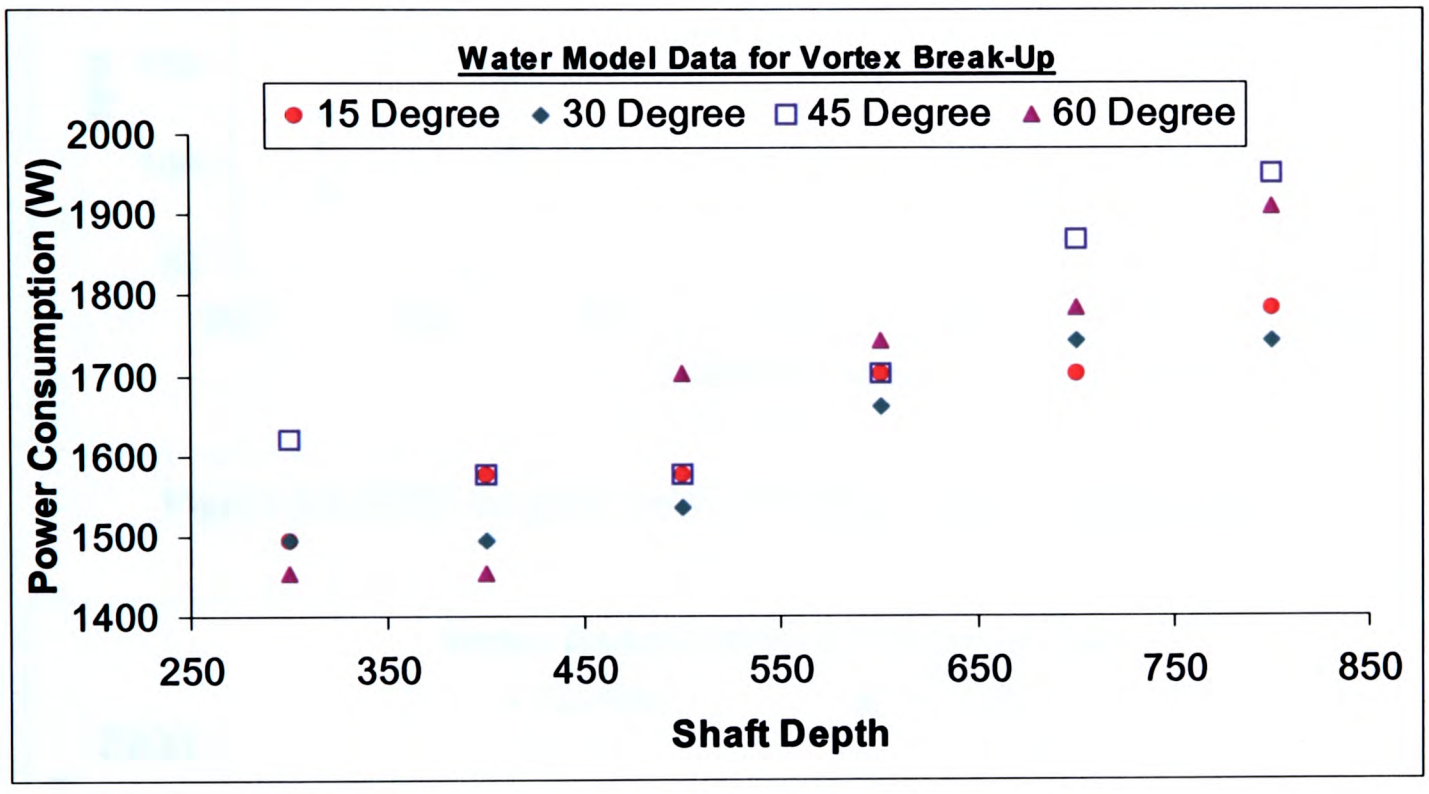

Figure 4.3: Power Consumption at the Point of Vortex Impingement

however, it is not the case for all readings. It should be noted that periodic break-up of central vortex (see Figure-4.1) causes corresponding fluctuation in power consumption. Here visual observation was used to judge the vortex impingement with the impeller blades. Obviously, such observations are open to subjective influence. However, even with these uncertainties, readings are valuable aid to the understanding.

Figure-4.4 gives data for the required rotational speed, Revolution Per Minute (RPM), of impeller to produce a vortex break-up at various shaft depths and blade angles. It is clear that higher RPM is required when the shaft depth and blade angle is increased. During this

trial, it was observed that for a given shaft depth, increasing the impeller speed increases the instability or oscillation of the fluid bulk. This pattern of oscillation causes the fluid to spill over the kettle rim if the impeller speed is increased beyond a limit. It should be noted that this pattern of oscillation increases with increasing the blade angle. However increasing the shaft depth increases the stability.

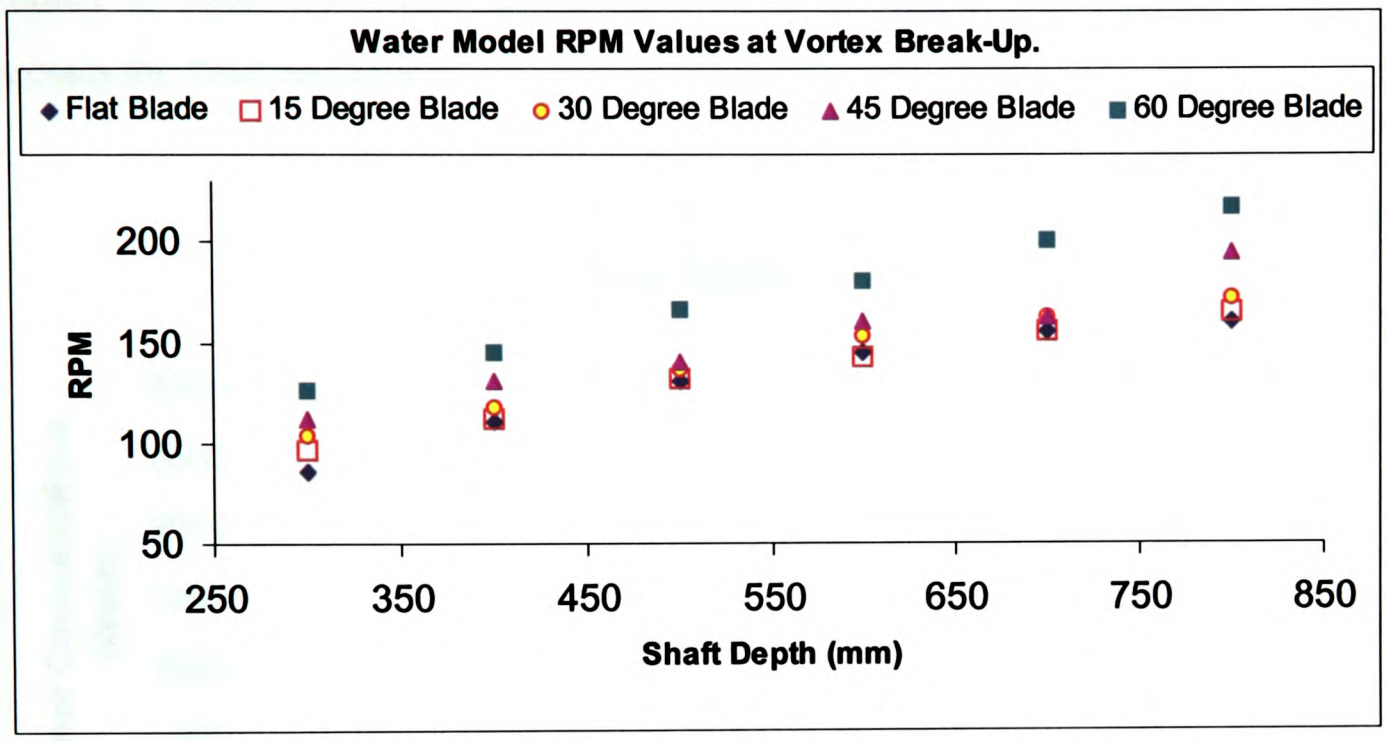

Figure 4.4: RPM Required at the Point of Vortex Impingement

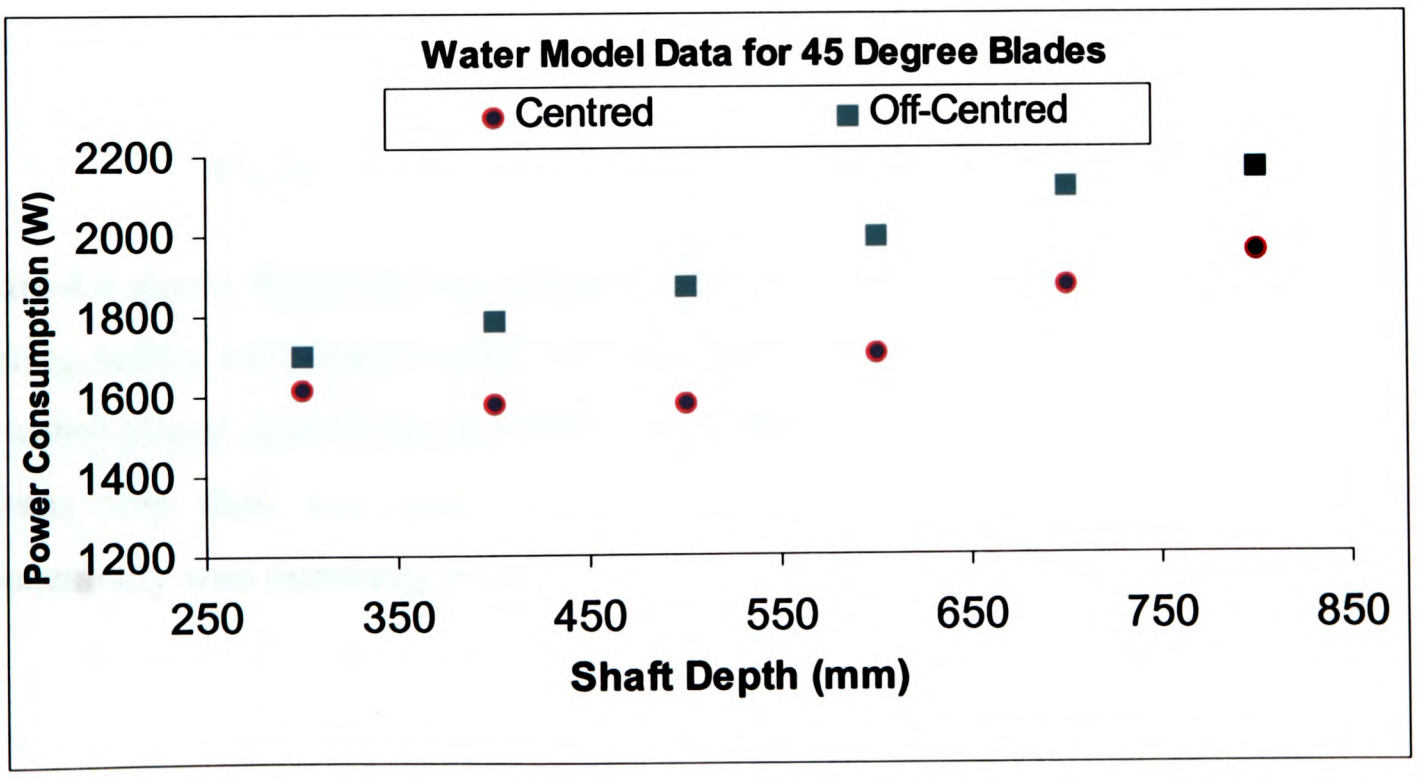

Figure 4.5: Power Consumption Required for Vortex Impingement in Centred and Off-centred Shaft Arrangement

Figure-4.5 shows comparison of power consumption for a 45-degree blade impeller on a centred and off-centred shaft for various shaft depths. For both the shaft positions, there is increasing trend in power consumption with increasing shaft depth. However, for a given shaft depth there is a drastic increase in power consumption for the off-centred shaft. Off-centred positioning of shaft breaks the symmetry of flow domain and hence, more power is consumed to rotate the fluid. It has been observed that positioning shaft off-centred suppresses the fluid oscillation.

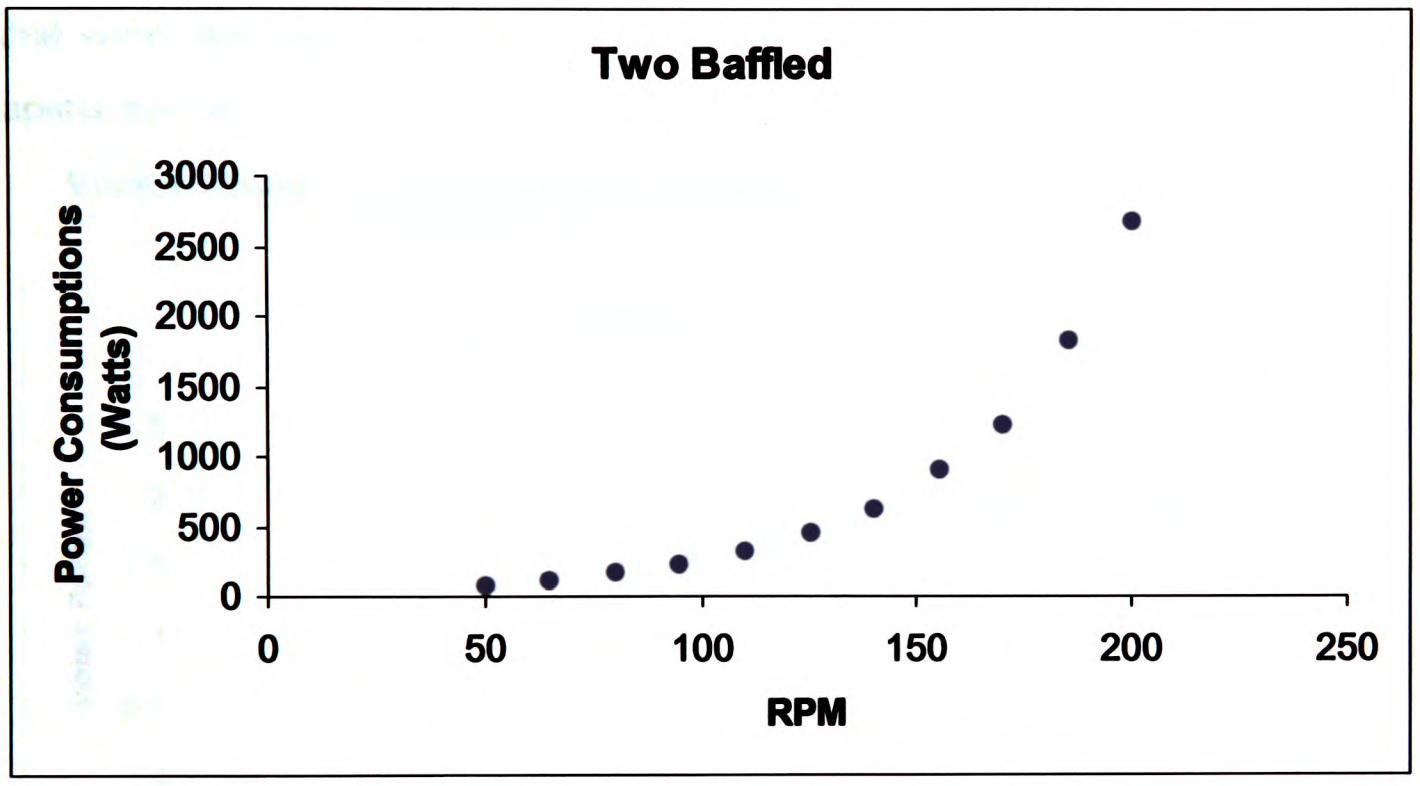

Figure 4.6: Power Consumption for Two-Baffled Kettle

Figure-4.6 shows the power consumption trend for water model that is fitted with two side entering baffles (of 254mm width and from kettle rim it is going down 659.4mm deep in the water) placed opposite to each other. Here standard 45-degree blade angle impeller and 750mm deep shaft was used. As we can see the power consumption is increasing exponentially with increasing impeller speed.

4.5 Vortex Depth

Drawdown and dispersion of floating particles very much depend on the shape of free surface [60-63]. That is why the study of the free surface and vortex shape is fundamental to this process. Owning to the transient nature, flow field in unbaffled water model develops uncontrollable swirl and makes vortex depth measurement impossible. This is the reason vortex depth measurements were mainly carried out for baffled kettle (two side entering baffles fitted opposite to each other). Dimensions of baffles, 254mm width and 659.4mm deep, were such that it helped preventing the swirl without suppressing the central vortex too much. These vortex depth measurements were also used to validate the computer models.

Vortex Factor = Vortex Depth /(Impeller Diameter × Froude Number) (4.1)

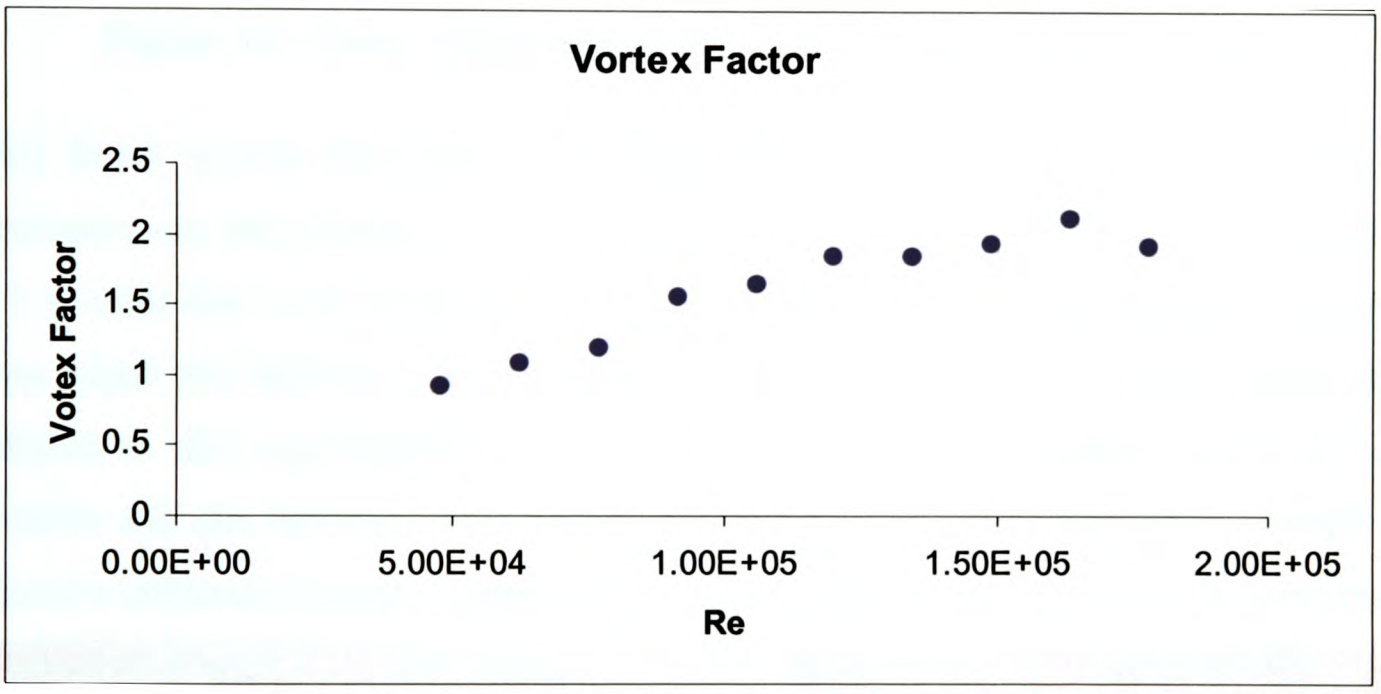

Figure 4.7: Vortex Factor against Reynolds Number

Even in the baffled kettle, continuous break-up of central vortex with impeller makes the whole pattern highly oscillatory. That is why it is required that the observation is made for sufficiently long period and a number of independent measurements are taken. In present experiment, for every set of data, 15-minute observation time was used and for each rotational speed four round of observations were made. Figure-4.7 presents the measured vortex depth in terms of a dimensionless number called vortex factor [64], defined in Equation-4.1, against Reynolds number.

The Figure-4.8 gives vortex factors, with 15% error bar, for Reynolds number bigger than 10^5, where straight line represents the mean value of given data. As it can be seen, plot of

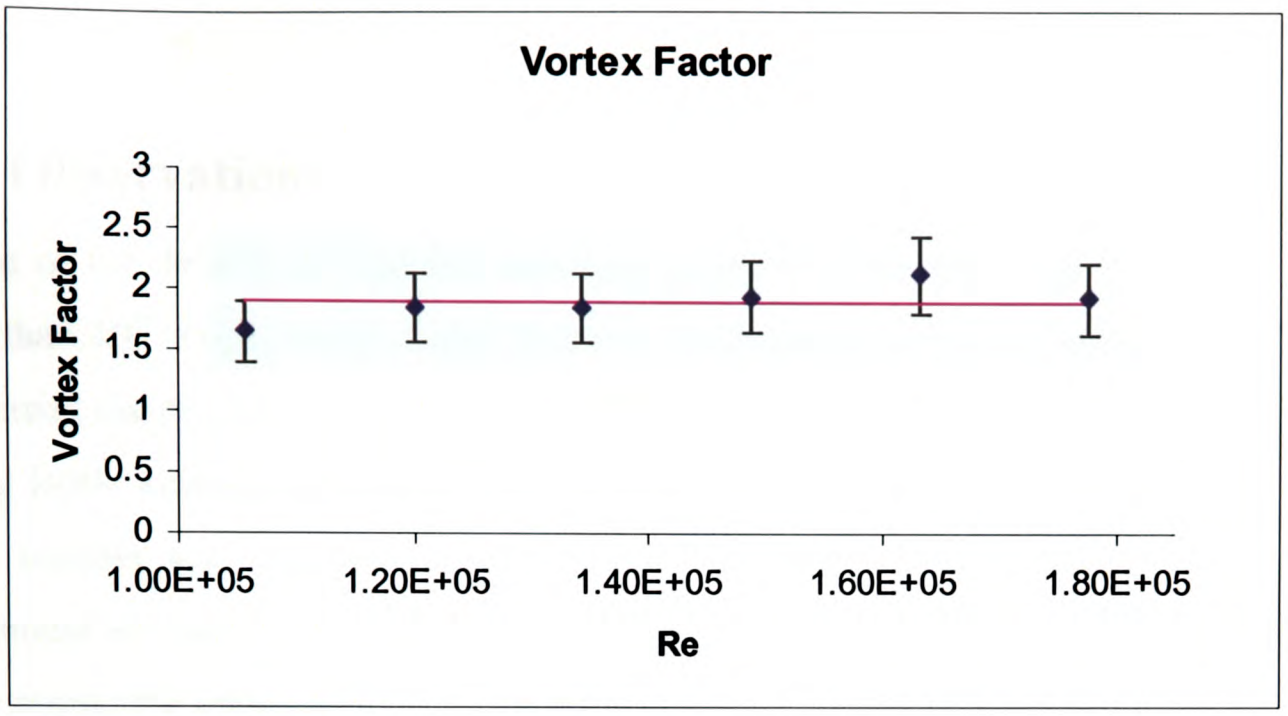

Figure 4.8: Vortex Factor against Reynolds Number Bigger Than 10^5

vortex factor against Reynolds, as an approximation, is assumed constant straight line representing the independence of vortex factor from the Reynolds number. From the Table-4.1 it is clear that most of the data points are within 3% of the average line, except two points which are between 12-13%. The large deviation in these two data points can be attributed to the experimental error. Because of the highly transient nature of vortex formation and also because of the nature of observation it is very difficult to minimize the subjective influence beyond a certain limit and this explains the uncertainty in experiment.

Reynolds Number	Vortex Factor	Mean Vortex Factor	Difference (%)
1.06E+05	1.647916667	1.888372	-12.73347271
1.20E+05	1.845833333	1.888372	-2.252663494
1.34E+05	1.846479167	1.888372	-2.218462958
1.49E+05	1.940416667	1.888372	2.75606007
1.63E+05	2.1225	1.888372	12.39840455
1.78E+05	1.927083333	1.888372	2.049984502

Table 4.1: Percentage Difference in Individual Vortex Factors from Their mean

Based on correlation equations for calculating vortex depth, [64] concluded that the corresponding vortex factor above Reynolds number 10^4 becomes constant. Here similarly,

based on the above data, it can safely be assumed (as a simplifying approximation) that vortex factor above Reynolds number 10^5 becomes constant.

4.5.1 Observation

Because of the density of lead the associate operating Reynolds number is always much bigger than 10^5 hence, vortex depth becomes independent of the Reynolds number. As it was pointed out previously (Chapter-3; Section-3.4.1) that developing water model for lead refining kettle keeping geometrical similarity along with matching Reynolds number and Froude number will require unrealistic kettle size or huge impeller speed. However, on water model we can easily match the Froude number with that of lead refining kettle hence we can mimic the vortex formation phenomena.

Suspension of floating particles through drawdown and dispersion depends on the Froude number [60-63] and the ratio of density differences of fluid and particle with the density of fluid. The density of lead is 10500kg/m^3 and average density of dross is 9000kg/m^3, hence above said ratio is (10500-9000)/10500 =0.143. The density of water is 1000kg/m^3 and if we select a particle with density about 857kg/m^3 then we can mimic the drawdown and dispersion of the dross on the water model too. In the present study, in order to mimic the drawdown and dispersion of dross on the water model polystyrene beads (with average density of about 900kg/m^3) are used. In conclusion, it can be said that identifying this fact has established the usefulness of water model in studying the vortex formation and drowdown and dispersion phenomena in the lead refining kettle.

4.6 Acoustic Doppler Velocimeter (ADV)

When a source of sound is moving relative to the receiver, the frequency of the sound at the receiver is shifted from the transmitted frequency. This is a well known phenomenon called Acoustic Doppler Effect [65]. In the form of equation it can be written as:

$$f_{Doppler} = -f_{Source}(V / C) \tag{4.2}$$

where V is the relative velocity between source and receiver, C is the speed of sound, $f_{Doppler}$ is the change in frequency at the receiver, and f_{Source} is the transmitted frequency.

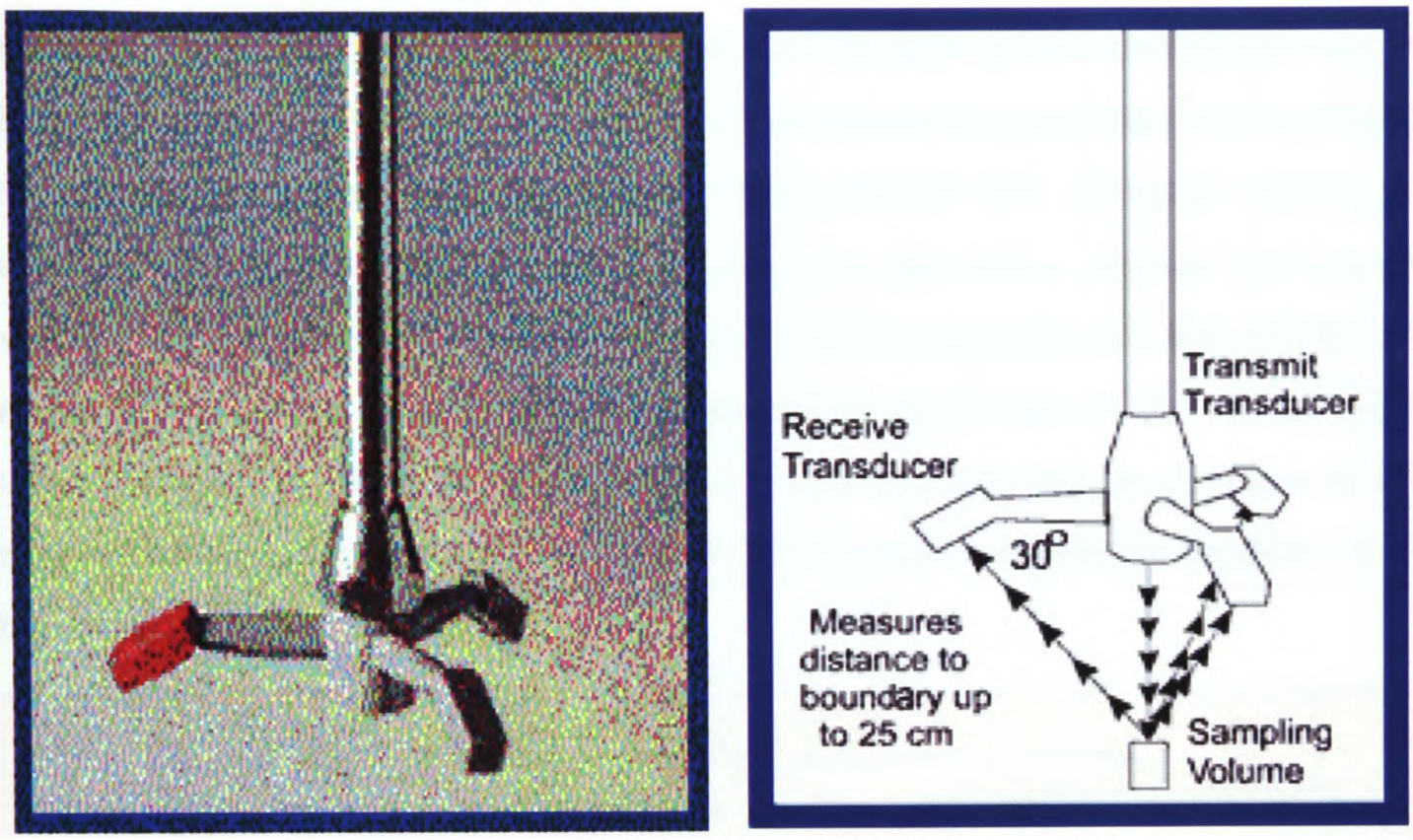

Figure 4.9: Acoustic Doppler Velocimeter (ADV)

The velocity measurement probe, Nortek Acoustic Doppler Velocimeter (ADV) [57] is based on this principle of Doppler frequency shift. Nortek ADV probe is a remote-sensing instrument that measures the three components of water velocity at single point un-obstructively. It transmits pulses of ultrasound that scatter back form particulate matter in water to the receiver and gives the measurement of water velocity. As we can see from Figure-4.9 the ADV probe consists of four ultrasonic transducers, a transmit transducer located at the centre of three receive transducers spaced at 120^o angular intervals, and slanted 30^o from the axis of the transmit transducer. The ADV has an acoustic frequency of 10 MHz and uses a small sampling volume, the volume of water in which measurements are made, which is less than a cubic centimetre. Both transmitter and receiver are constructed to generate very narrow beam patterns; the transmitters are mounted such that their beams intersect at a volume of water located some distance away. This distance can be

adjusted from standard 25cm (or 10cm) to 5cm for velocity measurement near boundary and this allows non-obstructed measurement at the target point. The beam intersection determines the location of the sampling volume [66].

The transmitter generates a short pulse of sound at a known frequency, which propagates through the water along the axis of its beam. As the pulse passes through the sampling volume, the acoustic energy is reflected in all directions by particulate matter (bubbles, particles etc.). Some portion of the reflected energy travels back along the receiver axis, where it is sampled by the ADV and the processing electronics measure the change in frequency. The Doppler shift measured by one receiver is proportional to the velocity of the particles along the axis located halfway between the central axes of the transmitted and received beams. The probe is linked with computer that provides an interface to allow instrument set-up and data processing along with the visual monitoring of the three velocity components in the real time [67].

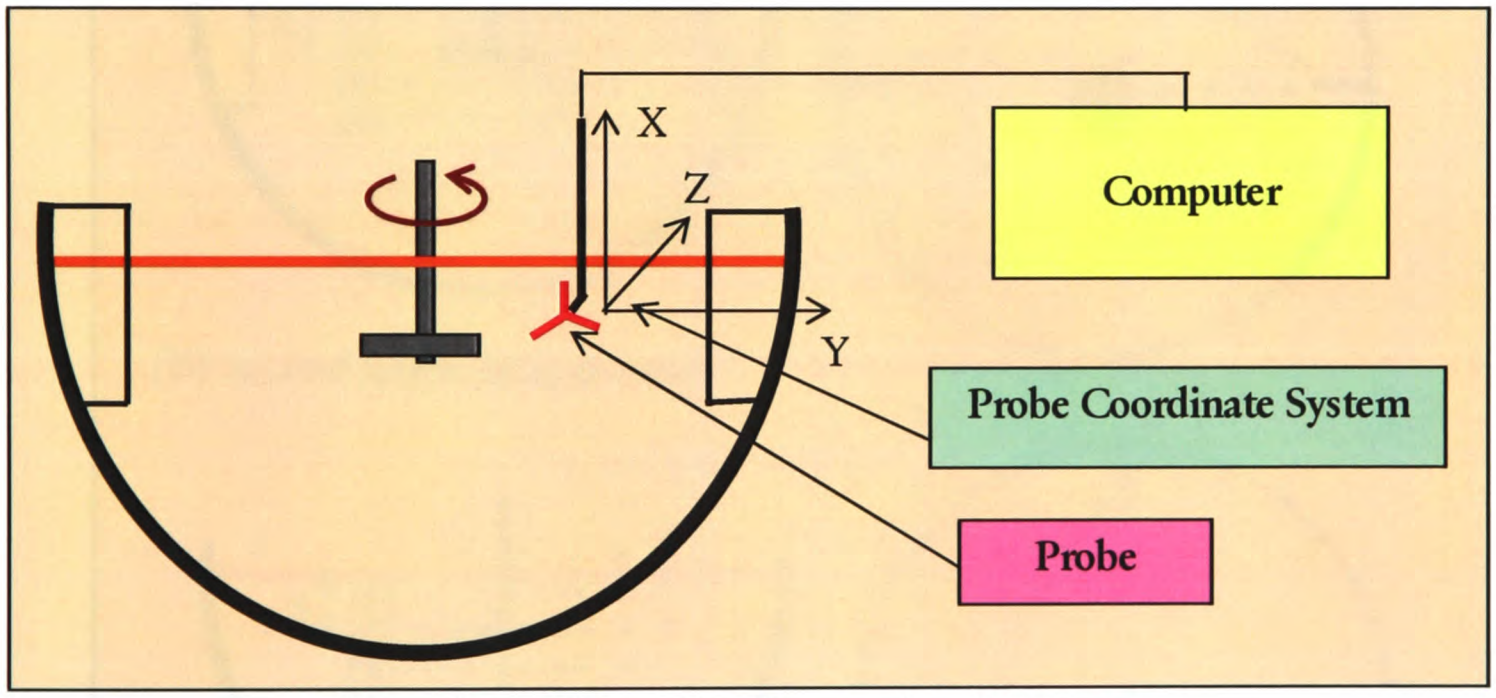

Figure 4.10: Schematic Diagram for ADV Set-up

Figure-4.10 gives the schematic representation of the ADV probe set-up in the water model. Here it also shows the coordinate system attached with the ADV probe and velocities are measured with respect to this.

Using above described Acoustic Doppler Velocimeter (ADV) probe, a range of velocity measurements were carried out at various locations in the water model for a number of different operating conditions. A number of measurements were carried out for three different shaft depth (S = 375mm, 500mm and 750mm deep from the water level) for impeller rotational speed 140 RPM. Impeller was standard 480mm diameter with four 45° degree angled blades of height 110mm. In order to control the swirl and instabilities in the fluid bulk caused by the impeller driven rotation of the water, the kettle was fitted with two baffles (254mm width and 659.4mm deep in water).

In the Figure-4.11 black dots represent the points where ADV probe was used to measure

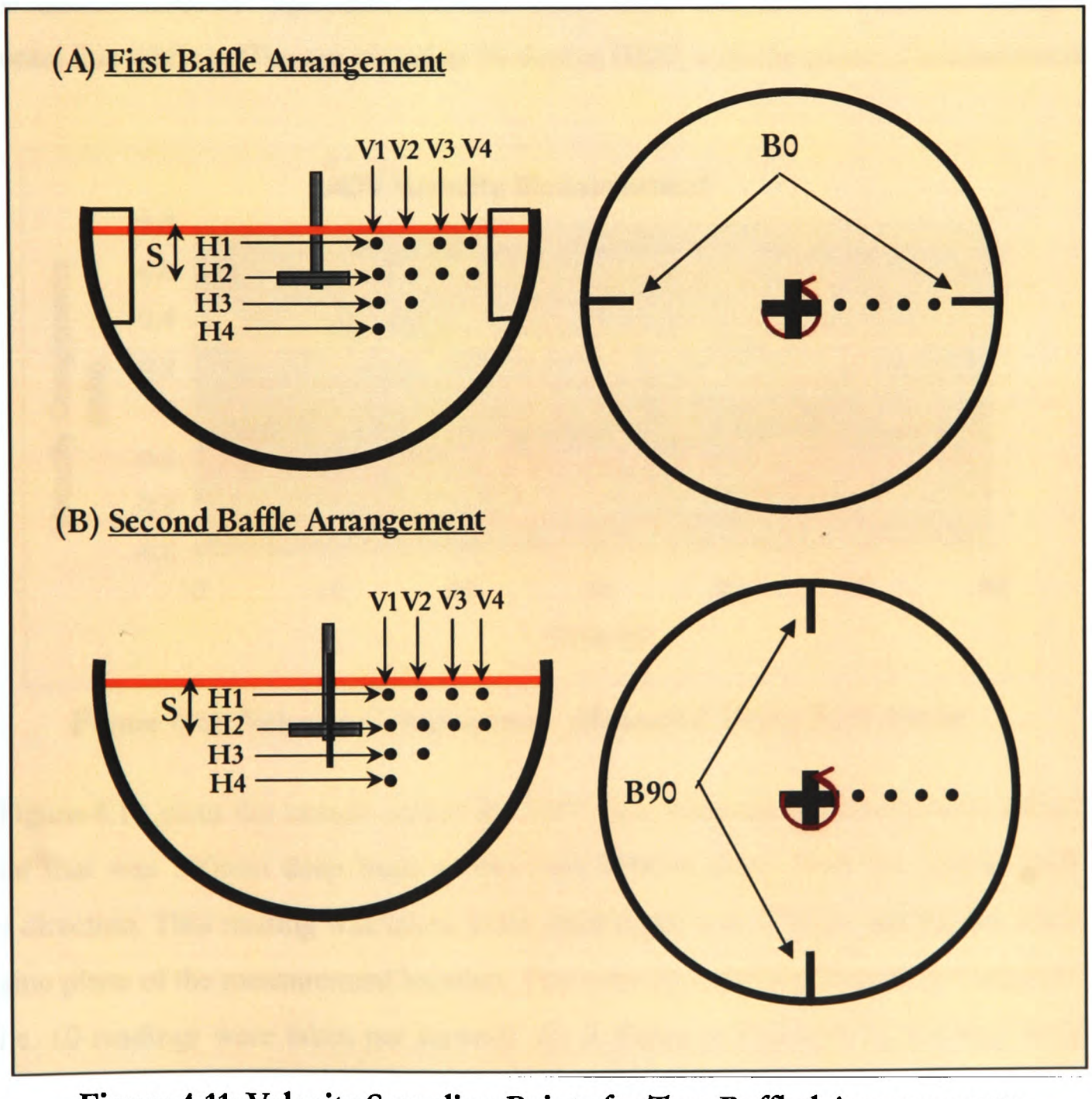

Figure 4.11: Velocity Sampling Points for Two Baffled Arrangements

the velocities. The points along horizontal line H1 are 100mm below the water surface level whereas points along line H2 are at the same depth as that of impeller. Points on H3 and H4 are 1000mm and 1200mm deep respectively. Points along vertical lines V1, V2, V3 and V4 are located 400mm, 600mm, 800mm and 1000mm away in radial direction from the central axis towards the kettle rim.

For every point two sets of measurements were taken – once when points were in the same plane of the baffles (B0) and other when baffles position was placed at 90-degree with the plane of velocity measurement (B90). The measurement is presented in following graphs, where legend represents the location of the probe and operating conditions. For example, legend (S375-H2-B90) represents 375mm deep shaft and probe locations along H2 horizontal line while baffles are placed at 90-degree (B90) with the plane of measurement.

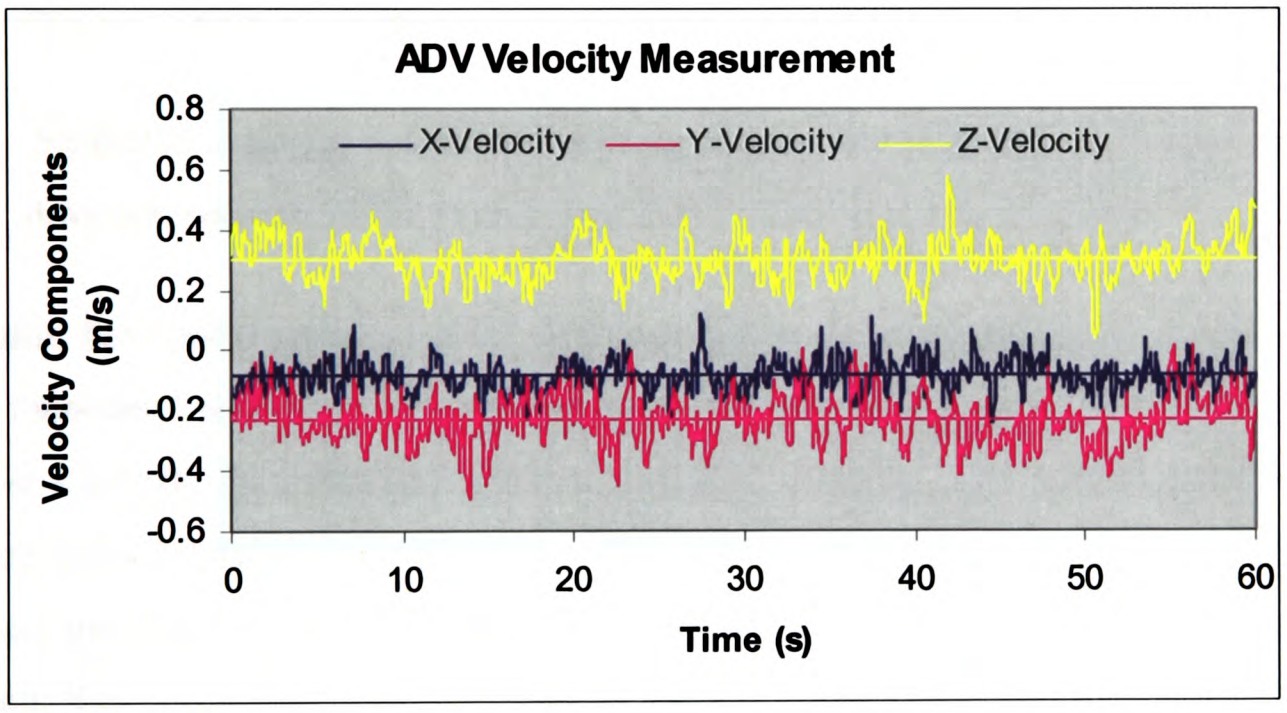

Figure 4.12: Velocity Components – Measured Using ADV Probe

The Figure-4.12 gives the sample output for ADV data when measurements were taken for a point that was 100mm deep from surface and 400mm away from the central shaft in radial direction. This reading was taken when shaft depth was 375mm and baffles were on the same plane of the measurement location. The velocity sampling frequency was set to 10 Hz (i.e. 10 readings were taken per second). As it shows in Figure-4.12, the total reading time was one minute.

It is clear from Figure-4.12 that random fluctuations are present in all the velocity components. This is mainly because of the turbulent nature of the flow field. Here system is operating on a very high Reynolds number ($\approx 1.35\times10^5$). In order to get the average value of velocity components, reading were taken over a longer period of time (one minute reading time in present case). In Figure-4.12 instantaneous velocity components are given along with their average values (straight line with same colour). Considering the coordinate system of probe (Figure-4.10) and the averaged values of instantaneous velocity components (Figure-4.12) it can be interpreted that:

1. Average velocity component in x-direction is pointing downwards, i.e. fluid is being pulled into the bulk from the surface towards the impeller.

2. Average velocity component in y-direction is pointing towards the central axis that means fluid is being drawn towards the impeller shaft and into the central vortex.

3. Similarly, a strong w-direction velocity component is present in counter clockwise direction because of the overall fluid rotation driven by the impeller.

The same flow pattern was visually observed during the experiment too. Location of the above mentioned point is in close proximity of the free surface and is located closer to the impeller shaft. By the rotational action of impeller, a central vortex form around the shaft and free surface deformation takes place. Here fluid is being drawn from the surface to the bulk near the shaft and hence we get negative x-velocity component here. To fill the void at the shaft, fluid from kettle rim rush towards the axis of rotation and hence, we see negative y-velocity component. The rotation of impeller drives the bulk in the rotational motion and this gives rise to strong positive z-velocity component. The rotational component of velocities tends to be more prominent near the surface as baffles on the kettle wall inhibit the rotation and direct fluid towards surface, giving rise to big re-circulation zone in the vertical plane.

In the following section, the rest of the ADV measured data are presented as an average of the instantaneous velocity magnitude. The instantaneous velocity magnitude is defined as

square root of instantaneous three velocity components whereas velocity magnitude is taken as the average of individual instantaneous velocity magnitudes:

$$V_{inst} = \sqrt{v_x^2 + v_y^2 + v_z^2} \tag{4.3}$$

$$V_{mag} = \frac{\sum_{n} V_{inst}}{n} \tag{4.4}$$

and where n is total sampling number.

4.7 Results from ADV Measurement

In order to establish the accuracy and reproducibility of the ADV measured velocities two sets of readings were taken for two different lengths of time. Figure-4.13 shows the ADV measured velocities in the case of 375mm deep shaft with reading time of 1 min and 10 min respectively.

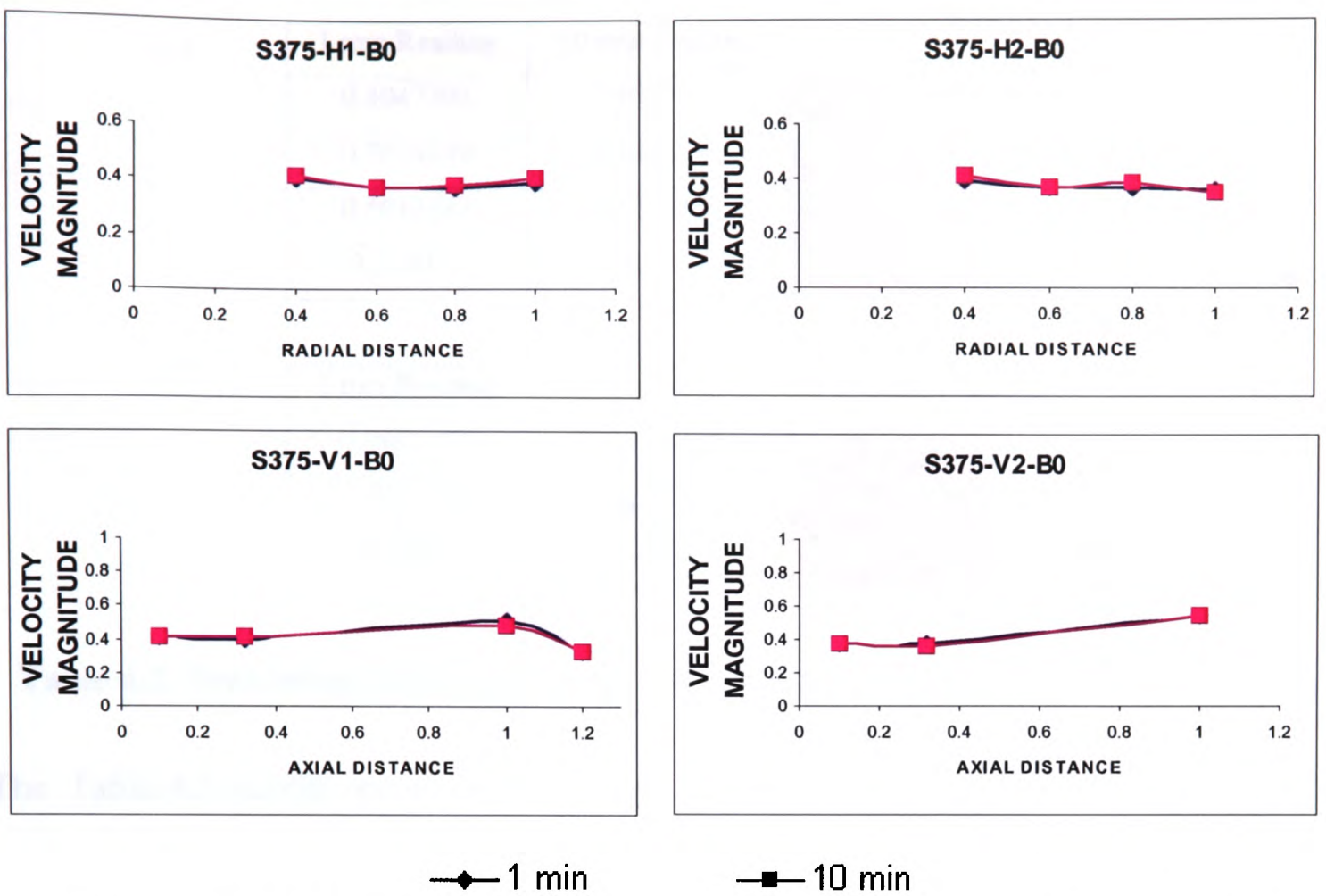

Figure 4.13: Velocities Measurement for Two Different Sampling Duration

(a)

1 min Reading	10 min Reading	Difference (%)
0.4047394	0.4099273	1.26556587
0.3685122	0.3658908	-0.716443267
0.3655315	0.3746861	2.443271848
0.3868985	0.3988791	3.003566745

(b)

1 min Reading	10 min Reading	Difference (%)
0.3874039	0.4045136	4.229697098
0.3677934	0.3615246	-1.733989886
0.3645783	0.3810621	4.325751629
0.3600135	0.3466611	-3.851715696

(c)

1 min Reading	10 min Reading	Difference (%)
0.4047394	0.4099273	1.26556587
0.3874039	0.4045136	4.229697098
0.5012382	0.4755279	-5.406685917
0.318473	0.3183772	-0.030090094

(d)

1 min Reading	10 min Reading	Difference (%)
0.3685122	0.3658908	-0.716443267
0.3677934	0.3615246	-1.733989886
0.544217	0.541708	-0.463164657

Table 4.2: Percentage Difference in the ADV Velocities Reading for 1min & 10min

The Table-4.2 (a)-(d) gives the corresponding data values and their differences for Figure-4.13 respectively. From the table, it can be seen that for most of the data points, differences are well below 5%. Any difference in measured value, for two different lengths of reading time, can be attributed to the inherently transient nature of the flow field. Here, apart from random turbulent fluctuation of velocities, non-random fluctuation, because of the periodic passage of impeller blades, is also present. The periodic sweeping of resultant vortices, generated by the impeller-flow interactions, by impeller over the stationary measuring points is a main source of influence on the difference in measurements caused by the non-random fluctuation. Along with this periodic break-up of the central vortex with impeller blades results in air entrapments, this further complicates the flow structure. Keeping these in mind, it is clear that the ADV measurements have reproduced the results within the 5% error range. That establishes its usefulness as a velocity measuring device for industrial scale mixing vessels.

In order to minimise the random error and to achieve better averaging, for the rest of the measurements reading time was 10 min with sampling rate 10 instantaneous velocities reading per second. To minimise the effect of perturbation in flow field caused by changing the probe position from one reading location to another, flow field was left to

settle for 10 min before resuming the readings. Similarly, every time whenever either shaft depth or baffles position was changed motor was restarted and fluid field was left for about 15-20 min to settle before taking the velocity measurements again.

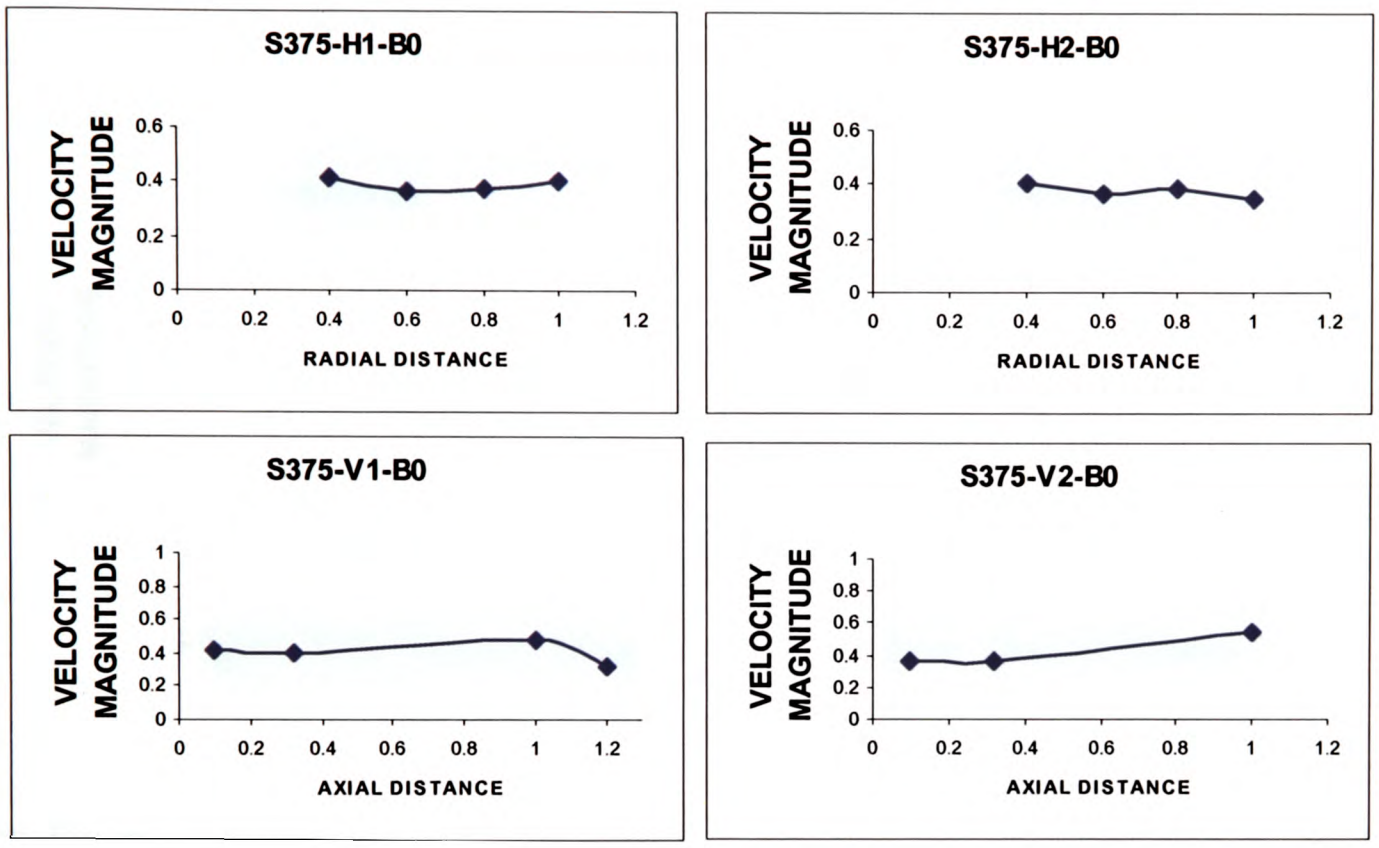

Figure 4.14: Velocity Magnitude for Short Shaft (375mm)

In Figure-4.14 for H1, velocity magnitude decreases up to middle and then increases towards the kettle rim. As interaction of fluid baffle become more prominent, it gives rise to kinetic energy and hence higher velocity near the baffles. However, velocities along H2 first decrease, then slightly increase, and finally decrease at the fourth measuring point. In first vertical line V1, we can see the increase in velocity at third measuring point. This point is located into the proximity of impeller generated angular jet of fluid that is being pumped towards the bottom of the kettle. As we go further away from the shaft, the strength of the jet reduces and hence velocity for V2 becomes somewhat smaller in magnitude.

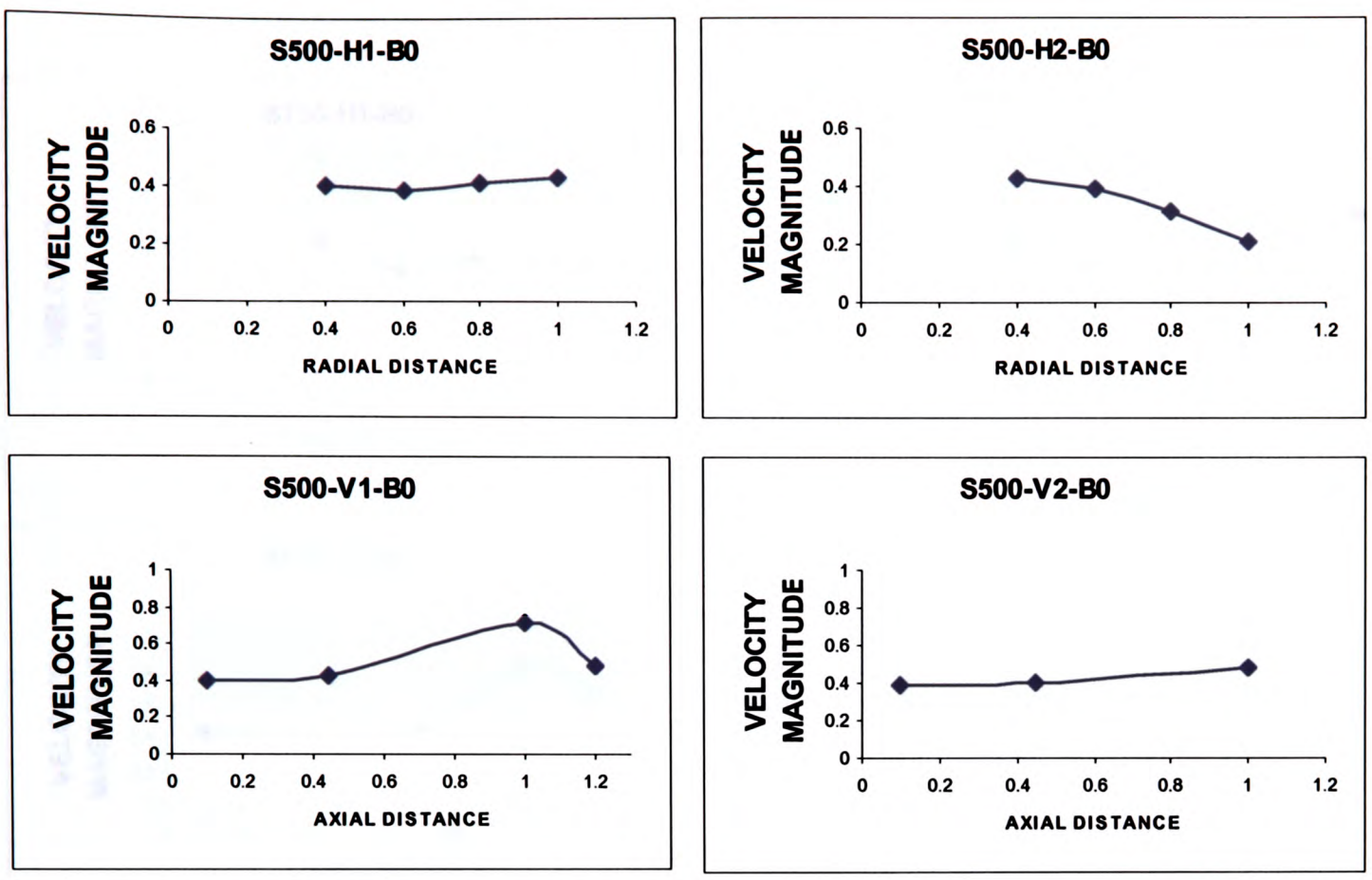

Figure 4.15: Velocity Magnitude for Medium Shaft (500mm)

From Figure-4.15 it can be said that overall pattern of velocity magnitudes are similar to those described for the 375mm deep shaft case (Figure-4.14). However, the main difference is in the third point, here velocity is much higher than the case before. This is only because this shaft is deeper and that measurement point is closer to the angular jet of liquid that is being pumped out of impeller in the downwards direction. Another noticeable difference is the magnitude of velocity along the second vertical line. In the case above (S375), the difference between velocities along first vertical line and second vertical line is not as big as in the present condition. It can be said that because it draws fluid much deeper into the bulk hence fluid loses energy more rapidly as we go towards the wall. However, in a shallow impeller much of the activities are confined to the upper part of the kettle. Hence, energy is more uniformly distributed, as it is not being consumed in drawing fluid in bulk as much as required in the present condition.

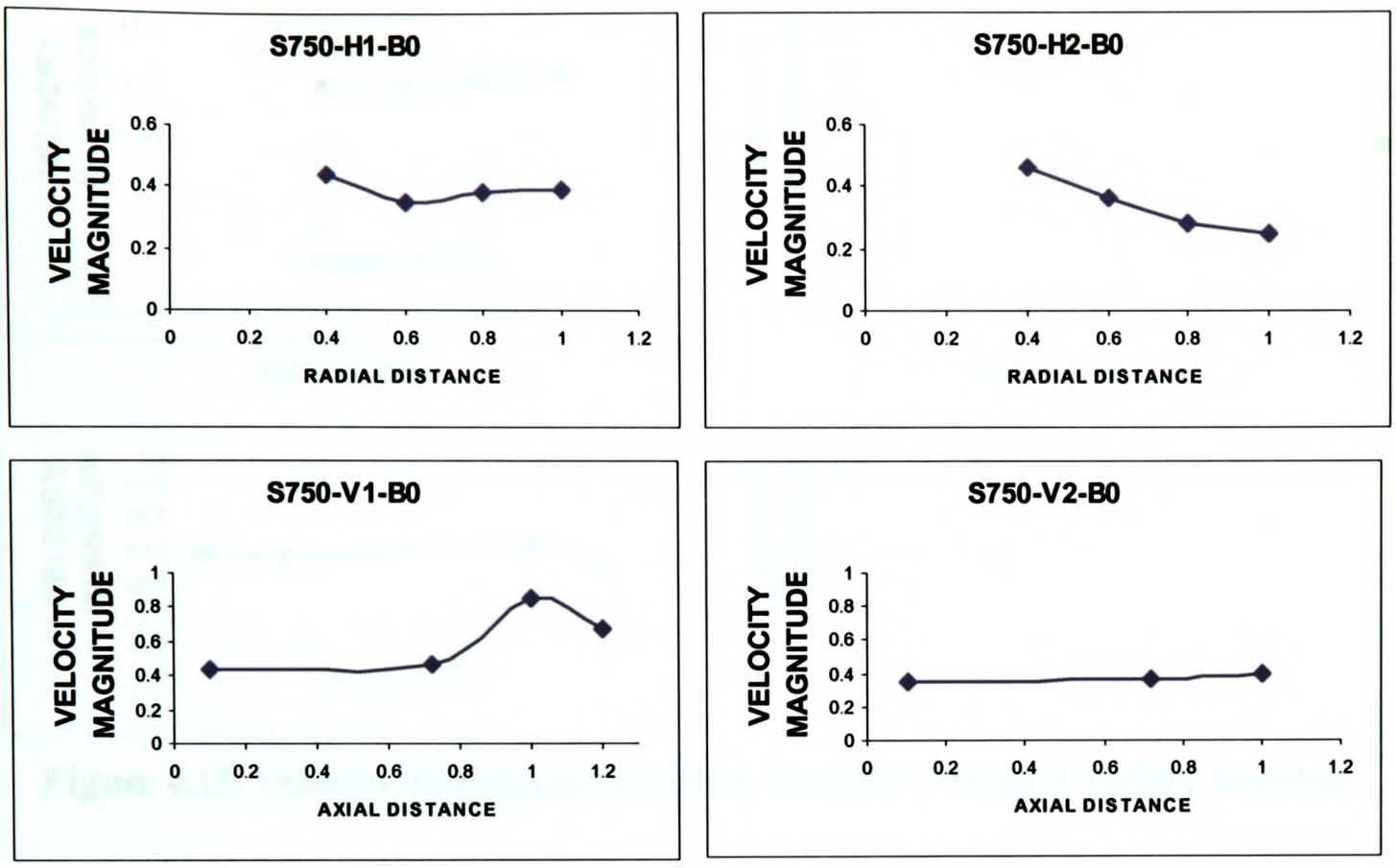

Figure 4.16: Velocity Magnitude for Deep Shaft (750mm)

Again, in this case (S750) overall trend is very much similar as for above two cases (S375 & S500). However, it can be seen here that velocity along H1 is more uniformly distributed here than the cases before. Along first vertical line, third point with high velocity magnitude is the point directly under the influence of impeller generated fluid jet. The velocity magnitude at this point is higher than both of the previous cases (S375 & S500). Along second vertical line velocity trend is more or less similar to the previous cases (S375 & S500).

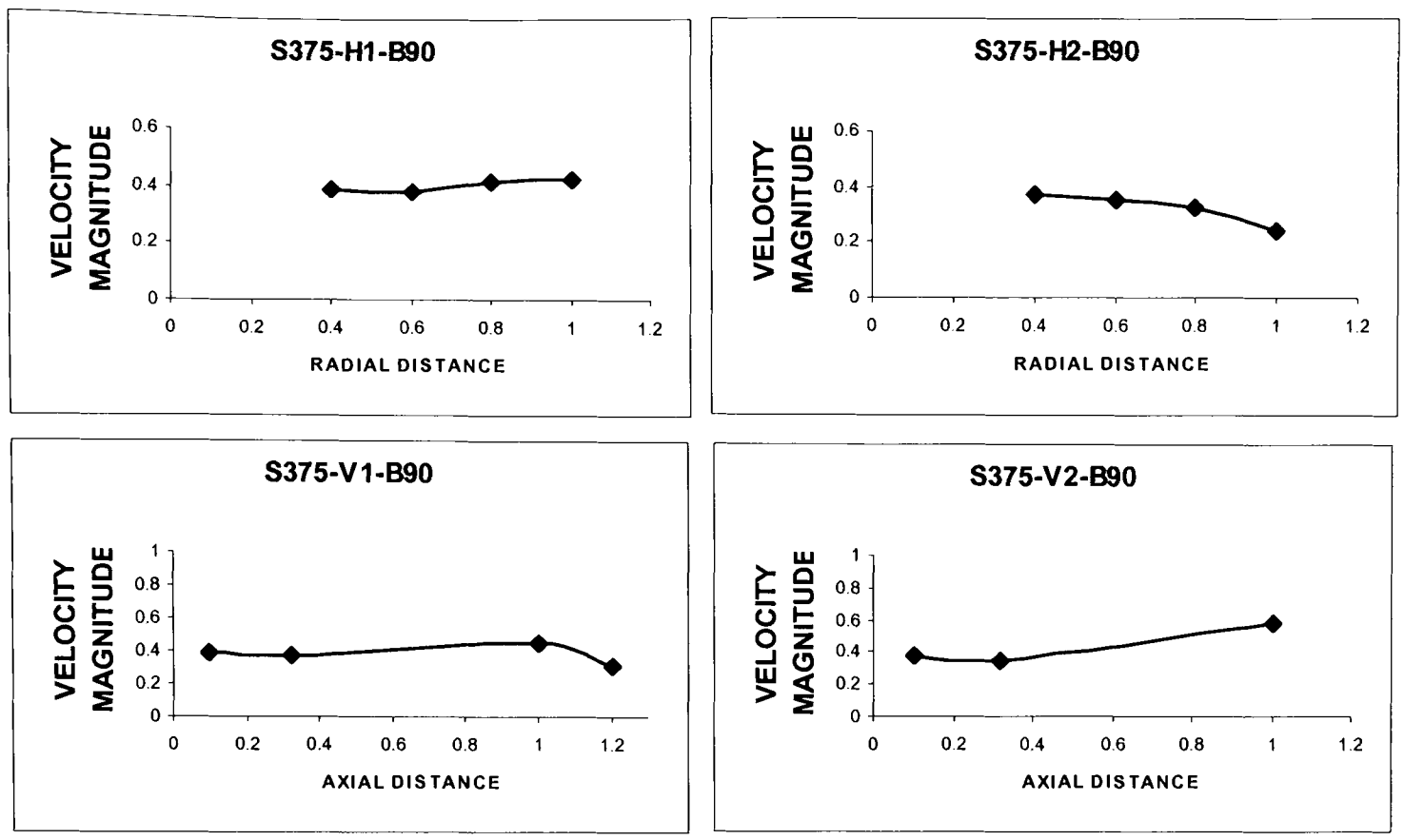

Figure 4.17: Velocity Magnitude for Short Shaft for Changed Baffles Position

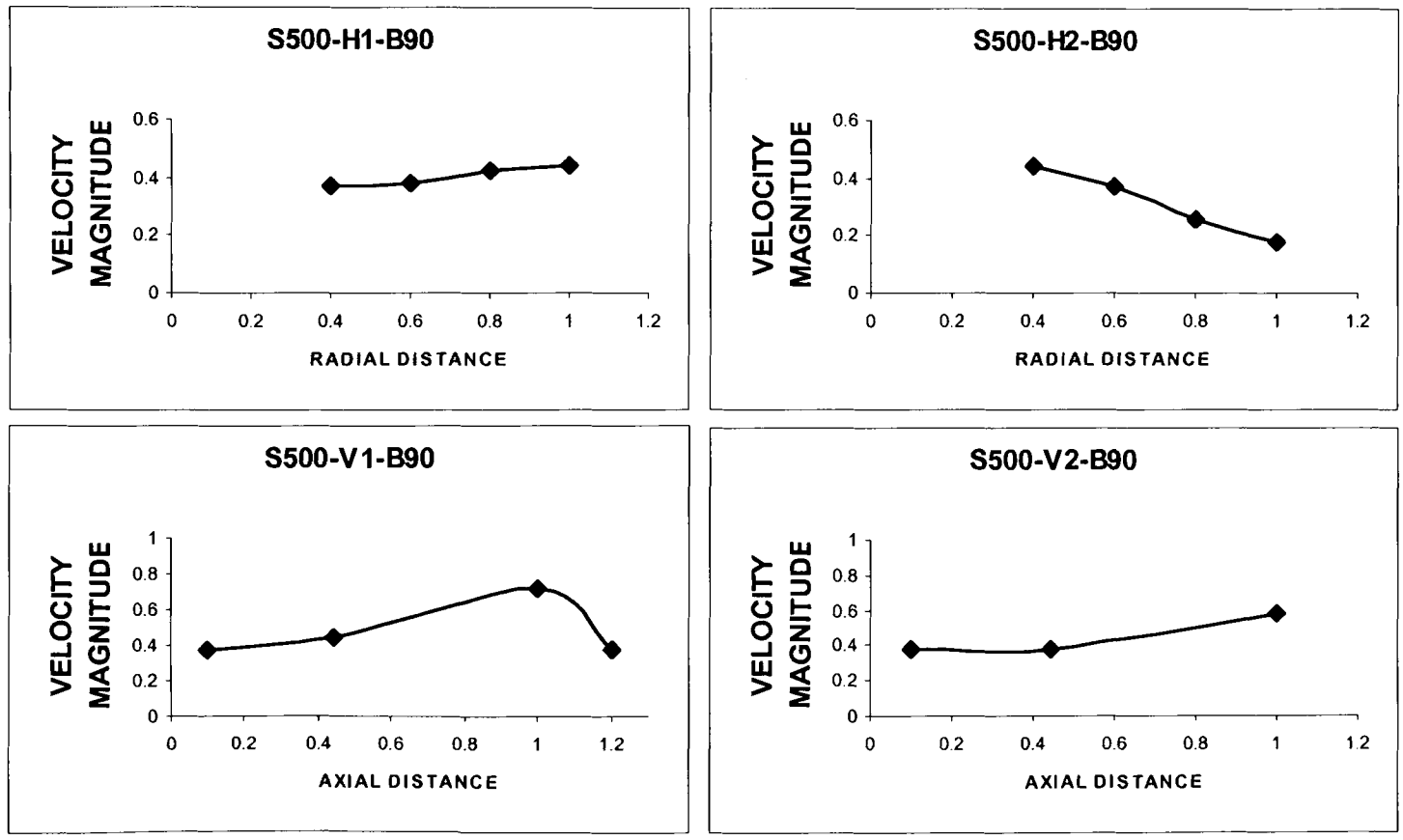

Figure 4.18: Velocity Magnitude for Medium Shaft for Changed Baffled Position

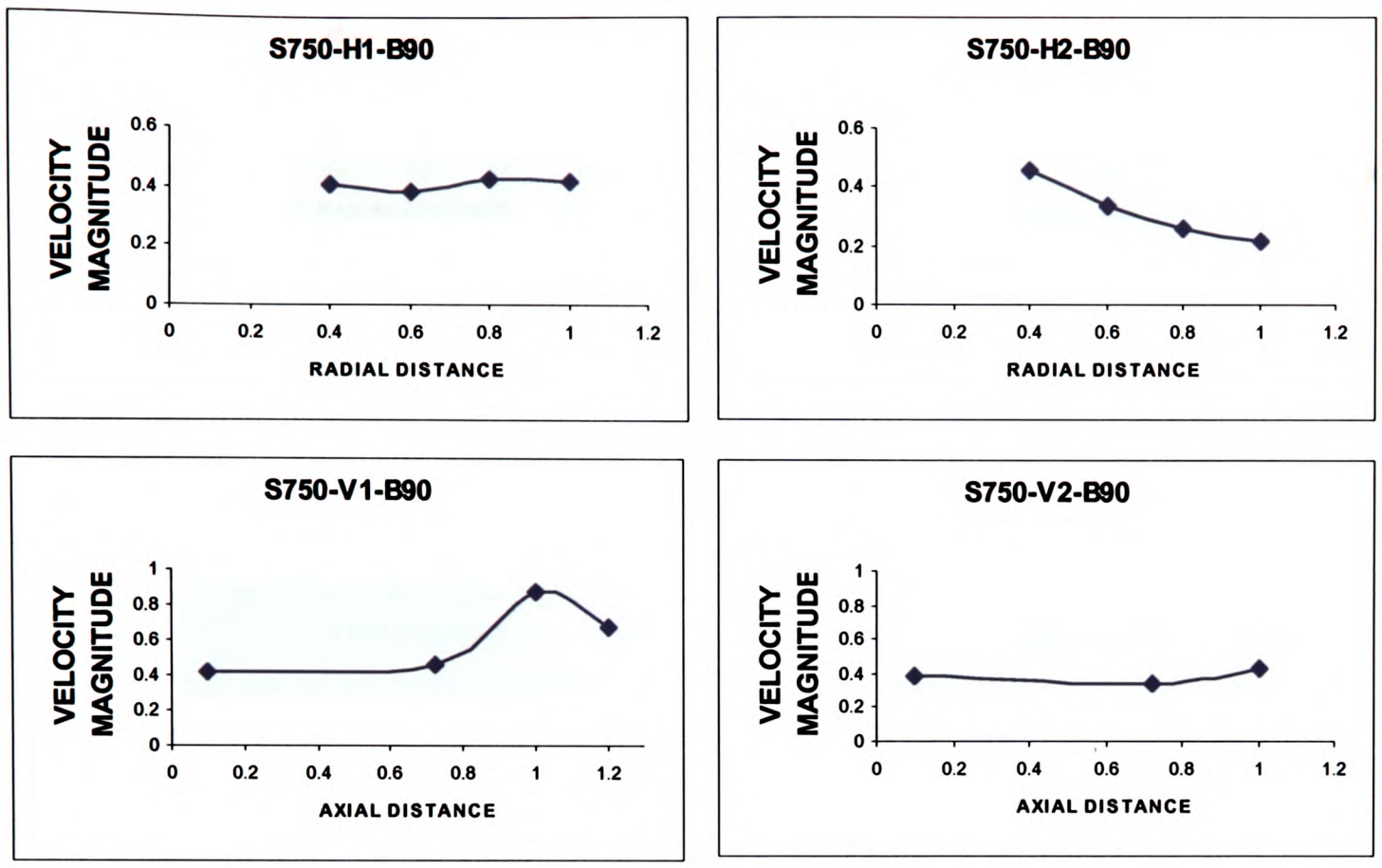

Figure 4.19: Velocity Magnitude for Deep Shaft for Changed Baffles Position

Figures – 4.17, 4.18 & 4.19 present the velocity measurements at various locations when baffles position (B90) is changed. It is apparent that these are very much similar to the trend as those for the corresponding cases (Figures – 4.14, 4.15 & 4.16) with baffles position B0.

4.7.1 Comparative Velocity Data for Two Baffles Positions

In order to investigate the relative influence of baffles positions on the velocity measurements a second set of experiments were carried out by changing the position of baffles. In this case, baffles were placed at 90° with respect to the original position and all the measurement locations were kept same as before. In the following figures both set of data (for B0 & B90) are presented on same graph with 15% error bar on the B90 baffled position data to highlight the difference in measured values.

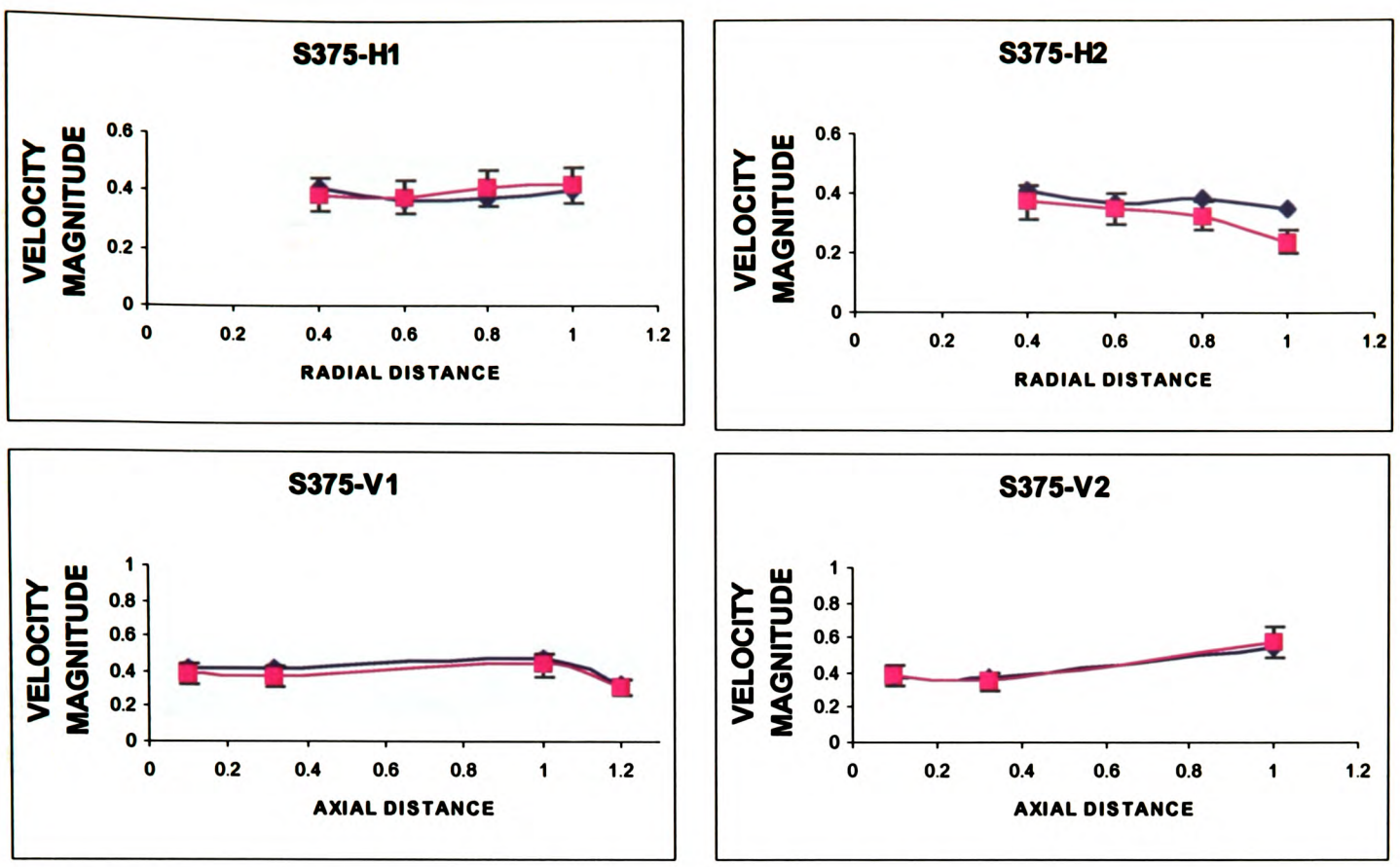

Figure 4.20: Comparative Velocity Data for Short Shaft for Two Different Baffles Locations

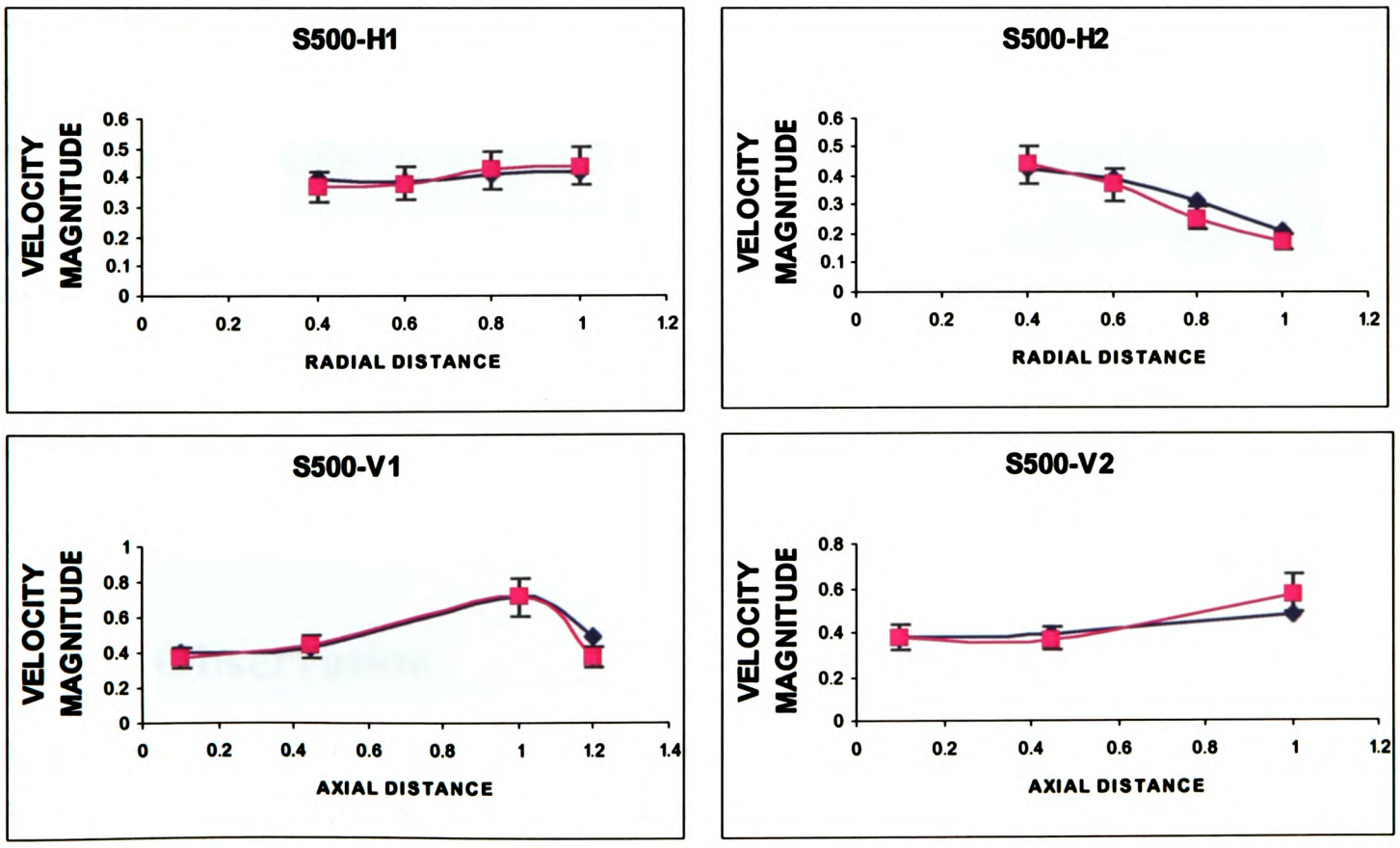

Figure 4.21: Comparative Velocity Data for Medium Shaft for Two Different Baffles Locations

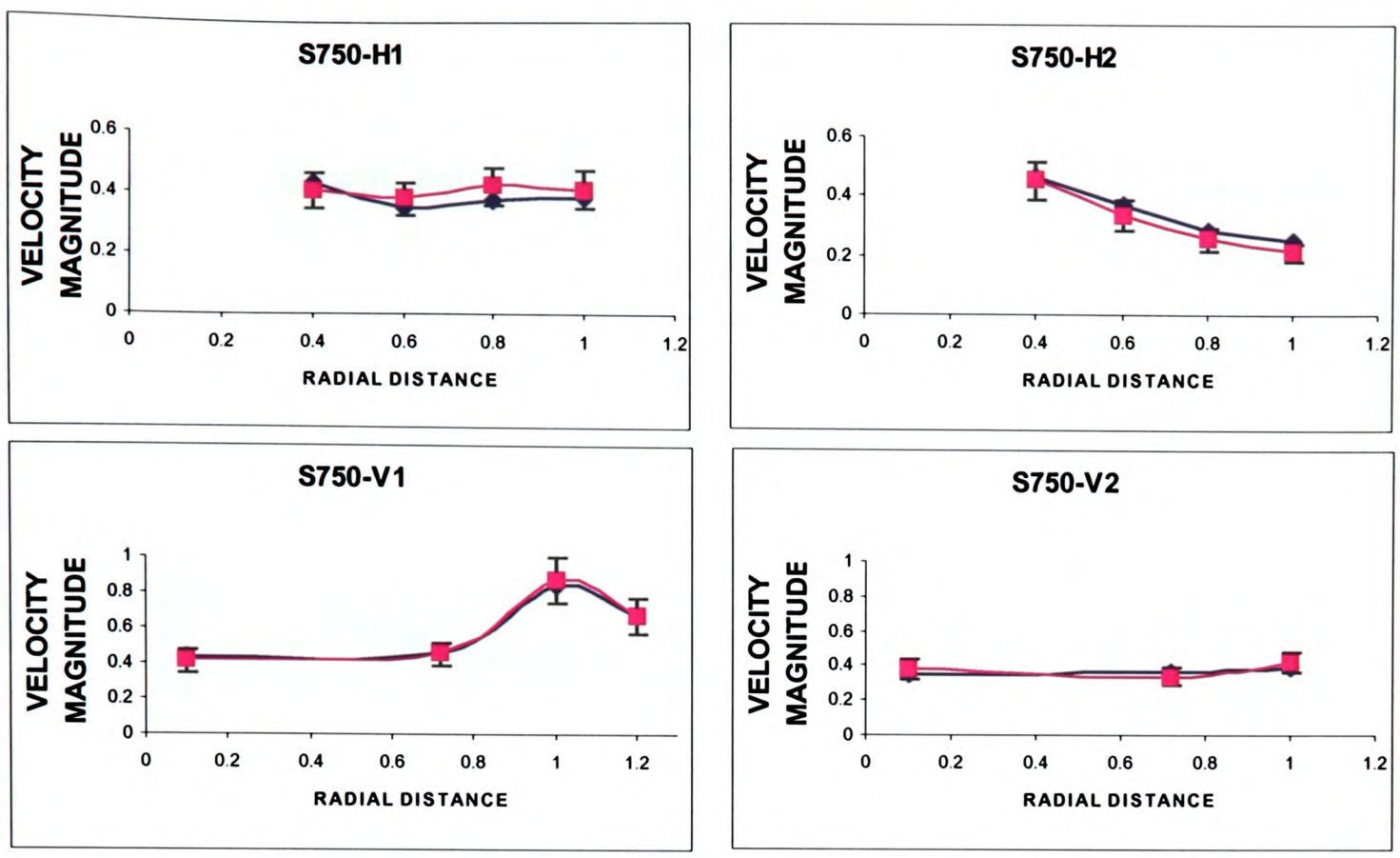

Figure 4.22: Comparative Velocity Data for Deep Shaft for Two Different Baffles Locations

As it can be seen from the above figures, differences for almost all data points are within 5-12%, except at third and fourth point in S375-H2. At third point difference is more than 17% and at fourth point it is about 50%. It is because for B90 with relatively shallow shaft depth velocities fed away relatively quickly towards the kettle rim. However, in B0 because of the strong fluid-baffle interaction near the measurement location, there is high kinetic energy in the fluid and hence, velocities are higher. It is interesting to note that in general there is no big difference in the measured value.

4.7.1.1 Observation

Based on the comparative data presented above it can be said that in general the fluid bulk exhibits near axisymmetric flow pattern as if effect of impeller baffle interaction is uniformly spread over the entire flow domain. It is a very significant observation and this can be used to simplify the computer model from three-dimensional to two-dimensional axisymmetric model.

4.7.2 Results for Unbaffled Kettle

Figure-4.23 shows the velocity magnitude measured for the case similar to the S750 but kettle was not fitted with baffles. Because of the high swirl that causes oscillations and instabilities in the fluid bulk measured velocities are more prone to uncertainties in this case than the baffled cases. Even then, it gives the semi-quantitative or qualitative estimation of the trend in velocities at different locations.

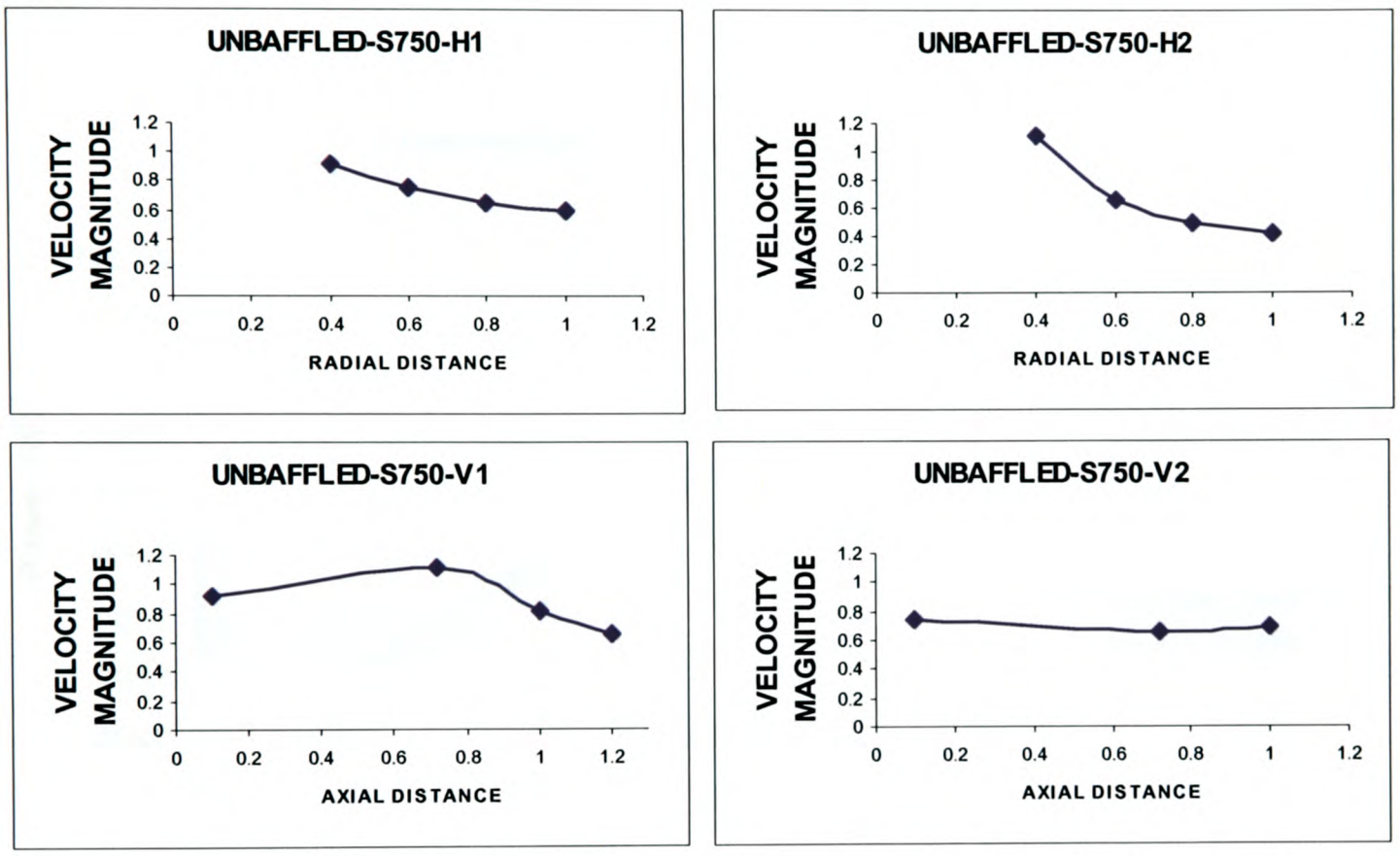

Figure 4.23: Velocity Magnitude in Unbaffled Kettle with Deep Shaft

From Figure-4.23 it is clear that as we move away from shaft towards the kettle wall velocity magnitude decreases. The velocity near shaft is much bigger in magnitude in this case than that for the similar baffled kettle (See Figure-4.16). Similarly, along H2 velocities decreases towards the wall and here also velocities are of bigger magnitudes than that of baffled kettle. Along the first vertical line there is a velocity peak indicating its proximity to impeller. In baffled case, this peak velocity is at the third point and hence, it can be said that baffles make the impeller generated jet to shoot deeper into the fluid bulk. Along the second vertical line velocity first decreases and then increases as we go down. The third point is closer to the curve wall of kettle where there are more activities as the wall forces the fluid direction to reverse.

4.8 Experimental Results for Refining Kettle

A number of tests were undertaken on a lead refining kettle with 3650mm diameter. The aim of this study was to obtain data such as RPM, vortex depth, surface velocity, and vortex shape for different shaft depths and blade angles. A hole was cut into the mixer frame to create a window where digital video equipment was used to capture visual data on the vortex shape, plus surface movement by floating a steel ball-bearing on the melt surface.

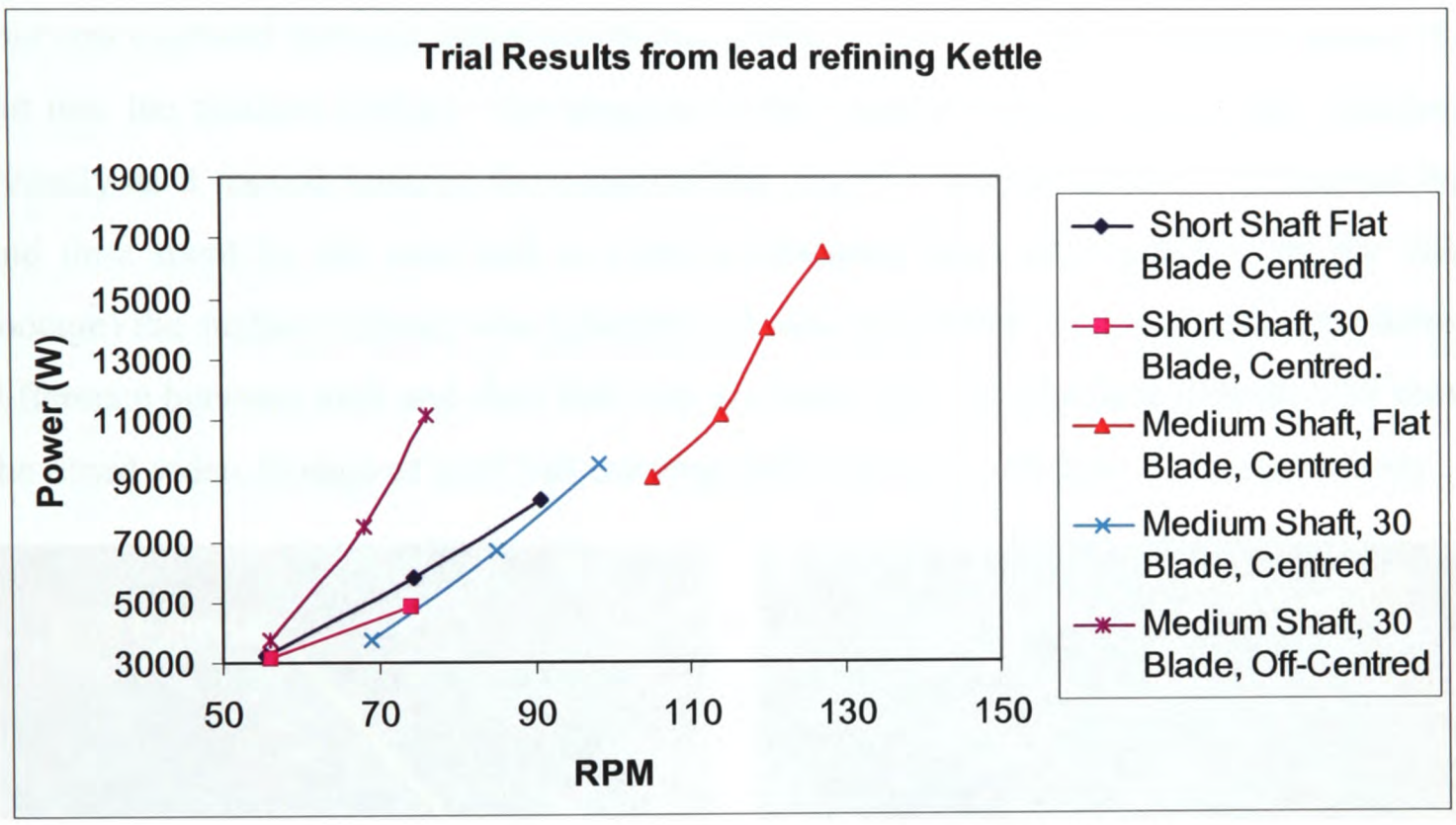

Figure 4.24: Data from Lead Refining Kettle Trials

Figure-4.24 details some of the data gathered during this trial. During each trial, the RPM and power consumption was noted, using an impeller of 638mm diameter and 156mm blade height, at different blade angles and shaft depths. For the short shaft (depth of 1/3 kettle radius), the 30-degree angled blades formed a large amount of oscillation at the surface. This was minimised using flat blades and longer shafts, the similar trend was also found in the water modelling. For the medium shaft (depth of 1/2 kettle radius), the flat blade impeller allowed much greater RMP values to be obtained, at the cost of much higher power consumption.

Data was also obtained on the medium shaft using 30-degree blades with both centred and off-centred shafts. It is interesting to note the large increase in power consumption for the off-centred shaft. However, the benefit of this was that the steady surface obtained at the higher RPM values. For the centred shaft, the maximum RPM reading resulted in extensive air entrapment and dross formation.

To obtain an estimate of the surface velocity, a steel ball bearing was dropped into the melt at the kettle rim. As steel floated into molten lead it followed the movement of surface and this was captured through digital recording within a reference frame (that is a square hole cut into the mixture bridge). The progress of this marker was then timed and monitored visually as it moved towards the centre of the vessel. Using dimension of reference hole and time spent by the steel ball to cross it (obtained from time signature on the video footage) the surface velocity was calculated. In this calculation of surface velocity, density difference between melt and steel ball was not taken into consideration. Figure-4.25 shows the timed video footage of steel ball entering and leaving the reference hole respectively.

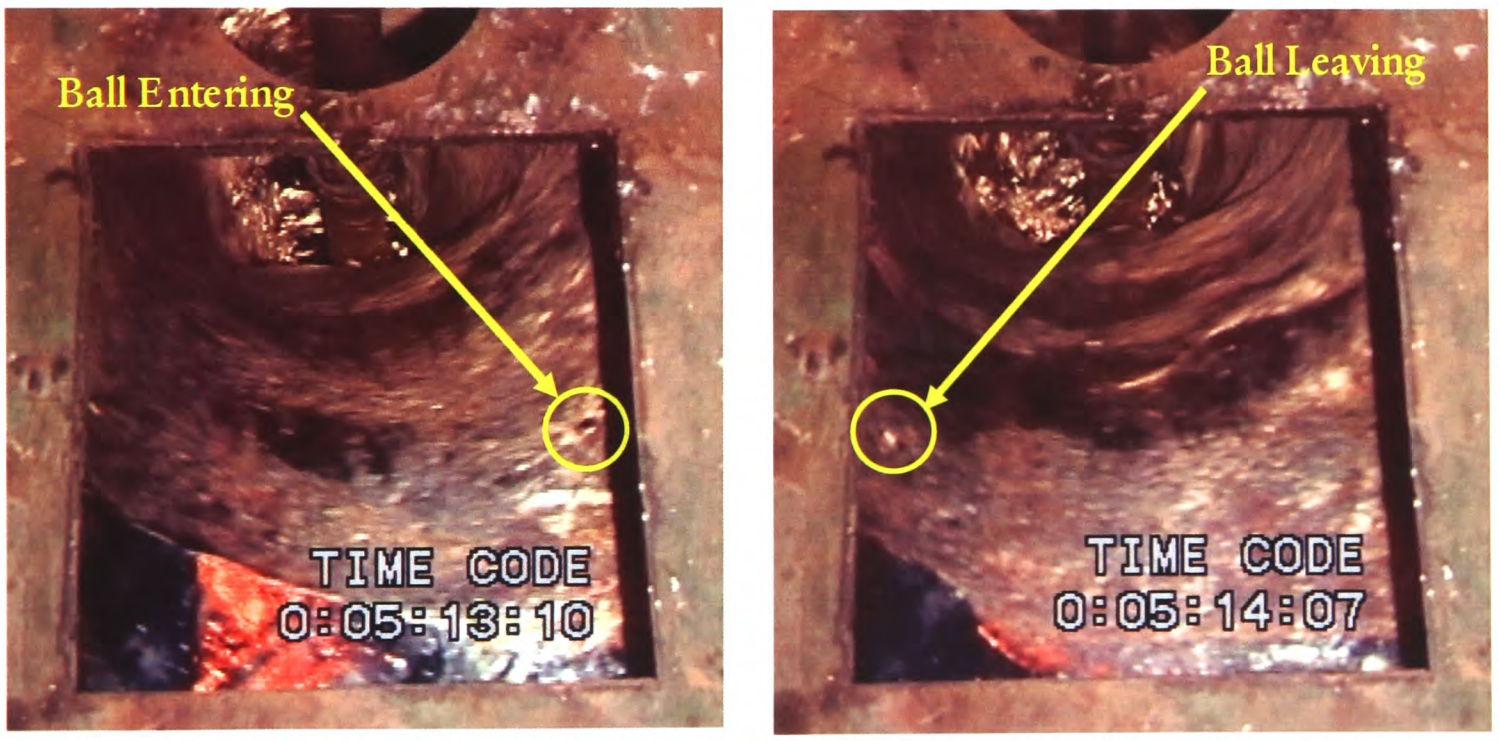

Figure 4.25: Monitoring of Floating Steel Ball Entering and Leaving the Frame

4.9 Conclusions

In the field of impeller-stirred mixing process, most of the available experimental data are mainly for cylindrical shaped vessels. The production scale hemispherical shape kettle is very little investigated. In the present experimental work investigation was solely carried out on hemispherical shaped industrial scale water model representing the lead refining kettle. Some experiments were also directly undertaken on the lead refining kettle.

A range of power consumption data was presented for water model (taken under different operating conditions). It was observed that for unbaffled kettle power consumption increased with the increasing shaft depth and with increasing the blade angles. For the two-baffled water model kettle, with medium shaft depth and 45-degree blade angle, power consumption grew exponentially with the impeller speed. Following this section data for vortex depth measurement on two-baffled water model with medium depth shaft were also presented in terms of vortex factor. Based on observations it was assumed (as a first approximation) that vortex factor became when operation went beyond Reynolds number 10^5. This has very important implication as it establishes the use of water model as a reliable representation of vortex formation in lead refining kettle.

A series of ADV measured velocity were also given for various locations inside the water model. From these data, it became clear that flow pattern in the bulk of water model exhibited axisymmetric pattern. This finding can be used to reduce the three-dimensional computer model to a two-dimensional model. Finally, results from direct experiments on the lead refining kettle were also presented.

Chapter 5

COMPUTATIONAL FLUID DYNAMICS (CFD)

5.1 Introduction

Most of the flow phenomena in real life situation exhibits considerable complexity in terms of flow behaviour and geometry of the flow domain. Applicability of the traditional methods of mathematical analysis is very limited in solving the governing nonlinear partial differential equations representing these flow fields. Hence, the majority of the industrially important flow problems cannot be addressed this way. However, it is possible to solve them numerically using the digital computer. This is achieved by converting the partial differential equations, which carry the exact information about the flow field, into discrete equations at a finite number of points in the flow domain.

Computational Fluid Dynamics (CFD) exploits this technique of numerically solving the flow equations at a finite number of discrete points in the flow domain. The CFD solution can provide a very close approximation to the exact solution when enough number of discrete points is employed in the calculations. CFD technology has evolved over the years by bringing knowledge and techniques from a number of areas namely:

- Mathematics
- Physics
- Chemistry
- Engineering
- Computer Science

This chapter deals with the mathematical foundation of CFD. Firstly, it outlines the governing equations that represent the various phenomena associated fluid flow. This is followed by details of the discretisation method and derivation of solution algorithms employed by CFD to solve the simultaneous algebraic equations.

5.2 Governing Equations for Fluid Flow

Transport of mass, momentum and energy associated with fluid flow are governed by the principle of conservation of mass, momentum and energy respectively. Additional terms need to be added to these standard equations to account for additional complexity, like turbulence, chemical reaction, etc., associated with the flow phenomena. There is a range of mathematical models available to represent turbulence, chemical reaction, etc. Though addition of these makes the mathematics much more complicated, they also make it possible to address a wide range of real world flow problems. However, the extended equations require greater processing power from the computer and take longer time to solve.

In following section, these principles are expressed in terms of partial differential equations using Cartesian tensor notation. Use of tensor notation makes the equations compact and easy to understand. Here the three space coordinates are denoted by x_1, x_2 and x_3 and the corresponding velocity components by u_1, u_2 and u_3. When a subscript is repeated in a term, then a summation over all the values of the subscript is implied; thus differential

$$\frac{\partial u_i}{\partial x_i}$$

stands for

$$\frac{\partial u_1}{\partial x_1}+\frac{\partial u_2}{\partial x_2}+\frac{\partial u_3}{\partial x_3}$$

5.2.1 Conservation of Mass (Continuity Equation)

Consider an incompressible fluid flowing through a Control Volume (CV), Figure-5.1. In this case, we can say that amount of fluid mass entering the CV equals the amount of fluid leaving it. There is no accumulation or destruction of fluid mass within the CV. This gives the continuity equation.

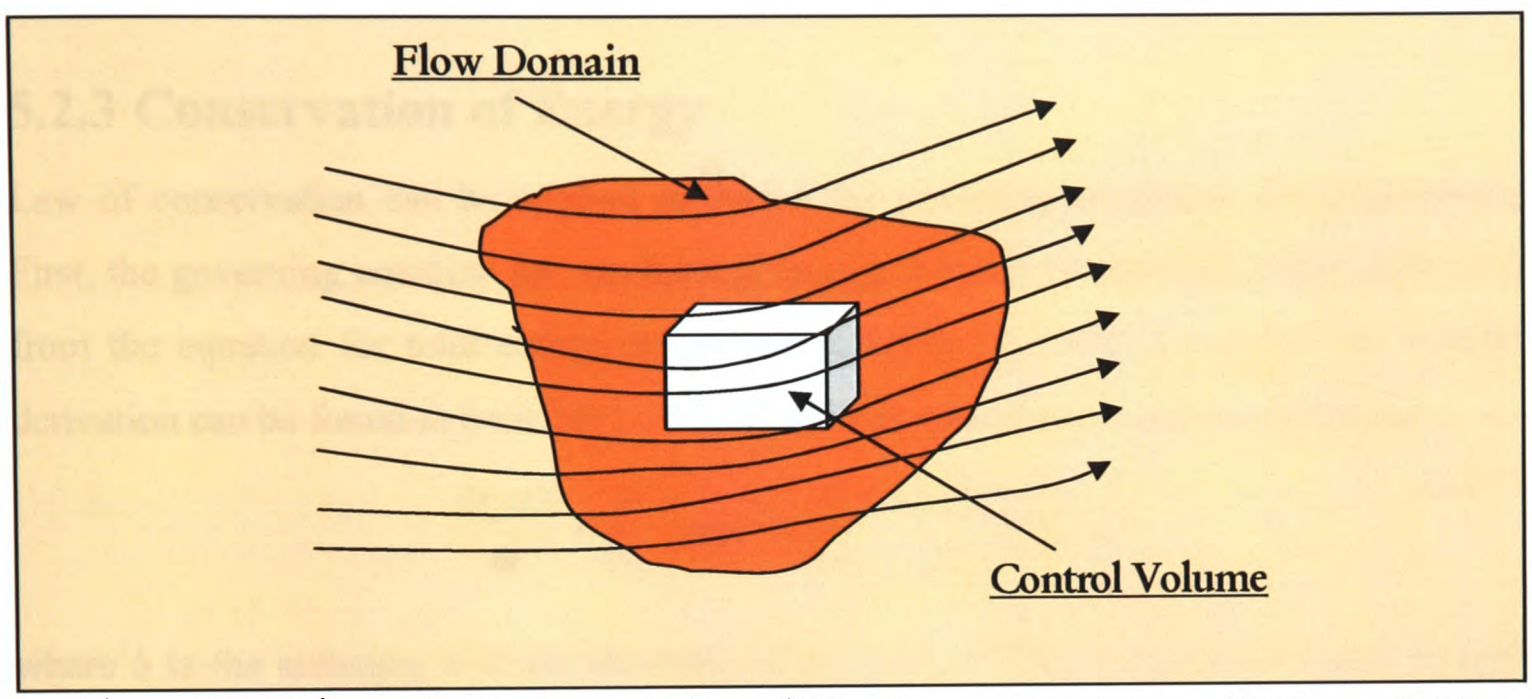

Figure 5.1: Schematic Representation of Flow Domain & Control Volume (CV)

$$\frac{\partial \rho}{\partial t} + \frac{\partial}{\partial x_i}(\rho u_i) = 0 \tag{5.1}$$

where ρ is the density and the u_i velocity component in ith direction.

5.2.2 Conservation of Momentum

Velocity components of fluid in the CV may change with both time and space. This results in the equation of acceleration and when multiplied with mass, gives resultant force acting on fluid in a certain direction, say x_i-direction. This is Newton's second law. In the x_i-direction resultant force is a combination of normal stress and tangential shear components acting along four sides of the CV. Combining these mathematically with the pressure, viscosity and density gives two equations for the conservation of momentum.

$$\frac{\partial}{\partial t}(\rho u_j)+\frac{\partial}{\partial x_i}(\rho u_i u_j)=\frac{\partial}{\partial x_i}\left(\mu\frac{\partial u_j}{\partial x_i}\right)-\frac{\partial p}{\partial x_j}+B_j+V_j \tag{5.2}$$

where μ is viscosity, p is pressure, B_j is the body force per unit volume and V_j consists of viscous terms other than those expressed by the first term the j direction.

5.2.3 Conservation of Energy

Law of conservation can be applied to derive the governing equations for total energy. First, the governing equation for mechanical energy is obtained and that is then subtracted from the equation for total energy to get the equation for internal energy. The detailed derivation can be found in book [48]. Following is the governing equation for energy:

$$\frac{\partial(\rho h)}{\partial t}+\frac{\partial}{\partial x_i}(\rho u_i h)=\frac{\partial}{\partial x_i}\left(\frac{k}{c}\frac{\partial h}{\partial x_i}\right)+S_h \tag{5.3}$$

where h is the enthalpy, k is the thermal conductivity, c is the constant pressure specific heat and S_h represents the volumetric rate of internal heat generation.

5.2.4 Conservation of Chemical Species

For a kth chemical species with mass fraction m_k the governing equation is given as:

$$\frac{\partial}{\partial t}(\rho m_k)+\frac{\partial}{\partial x_i}(\rho u_i m_k)=\frac{\partial}{\partial x_i}\left(\Gamma_k\frac{\partial m_k}{\partial x_i}\right)+R_k \tag{5.4}$$

where Γ_k represents the diffusion coefficient and R_k is volumetric rate of generation for kth species.

5.2.5 Turbulence Equation

At the higher velocities, flow field undergoes three-dimensional random fluctuations called turbulence. In this situation, only instantaneous velocities of the flow field can be

represented by the standard Navier-Stokes equations. The existence of the wide range space and time scale of fluctuations greatly limits the applicability of direct numerical solution for this kind of problems. The exact simulation by numerically solving standard Navier-Stokes equations is possible only for a flow domain with very simple geometry and low Reynolds number. Even in this case cost of computation, in terms of computing time and memory, is enormous. This is why for most of the practical cases turbulence is represented as the time-averaged properties of the flow field.

The equations for the time-averaged properties are obtained from the equations for unsteady laminar flow. However, the time averaging of variables in standard Navier-Stokes equations gives rise to some additional terms. These are called the Reynolds stresses, turbulent heat flux, turbulent diffusion flux, etc. These stresses and fluxes are represented in terms appropriate flow properties by using suitable turbulence model.

In some of the turbulence models, additional terms of stresses and fluxes are accounted for through replacing the laminar viscosity/conductivity with eddy viscosity/conductivity. Application of turbulence model retains the general appearance of equation same as that of the laminar flow equation. Hence, from computational point of view we solve the same equation as that of laminar flow except laminar viscosity is to be replaced by the eddy viscosity. One of the most widely used and tested such models is two equations k-ε [68]. At present, this model is the basis for most of the engineering simulations of complex flow including impeller-stirred tank.

In two equations k-ε turbulence model the eddy viscosity is obtained from certain mean parameters of the fluctuating motion itself. These parameters are calculated by solving additional differential equations. Here, turbulence is characterised by kinetic energy k of the fluctuating motion and its dissipation rate ε. Governing equation for these can be given as follows:

$$\frac{\partial}{\partial t}(\rho k)+\frac{\partial}{\partial x_i}(\rho u_i k)=\frac{\partial}{\partial x_i}\left(\frac{\mu_t}{\sigma_k}\frac{\partial k}{\partial x_i}\right)+G-\rho\varepsilon \tag{5.5}$$

$$\frac{\partial}{\partial t}(\rho\varepsilon)+\frac{\partial}{\partial x_i}(\rho u_i \varepsilon)=\frac{\partial}{\partial x_i}\left(\frac{\mu_t}{\sigma_\varepsilon}\frac{\partial \varepsilon}{\partial x_i}\right)+(c_1 G-c_2\rho\varepsilon)\frac{\varepsilon}{k} \tag{5.6}$$

Here μ_t is the turbulence viscosity, G is the rate of generation of turbulence, and σ_k, σ_ε c_1 and c_2 are empirical constants in the model [68].

5.3 Boundary Conditions

Complete mathematical description of flow field must also be accompanied by details of the boundary conditions of the flow domain. The three most important boundaries encountered are: wall boundary, inlet boundary and outlet boundary. Wall boundary is generally an impermeable wall. At this boundary either value of dependent variable ϕ or a relationship describing diffusion flux is known. For example, if ϕ represents temperature then either wall temperature or wall heat flux or an external convective heat transfer coefficient is known. At an inlet boundary, the value of ϕ in the coming stream is required to be specified and it is generally know in the context of the problem definition itself. At an outlet boundary, neither the value nor the flux of ϕ is known in advance. It is generally calculated as a part of problem solution when conditions for conservation are satisfied.

5.4 Discretisation Methods

As mentioned above, the governing equations describing flow phenomena are given by partial differential equations. However, the computer works only in binary, and hence, can only solve the equations in algebraic form. Consequently, all the partial differential equations need to be transformed into simultaneous algebraic equations. The technique of converting a partial differential into its algebraic equivalent is called discretisation.

Basic to all the discretisation process is breaking down the computational domain (geometry associated with problem) into number of smaller sub-domains. Here, appropriate mathematical techniques are employed to convert the governing equations into numerical analogue locally for each sub-domain. During this process the effect of surrounding sub-

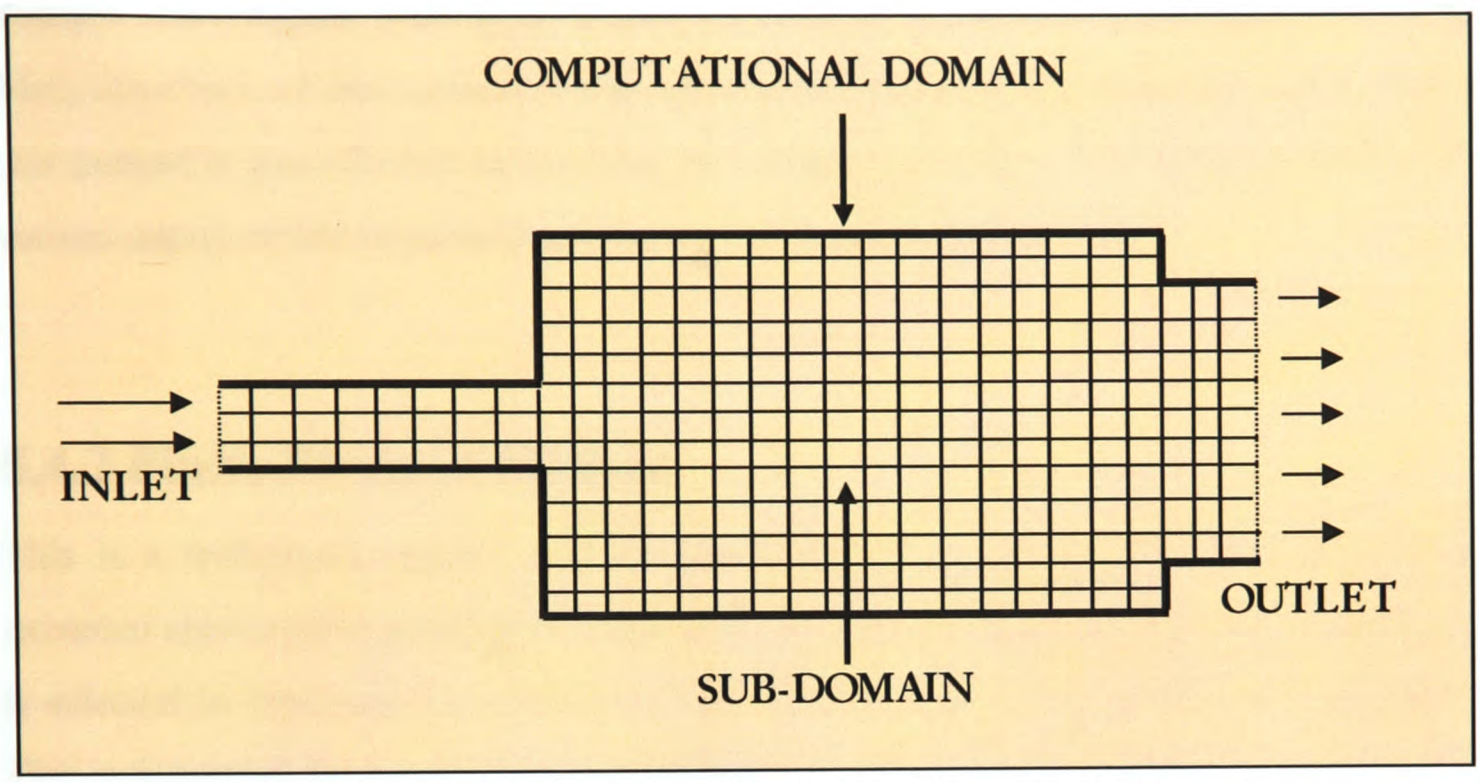

Figure 5.2: Computational Domain and Sub-domain

domains into each sub-domain and vice versa are also taken into account to keep the conservation principles valid. And finally, a high-level computer language is employed to implement the resultant numerical scheme to calculate the flow field in the whole domain. Figure-5.2 illustrates the computational domain and sub-domain for a typical pipe flow. The Computational Fluid Dynamics (CFD) has been an active area of research for last two decades. Over this period of time a number of discretisation techniques have been developed. Following are the brief discussion for the some of the widely employed methods of discretisations.

5.4.1 Finite Difference Method

The basics of the finite difference method is that the partial differential equations are broken down into dependent variables (velocity, pressure), independent variables (spacial co-ordinate and time) and reference variables. All three are related in a Taylor series

expansion equation to form the numerical equations the solver requires. Each numerical equation, at a given point, is based on the values from neighbouring equations. It is this difference between the central element and its neighbours from which the technique gains the name, finite difference. The scheme leads to high accuracy solution for the simple flow domain where regular rectangular shaped (structured) sub-domain (grid/mesh) is employed. Main drawback of this method is that strict conservation is not enforced. Apart from that this method is less efficient in handling the complex geometry. The thorough details of the various aspect of this numerical scheme can be found in the book [69].

5.4.2 Finite Element Method

This is a techniques mainly used for stress analysis in solid. However, this has been extended also to solve problems of fluid flow. First of all a type of interpolating polynomial is selected to represent the variation of the field variable over an element (sub-domain). This polynomial for a variable is substituted in the governing equations, which should satisfy exact solution for a variable. Any residual error if present is minimised by multiplying them by a set of weighting function. Then it is integrated over an element. The unknowns in the resulting equations are assembled to form a single matrix equation expressing the behaviour of whole domain, modified to account for boundary conditions. This is then solved using a standard matrix solver for the unknown values of the field variable at the nodes. Most important advantage of this method is its ability to handle the arbitrary geometries. But this leads to the disadvantage of being a less efficient solution algorithm. The standard book [70] covers all the major aspects of this method.

5.4.3 Spectral Method

Some time it is also possible to decompose a differential equation in terms of orthogonal basis functions, for example by applying a Fourier transform. This decomposition can transform differential equation in equivalent algebraic equation. This method is called spectral method. Here variables of the governing equations for fluid flow are substituted by

approximate (truncated) Fourier series. Unlike finite difference or finite element method here approximations are not locally but valid for entire computational domain. Applying method of weighted residual (similar to finite element method) or by making the approximate function coincide with the exact solution at a number of grid points governing equations are transformed into equivalent algebraic equations. This scheme is mainly suited for some of the specialised flow problems with simple geometry and hence, cannot be used as the general-purpose scheme. Details about the applicability of the method in fluid flow computation can be found in [71].

5.4.4 Finite Volume Method

In this method flow domain is divided into a number (finite) of small control volumes. The governing equations, representing the flow processes such as convection, diffusion and sources, are integrated over all the smaller control volumes. The resultant equations are then dicretised by applying a variety of finite-difference type approximations. This process converts the partial differential equations into a system of linear algebraic equations. Solution of the algebraic equations is then carried out by using an iterative process. This method is most general and can easily be adopted to handle the complex flow problems. Finite volume method is the most established and thoroughly validated general purpose CFD technique. Solvers for the majority of commercially available codes are based on this method. The most standard textbooks describing this method are [72-74].

5.5 Formulation of Finite Volume Algorithm

The development of the numerical algorithms based on finite volume formulation consists of the following main steps:

1. Before numerical scheme can be developed, the required governing equations must be assembled. As these individual equations share a common form, it possible to focus on a general equation and work out a solution method for it.

2. The solution domain is filled with a grid that divides the domain into a finite number of small control volumes. Then a numerical algorithm is developed using these discrete points.
3. Integration of governing equations of fluid flow is carried out over all the (finite) control volumes spanning the computational domain.
4. The integrated equations are converted into a set of simultaneous linear algebraic equations by employing variety of finite-difference type approximations maintaining the conservation of flow quantities.
5. Iterative method for solving linear equation is employed to solve the simultaneous equations resulted from discretisation.

The following sections present the further details of these steps. The development of the finite-volume based algorithm for CFD solver presented in the following sections is the basic building block of the solver of the commercial CFD code FLUENT [75]. This is the code used for carrying out the simulations in this research project.

5.5.1 Generic Flow Equation

Close inspection of governing conservation equations (Eq-5.1—Eq-5.6) for various variables associated with flow phenomena reveals the similarity in their form. The recognition of this common form provides a major convenience for the construction of the numerical procedure. At least in principle, all that is necessary is to formulate the numerical method solving the equation of the common form. Individual governing equations can be represented as a particular case of a generic equation:

$$\frac{\partial}{\partial t}(\rho\phi)+\frac{\partial}{\partial x_i}(\rho u_i\phi)=\frac{\partial}{\partial x_i}\left(\Gamma\frac{\partial\phi}{\partial x_i}\right)+S \tag{5.7}$$

This equation contains all the mechanism of transport of a conserved variable ϕ. The four terms in the generic equation are, from left to right, the transient term, the convection term, the diffusion term, and the source term. The symbol ϕ can be used to represent any scalar-dependent variable, such as velocity components, temperature, enthalpy, turbulent kinetic energy, etc. Γ and S are the diffusion coefficient and the source term, respectively, and specific to a particular meaning of ϕ. The S generalised source term contains body forces, the influence of boundaries, sources or sinks and any other terms that do not conform to LHS. Table-5.1 summarises the meaning of various terms (ϕ, Γ and S) appearing in the generic equation.

	ϕ	Γ	S
Mass	1	0	0
Momentum	u	μ	$-\frac{\partial p}{\partial x_j} + B_j + V_j$
Energy	h	$\frac{k}{c}$	S_h
Species	m_k	Γ_k	R_k
Turbulence Kinetic Energy	k	$\frac{\mu_t}{\sigma_k}$	$G - \rho\varepsilon$
Turbulence Dissipation Rate	ε	$\frac{\mu_t}{\sigma_\varepsilon}$	$\left(c_1 G - c_2 \rho\varepsilon\right)\frac{\varepsilon}{k}$

Table 5.1: Meaning of Various Terms of Generic Equation

5.5.2 Grid Layout for Finite Volume

There can be many possible arrangements for the grid layout and distribution with their relative advantages or drawbacks. For example, control volume face can be placed in the middle of the two neighbouring grid points as shown in Figure-5.3. The advantage of this arrangement is the greater accuracy in calculating flux across the face. But the point P in general may not lie in the geometric centre of control volume hence, cannot be regarded as good representative value for the entire control volume in calculation of the source term, the conductivity and similar quantities. At the same time in this practice, it is very difficult to arrange that the control volume faces fall at the desired locations, because one must first specify the position of grid points. The design of control volumes near the boundaries of

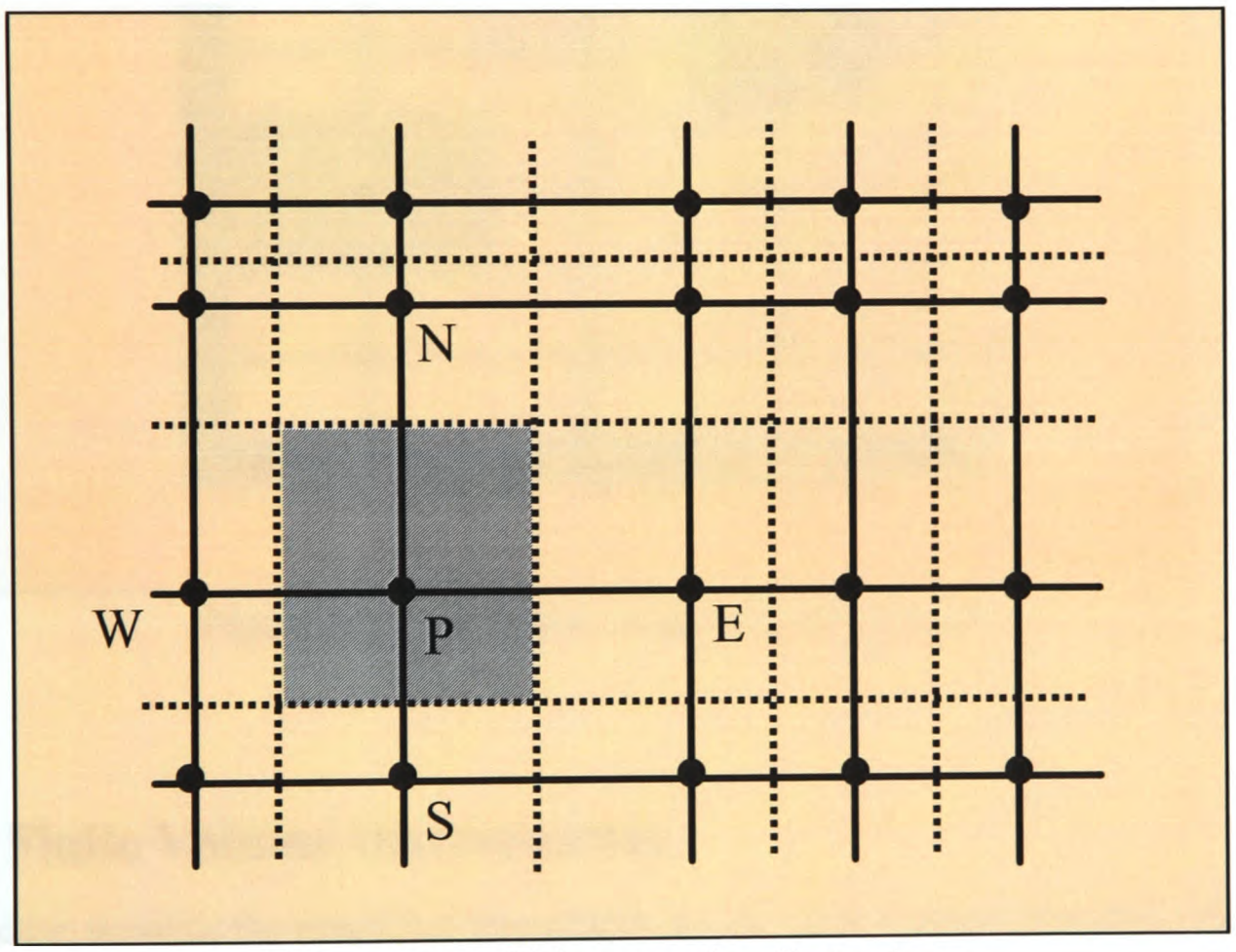

Figure 5.3: Grid layout using first scheme

the calculation domain requires additional consideration. This practice leads to the 'half' control volumes around the boundary grid points.

Other more preferred and relatively convenient way of grid layout is to decide the location of control volume first and then place the grid points at the geometric centre of control

volume, as shown in Figure-5.4. As fluid properties are assumed to remain constant over a control volume, it is desirable to place the control-volume faces where discontinuities in fluid properties, source terms, and boundary conditions are likely to be present. It is easier to treat the boundary condition in this arrangement by assuming control volume infinitesimal thickness around the grid points on the boundary.

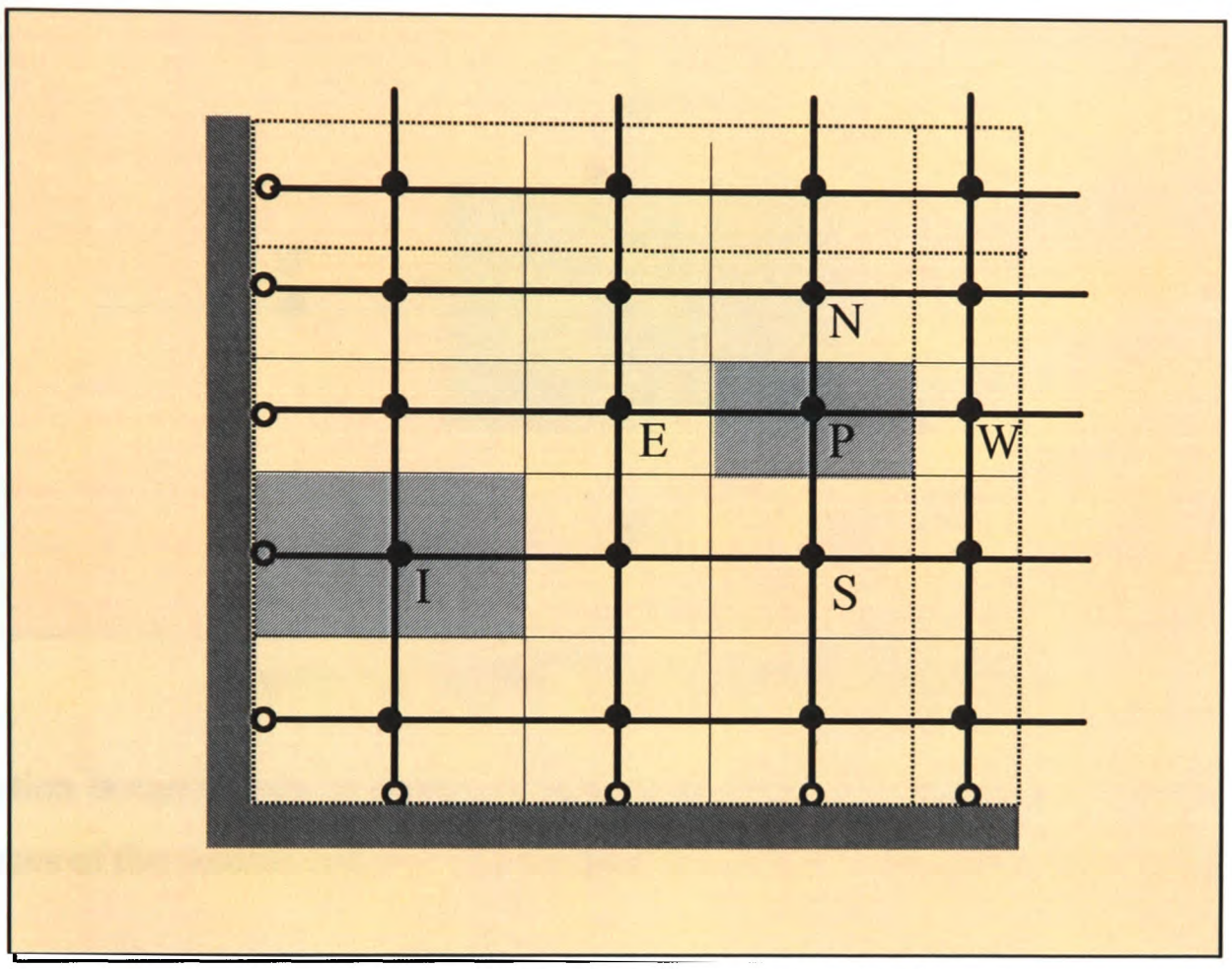

Figure 5.4: Grid layout using second scheme

5.5.3 Finite Volume Discretisation

This section presents the simplified formulation for the finite volume algorithm. The details can be found in references [72-73] and also, in [76-78]. For the formulation of finite volume algorithm the generic equation is written in the form where convection and diffusion fluxes are together represented as total flux J_i:

$$J_i = \rho u_i \phi - \Gamma \frac{\partial \phi}{\partial x_i} \tag{5.8}$$

The generic Eq-5.7 now can be written as

$$\frac{\partial}{\partial t}(\rho\phi)+\frac{\partial J_i}{\partial x_i}=S \tag{5.9}$$

To obtain equivalent algebraic equations that can be solved on a digital computer, this equation is integrated for each control volumes (resulted from the meshing of geometry) of the computational domain. A typical two-dimensional control volume, over which

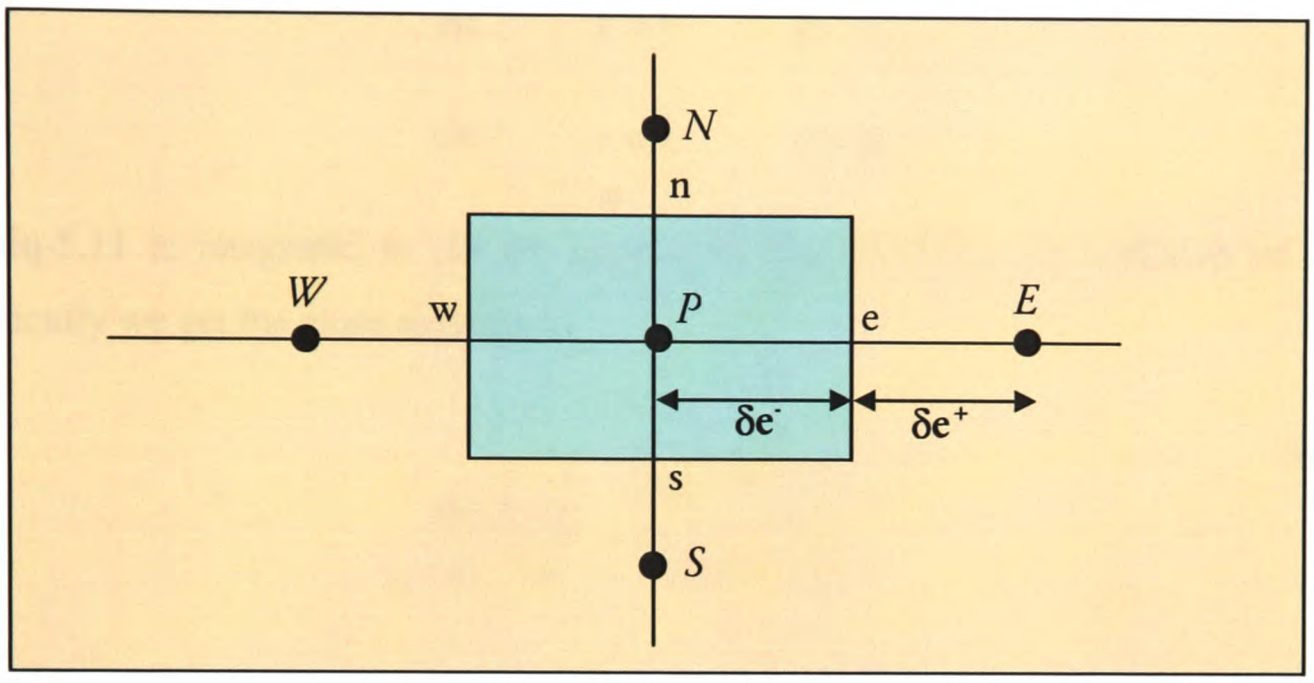

Figure 5.5: Control Volume (CV) for Integration

integration is carried out, is shown in Figure-5.5. The lower cases e, w, n and s denote the four faces of the control volume. The integration of Eq-5.9 over this control volume gives

$$\left(\rho_P\phi_P-\rho_P^0\phi_P^0\right)\left(\frac{\Delta V}{\Delta t}\right)+J_eA_e-J_wA_w+J_nA_n-J_sA_s=\bar{S}\Delta V \tag{5.10}$$

the superscript *0* denotes the value of ρ and ϕ at time t and values without superscript denotes the variables at time $t+\Delta t$. The $\bar{S}$ represents the volume averaged source term and J with subscripts denotes the total fluxes at respective control-volume faces.

5.5.3.1 Evaluation of Total Flux

It is clear from the Eq-5.10 that we need to evaluate the total flux at the control volume faces. As values for fluxes are available for nodes only so some sort of interpolation

scheme is needed to evaluate the values at face [72]. Let us consider a one-dimensional convection-diffusion problem for a domain $0 \leq x \leq L$ and for that equation is given as:

$$\frac{\partial}{\partial x}(\rho u \phi) = \frac{\partial}{\partial x}\Gamma\frac{\partial \phi}{\partial x} \tag{5.11}$$

where Γ and ρu are constant across the interval ∂x with boundary conditions

$$\text{At} \qquad x = 0 \qquad \phi = \phi_0$$

$$\text{At} \qquad x = L \qquad \phi = \phi_L$$

The Eq-5.11 is integrated to get the expression that describes the variation of ϕ. Here analytically we get the exact solution as

$$\frac{\phi(x) - \phi_0}{\phi_L - \phi_0} = \frac{\exp\left(Pe\frac{x}{L}\right) - 1}{\exp(Pe) - 1} \tag{5.12}$$

where Pe is a dimensionless quantity called the grid Peclet number. It gives the ratio of the strength of convection and diffusion for a grid and mathematically it is given by:

$$Pe = \frac{\rho u L}{\Gamma} \tag{5.13}$$

From this solution (Eq-5.12) for ϕ between $x = 0$ and $x = L$ we can plot the variations of $\phi(x)$ with respect to x for various Peclet number as follow:

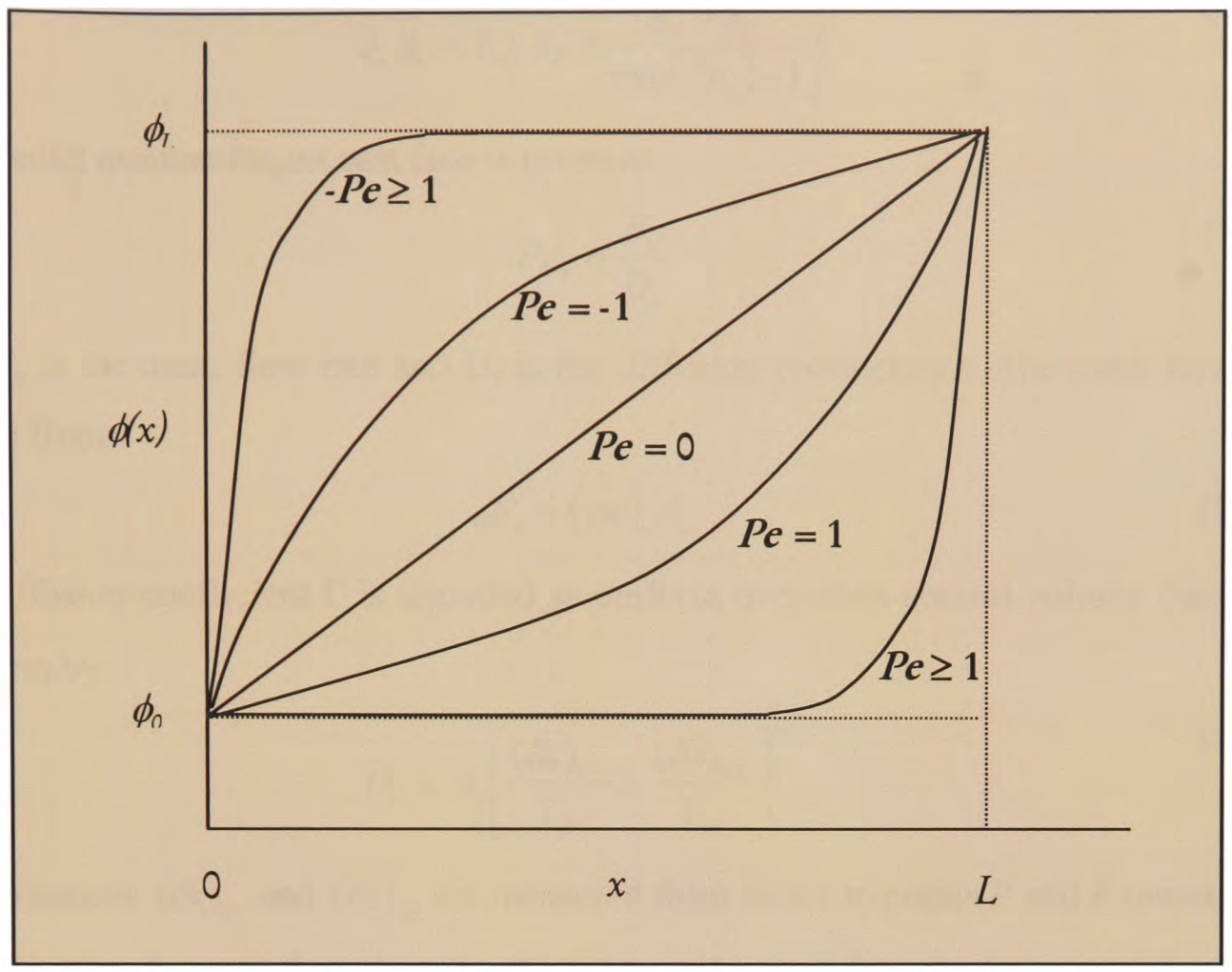

Figure 5.6: Variation of ϕ for Various Peclet Number

From the Figure-5.6 it is clear that for flow in positive direction (i.e. for positive *Pe*), the value of ϕ in the domain is more influenced by the ϕ_0. For a large positive *Pe*, the value of ϕ at x = L/2 approximately equal to the upstream value. Similarly situation is reversed for negative Peclet number. This implies that when the flow is dominated by convection, interpolation can be achieved by simply letting the face value of a variable be set equal to its upstream or upwind value. When *Pe* = 0 (no flow, or pure diffusion) ϕ may be interpolated through a simple linear average between the value as x = 0 and x = L. When the *Pe* has an intermediate value for ϕ must be derived by exponential scheme given by Eq-5.12.

Now consider the face *e* of control volume where a one-dimensional convection-diffusion, without source term, is solved between points P and E and obtain an exponential profile for ϕ with respect to x. as an exact solution and which is given as:

$$J_e A_e = F_e\left(\phi_P + \frac{\phi_P - \phi_E}{\exp(Pe_e) - 1}\right) \tag{5.14}$$

where Peclet number Pe_e on east face is given as

$$Pe_e = \frac{F_e}{D_e} \tag{5.15}$$

where F_e is the mass flow rate and D_e is the diffusion conductance. The mass flow rate is obtained from

$$F_e = (\rho u)_e A_e \tag{5.16}$$

If the diffusion coefficient Γ is regarded as uniform over each control volume then D_e can be express by

$$D_e = A_e\left[\frac{(\delta x)_{e-}}{\Gamma_P} + \frac{(\delta x)_{e+}}{\Gamma_E}\right]^{-1} \tag{5.17}$$

where distances $(\delta x)_{e-}$ and $(\delta x)_{e+}$ are measured from face e to points P and E respectively. The expression for total flux given by Eq-5.14 can be used for calculation in the numerical procedure but unfortunately, calculation involving exponential function is somewhat time-consuming to perform. Consequently, certain approximation for the flux expression is used. The most widely used approximation scheme has form:

$$J_e A_e = F_e\phi_P + \{D_e A(|Pe_e|) + \max(-F_e, 0)\}(\phi_P - \phi_E) \tag{3.18}$$

where function $A(|Pe|)$ takes values as follow:

$$A(|Pe|) = \begin{cases} 1 & \text{for the upwind scheme} \\ \max(0, 1 - 0.5|Pe|) & \text{for the hybrid scheme} \\ \max(0, 1 - 0.1|Pe|^5) & \text{for the power - law scheme} \end{cases}$$

5.5.3.2 Linearization of Source Term

When source term is known then no particular difficulty arises. However, often the source term $\overline{S}$ depends on variable itself. This dependency is represented in the discretised equation by expressing source term as the linear function of variable

$$\overline{S} = S_C + S_P \phi_P \tag{5.19}$$

where S_P and S_C can be function of any stored value including ϕ. To maintain diagonal dominance of the matrix resulted from the discretised the value of S_P must not be negative otherwise solution will diverge. The equations used to evaluate the values of S_P and S_C can significantly affect both the rate of convergence and the stability of the solution procedure. For speed both S_P and S_C should as small as possible with as much put into S_P as possible. Stability will be affected if change in any of the solution results of S_P and S_C.

5.5.3.3 Discretisation of Continuity Equation

Flow field represented by Eq-5.2 must also satisfy the mass conservation Eq-5.1. Similarly any discretisation of Eq-5.2 must also satisfy the dicretised mass conservation equation. Integrating the mass conservation over the control volume given by Figure-5.5, we get

$$\left(\rho_P - \rho_P^0\right)\left(\frac{\Delta V}{\Delta t}\right) + F_e - F_w + F_n - F_s = 0 \tag{5.20}$$

where F's are mass flow rates on the control volume faces and evaluated as from Eq-5.16. This discretised form of mass conservation equation is used for manipulating the discretised equation for ϕ to develop the solution algorithm.

5.5.3.4 Final Discretised Equation

Substituting expression for linearised source term (Eq-5.19) into discretised equation for ϕ (Eq-5.10) we get the resultant discretised equation of form:

$$a_P\phi_P = a_E\phi_E + a_W\phi_W + a_N\phi_N + a_S\phi_S + b \tag{5.21}$$

where

$$a_W = D_w A(|Pe_w|) + \max(F_w, 0)$$

$$a_E = D_e A(|Pe_e|) + \max(-F_e, 0)$$

$$a_S = D_s A(|Pe_s|) + \max(F_s, 0)$$

$$a_N = D_n A(|Pe_n|) + \max(-F_n, 0)$$

$$b = S_C \Delta V + a_P^0 \phi_P^0$$

$$a_P = a_E + a_W + a_N + a_S + a_P^0 + S_P \Delta V$$

Here the coefficient a_P^0 arises from the unsteady terms and is defined as

$$a_P^0 = \rho_P^0 \frac{\Delta V}{\Delta t}$$

Now Eq-5.21 can be written in compact form as

$$a_P\phi_P = \sum_{nb} a_{nb}\phi_{nb} + b \tag{5.22}$$

where the subscript denotes a neighbouring grid point of P, and the summation is to be taken over all neighbours.

5.5.3.5 Solution of Algebraic Equation

Discretisation converts Navier-Stokes equation into linear algebraic equations of the form Eq-5.22 for each variable. The assembly of all the unknown variables over the entire flow domain results in set of simultaneous linear equations. This is represented in the matrix of the form as:

$$A\phi = B \tag{5.23}$$

where A is the square matrix (since the number of equations and unknown must be equal), ϕ is a vector of unknown variable values at the grid nodes of flow domain and B is the vector containing remaining terms. The matrix A is usually a sparse matrix, as most of its elements are zero. There are direct methods, for example Gaussian Elimination [79], which can be used to solve this matrix.

However, for most of the practical situation the number of unknown is so huge that it makes direct method useless. In this situation iterative solution is an attractive method and this is the method employed by most of the commercial CFD software. In these methods, one solution of the linearised equation is used to update the coefficients for next solution and the process is repeated until residual, the difference between current value and previous value, comes down below a prescribed value, this is called convergence. In iterative solution of Eq-5.22 the coefficients (a_P and a_{nb}) and source term, S_C, are estimated using the initial guess or previous iteration value and solution for each unknown, ϕ, is solved at all points within the domain.

This solution process may be accomplished through a "line-by-line" solver, in which the equations along a single "line" of grids are solved simultaneously. The line-by-line solver gives rise to a tri-diagonal matrix which is solved via Gaussian elimination, called Tridiagonal Matrix Algorithm (TDMA), to update the value of ϕ along the line considered. This procedure, also referred to as Line Gauss-Seidel (LGS) [79], is repeated for all the lines in the domain so that ϕ is updated at all the points in the domain.

5.5.3.5.1 Line-by-Line Method

To illustrate the line-by-line iterative solution algorithm we consider the Eq-5.22 in the expanded form

$$a_P\phi_P = a_E\phi_E + a_W\phi_W + a_N\phi_N + a_S\phi_S + b \tag{5.24}$$

We apply the line-by-line technique in the x-direction lines. The values for neighbouring nodes in y direction are estimated. Hence, Eq-5.24 can be written as:

$$a_P\phi_P = a_E\phi_E + a_W\phi_W + (a_N\phi_N^* + a_S\phi_S^* + b) \tag{5.25}$$

where the asterisk denoted an estimated value and the terms in the parentheses is temporarily known. Now the Eq-5.25 can be expressed in the form

$$a_i\phi_i = b_i\phi_{i+1} + c_i\phi_{i-1} + d_i \tag{5.26}$$

where the subscript i denotes the successive grid-point locations in x-direction, and the quantities a_i, b_i, c_i are the known coefficients in the equation. This is now one dimensional equation and can be solved using TDMA algorithm as described next.

5.5.3.5.2 Tridiagonal Matrix Algorithm

Suppose that the grid points aloing the chosen line are numbered as I = 1, 2, 3,……,M+1, where 1 and M denote the boundary points and the range i = 2 to M includes all the internal points. Since the unknown boundary value have been eliminated, Eq-5.26 applies to all internal points (i =2 to M) with the requirement that

$$c_2 = 0 \text{ and } b_M = 0$$

The procedure for solving Eq-5.26 is

1. Set

$$P_2 = \frac{b_2}{a_2}$$

$$Q_2 = \frac{d_2}{a_2}$$

2. Calculate P_i and Q_I for i =3,4,…..,M from the recurrence relations

$$P_i = \frac{b_i}{a_i - c_iP_{i-1}}$$

and

$$Q_i = \frac{d_i + c_iQ_{i-1}}{a_i - c_iP_{i-1}}$$

3. Note that $P_M = 0$. Set $\phi_M = Q_M$
4. The expression

$$\phi_i = P_i \phi_{i+1} + Q_i$$

is used to obtain ϕ_{M-1}, ϕ_{M-2},....., ϕ_4, ϕ_3 and ϕ_2 by successive back-substitution.

The boundary values ϕ_1 and ϕ_{M+1}, if unknown, can now be calculated from the appropriate relationship involving the boundary flux.

5.5.3.5.3 Use of Underrelaxation

The linear algebraic equation obtained from discretisation is the approximation of the original non-linear equation. Hence, value of variable influence the magnitude of coefficients in dicretised equation. Furthermore, the variable ϕ is used to represent many physical quantities. Where one physical quantify may influence the value of other physical quantities. For example ϕ can represent pressure and velocity where influence of each other is intrinsically interlinked.

This kind of non-linearity and interequation coupling affects the solution procedure of iterative method. Because of this at times, the value of ϕ may oscillate or drift away from the true solution (this is called divergence of solution). To avoid any divergence it is desirable to control the magnitude of change during each iteration and this is achieved by introducing an underrelaxation factor, α_ϕ as follows:

$$\phi_P^{new} = \alpha_\phi \phi_P^{new} + (1 - \alpha_\phi)\phi_P^* \tag{5.27}$$

using this expression into the Eq-5.22 we get the modified form of discretised equation as

$$\left(\frac{a_P}{\alpha_\phi}\right)\phi_P = \sum a_{nb}\phi_{nb} + b + \left(1 - \alpha_\phi\right)\left(\frac{a_P}{\alpha_\phi}\right)a_P\phi_P^* \tag{5.28}$$

The value of underrelaxation is generally chosen somewhere between zero and unity.

5.5.3.6 Need for a Special Procedure

The steps for the development of numerical algorithm solving Navier-Stokes equations as described above covers almost all the fundamentals for finite-volume method. However,

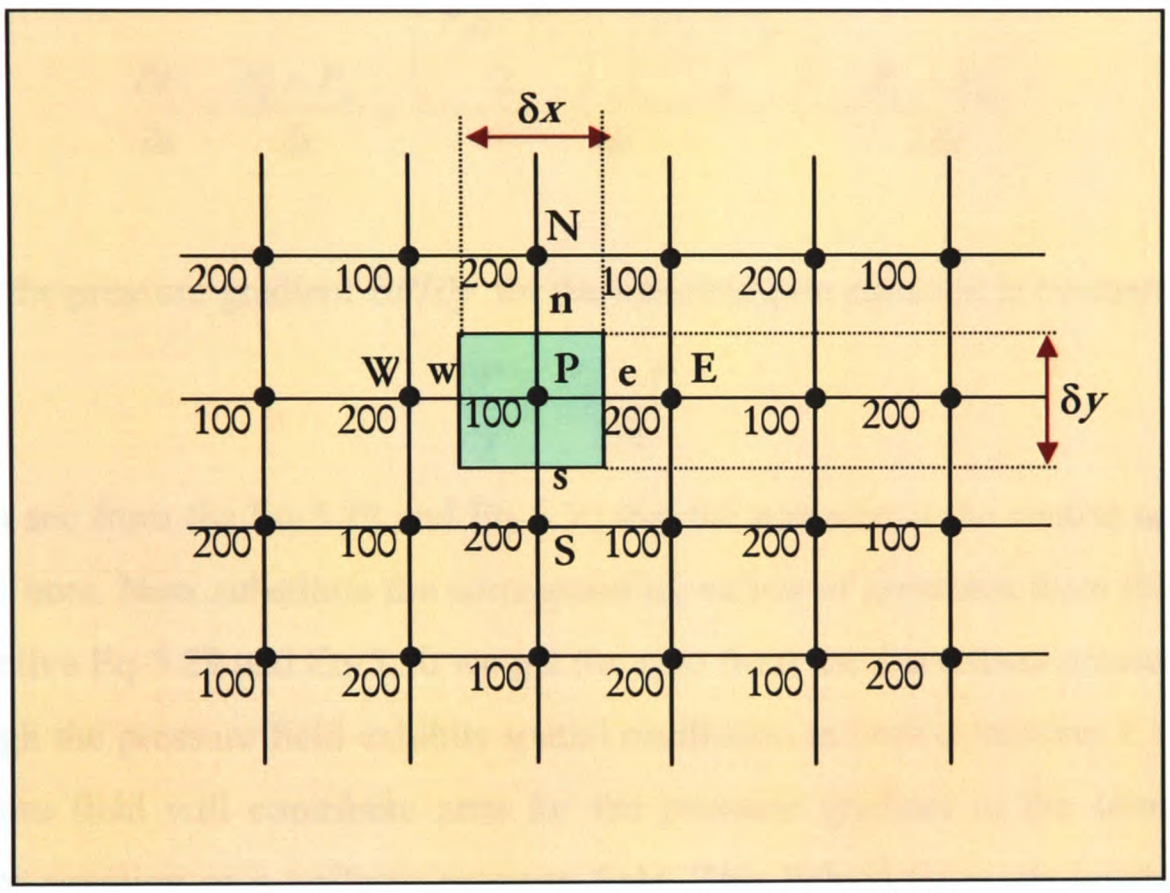

Figure-5.7: Checker-board pressure field

the storage locations for variables and their effect on solution algorithm are not addressed so far. One of the most obvious choices is to store all the variables, namely velocities and pressure at the same location; however, this gives raise to solution difficulties. As we can see from the close examination of Navier-Stokes equation pressure gradient is implicitly present as an important source term. However, there is no way in which this cannot be expressed explicitly in terms of velocities or other ϕ's. As pressure gradient is the driving factor for velocities field the specification of right pressure field is essential in order to solve the momentum equation that can also satisfy the equation for conservation of mass. However, if the velocities and pressures are both defined at the same node of a control

volume even a highly non-uniform uniform pressure field can act like a uniform field in the discretised equation. In turn, this will lead to unphysical solution of velocities and other variables. This situation can be illustrated by the following simple calculation over a uniform grid. Consider a highly irregular "checker-board" type pressure field with value as given in the Figure-5.7. Now calculate the pressures at 'e' and 'w' by the linear interpolation of the pressure gradient term $\partial P/\partial x$ in the u-momentum equation and which is given by

$$\frac{\partial P}{\partial x} = \frac{P_e - P_w}{\delta x} = \frac{\left(\frac{P_E + P_P}{2}\right) - \left(\frac{P_P + P_W}{2}\right)}{\delta x} = \frac{P_E - P_W}{2\delta x} \tag{5.29}$$

Similarly, the pressure gradient $\partial P/\partial y$ for the v-momentum equation is evaluated as

$$\frac{\partial P}{\partial y} = \frac{P_N - P_S}{2\delta y} \tag{5.30}$$

As we can see from the Eq-5.29 and Eq-5.30 that the pressure at the central node, P, does not appear here. Now substitute the corresponding values of pressures from the Figure-5.7 into respective Eq-5.29 and Eq-5.30 we get the zero from the discretised pressure gradients even though the pressure field exhibits spatial oscillation in both directions. Consequently, this pressure field will contribute zero for the pressure gradient to the source term for momentum equation as a uniform pressure field. This behaviour is obviously unrealistic and is referred "checker-board effect" [72]. Form this conclusion can easily be drawn that if the velocities and pressure are defined at the same grid location then the effect of pressure is not properly represented in the discretised momentum equation. To tackle this situation a special procedure is required. Following section explains two of these special procedures.

5.5.3.6.1 Staggered Grid

In staggered grid arrangement, not all variables are stored at the same grid points. In order to avoid the checker-board effect the velocity components are placed at displaced or staggered locations with respect to the location for pressure. This arrangement can be seen

from Figure-5.8 that the locations for two velocity components are indicated by short arrows and pointing in the direction of flow. Here locations for the velocity components are placed perpendicularly on the faces of control volume. Consequently, normal velocity

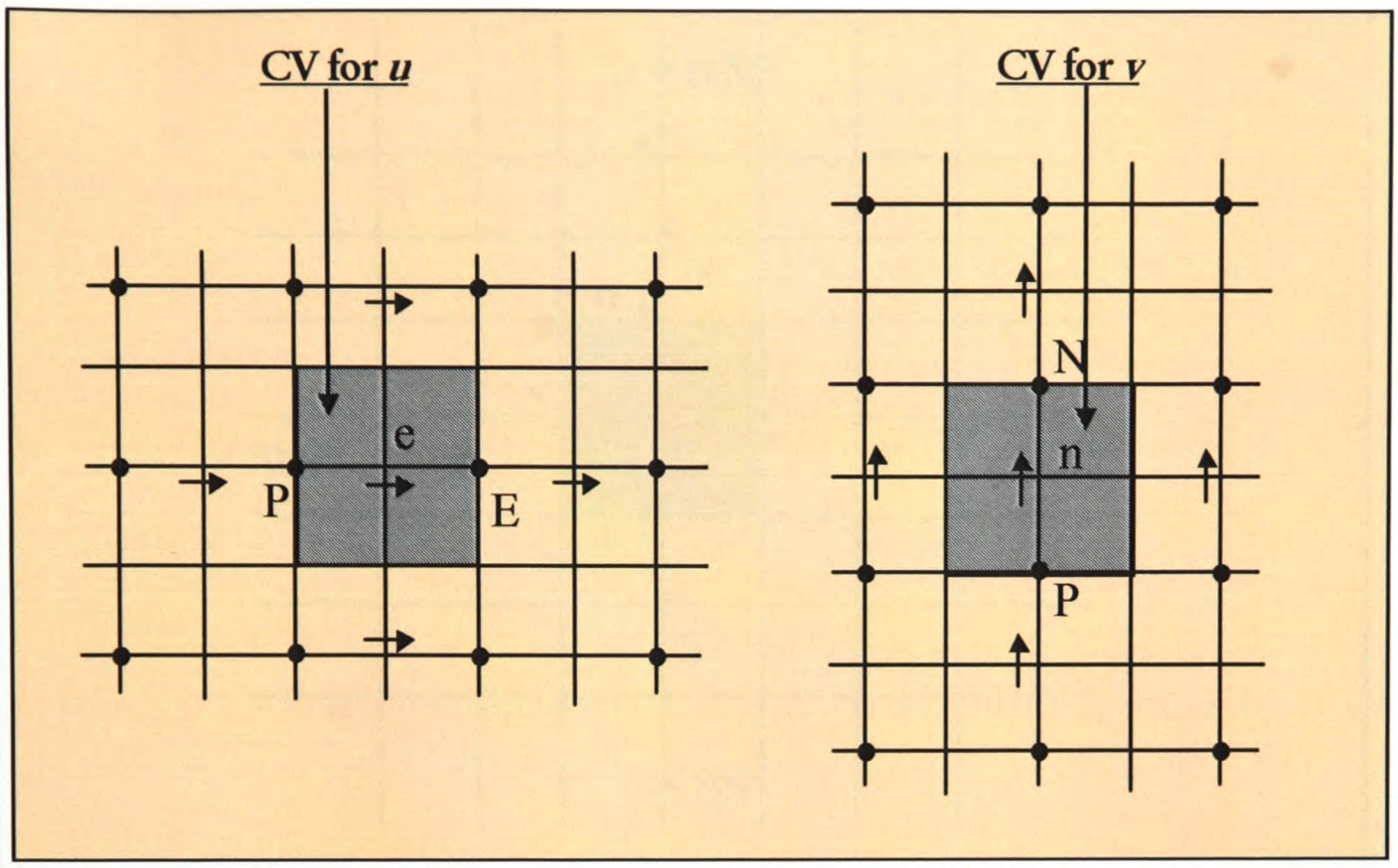

Figure 5.8: Velocity Location in Staggered Grid Arrangement

components are directly available at the control volume faces, where they are needed for the calculation of mass flow rates. Furthermore, the discretised pressure gradient between two adjacent grid points can used as the source term for discretised momentum equation that calculates the velocity on intermediate face.

5.5.3.6.2 Non-staggered Grid

In non-staggered grid arrangement velocities and pressure are located at the same grid point (Figure-5.9). In order to avoid the checkerboard effect the velocity components at faces are calculated by interpolating the grid point velocity components. The most widely used interpolation technique for this is Rhie-Chow interpolation [80]. This is based on the assumption that if the velocity values at the cell faces can be obtained by solving the momentum equations applied at the face points, then these momentum equations contain

pressure gradients which can be evaluated as the difference between neighbouring pressure locations.

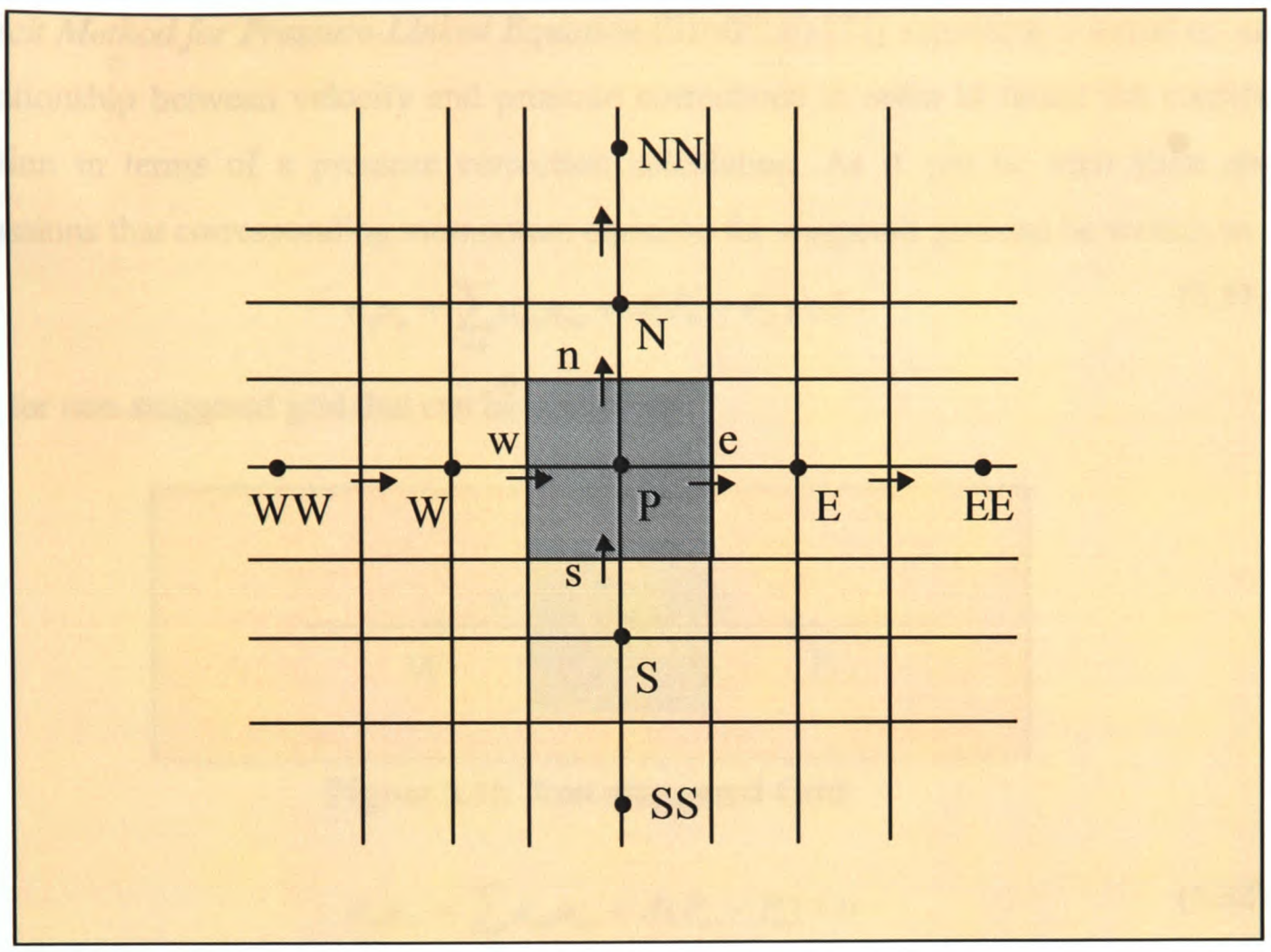

Figure 5.9: Velocity and Pressure Location in Non-staggered Arrangement

5.5.3.7 Solution Procedure

The continuity and momentum equations, in two dimension, provides three unknowns: u, v and P. Simultaneous solution of this (linearised) equation set would provide a solution in which all three unknowns satisfy each of the (linearised) mass and momentum equations. Because a simultaneous solution is computationally intensive, hence equations are solved

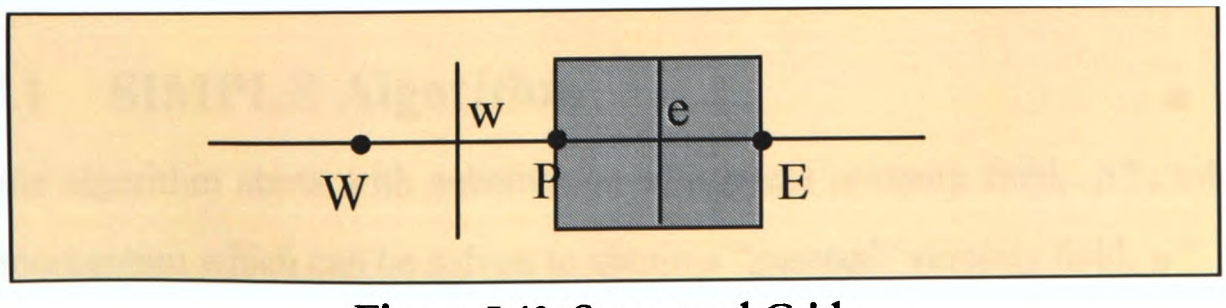

Figure 5.10: Staggered Grid

sequentially. In the sequential process, an equation describing the update of pressure is required, and is not explicitly available via the mass or momentum balances. The ***Semi-Implicit Method for Pressure-Linked Equation*** (SIMPLE) [72] algorithm is based on using a relationship between velocity and pressure corrections in order to recast the continuity equation in terms of a pressure correction calculation. As it can be seen from above discussions that corresponding momentum equation for staggered grid can be written as

$$a_e u_e = \sum_{nb} a_{nb} u_{nb} + A(P_P - P_E) + b \tag{5.31}$$

That for non-staggered grid that can be written as

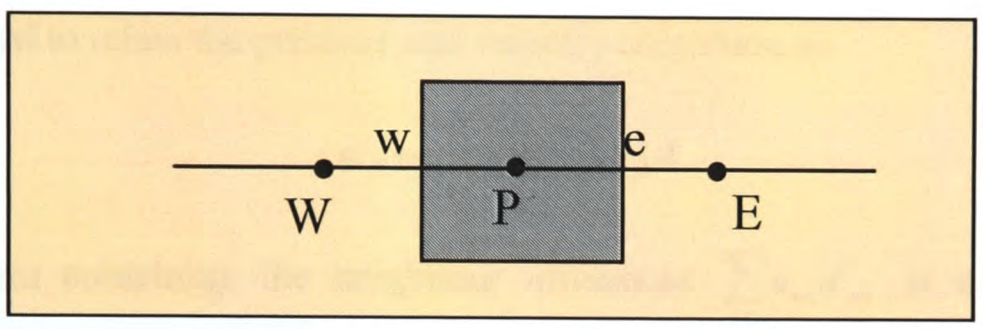

Figure 5.11: Non-staggered Grid

$$a_P u_P = \sum_{nb} a_{nb} u_{nb} + A(P_w - P_e) + b \tag{5.32}$$

For both the Eqs 5.31 and 5.32 term b includes the source term other than the pressure gradient and A represents the area over which the pressure force acts. It can be seen that both equations have a similar form except for the subscripts that are written to take account for the control volume location. Hence same solution procedure is applicable for both. The pressure correction equation SIMPLE is deduced in the same way for the staggered and nonstaggered calculation methods as explained below.

5.5.3.7.1 SIMPLE Algorithm

The simple algorithm starts with substitution of a guess pressure field, p^*, into the Eq-3.32 for momentum which can be solved to obtain a "guessed" velocity field, u^*

$$a_P u_P^* = \sum_{nb} a_{nb} u_{nb}^* + A(p_w^* - p_e^*) + b \tag{5.33}$$

Eq-5.33 is solved for the "guessed" velocity field (e.g. u_P*). The actual velocity and pressure fields are related to the "guessed" values, u_P* and $p*$, and

$$u_P = u_P* + u'_P \tag{5.34}$$

$$p_e = p_e* + p'_e \tag{5.35}$$

where u'_P and p'_e are the velocity correction, respectively. Substituting Equations 5.34 and 5.35 into Eq-5.32, followed by substitution of Eq-5.33 yields a "momentum balance" in terms of the velocity and pressure corrections:

$$a_P u'_P = \sum_{nb} a_{nb} u'_{nb} + A(p'_w - p'_e) + b \tag{5.36}$$

Eq-5.36 is used to relate the pressure and velocity correction as

$$u'_P = \frac{1}{a_P}(p_w' - p_e')A \tag{5.37}$$

where the term containing the neighbour influences $\sum_{nb} a_{nb} u'_{nb}$ is simply dropped for convenience (and will be zero at convergence since it involves only velocity corrections at the neighbour points). Equations similar to Eq-5.37 are used to cast the continuity equation in terms of an equation for the pressure correction. The basic mass balance

$$(\rho u A)_e - (\rho u A)_w = 0 \tag{5.38}$$

is first written in terms of the velocity $u* + u'$:

$$(\rho A)_e (u* + u')_e - (\rho A)_w (u* + u')_w = 0 \tag{5.39}$$

Using equations like Eq-5.37, the continuity equation can be recast as an equation for the pressure correction:

$$(\rho A u*)_e - (\rho A u*)_w + (\rho A)_e \frac{1}{(a_P)_e}(p'_P - p_E') - (\rho A)_w \left(\frac{1}{a_P}\right)_w (p'_W - p'_P) = 0 \tag{5.40}$$

Eq-5.40 can be now solved for a correction to the pressure field that is then used to compute the velocity correction via Eq-5.37. Finally, the velocity and pressure are updated via Eqs- 5.34 and 5.35.

The derivation of the solution algorithm presented so far covers most of the fundamental for a finite-volume based CFD solver. The whole solution procedure can be illustrated by the flow chart as follow (Figure-5.12):

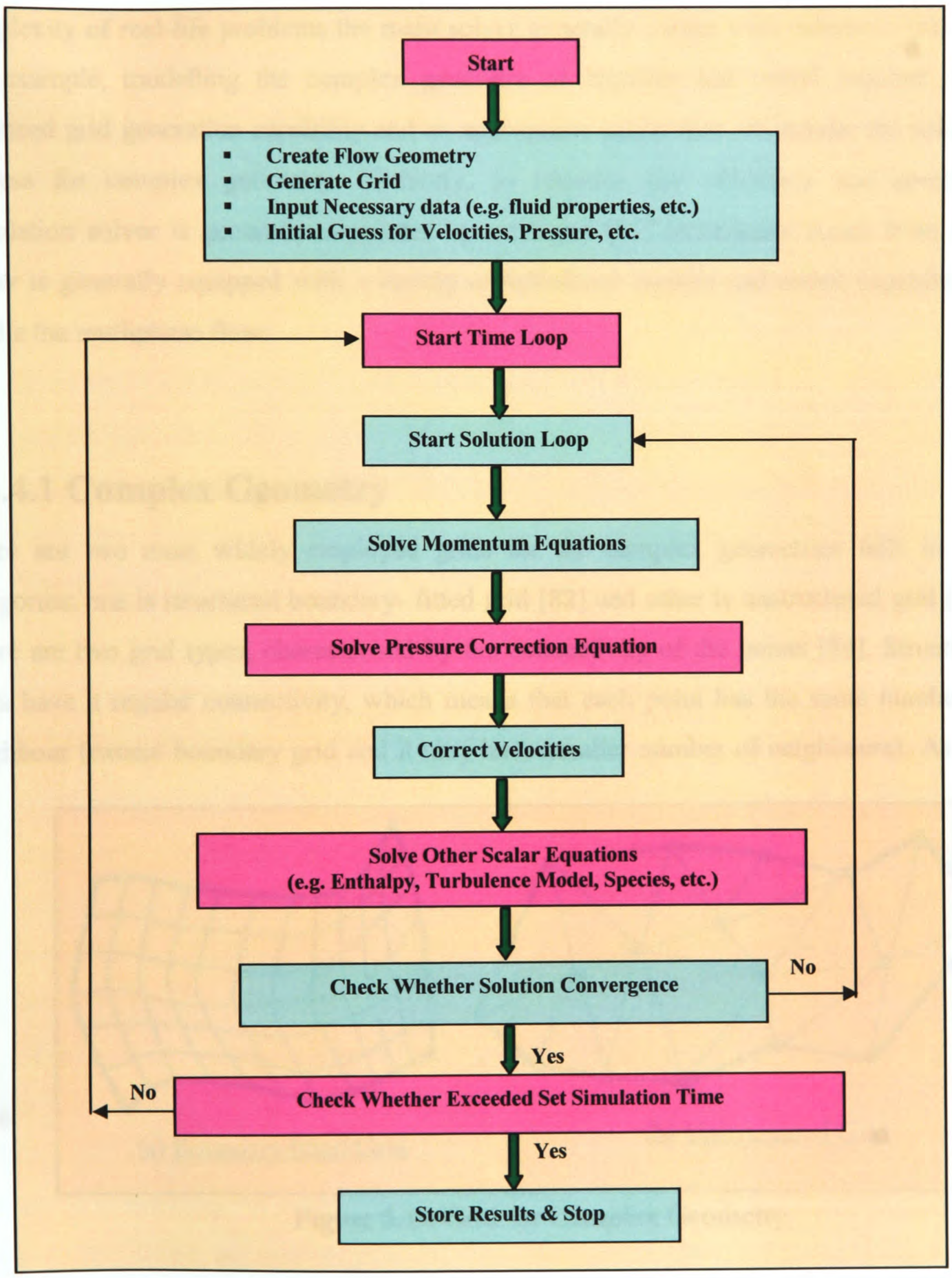

Figure 5.12: Solution algorithm for finite volume method

5.5.4 Extension of Basic Finite-Volume Solver

The fundamentals of finite-volume algorithm as presented above form the basis of most commercial Computational Fluid Dynamics (CFD) software. However, to tackle the complexity of real-life problems the main solver generally comes with enhanced features. For example, modelling the complex geometry of impeller and vessel requires more advanced grid generation capability and an appropriate solver that can handle the solution process for complex geometry. Similarly, to improve the efficiency and speed of calculation solver is generally supported by multigrid [81] techniques. Apart from that, solver is generally equipped with a variety of turbulence models and added capability to handle the mutliphase flow.

5.5.4.1 Complex Geometry

There are two most widely employed grids for the complex geometries falls in two categories: one is structured boundary- fitted grid [82] and other is unstructured grid [83]. There are two grid types, characterised by the connectivity of the points [84]. Structured grids have a regular connectivity, which means that each point has the same number of neighbour (except boundary grid and it may have smaller number of neighbours). As can

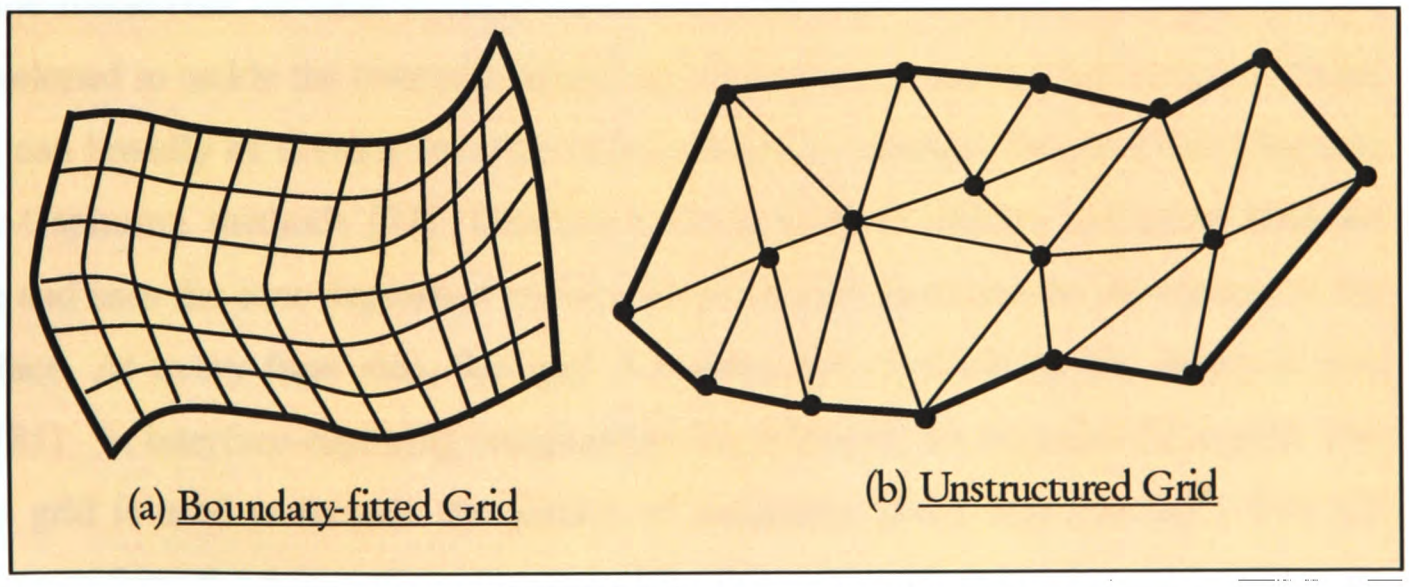

Figure 5.13: Grid for Complex Geometry

be seen from Figure-5.13 (a) boundary-fitted grid it is required that grid be aligned with the boundary and this pattern spans the whole domain. Unstructured grids have irregular

connectivity that is each point can have a different number of neighbours, Figure-5.13 (b). Fundamentals of solution algorithm, as present in the previous section, still holds true with some alteration to account for the nature of grid. Details of these could be found in [74].

5.5.4.2 Multi Phase Flow

Most often flows encountered in nature and in industries is a mixture of phases. These flows can broadly be classified in two categories. In the first, interaction of two phases takes place at a distinct boundary between the phase, here two fluids are not interpenetrating each other. For example, the air-fluid interface at the top surface of impeller-stirred vessels. In the second category of multiphase flow there is no distinct boundary between two phases. In this case two phases can be interpenetrating and act like a single phase. For example, impeller-stirred mixing of particulate suspension or dispersed liquid into the main liquid. Modelling techniques for both category of multiphase have been discussed below.

5.5.4.3 Modelling of Free Surface

Within the framework of finite-volume based CFD algorithm a number of methods have been developed to tackle the transient behaviour of air-fluid interface (free surface). These methods can broadly be divided into two main categories, namely, Interface-Tracking and Interface-Capturing methods [74]. Interface-tracking method defines the sharp fluid air interface and uses the time dependent surface adoptive grid simulates the movement of the free surface. At every time step, the grid is regenerated conforming the shape of free surface [85]. In interface-capturing computation is performed on extended fixed grid. The extended grid is used to include the portion of secondary phase that interfaces with the main phase to form the free surface. For example, in impeller-stirred tank working liquid at the top surface forms the interface with air and hence, computational domain is required to include the air too.

Volume-Of-Fluid (VOF) [86] is one of the interface-capturing methods. In this method, both fluids are considered as single phase and its properties are considered to vary in computation domain according to their volume fraction. Here, in addition to solving common mass and momentum conservation equations the shape of free surface is determined by solving the advection equation [74,86] for the volume fraction. Overview of the governing equations for VOF method can be found in APPENDIX-C.

5.5.4.4 Modelling of Particulate Second Phase

There are two possible ways to define the flow field in a computational domain. First one called Eulerian method, specifies the flow properties with respect to a fixed reference frame attached with the grid. The second one called Lagranginan method, specifies the flow properties with respect to reference frame attached with the moving particle itself. Consequently, there are two ways to model the particulate second phase as well. The computation for the main carrier fluid (continuous phase) is always carried out by Eulerian method, whereas particulate second phase can either be handled using Eulerian method or Lagranginan method. Therefore, these are called Eulerian-Eulerian and Eulerian-Lagrangian approaches respectively.

If the mass loading for particle is not very large motion of finite number of particles, representing the particulate second phase, through the continuous phase can be computed in Lagrangian approach. Here, the pre-calculated velocity fields for the continuous phase acts like a carrier medium when trajectory of particles is tracked. In the situation when the mass fraction of particles is large then, Eulerian approach is more appropriate choice that computes the flow field for both the continuous phase and the particulate second phase. Eulerian-Eulerian approach, however, puts heavy demand on the computer resources, as the number of equations for both the phases required to be solved. The details of Eulerian-Eulerian techniques can be found in [87] and a thorough description of Eulerian-Lagrangian method can be found in [88] and in APPENDIX-D.

Considering the modelling complexity associated with impeller-stirred mixing, the calculation of particulate second phase using Eulerian-Eulerian would be prohibitively difficult. In the situation like this Algebraic Slip Mixture (ASM) model can be used as a sufficiently accurate approximation, with only a moderate increase in the computational effort compare to a single-phase model.

The Algebraic Slip Model was first developed by [89]. In this model flow field for two phases are calculated by solving the continuity and momentum equation for the mixture. Here, the governing equation largely resembles those for a single-phase flow where single-phase density and velocity are replaced by the mixture density and velocity respectively. However, to account for the slip of second phase relative to the continuous phase an additional term in the mixture momentum equation is added. An algebraic equation is used to represent this relative velocity of second phase with respect to continuous phase, and the volume fraction for second phase is solved calculated from the phase continuity equation. The governing equation is simplified further by assuming that the time taken by particle to reach the terminal velocity is very short compared to the characteristic time scale for the flow of the mixture. Furthermore, the terms for the viscous and turbulent stresses in mixture momentum equation are usually combined to give a generalised stress. The excellent details for the formulation of ASM model can be found in [90, 91]. APPENDIX-E presents an overview of the governing equations for this method.

5.6 Commercial CFD Codes

Almost all the established commercial packages provides easy accessible user interfaces in form of alpha-numeric or/and graphic to input problem parameters and to examine results. Function of three main components of a CFD package can be classified as:

- Pre-processing
- Solution
- Post-processing.

In the pre-processing stage user of package create the problem geometry and generate an appropriate grid. This is followed by the specification of problem parameters, namely

boundary conditions (for example flow rate at a pipe inlet) and material properties (for example fluid density and viscosity).

At solution stage solver performs similar steps as given in the flow chart. Before starting the simulation solver configures itself by reading in the input data supplied during pre-processing stage. After those numerical calculations commences which iteratively proceeds to obtain complete description of flow field. At each step of iteration a guess and correct strategy is applied to calculate each flow variables. When an iteration is performed a residual value, difference between previous and current value, is produced for each flow variables and should become smaller and smaller as solution progresses. When residual becomes smaller than a pre-set value the solution is considered to be converged. Convergence of solution is the first criterion for successful simulation run. After convergence is achieved solution data is stored for further analysis and interpretation.

At the post-processing stage solution data is subjected to a variety of qualitative and quantitative analysis. CFD solution generally produces huge number of data points and its interpretation requires special technique. Most of the CFD commercial software is equipped with facilities to display the data in graphical form for visualisation. Depending on the analysis undertaken graphical output can be velocity vector plot, temperature contour plot, etc. The graphical display makes it easier to identify the area of interest, for example from graphical display dead zone in impeller-stirred mixing tank can be identified. This information can be used to improve the design and with this feedback user may re-visit the pre-processing stage and possibly change the geometry slightly and then re-run the solver.

In this section we present a brief description of some of the leading commercial codes. These codes are widely used to solve the complex real life flow problems and are capable of handling vast range of industrial strength flow problems. However, it should be noted that the capabilities of these software products are always changing. Our aim here is to highlight the most essential features of these packages in most general term. Details of the exact specification can be obtained from the web sites of respective vendors [92-95,75, 96].

- **PHOENICS:** This is the first commercial CFD code. It has been continuously marketed, used and developed since early eighties. This employs boundary-fitted grid for modelling. It can be used to generate grid for both Cartesian and cylindrical polar geometries. The solution algorithm is based on staggered finite-volume method. Apart from some standard feature, main solver can also handle a range of flow situations (e.g. compressible flow, non-Newtonian, fluids through porous medium, melting/solidification etc.) through enhanced capabilities of solver. This uses k-e as main turbulence model with flexibility to change its parameters for improved performance. Apart from this standard turbulence model a range of other models like RNG, Large Eddy Simulation, etc., are also available. The power-law or hybrid differencing scheme could be used for the solution.

- **FLOW-3D:** It is a finite-difference, transient-solution algorithm solving the conventional, conservation equations of fluid dynamics. The algorithm is largely based on the similar methodology as that of SOLA. However, it is a completely independent implementation of these techniques. The solver is based on a combination of finite difference and finite volume techniques. The discretisation is performed on staggered grid using transient flow equations written in terms of primitive variables. The grid generation for problem geometry can be non-uniform in Cartesian cylindrical-polar co-ordinate system in one, two or three dimensions. It also has capability of tracking the movement of free surface using "Volume of Fluid" (VOF algorithm). It incorporates physical models for porous media flow, conjugate heat transfer, dynamic fluid interaction motion, surface tension, wall adhesion, turbulent flow, incompressible and compressible flow, non-Newtonian fluids, non-inertial reference frames, solidification and melting, thermal buoyancy, and simplified bubble models. It models turbulent flows with either a Prandtl mixing length model, a standard two-equation k-e model, RNG model (renormalised group theory model, an extension of the standard k-e model), or a Large Eddy Simulation. Finally, it uses either a first-order method or a second-order method of space and time derivatives.

- **CFX**: CFX is another widely used CFD software for the industrial application. It employs the block-structured grid. In block-structured the whole problem geometry is segmented into number of block where boundary-fitted structured grid fills the segment locally. This makes it possible to handle the globally complex structure of flow domain with greater flexibility and efficiency. The solver is based non-staggered finite-volume method. It has turbulence model like k-e, RNG and Large Eddy Simulation. The solver uses first order and second differencing scheme. The main solver is supported by number of algorithms to solve range of flow problems like compressibility, multiphase, rotating flow, etc. Here user subroutine can be used to introduce new governing law or solve new variable.

- **PHYSICA**: This software is based on unstructured grid framework (elements not restricted to 90 degree angles, or bricks) that provides flexibility for modelling complex geometry with relative ease. This software provides a general modelling capability for predicting multi-physics phenomena. This is also a finite-volume based solver with the capability of solving fluid flow and solid structural problems simultaneously. This is an ideal tool for predicting flow-structure interaction. Furthermore, framework of this software is such that source code can be modified with relative ease to introduce new governing principles. The fluid flow part of the solver employs SIMPLE algorithm where first order or second order differencing scheme is used. The solver is equipped with k-e model to tackle the turbulent flow. Apart many other capabilities this can also solve solidification/melting problems.

- **FLUENT:** FLUENT4.5 solves the governing conservation equations of fluid dynamics by a finite-volume formulation on a structured, non-orthogonal, curvilinear co-ordinate grid system using a non-staggered variable arrangement. Within the framework of this software an exclusive grid generation package, called GAMBIT, is included. This provides greater flexibility in handling the grid generation task for wide verities of complex geometry. In FLUENT4.5 three different spatial discretisation schemes may be used; i.e., Power-Law, second-order upwind, and QUICK. The pressure-velocity coupling is achieved by the SIMPLEC algorithm. The matrix resulted from discretised

equation is solved using a line-by-line tridiagonal matrix algorithm and its performance can be accelerated by an additive-correction type of multigrid method and block-correction. Facility for adding user defined subroutine is given which can be used to solve extra variables, etc. It models turbulent flows using an RNG model and a second-moment closure or Reynolds-stress model (RSM). In general, it includes models of single or multiphase flow, compressible flows. Within the framework of this software an exclusive interface for modelling impeller stirred tanks, called MixSim, is available; this makes it an attractive option for our modelling work. . In fact, FLUENT is currently the world leading software product for modelling stirred tanks.

- **STAR-CD:** It is another general purpose, finite volume algorithm which uses an unstructured grid system to resolve the conservation equations. The unstructured grid allows for a range of optional cell shapes. These cells may exhibit arbitrary deformation, have sliding interfaces, and permit cell insertion and deletion. In addition, local mesh refinement may be utilised to locally enhance accuracy of simulations without encumbering the global solution. Extended versions of the SIMPLE and PISO algorithms are used for steady-state and transient calculations, respectively, solving all variables on collocated Cartesian velocity components. Spatial differencing is second-order and a fully-implicit first-order temporal differencing is used. It models turbulent flow using a number of different Reynolds-averaged models, and a two-layer variant of the k-e model in which the low Reynolds number model is used in the near-wall region. In general, this package has extensive flow, heat and mass transfer capabilities, including compressible, multiphase and chemical-reacting flows.

5.7 Conclusions

This chapter described the basic building block of the solution algorithm for Computational Fluid Dynamics. First of all governing equations for the flow phenomena was outlined. The flow equations are continuous partial differential equations that could not be solved analytically for majority of practically important flow problems. Fortunately, with the use of various numerical techniques this could be converted into linear algebraic equation. The

process of converting partial differential equation into linear algebraic equations, which can be solved using digital computer, is called discretisation process. In this chapter a brief description of a number of important discretisation methods was presented. This was followed by the detailed derivation of finite-volume discretisation. Finite-volume is the most widely used technique in the field of fluid dynamics and forms the basis for most commercial CFD codes. Finally, a brief outline of leading commercial CFD packages was presented.

Chapter 6

CFD MODELLING RESULTS

6.1 Introduction

Impeller-stirred mixing of molten lead bullion is the most important process in the lead refining industries. Efficiency of the process to remove impurities very much depends on the control and optimisation of the impeller driven flow patterns in the melt. Obviously, for any improvement in existing practice a necessary condition is to gain an understanding of the flow behaviour and its dependency on key process variables. Unfortunately, there is little knowledge available about this process, mainly because it is almost impossible to conduct any direct experiments on the real kettle.

Recent advances in computer technology, numerical techniques and the development of user-friendly pre and post processors have emerged to play an important role in engineering research and development. Computational Fluid Dynamics (CFD) is now a widely used tool in the design of stirred tank reactors, especially in the chemical industry, where it is used to identify optimal process conditions. CFD can be used to carry out parametric studies for different designs and operating schemes to optimise the process. Hence, this can greatly reduce the cost of experiments and eliminate the problems of scale-up.

This chapter presents CFD modelling results for both the water model and the real lead kettle detailed in previous chapters. All the complex phenomena associated with the flow field (e.g. impeller rotation, vortex formation, multiphase mixing, etc.) have been captured in the CFD simulations. The results detailed in this chapter demonstrate this complexity and these are validated against corresponding experimental data. All the CFD simulations are carried out using a commercial code FLUENT [75].

6.2 Contributions from this Research

Most of the CFD work available in literature on the stirred tank is mainly based on laboratory scale cylindrical shaped vessels. However, impeller-stirred mixing taking place in the lead refining industry uses hemispherical shaped kettles and this complex shape is not a well-studied system. The CFD based analysis of the impeller-stirred flow field taking place inside the hemispherical shaped refining kettle is one of the main objectives of this research project.

First of all a feasibility study, to ensure applicability of CFD modelling in the lead refining process, was carried out. The results from initial simulations were validated with experimental data and comparisons were found encouraging. This exercise established the applicability of CFD modelling for the lead refining process. The next stage involved predicting flow behaviour in the corresponding water model. This is the first systematic attempt to apply CFD modelling for the simulation of impeller-stirred flow field in hemispherical kettle.

To tackle the problem of vortex shape calculation within the constraint of available computer resources a novel technique was developed. The three-dimensional model was reduced to two-dimensional model by mathematically representing the rotation of the impeller; this was implemented through user subroutine (see Section-2.1.2 and APPENDIX-A for details). The calculated vortex shape was then incorporated into a three-dimensional model to calculate the full flow field. This three-dimensional model was further extended to include the particulate second phase as well. A number of publications [97-101, 8] have resulted from the research detailed in this chapter.

6.3 CFD Model Setup - Flat Surface Approximation

The objective is to develop technique that does not require the experimental data for the representation of the impeller (as no experimental data is available to assign impeller boundary conditions). As a starting point, a three-dimensional steady-state model that uses

rotating/multiple-reference-frame technique to model rotating impeller (see Section-2.1.6 & Section-2.1.7 for details) is developed.

This model is further simplified by assuming a flat surface approximation at the air-lead interface. All the test cases that have been selected for the simulation operate in the turbulent flow regime. To account for the turbulence into the CFD models a standard k-ε model [68] is used. The governing equations are solved in cylindrical-polar co-ordinates [48] using structured boundary-fitted grid [82]. For this purpose, the structured code version of FLUENT 4.5 is used. The boundary conditions for the model are summarised as follow:

1. Solid walls are considered to be no-slip impermeable surfaces where normal components of velocities are zero, and k and ε are zero. In order to eliminate the need for very fine grid near the wall the logarithmic wall function [68] is used to specify the shear stress.

2. The free surface at the air-liquid interface is assumed to be a shear free flat surface where the normal velocity, tangential stress and the normal fluxes of k and ε are zero.

3. At the axis of symmetry below the impeller, components of radial and angular velocity are zero, and because of the symmetry gradient of all the other variables in the radial direction is also zero.

4. Taking advantage of the geometrical symmetry of the system, only a quarter of the geometry is meshed. Periodic boundary condition on the vertical sides (resulting from vertically cutting the geometry in a quarter size) is applied to account for the complete flow field.

During the computation underrelaxation factors (0.5 for pressure, 0.3 for u-velocity, 0.3 for v-velocity, 0.2 for w-velocity, 0.7 for turbulence kinetic energy (k) and 0.7 for turbulence dissipation rate (ε)) are used in order to keep the solution divergence under check.

6.3.1 CFD Results for Lead Refining Kettle

CFD modelling is applied to ascertain its feasibility in simulating the impeller-stirred flow behaviour of molten lead in the refining kettle. For this purpose CFD simulations are carried out for those operating configurations where experimental data has been gathered. A hemispherical shaped kettle of 3.65m diameter is used where mixing is carried out using an impeller of 0.638m diameter and 0.156m blade height. Section-4.8 gives the details of the experiment and Table-6.1 summarises the operating conditions (N1-N5) for each test

No.	Shaft Depth (from top)	Blade Angle	RPM
N1	0.72m (Short Shaft)	Flat	78
N2	0.72m (Short Shaft)	Flat	95
N3	0.75m (Short Shaft)	30°	56
N4	0.75m (Short Shaft)	30°	76
N5	1.2m (Medium Shaft)	Flat	127

Table 6.1: Operating Configurations for CFD Models for Lead Refining Kettle

case. The procedure for setting up these models is already described in Section-6.3. At the early stage of model development, MixSim, a user interface for setting up impeller stirred mixing models, of FLUENT was used. MixSim is a user friendly interface where grid

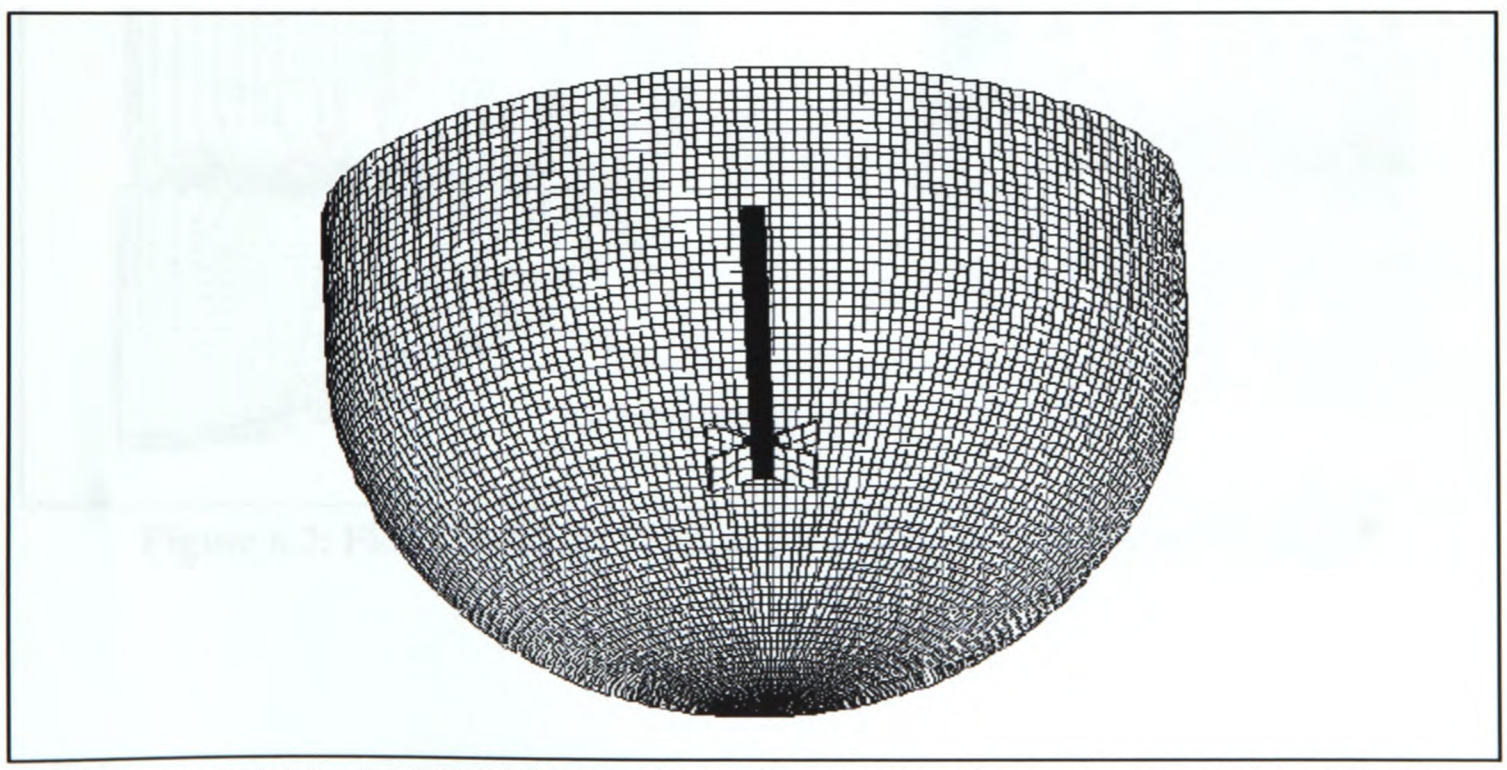

Figure 6.1: A Typical Grid for Kettle Wall and Impeller as Generated by MixSim

generation and solver set up are done automatically for standard geometry and operating conditions. MixSim uses the rotating/multiple-reference-frame (see Section-2.1.6 & Section-2.1.7 for details) when a three-dimensional geometry based steady-state model is set up.

Figure-6.1 shows a typical computer representation of the kettle and impeller (half kettle and all impeller is shown for clarity). In all the test cases, because of symmetry in the domain, only a quarter of the domain is modelled and a high-resolution mesh density of 67,200 elements is used. The material properties of molten lead (Density = 10500 kg/m^3 and Viscosity = 2.12×10^{-3} N-s/m^2) [52, 102] are used.

Figure-6.2 shows the CFD calculated velocity profiles, for a typical test case with flat blade impeller. As expected, we can see a radial jet of liquid shooting out towards the kettle wall. In addition, because of this, two large re-circulation zones occur in the bulk region of the kettle.

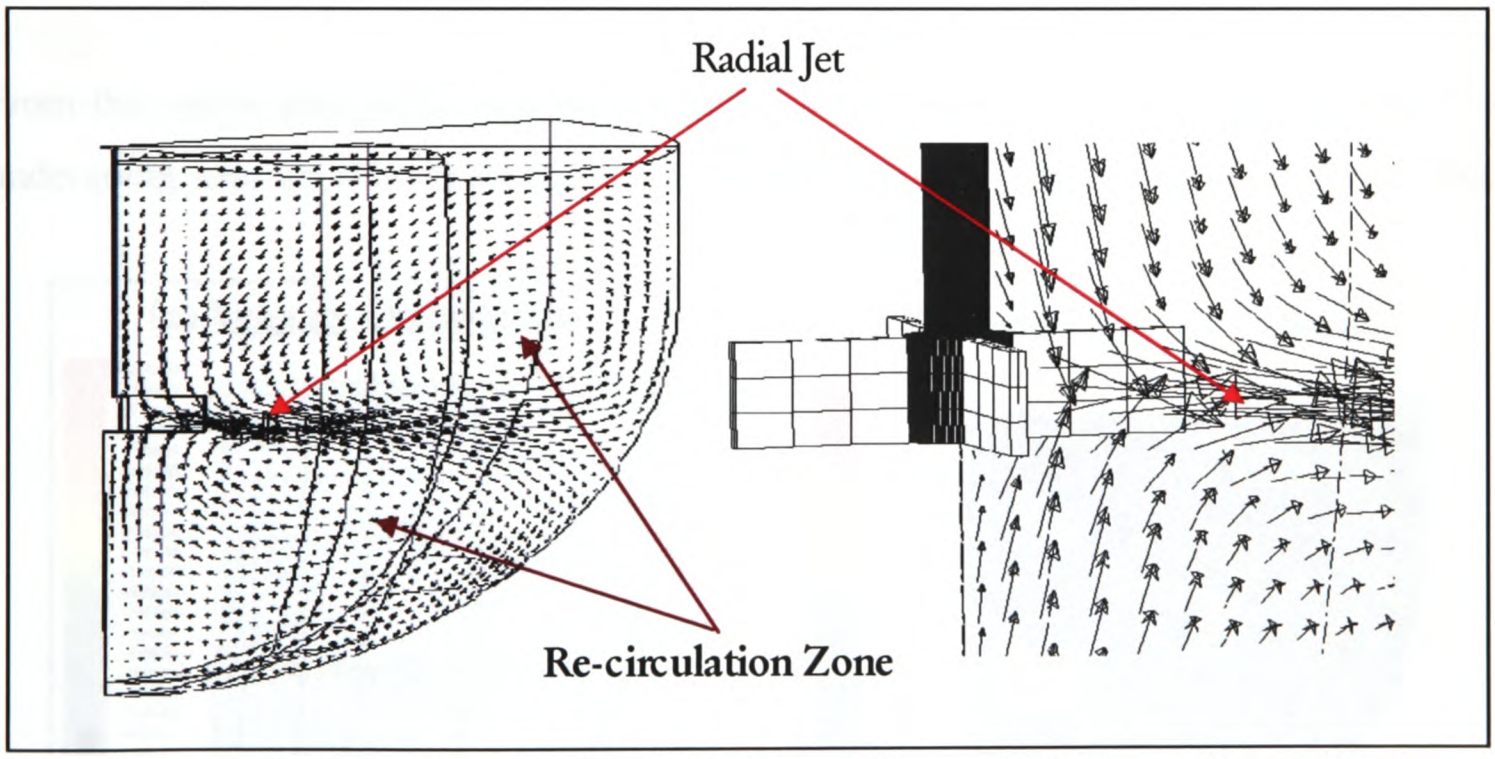

Figure 6.2: Flow Profile in Vertical Plane Through Kettle and Impeller

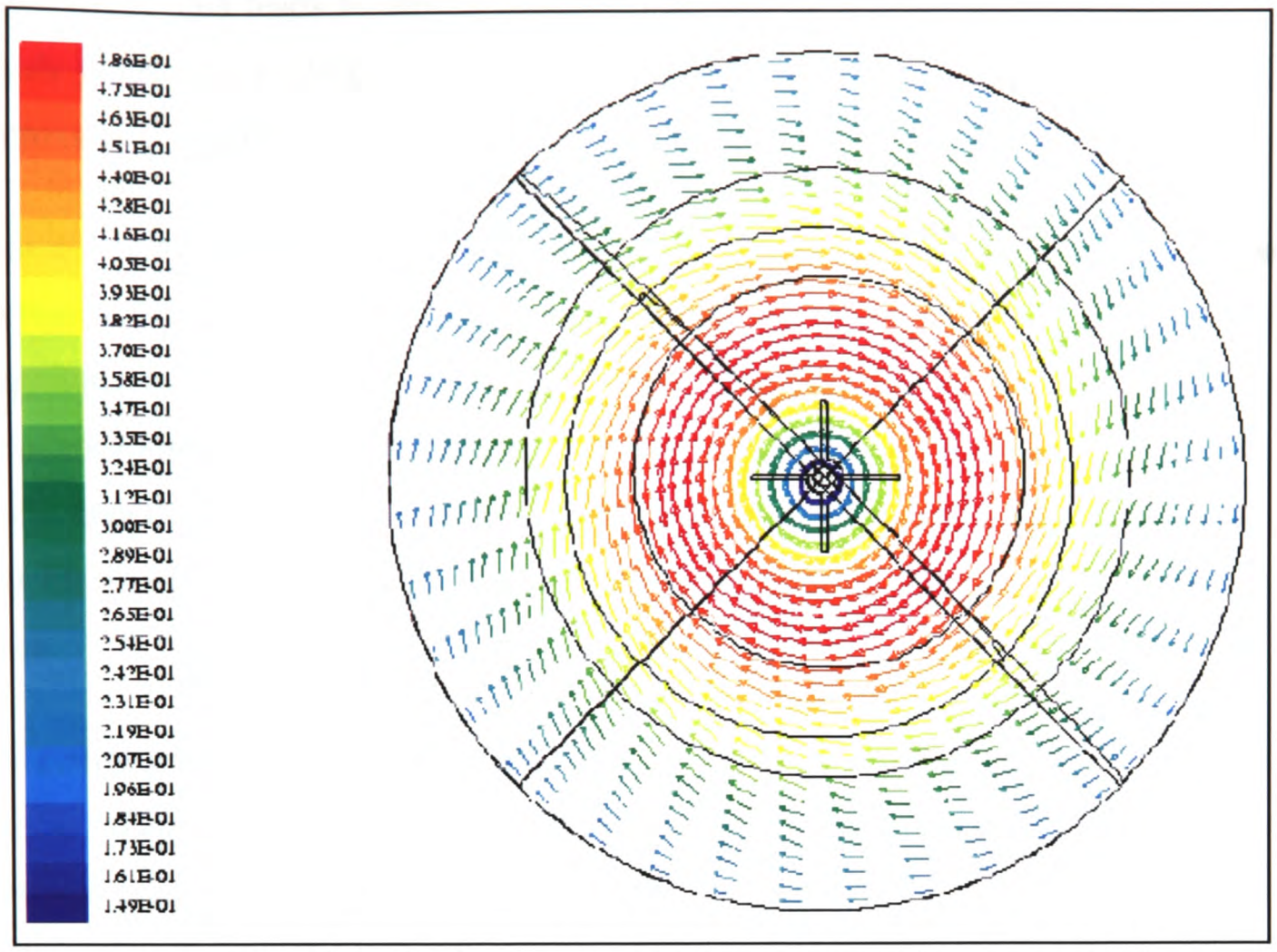

Figure 6.3: Flow Profile on Top Surface of Kettle (Test Case N1)

From the vector plot on the top surface of the kettle, Figure-6.3, it is clear that liquid is undergoing near solid-body rotation. The similar pattern is also observed in the refining

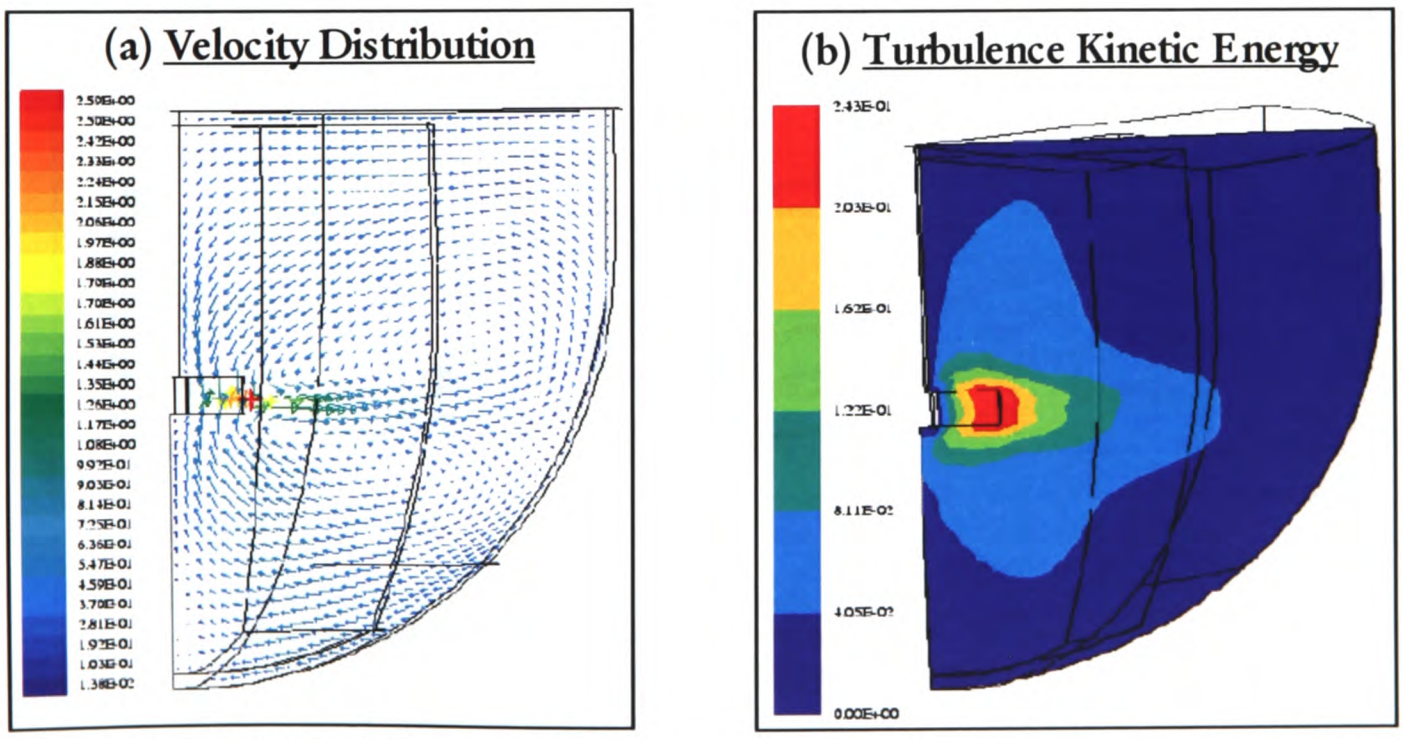

Figure 6.4: (a) Velocity and (b) Turbulence Kinetic Energy Distributions (Test Case N1)

kettle where this leads to strong surface swirl. Owing to the dominant circular motion, which gives rise to large body force, computation time is generally very high. The approximate simulation time required for this analysis is about 12 hours.

Figure-6.4 (a) shows the velocity distribution, clearly, it is highest at the impeller and decreases towards the kettle wall. At the axis line, just below the impeller, velocity magnitude is lowest and forms a dead zone. A similar pattern for the distribution for turbulence kinetic energy can be seen from Figure-6.4 (b), where highest magnitude occurs in the impeller swept zone and fades away in the bulk. It is interesting to note that in the real life situation in the region of high turbulence kinetic energy vigorous mixing takes place.

The results presented so far are typical flow patterns that occur in any impeller-stirred tank. Hence, it can be said that the CFD simulations for lead refining qualitatively captures the essential features of the flow field. However, we do not have any observation data from bulk region of the refining kettle to assess the accuracy of these results. In this situation comparison of experimentally measured surface velocity (see Section-4.8 for the details of experiment) with the computed results was undertaken as a validation test.

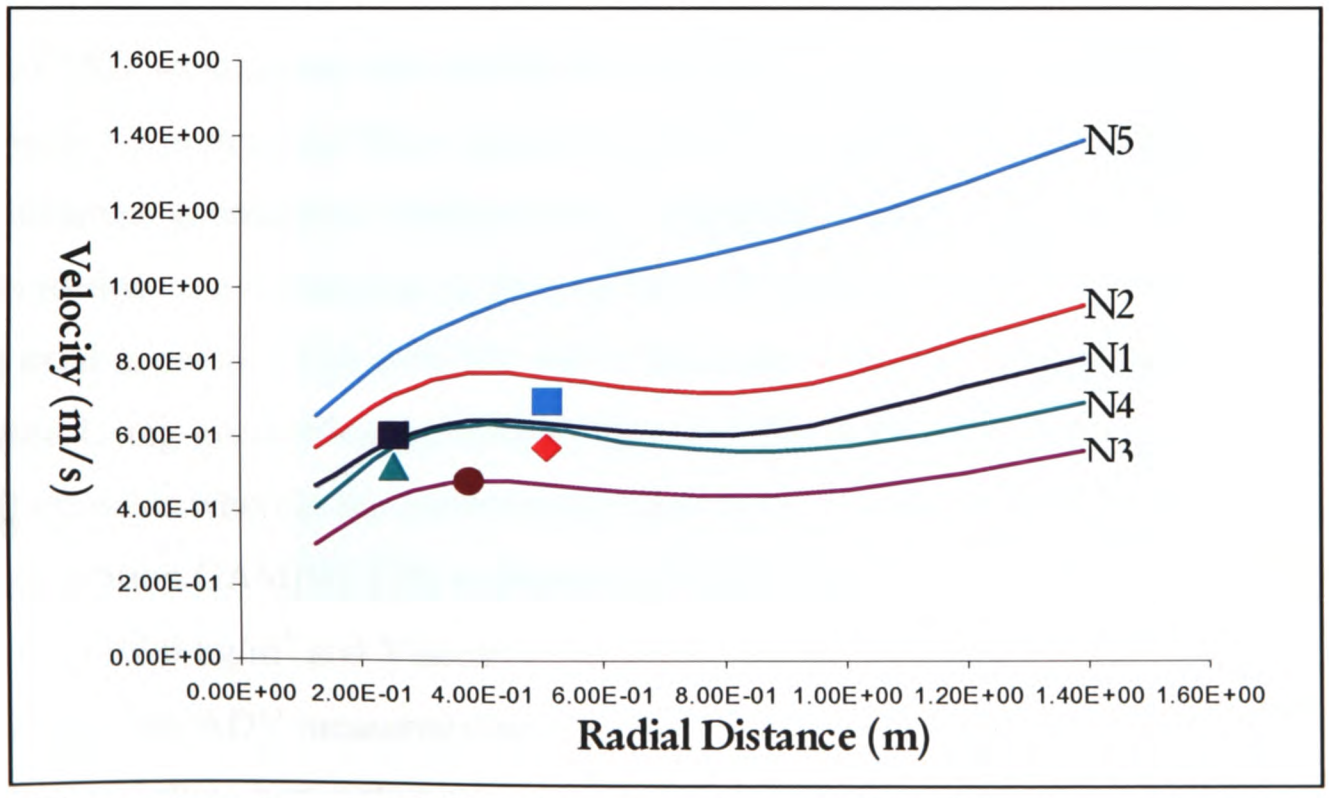

Figure 6.5: Computed (lines) & Experimental (dots) Surface Velocities

In the Figure-6.5 experimentally measured surface velocities for a number of operating conditions (see Table-6.1) are compared with the computed velocities. Here same colour is used to represent an experimental data point (dot) and corresponding CFD result (line). We can see that for the lower shaft speeds (N1, N3, N4) the comparisons are very close, but for the higher speed (N2, N5) a clear difference is present. In addition, this difference increases with the increasing rotational speed. This discrepancy can be attributed to both the experimental measurements and CFD model results. Data from the experiment, in strict sense, can only be regarded as estimation. This is because a number of factors namely lift, drag and buoyancy forces affecting the movement of steel ball on the melt surface have not been taken into account. The effect of these factors increases with increasing speed. Furthermore, the flat surface approximation for air-lead interface in the CFD model may also have contributed to the difference between computed and measured results. Keeping above said factors in mind, it can be concluded that the comparison is very encouraging and warrants further refinement in both the experimental method and CFD modelling technique.

6.3.2 CFD Results for Water Model

A set of CFD simulations was carried out for a 0.75 scaled water model (physical model) kettle with 2.9 m diameter (See Section-3.4.10 for the details of water model setup). Here, three different geometrical configurations (unbaffled, baffled and off-centred shaft) are used to identify the differences in flow profiles. Models are set up for a four bladed (angle = 45°) axial impeller which is 0.75m below the water surface and rotates at 140RPM for all the cases. Using geometrical symmetry, the unbaffled kettle (one quarter) is meshed using 50,000 elements whereas the baffled kettle (one half) is meshed using 98,000 elements. For mesh generation GAMBIT [75] software of FLUENT is used. Material properties of water (Density = 1000 kg/m^3 and Viscosity = 0.9×10^{-3} $N\text{-}s/m^2$) are used. For both unbaffled and baffled cases the ADV measured data (see the Section-4.7) are available for validation. The rest other modelling parameters are same as discussed in the Section-6.3.

Figure-6.6 shows the velocity profile in a plane vertically passing through the middle of the kettle. It can be seen that angular jets of high velocity shooting out of the impeller blades

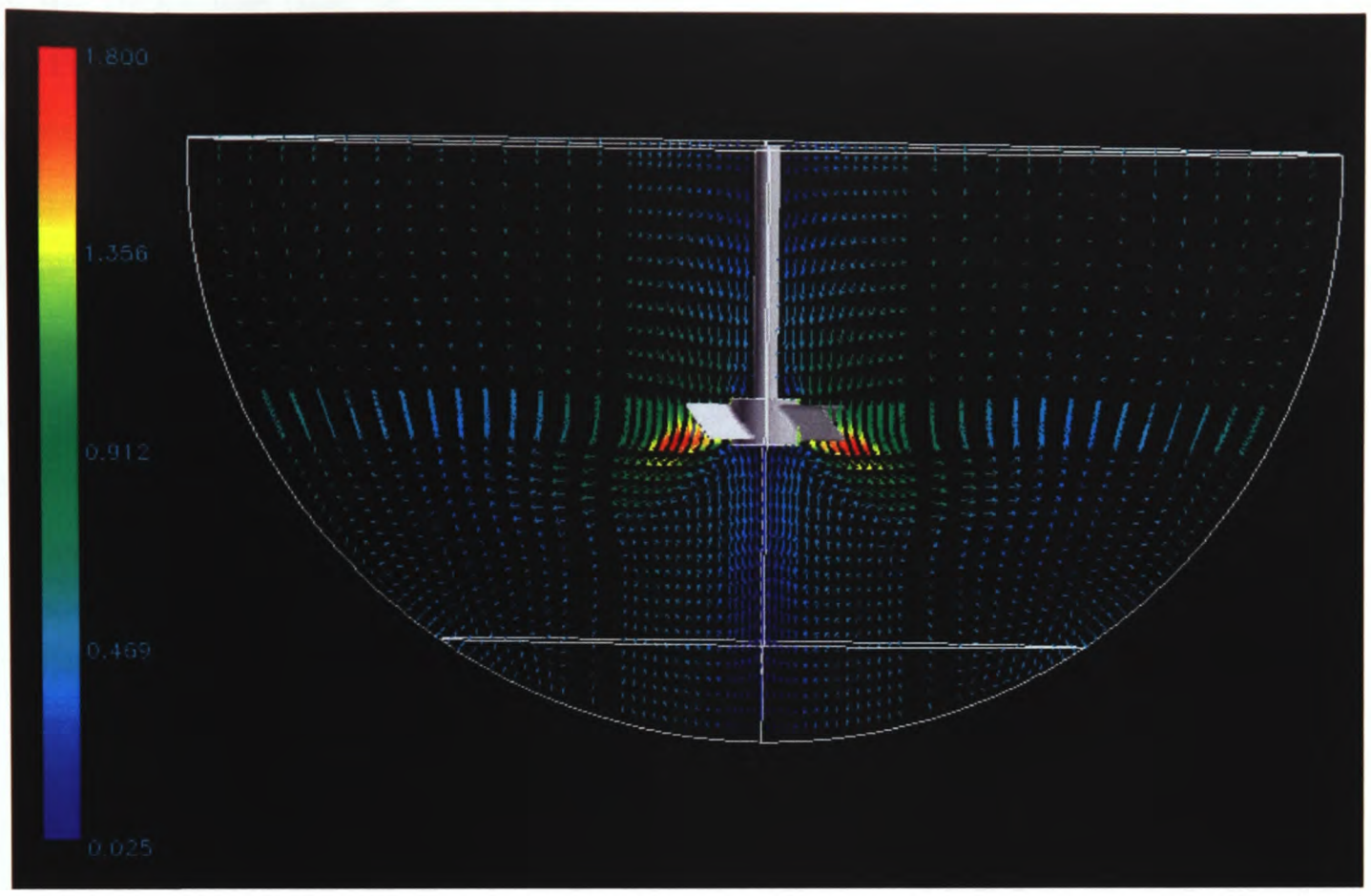

Figure 6.6: Velocity Vectors in the Vertical Plane of Unbaffled Water Model

downward towards the kettle wall. A zone of very low velocity can be observed in the region just beneath the impeller along the axis of symmetry and the magnitude decreases as we go towards the bottom of the kettle. This is also experimentally observed in the water model. This is the region where particle and bubbles remain trapped for relatively longer periods. It is also visible in the picture that the jet from the impeller forcing the fluid to undergo re-circulation by splitting it into two zones where one re-circulation zone is above the impeller and second below the impeller. However, most of the velocities point towards the perpendicular to the vertical plane and hence, indicate dominance of circular motion around the axis of symmetry. This signifies that a large amount of solid body motion is taking place in comparison with vertical re-circulation. This was also observed for the real lead refining kettle simulation results.

Figure-6.7 shows the velocity profile at the top surface and through the kettle. It is obvious from the figure that fluid is strongly moving in circular motion around the impeller shaft. From Figure-6.6 & 6.7 it can be concluded that in the unbaffled water model a large solid body rotation takes place that results in poor mixing performance. This is also observed in the experiment on the water model. This solid body rotation of fluid, after a certain period of time, gives rise to instabilities in the fluid bulk where it starts to oscillate laterally. This swirling motion causes water to spill over the kettle rim. It should be noted that when running a lead refining kettle with a central shaft similar swirl motion also occurs. This is one of the reasons for using off-centred shaft-impeller position while stirring lead bullion.

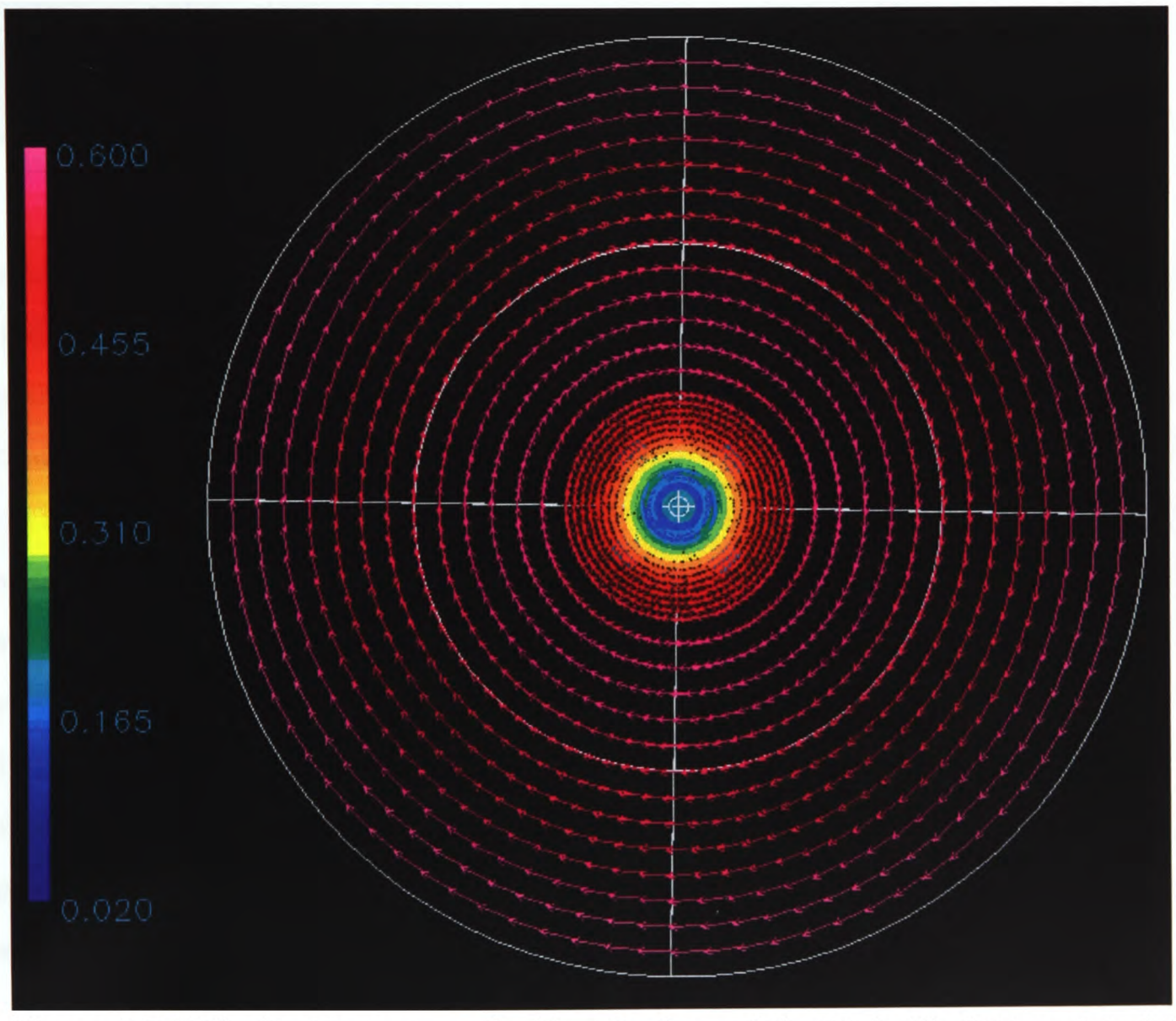

Figure 6.7: Velocity Vectors on the Top Surface of the Unbaffled Water Model

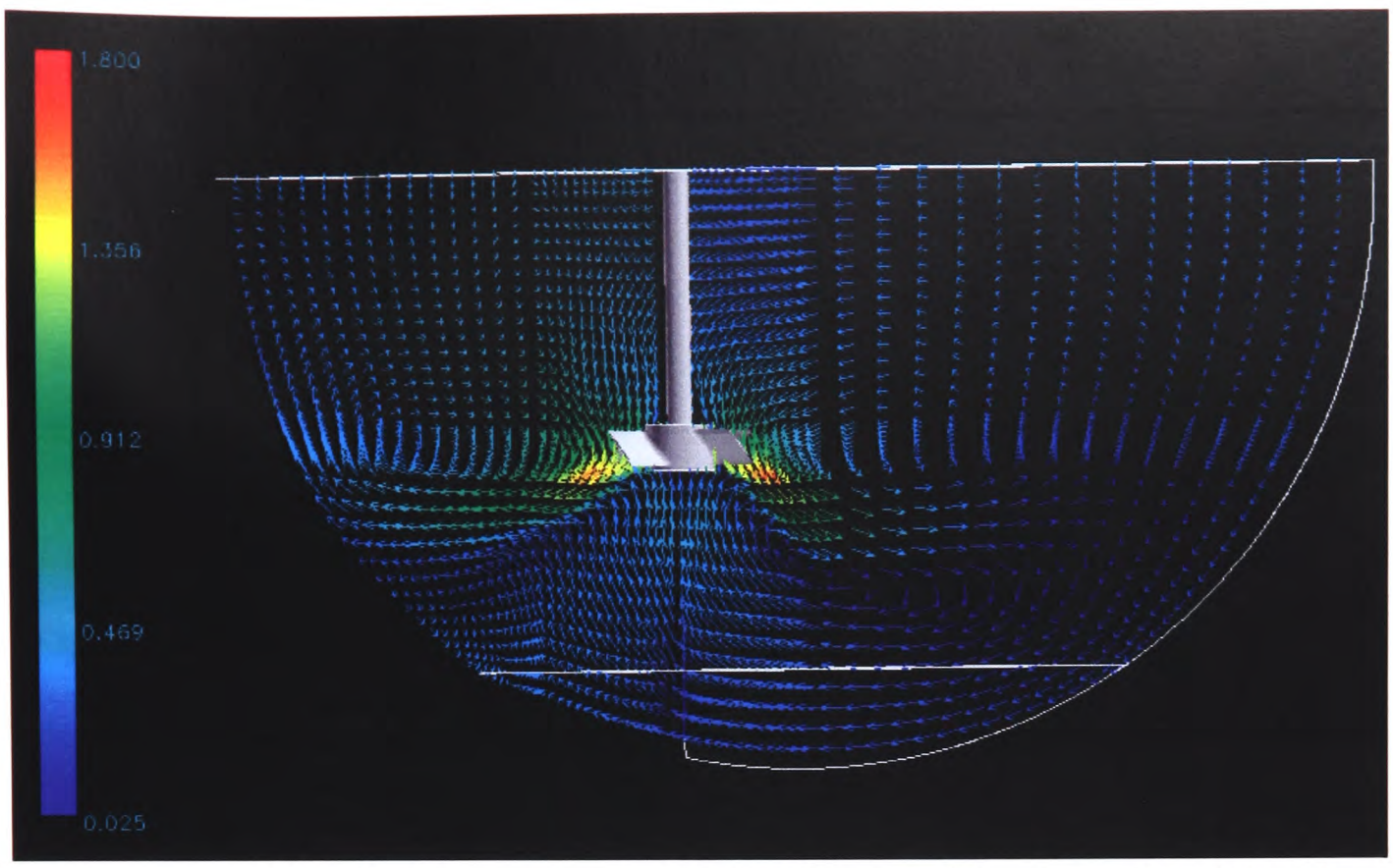

Figure 6.8: Velocity Vectors in the Vertical Plane of the Water Model with Off-centred Shaft

Figures-6.8 shows the velocity profile in the vertical plane through the kettle with an off-centred shaft position. We can clearly see the angled jet shooting out from the impeller and the pattern is similar as it is observed in the case of unbaffled set-up (Figure-6.6). However, the magnitude of jet velocity (by comparing the colour of vector with given colour scale) is less in this case. It is because in this case more energy is consumed in driving the fluid than in the unbaffled (centred shaft) case. It is also evident that vertical re-circulation zones, one above and one below the impeller, are present both in left and right side of the kettle (shaft is positioned at 0.2m left away from the centre). At the same time it is also apparent that rotational motion is higher on the left side. However, the overall solid body motion is less dominant than unbaffled (centred shaft) case. The off-centre positioning of shaft suppresses the surface swirl and hence, more mixing can be achieved using the higher impeller speed.

Figure-6.9 shows the velocity profile on the top surface of the water model. The general trend of velocity vectors is largely circular; however, distribution of velocity magnitude is not uniform as it is found in the unbaffled (centred shaft) case. It can also clearly be seen that the zone of higher velocity is shifted toward one half of the kettle. Furthermore, the flow field shows the tendency to circulate around the central axis, where a vortex pattern with a core of zero velocity forms, of the kettle that is located away from the shaft position.

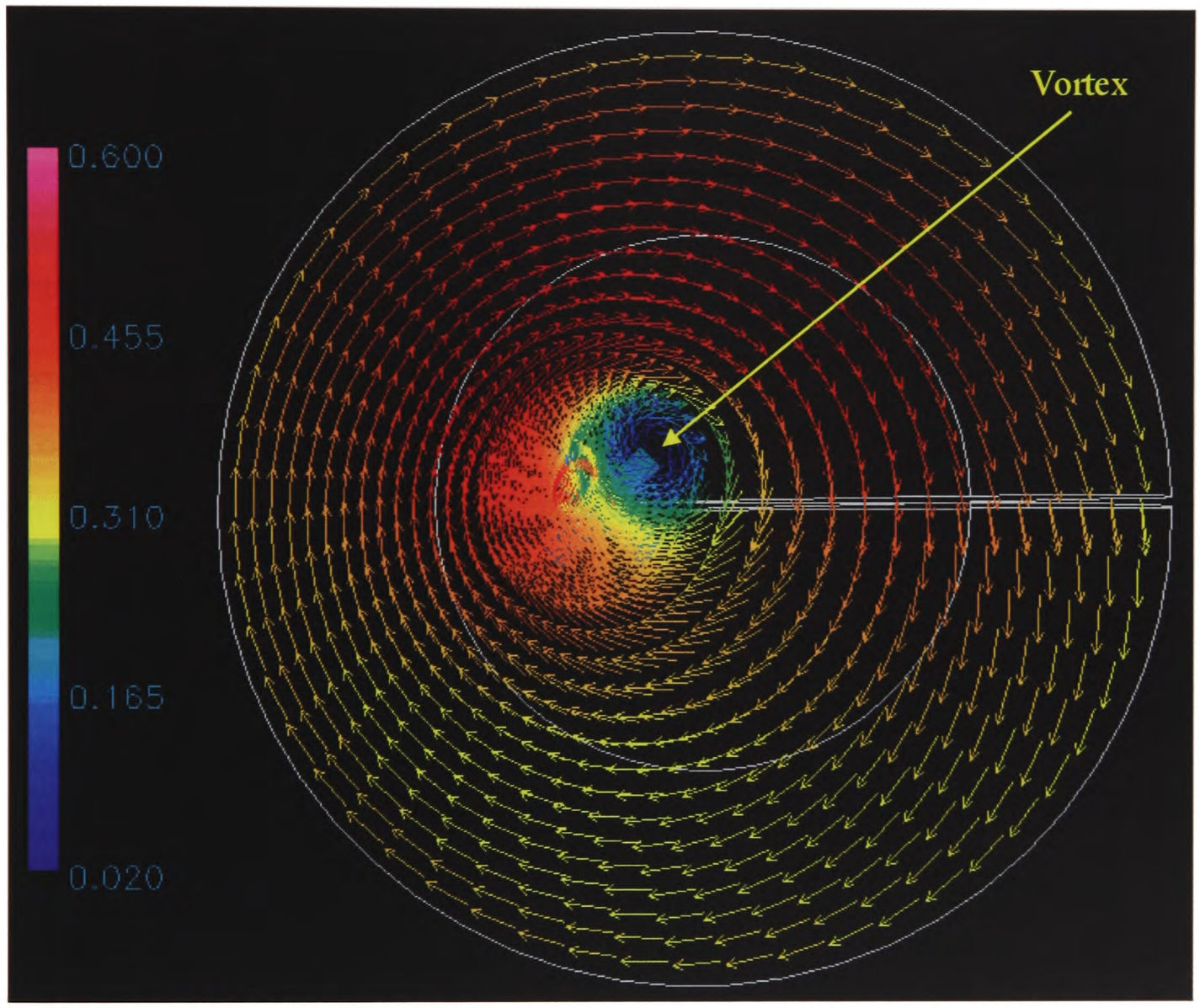

Figure 6.9: Velocity Vectors on the Top Surface of the Water Model with Off-centred Shaft

This vortex structure extends from the top surface towards the impeller. It is interesting to note that the similar vortex pattern is also observed on the experimental water model from the surface to the impeller. It is this vortex core where air is drawn into the kettle that periodically wraps around the shaft and intermittently breaks into the impeller.

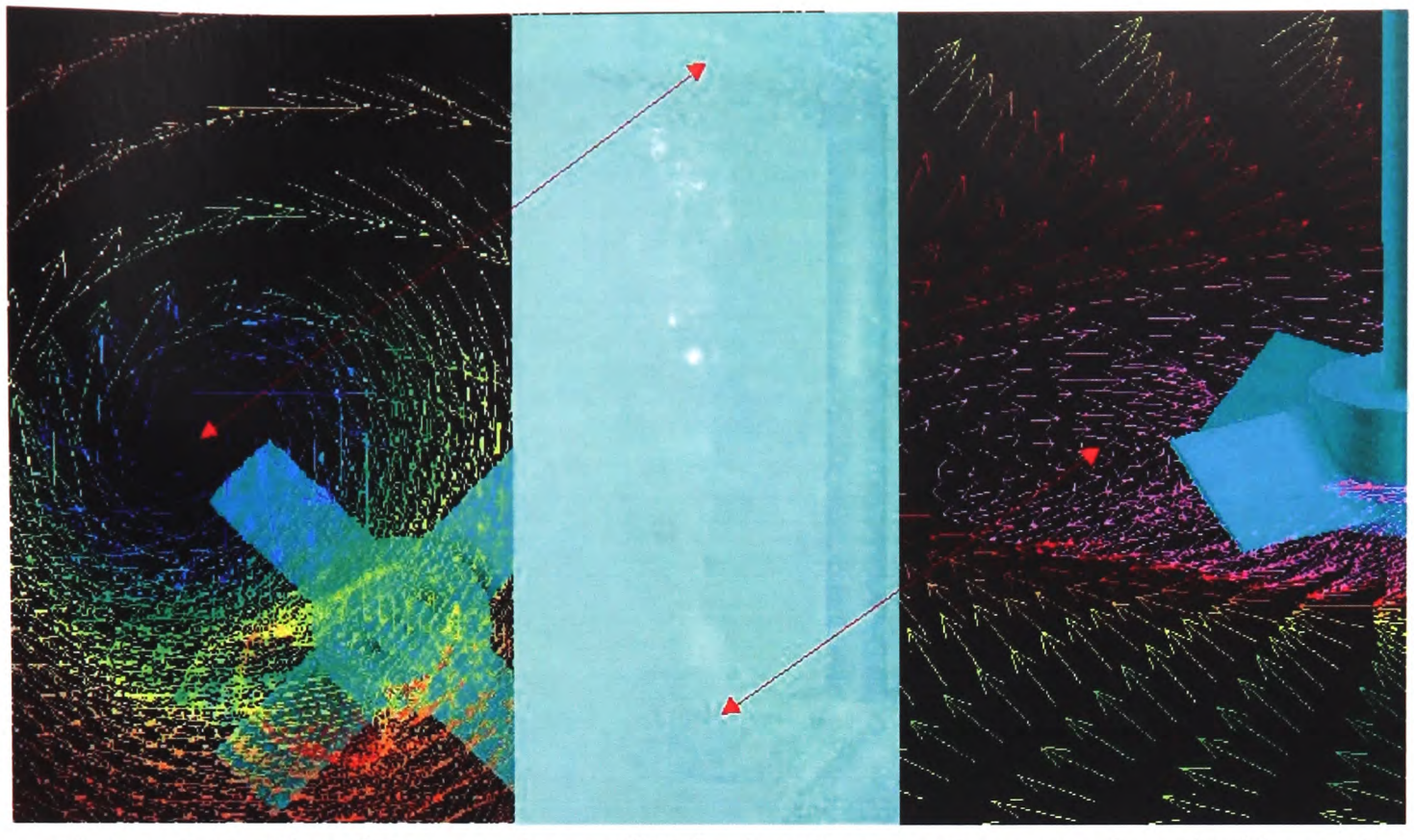

Figure 6.10: Visual Comparison of Velocity Vectors Representing the Tornado Shape Vortex Form in the Of-centred Water Model Kettle

The Figure-6.10 presents the visual comparison between experimentally observed structure and computed result. In this figure the middle picture is from the video footage taken from the water model. Left and right pictures are the computed vortex structure on the top surface and on the horizontal plane passing through the impeller respectively. It can be seen that the CFD model has successfully predicted this tornado shaped vortex structure that starts from the surface and extends up to impeller. Although in reality this phenomenon is highly transient, this result can be regarded as time averaged value.

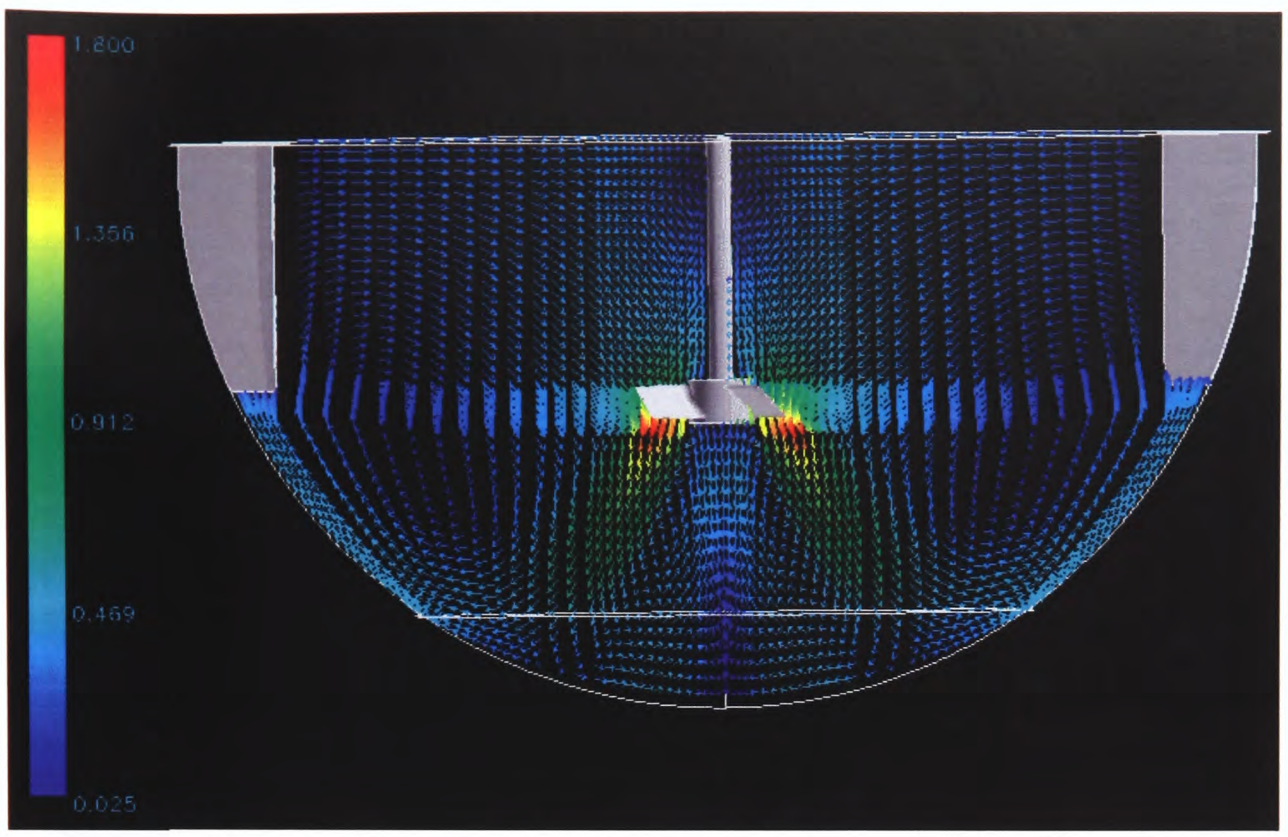

Figure 6.11: Velocity vector in the vertical plane passing through two baffled water model kettle

Figure-6.11 shows velocity vectors in the vertical plane passing through the kettle that has two side-fitted baffles. Clearly, we can see that the strong angular jet is being discharged from the impeller region that is at the wall forcing flow to split in two directions. One is moving upwards to the surface where it is being drawn towards the shaft and other one hits the bottom and then changes the direction and moves towards impeller region. These two re-circulation zones are much more dominant than what is observed in the unbaffled case using either centred or off-centred shaft. It is clear that the presence of the baffles stops the solid body rotation and forces the fluid to undergo larger re-circulation in the vertical plane and hence, good mixing.

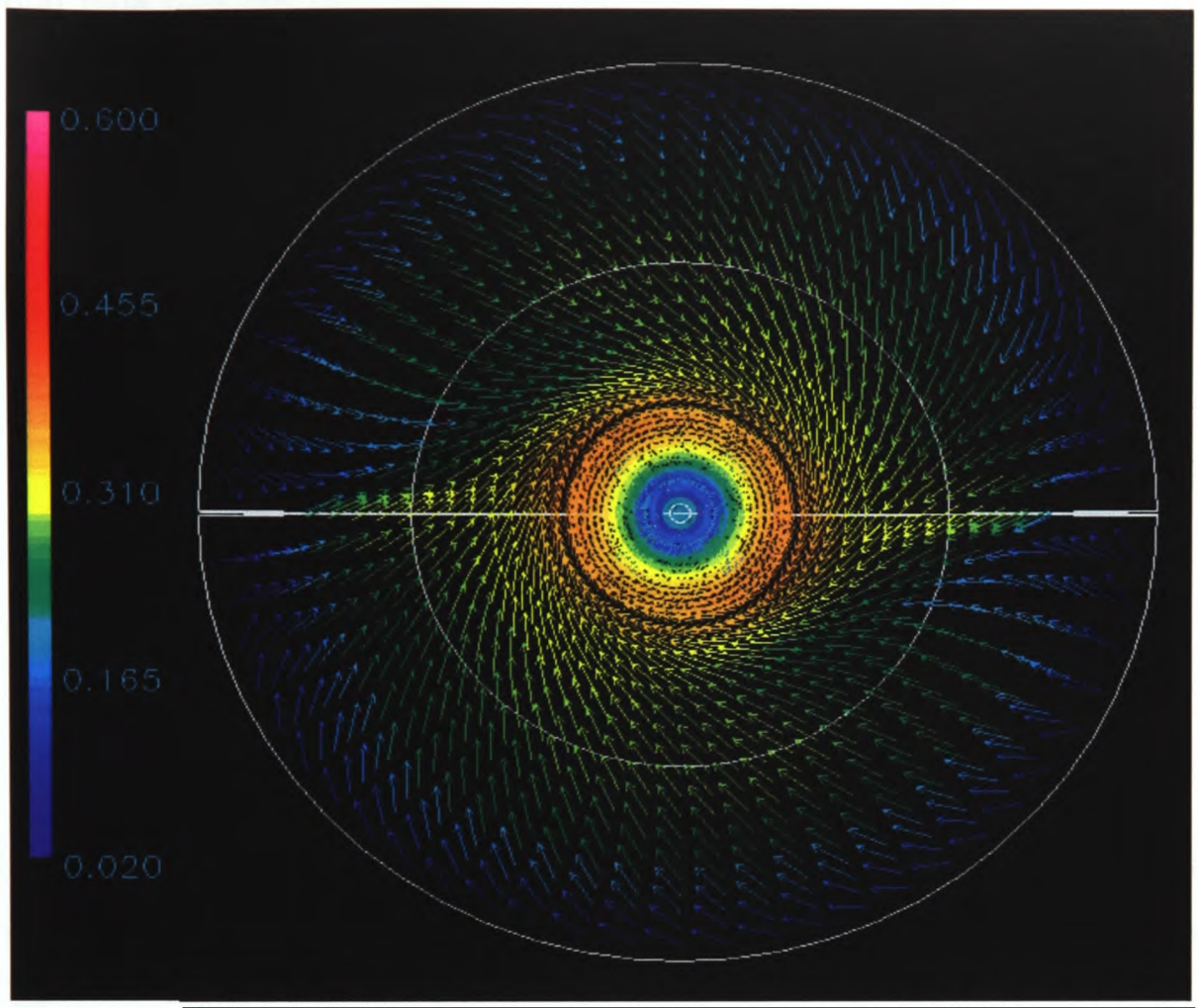

Figure 6.12: Velocity Vector on the Top Surface for Two-baffled Water Model Kettle

Figure-6.12 shows the velocity vectors on the top surface for the two-baffled kettle. It is evident from the figure that fluid is being redirected towards the shaft at the baffles. The presence of circular motion is not prominent as it is found in the unbaffled cases. The presence of a dominant vertical re-circulation field signifies good mixing. At the same time, baffles also kill the surface swirl and hence, vigorous mixing can be achieved at higher impeller speed without the danger of spilling the fluid out of the kettle. This was a major finding from both the water model and the CFD analysis. Baffles help eliminate swirl and promote good mixing.

The above presented CFD results for the water model kettle are compared with the corresponding experimental results (see the Chapter-4 for the details of experiment). The experimental data that are presented here are taken along vertical line V1 and horizontal

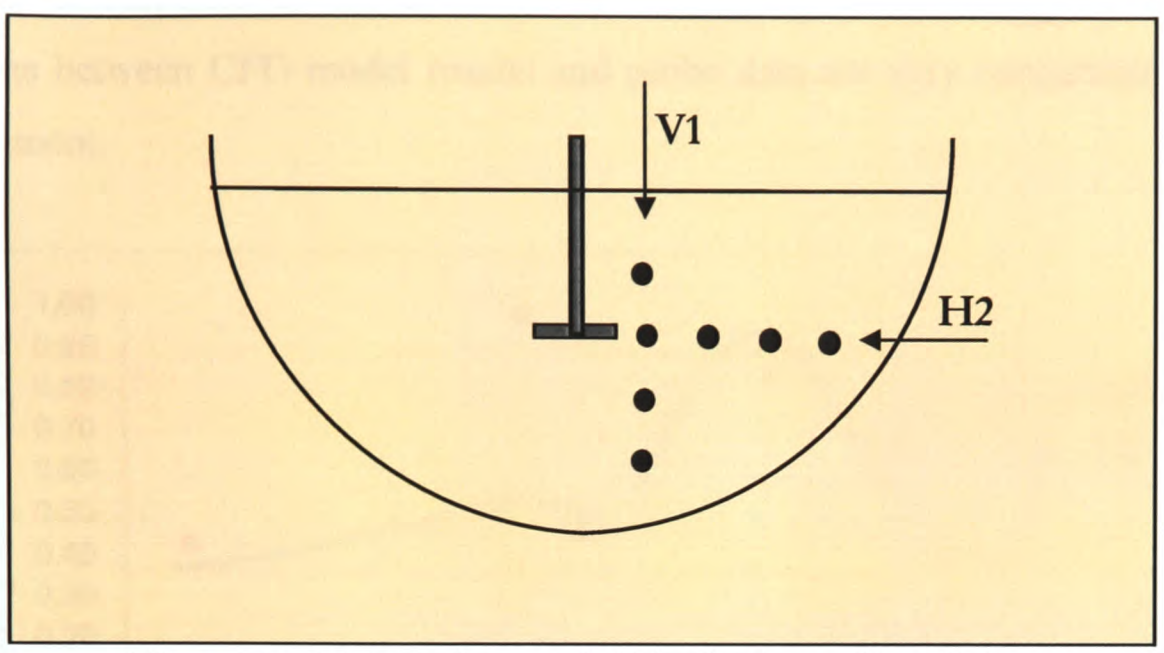

Figure 6.13: Experimental Velocity Sampling Points

line H2 (see Figure-4.11 of Section-4.6 for the detailed description of these experimental velocity sampling points). For the sake of clarity, these are illustrated again in picture Figure-6.13.

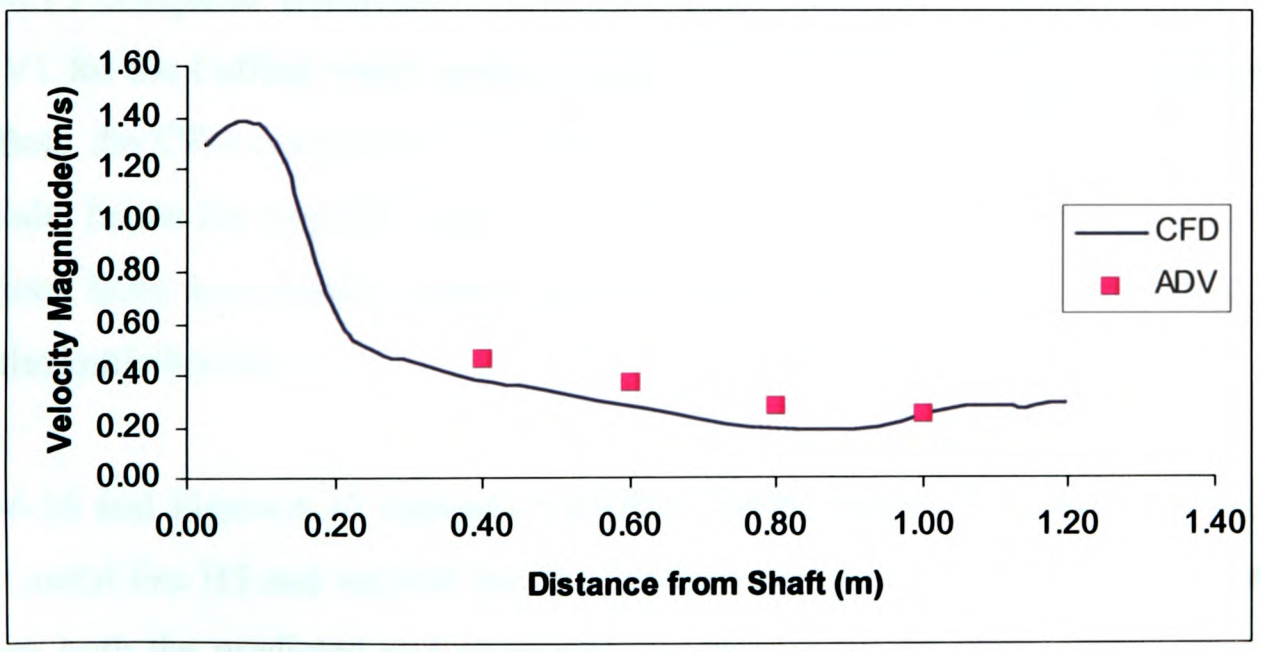

Figure 6.14: Comparison of CFD & Probe Velocities along Horizontal Line (H2) for the Baffled Water Model

Figure-6.14 compares the CFD results for velocity along the horizontal line H2 originating near the impeller and ending near the kettle edge. As expected, near the impeller region the velocity is at its highest and then drops off sharply away from the blades. This region close to the shaft corresponds to the downward jet region observed in Figure-6.11. Clearly, comparisons between CFD model results and probe data are very encouraging and show close agreement.

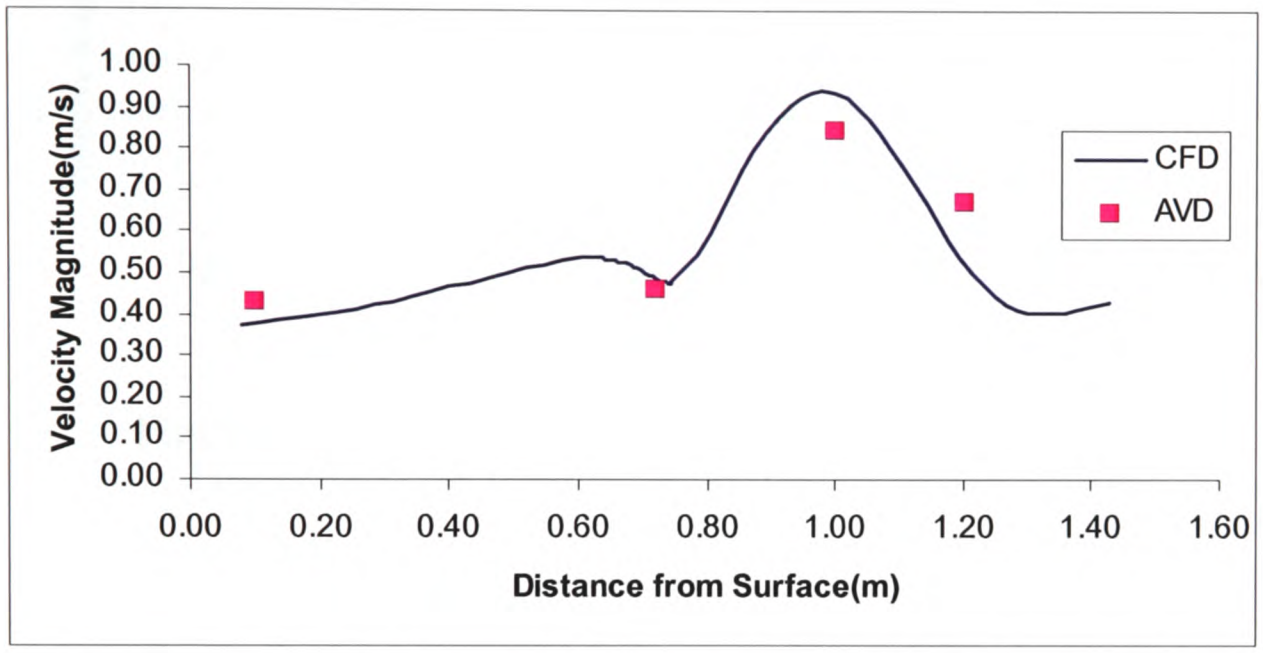

Figure 6.15: Comparison of CFD & Probe Velocities along Vertical Line (V1) for the Baffled Water Model

Figure-6.15 compares computed results with experimental data along vertical sampling points V1 for the baffled water model. Again, we can clearly see that comparison is very good. Both the CFD computation and the probe readings capture the peak in the velocity magnitude, below the impeller approximately one-meter from the kettle surface. The CFD predictions have successfully picked up the flow velocities nearer the surface and also nearer the kettle bottom.

Figure-6.16 and Figure-6.17 compare the CFD results with the gathered probe data along the horizontal line H2 and vertical line V1 for the water model without baffles respectively. Although both the predicted and measured results pick up the same trends, there is some degree of discrepancy between the data especially close to the shaft and the bath surface. Cause for this deviation can be attributed to both the experimental measurement and approximation applied to the CFD model. It is believed that the large amount of swirl

brings more random errors into the measurements. In the CFD model the surface swirl and vortex formation phenomena have been neglected at this stage, and free surface is approximated as shear free flat surface.

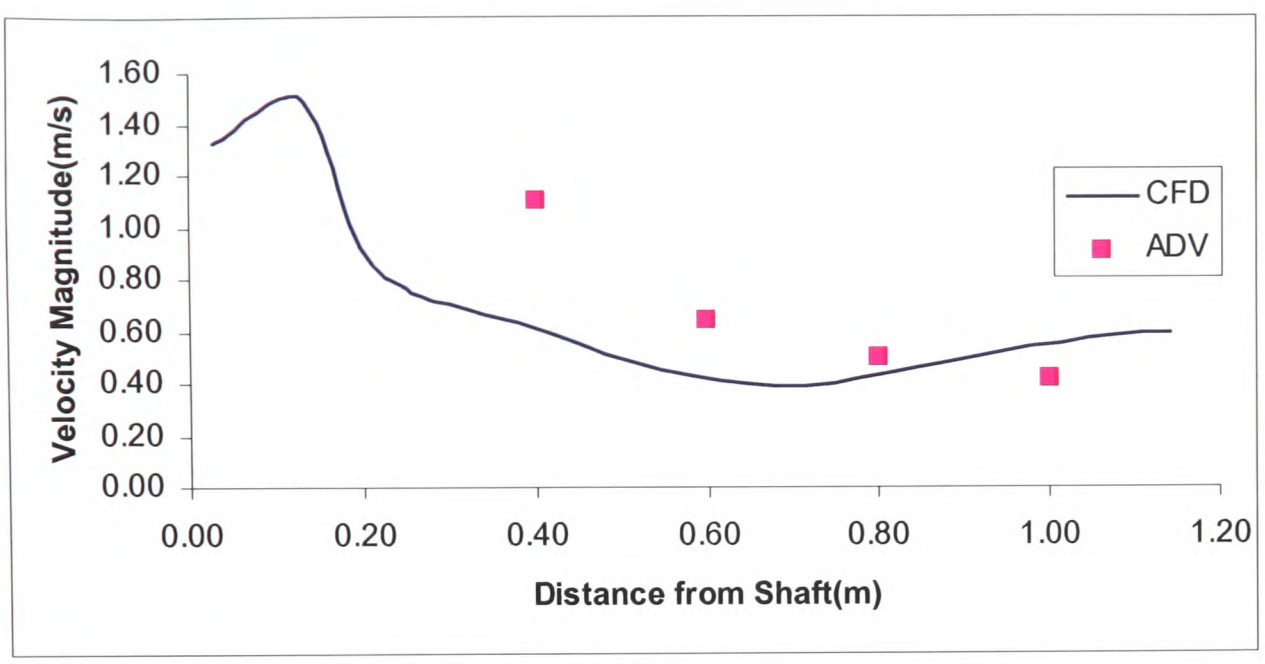

Figure 6.16: Comparison of CFD & Probe Velocities along Horizontal Line (H2) in the Unbaffled Water Model

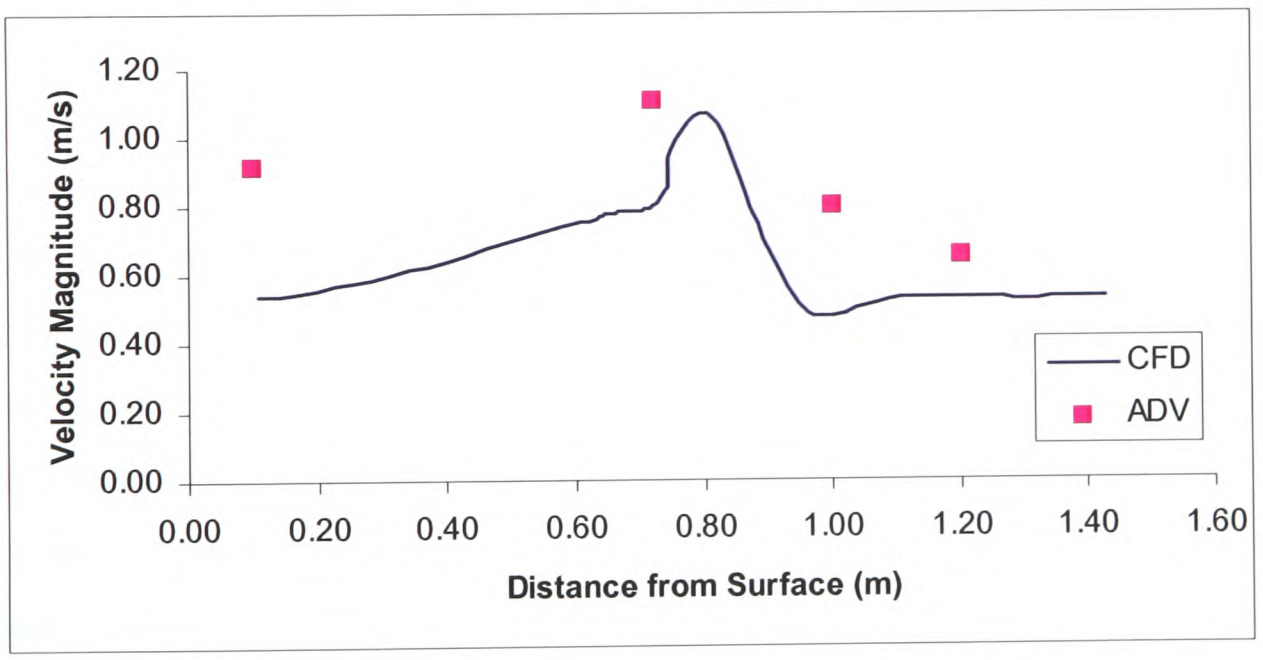

Figure 6.17: Comparison of CFD & Probe Velocities along Vertical Line (V1) for the Unbaffled Water Model

6.4 Modelling of the Vortex Formation

Most of the published work on vortex formation in stirred vessels is based on the simplified theoretical analysis and experimentally determined empirical models. For the cylindrical shaped unbaffled vessel equipped with flat blade impeller an equation describing the vortex

geometry can be derived on the basis of Nagata Model [50]. APPENDIX-B gives an overview of this method. This model is based on the tangential fluid velocity distribution in the vessel and requires knowledge of the radius of the boundary between the forced vortex (the central region of fluid which undergoes rigid body motion with the rotational speed of impeller) and the free vortex (the rest of the fluid region which has constant angular momentum). This radius can be calculated from experimentally measured vortex depth and liquid elevation at the vessel wall.

On the basis of extensive experiments, [103] developed correlation equations to calculate vortex depth under various operating conditions. [104] developed correlation equations for the vessel with drainage at bottom that is being stirred by means of an anchor impeller. More recently, [64] presented an extensive literature review on the correlation equations to determine the vortex depth and proposed an improved model for the vortex geometry. However, none of the above mentioned methods are applicable and/or validated for the industrial scale hemispherical shaped vessels.

Very limited work has been carried out for the CFD modelling of free surface in impeller-stirred tanks. This is mainly because most of the CFD application for impeller-stirred tank so far has been focused on baffled tanks. Baffles are used to inhibit the central vortex formation and hence, free surface can be approximated as a flat no-shear boundary [105]. However, when vortex formation becomes significant then an appropriate computational modelling technique is required. First published work [106] in this field applied interface-tracking method using surface adaptive grid to model the free surface for unbaffled vessels. The main drawback of this approach is that when the free surface undergoes large deformation, for example very deep vortex, the mesh becomes too skewed and gives rise to solution difficulties. Also, this method can not be used to model the vortex break-up and air entrapment.

The following section describes the present CFD modelling strategy adopted to simulate the free-surface deformation (vortex formation) taking place in the kettle. The theoretical background is already presented in Section-5.5.4.3.

6.4.1 Strategy for CFD Modelling of Vortex Formation

The Volume-Of-Fluid (VOF) method [80] is applied to simulate the vortex formation in the refining kettle. Basically, the VOF method computes the shape of free surface transiently. Combining this with a three-dimensional CFD model for impeller-stirred mixing would require a huge computer resource. In this situation, any parametric study with a number of operating conditions would be prohibitively costly. To resolve this limitation the present study uses blade element theory based impeller model [23] (see Section-2.1.2 for details and Appendix-A) to reduce the three-dimensional model to two-dimensional axisymmetric model. By combining this model with the VOF [86] method, we can compute the vortex shape economically.

6.4.1.1 Simulation Results for Vortex Formation

All of simulations are carried out to calculate the vortex shape during impeller stirring of fluid. This is performed using a two-dimensional axisymmetric model that combines the

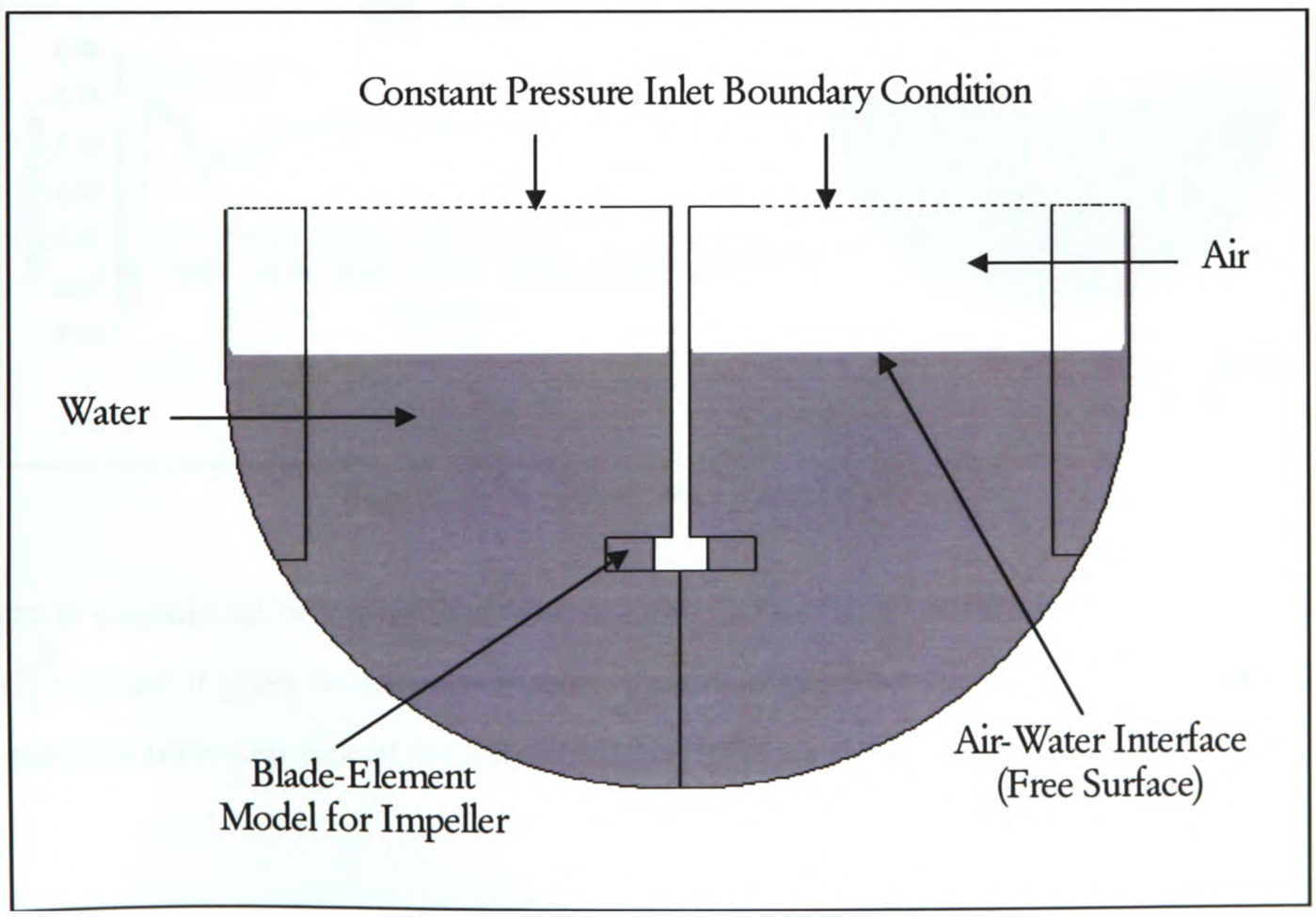

Figure 6.18: Model Setup for Calculating Vortex Shape

source/sink technique for impeller/baffle (see Section-2.1.2 for details), that is implemented through user subroutine, and the VOF method to calculate the free surface deformation. Vortex shapes are calculated for the two baffled water model with 0.75 m deep shaft and 45^0 angled four bladed impellers for three different rotational speeds - 110, 140 and 170 rpm. Figure-6.18 shows the model set up where we can see that computational domain has been extended to include a portion for air too. The top surface is considered to be open to the atmosphere and hence, a constant pressure inlet boundary condition is applied there.

The VOF technique essentially calculates the evolution of the vortex shape at every time step but in reality we are only interested in the time averaged final shape. The decision about the final shape of vortex is taken by monitoring the fluctuation in axial velocity at a certain location within the fluid bulk. After initial fluctuations, the velocity field reaches equilibrium and then the vortex shape and axial velocity become constant. From Figure-6.19, it is clear that axial velocity becomes constant after 80 seconds, hence the vortex

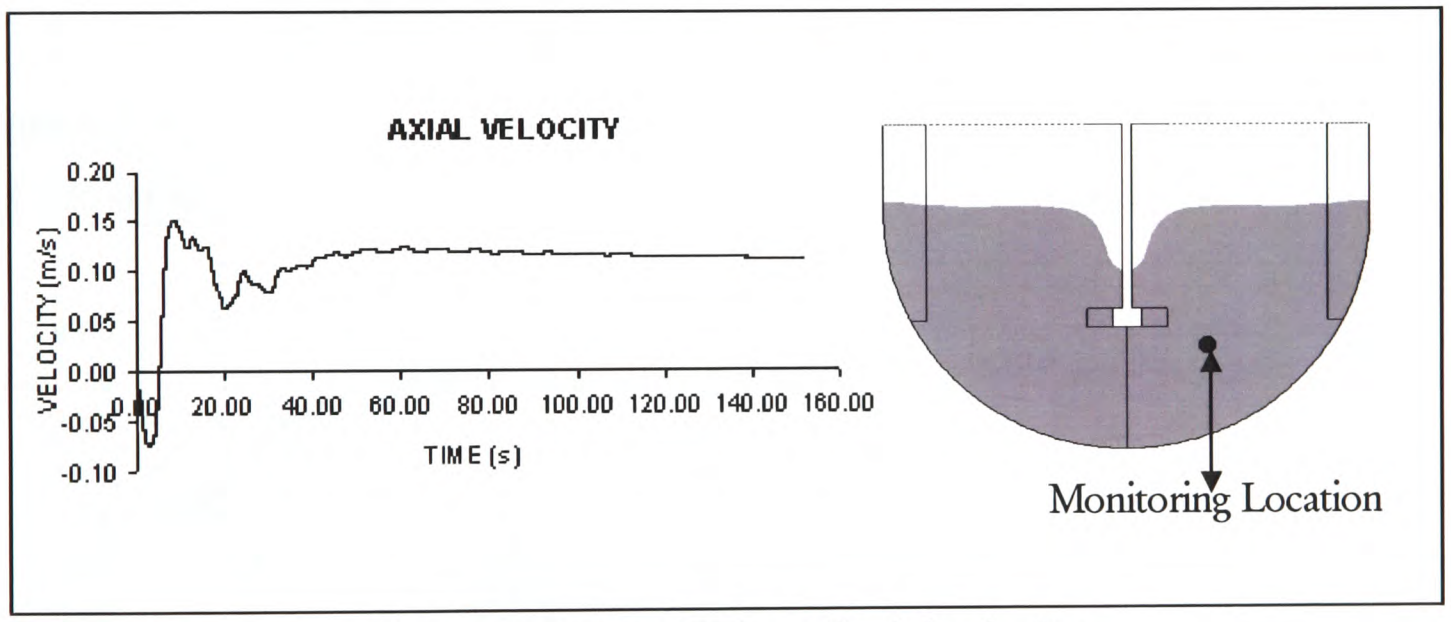

Figure 6.19: Monitoring of axial velocity

shape is considered being its final shape. This simulation uses RNG k-ε turbulence model [107] because it gives better convergence than standard k-ε turbulence model. For all these simulations time step size of 0.05 second is used for calculation.

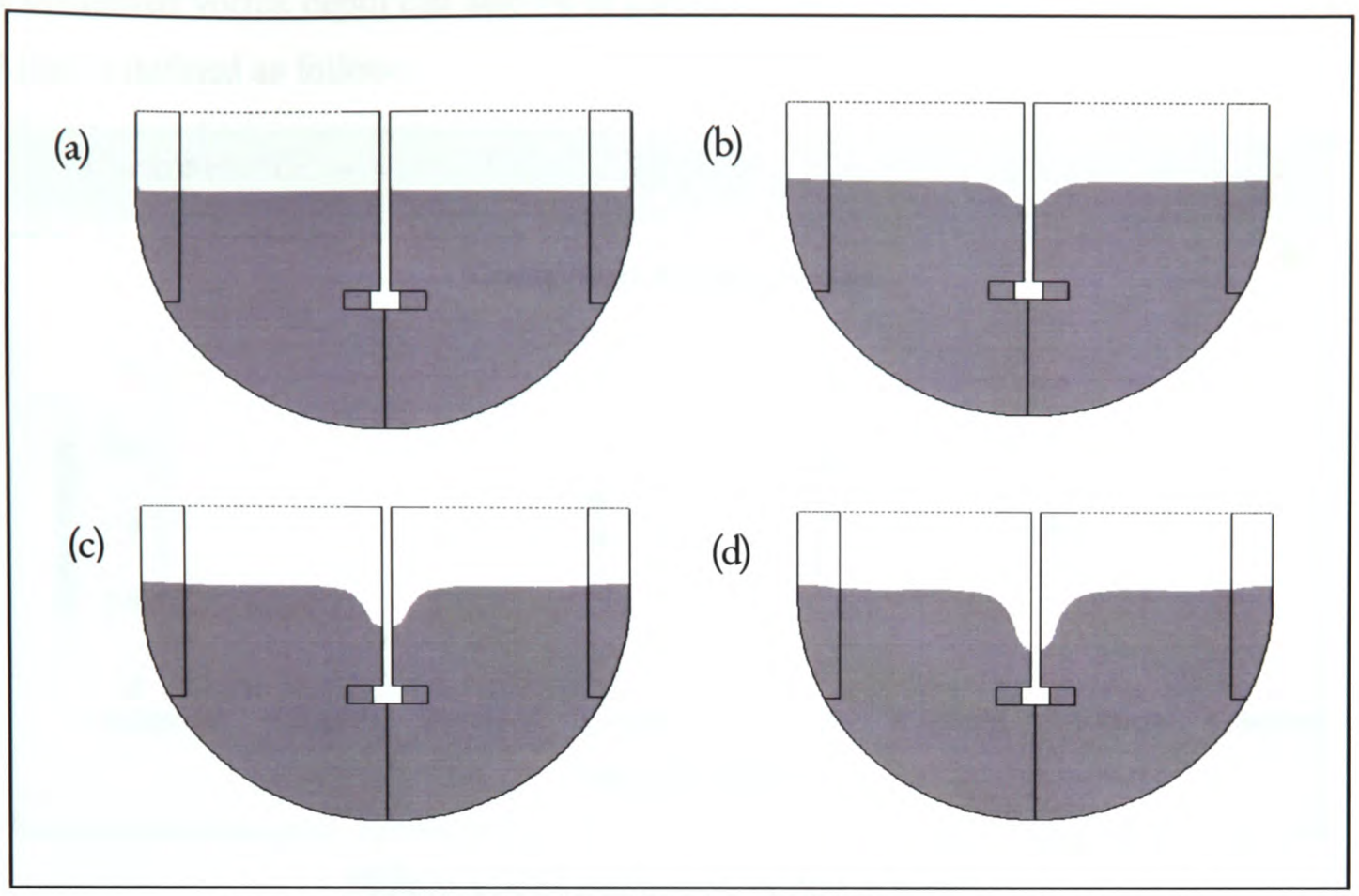

Figure 6.20: (a) Initial surface level, (b) Vortex at RPM = 110, (c) Vortex at RPM = 140, (d) Vortex at RPM = 170

Figure-6.20 shows the final vortex shapes for various impeller speeds (110 RPM, 140 RPM and 170 RPM). Figure-6.21 presents these vortex shapes in graphical form. As expected,

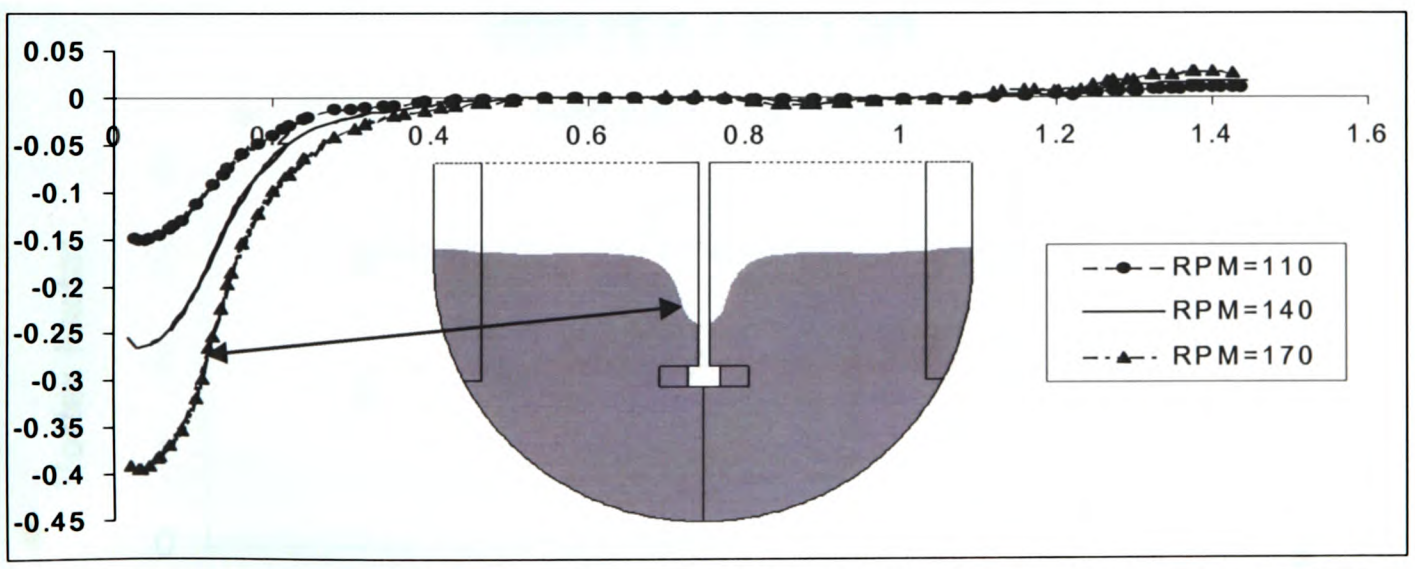

Figure 6.21: Quantitative Comparison of the Vortex Shape for Various RPM

the vortex depth increases with increasing impeller speed. Data from this graph is used to generate a three-dimensional mesh for the full three-dimensional flow field calculations.

The computed vortex depth can also be expressed in terms of a dimensionless vortex factor and that is defined as follow

Vortex Factor = Vortex Depth /(Impeller Diameter × Froude Number)

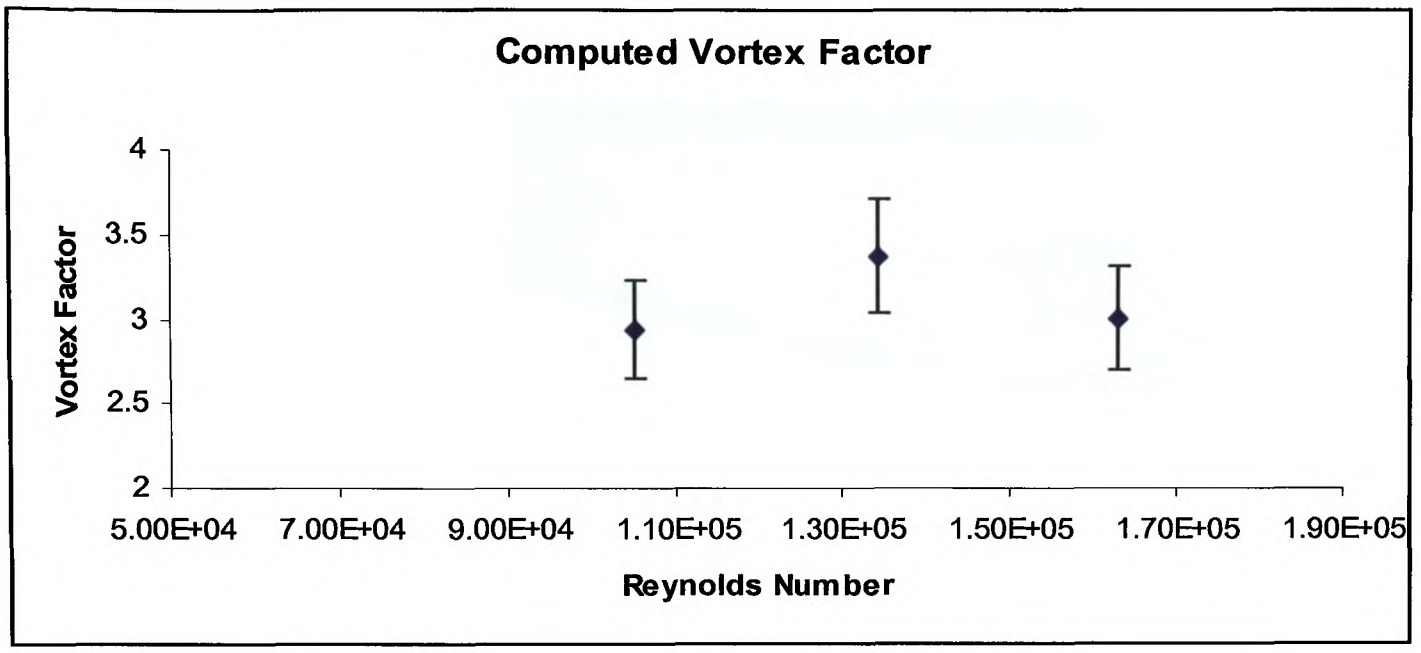

Figure 6.22: Computed Vortex Factor

Based on the experimental results it was assumed (as a first approximation; see Section-4.5 and Figure-4.8) that the vortex factor becomes constant above Reynolds numbers of 10^5. The computed vortex factor, Figure-6.22, also shows the similar pattern within 8% error.

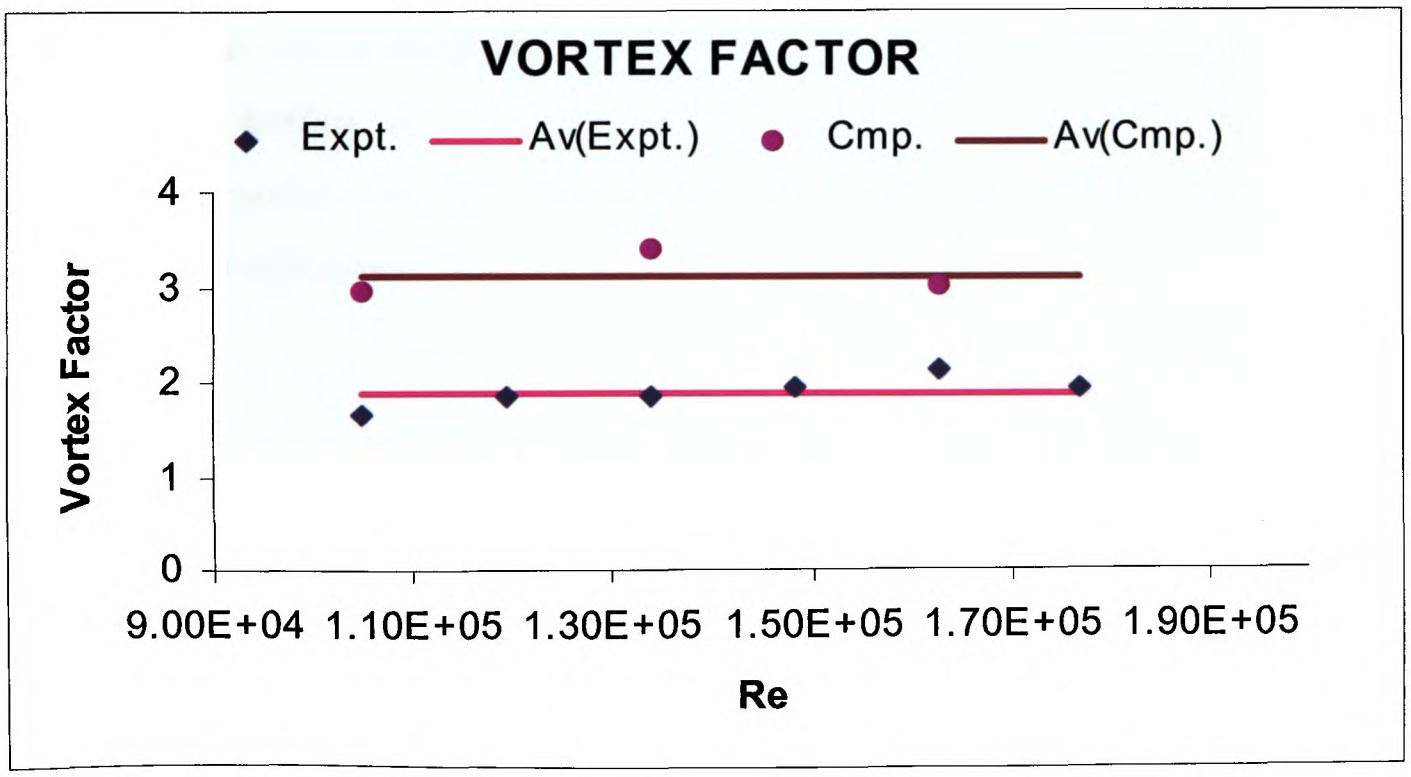

Figure 6.23: Comparison - Experimental and Computed Vortex Factors

The Figure-6.23 compares the experimental and computed vortex factors. It is clear that the computed vortex factor is consistently over predicted and on average it is about a factor of 1.24. This discrepancy can be attributed to the averaging assumption applied in CFD model to represent the impeller and baffles.

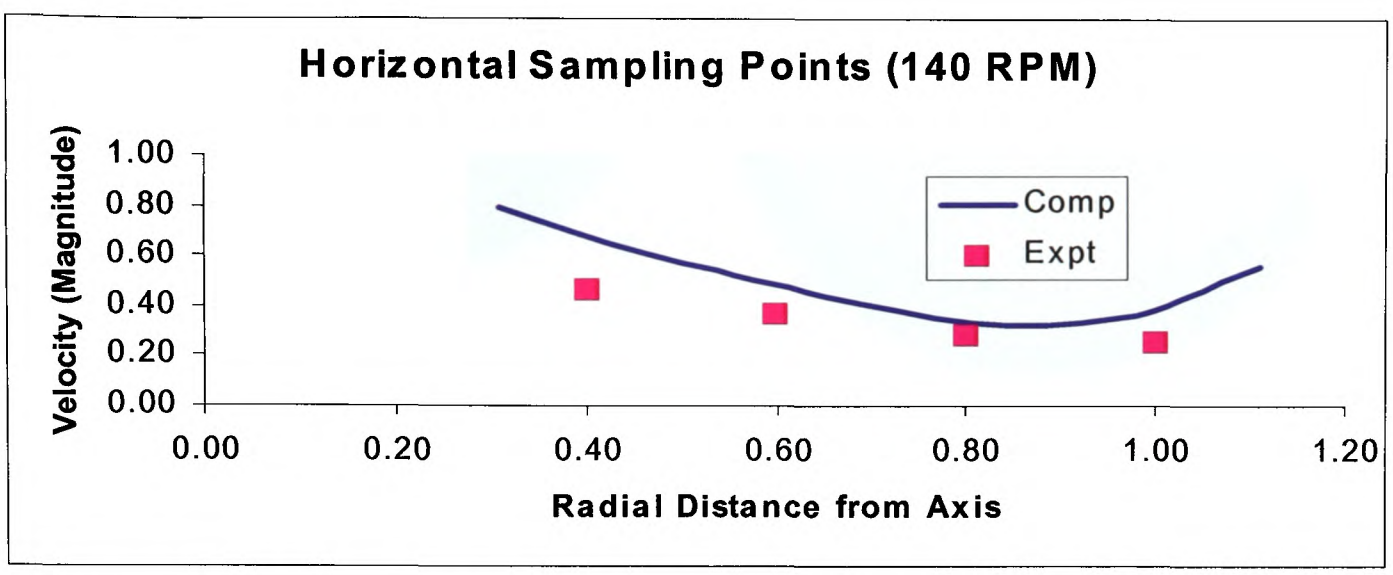

Figure 6.24: Comparison of Computed and Experimental Velocity along Horizontal Line (H2)

Figure-6.24 presents the comparison of computed velocity against measured values that shows good agreement. This establishes the capabilities of CFD model in predicting the vortex formation phenomena. However, on average the computed vortex factor is over predicted and that can be attributed to the averaging assumption applied in the modelling of impeller and baffles. As it is first attempt to model the vortex depth using this technique, the results can be considered encouraging and hence, warrants further investigation and refinement.

6.4.2 Three Dimensional CFD Model with Vortex Shape

As a representative test case, the calculated two-dimensional vortex shape, Figure-6.21, for 140 RPM is now used to regenerate a three-dimensional grid (using software GAMBIT). This grid is then used to run a full three-dimensional multiple-reference-frame based steady-state simulation. Figure-6.25 shows a full domain grid that includes the vortex shape too. In this figure the full domain is shown for the sake of clarity,

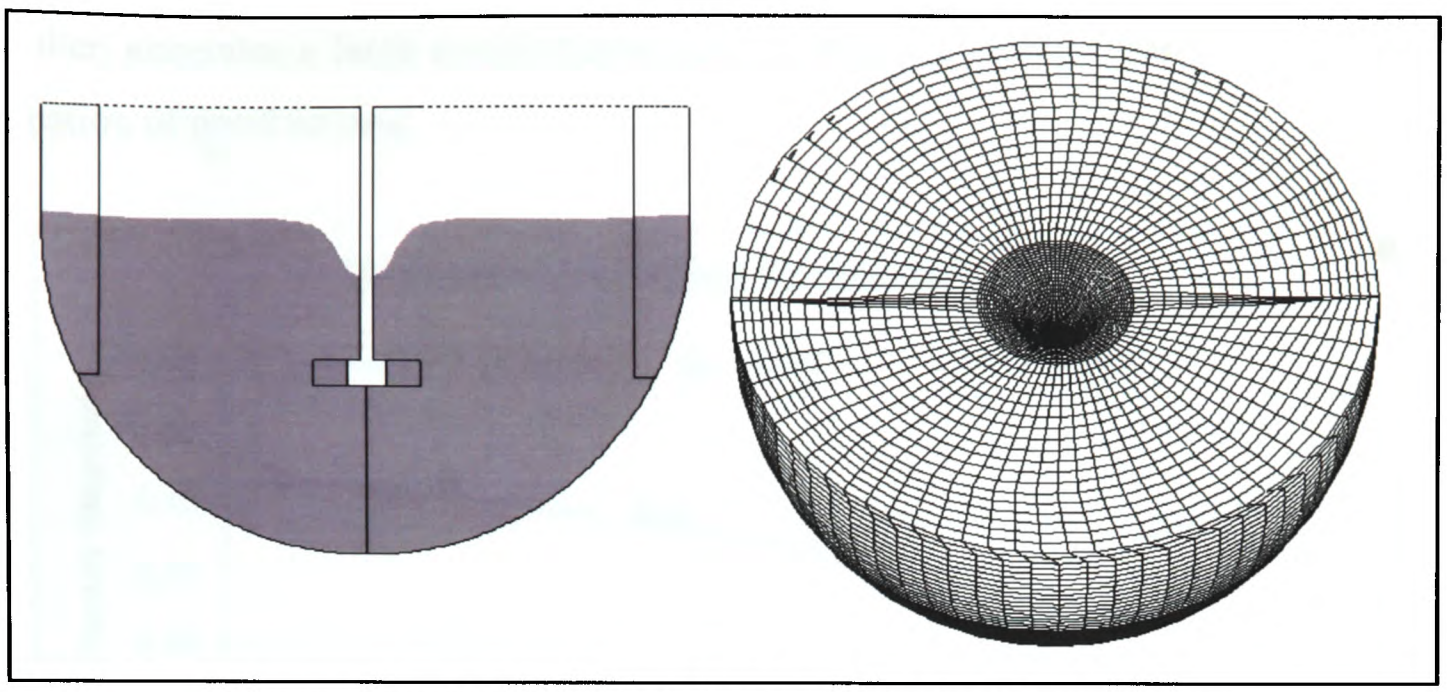

Figure 6.25: 3D Grid that also includes the Vortex Shape

however, only half of the domain is used for the grid generation owing to the geometrical symmetry. Total of 124,000 elements used for this grid. At all solid walls the no slip boundary condition is applied and the top surface is treated as no-shear surface. Furthermore, the RNG k-ε turbulence model is also used in the computation.

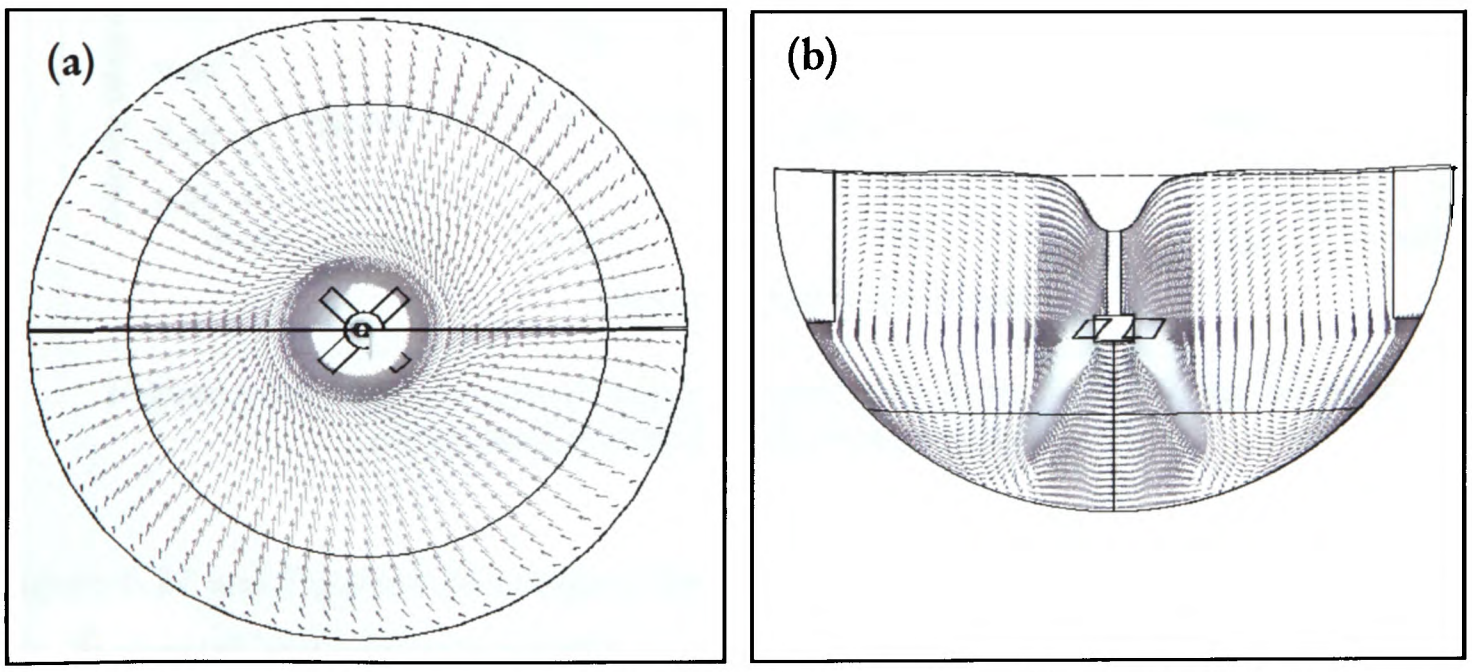

Figure 6.26: Computed Velocities (a) Top Plane (b) Vertical Plane

Figure-6.26(a) shows the flow pattern at the top surface of the kettle. It can be seen that the fluid is drawn towards the central vortex. A similar pattern was also observed on the water model experiment. Figure-6.26(b) shows the flow pattern on the vertical plane

passing through the kettle. Here it is evident that the baffles redirect the flow downwards and then generates a large re-circulation zone in the bulk region. This flow pattern is an indication of good mixing.

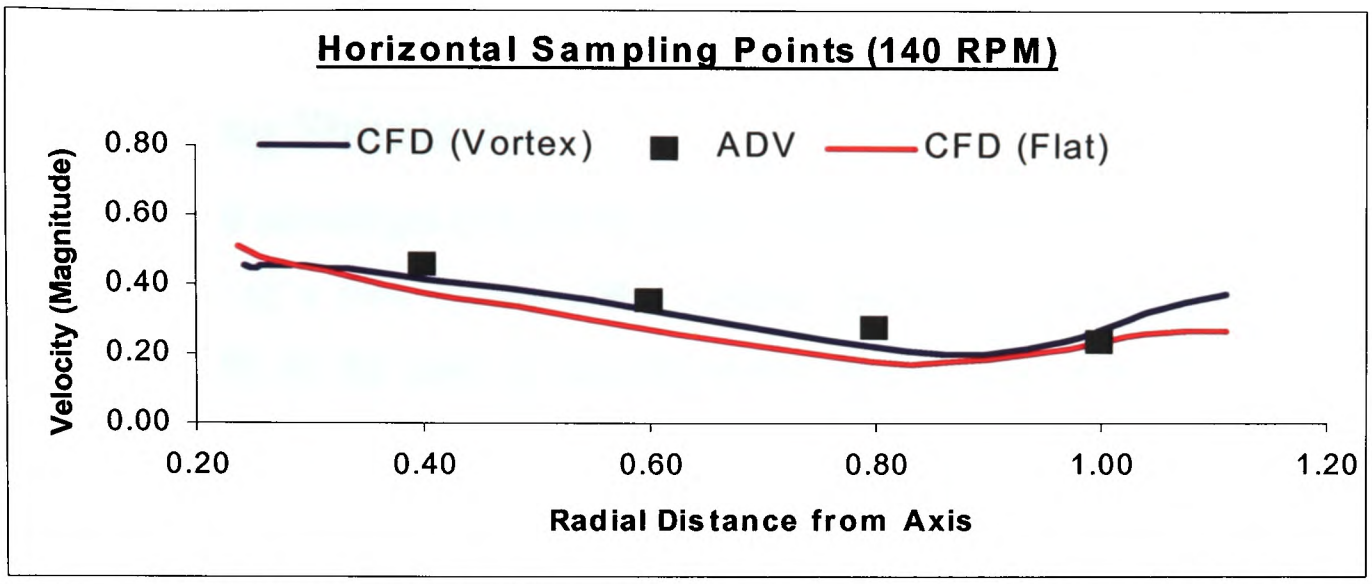

Figure 6.27: Comparison of Experimental Data along Horizontal Line H2 with Computed Results for 3D Model with Vortex

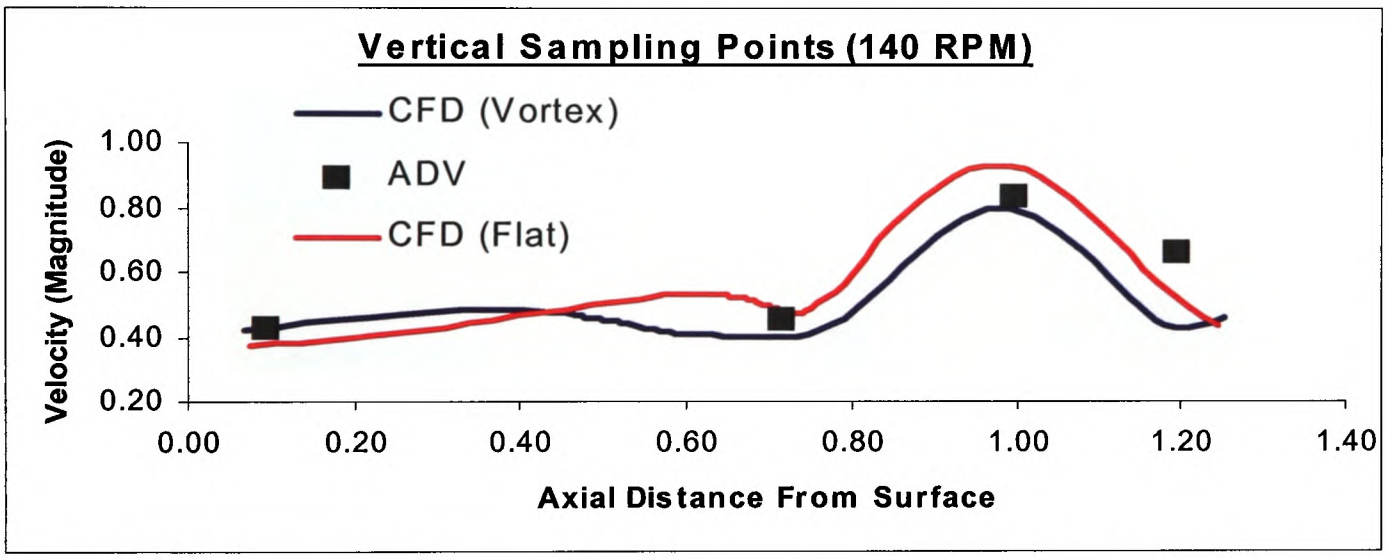

Figure 6.28: Comparison of experimental data along vertical line V1 with computed results for 3D model with vortex

Figure-6.27 and Figure-6.28 compare the CFD results with the velocities measured along the horizontal and vertical sampling points respectively. In these figures blue curves represent velocities for CFD model with vortex shape and red curves represent CFD model with flat surface approximation. There is an excellent agreement between computed results with experimental data along horizontal line. Along vertical line too computed results in general agree very well with experimental data, however, there is a slight discrepancy in vertical line at the lower section. From this validation it can be

concluded that accuracy of computed results have improved by incorporating the vortex shape into the model. The further improvement can be achieved by using more accurate vortex shape.

6.5 Blending Simulation

One of the biggest advantages of CFD modelling is that it can provide the opportunity for a parametric study of a flow system under various operating conditions. The parametric study, using CFD, in the case of impeller-stirred mixing can provide a great deal of information regarding the flow structures in terms of velocity vectors, turbulent kinetic energy, dissipation rate, etc. However, these flow properties can only provide a very limited knowledge about the actual fluid mixing process. It is important to note that in reality the motion of the fluid material characterises the fluid mixing. Hence, detailed mixing information can be obtained only from spatial distribution (that may be evolving in time) of fluid material.

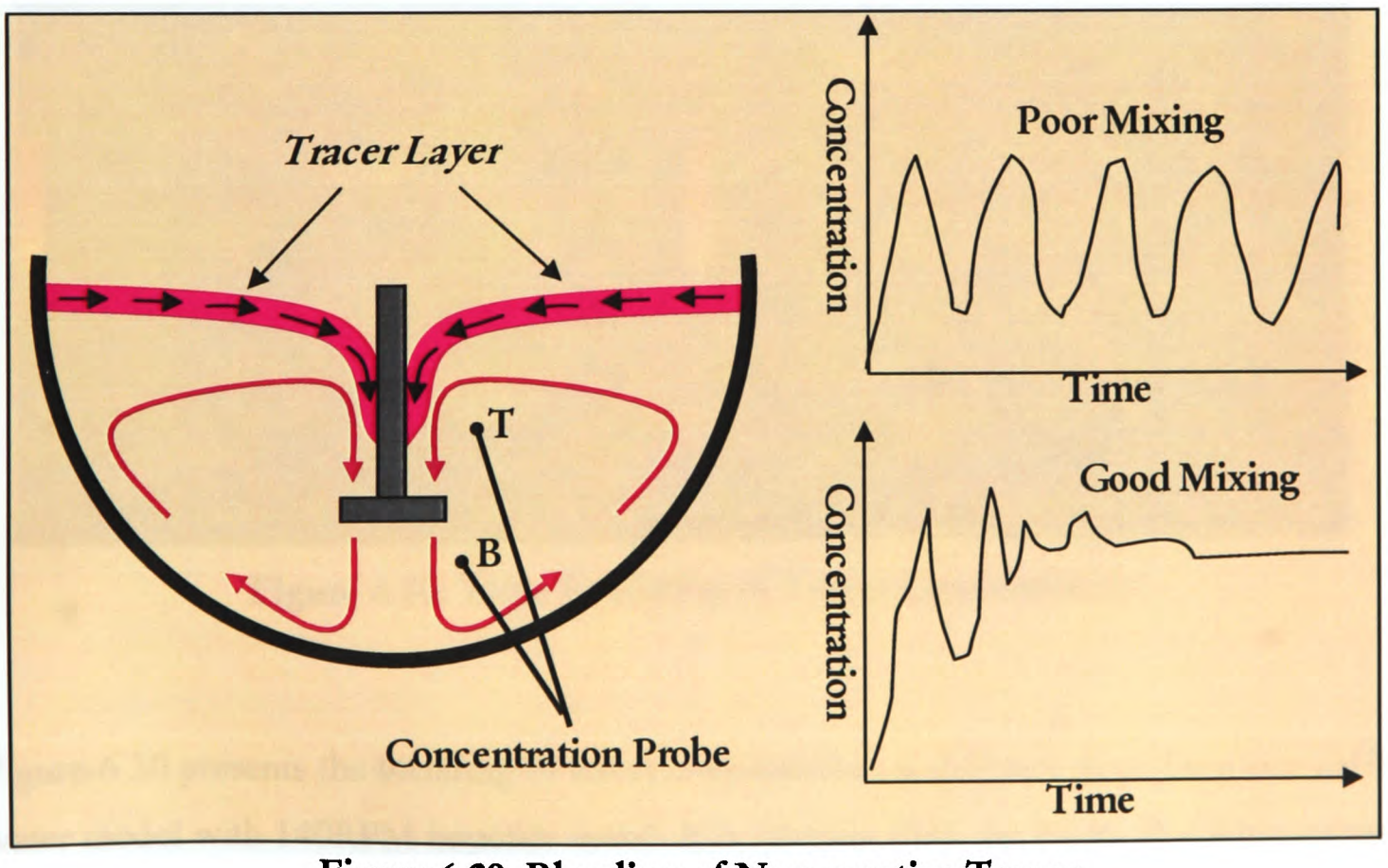

Figure 6.29: Blending of Non-reactive Tracer

Here, in order to quantify the relative mixing efficiency under various operating conditions a blending simulation technique is used. This technique is adopted from [108], where it was used to simulate the blending of reactants fed from different locations. In the present simulation strategy, first a thin layer of non-reactive tracer is introduced into an already calculated flow field (for example, flow field given in Figure-6.26). Here, the same material properties for the tracer are used as that of the main fluid. The transient blending of the tracer is then calculated by solving the discretised form of species concentration equation, Equation-5.4, where the calculated flow field for the main fluid acts like a driving medium. In addition, time evolution of tracer concentration at two locations, one above and one below the impeller are monitored. Figure-6.29 shows the schematic representation of this modelling strategy.

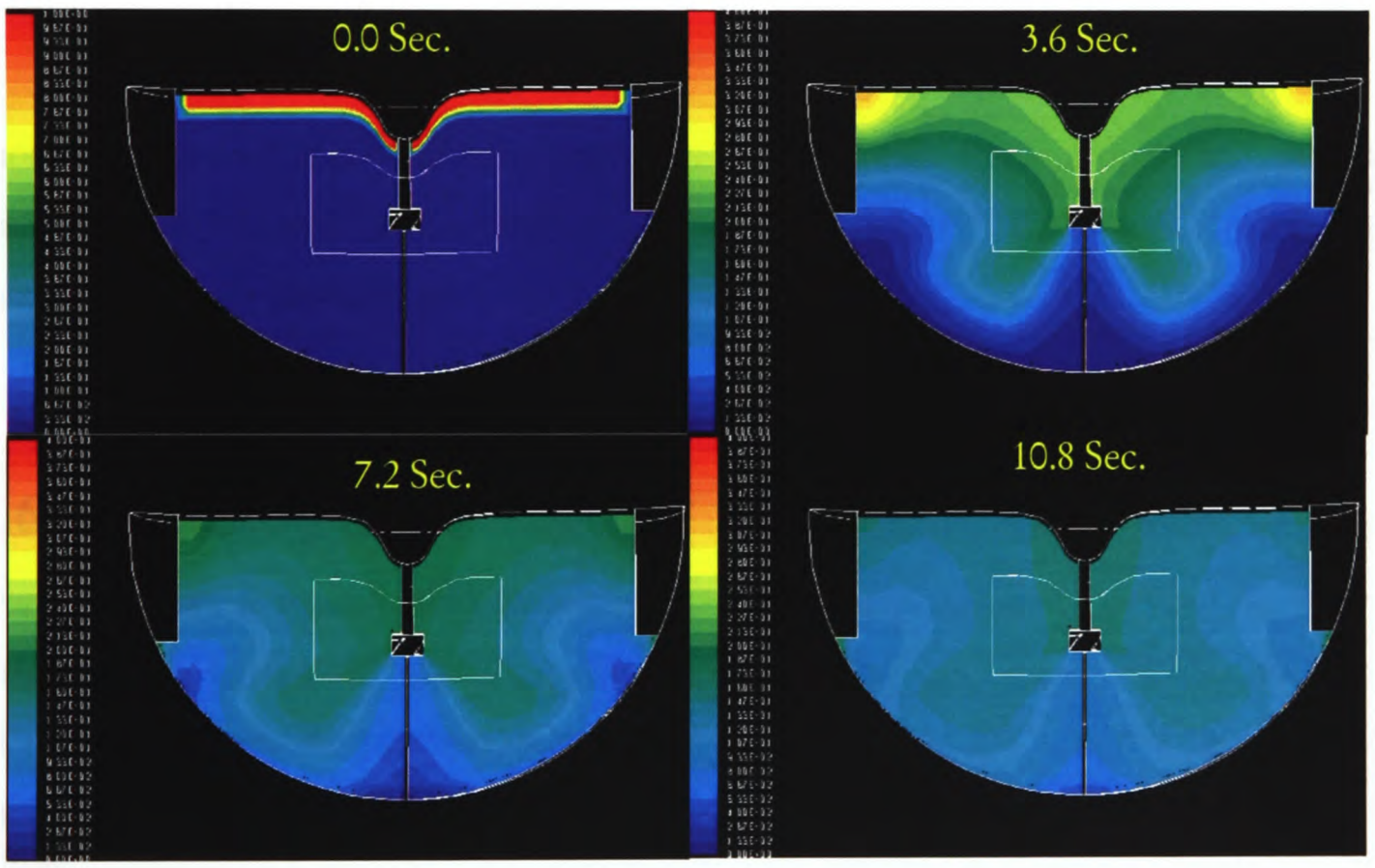

Figure 6.30: Time Evolution of Tracer Concentration

Figure-6.30 presents the blending of tracer concentration at different time for a two-baffled water model with 140RPM impeller speed. It is obvious from the figure that homogeneous concentration has been achieved after about 10.8 seconds of mixing.

Figure-6.31 gives the comparative concentrations at the two monitoring locations (T – above and B-below the impeller) for three impeller speed, 110RPM, 140RPM and 170RPM. As expected it is clear that the time taken to achieve homogeneous blending is

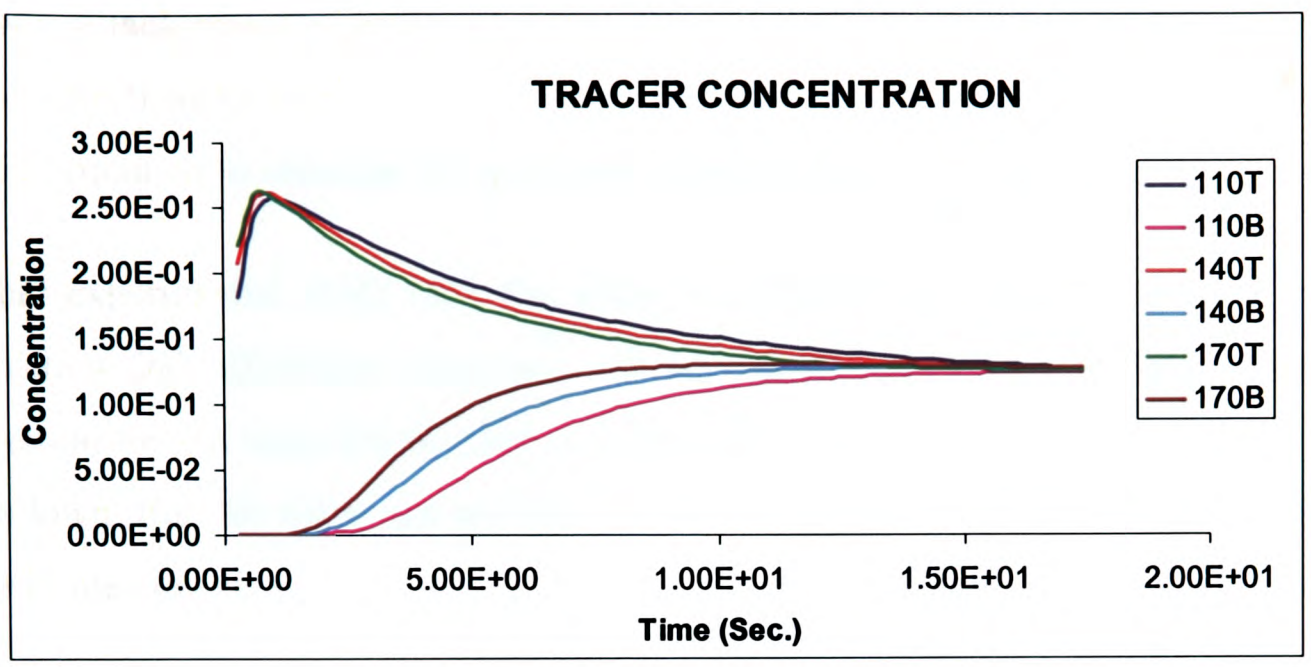

Figure 6.31: Concentration at Two Probe Locations

shortest in the case of 170 RPM. Although no experimental data is available to validate the results, the usefulness of this modelling strategy is self-evident in assessing the relative mixing efficiency under varying operating conditions.

6.6 Modelling the Drawdown of Floating Particles

Over the years a considerable amount of research effort has been invested to study the suspension of particulate second phases in impeller-stirred mixing. However, the majority of published work mainly investigates the conditions for off-bottom suspensions where particles are heavier than the fluid medium. These efforts have largely been experimental in nature and they can broadly fall into two categories. One is experimentally developed correlation equation that can calculate the minimum impeller speed for achieving complete off-bottom suspension [109]. The detailed measurement of the fluid-particle flow field for impeller-stirred was given in [110].

Probably the first systematic effort to investigate the effect of vessel geometry and impeller type on the minimum speed for drawdown and suspension of floating particles was given in

[111]. This work also examined the pattern of associated power consumption. According to this work, a tank with four baffles and stirred with disc turbine impeller is very inefficient for drawdown of floating particles. To overcome this limitation they suggested an efficient design where tank was equipped with one wide side baffle to create an eccentric vortex to drawdown the floating solid particle. Further, by using experimental data they developed a correlation equation to calculate the minimum impeller speed for drawdown.

In another experimental study [62], the effect of impeller type, number of baffles, solid mass fraction and off-bottom clearance was investigated. It was observed that particle concentration for low mass fraction had no effect on the minimum required rotational speed for drawdown. But this value and associated power consumption increased with increasing impeller immersion depth and also with increasing the number of baffles.

In a similar work [61], the effect of baffled arrangement on the minimum drawdown speed for slurries of polypropylene particles was investigated. Here, the conclusion was drawn that homogeneous suspension can be achieved through controlling the vortex shape resulted from the four narrow baffles (partial baffles). Other work [112], investigated the minimum drawdown speed and associated power consumption for the various operating configurations namely, baffle geometry, impeller type, impeller clearance and solid concentration. The conclusion was that the baffle configuration did not significantly influence the minimum drawdown speed but strongly affected the power requirement.

A similar study [63] also supported the above conclusion. Probably the only published paper [60], investigated the minimum drawdown speed for aerated condition. Here, it was concluded that impeller hydrodynamics, especially the formation of large gas cavities behind the blades, has a significant influence on the minimum drawdown speed. It was found that upward pumping pitched blade impeller were more energy efficient than the disc turbine.

Following two sub-sections describe the CFD modelling techniques used to simulate the particulate second-phase. Here, brief reviews on previous work are presented and then

modelling strategies are described. The theoretical background for these techniques is already covered in Section-5.5.4.4 and in APPENDEX-D and APPENDIX-E.

6.6.1 Eulerian-Lagrangian Model for Particulate Second Phase

In order to model the dispersion of gas through an impeller-stirred tank [113] used the Lagrangian particle tracking method. First of all a three-dimensional CFD simulation was run to obtain the flow field and then individual bubbles were tracked through out the flow field. [114] applied the method of particle tracking to simulate the particle suspension in an impeller-stirred tank. In this simulation a three-dimensional flow field was calculated by using mathematical representation for the rotation of impeller. Then about two hundred particles were injected into the impeller flow stream. Particles were injected into the impeller flow stream to achieve quick steady-state condition. The particles were kept in the flow domain till local particle concentration reached a pre-specified level. And also, to account for the impeller-particle collision an expression representing was incorporated into the model.

In another work, [115] used Lagrangian particle tracking techniques to characterise the flow field in the impeller stirred vessels. First of all, flow field was calculated where impeller was modelled using experimental data. Then a particle was tracked for long period of time. Here, probability of presence of the particle in the various regions of flow domain was calculated. And this was used to quantify the comparative mixing efficiency. Furthermore, Poincare section, which represents the geometric intersection surface with the particle trajectory, was used to characterise the mean flow behaviour.

In the present modelling strategy the CFD computed flow field that also includes the VOF calculated vortex formation, from Section-6.3.3 is used as the driving medium for Lagrangian Particle tracking. 100 particles of 3×10^{-3}m diameter and 900kg/m^3 density (representing the polystyrene beads that were used in the water model) are introduced into the impeller flow stream and are tracked for 150 seconds.

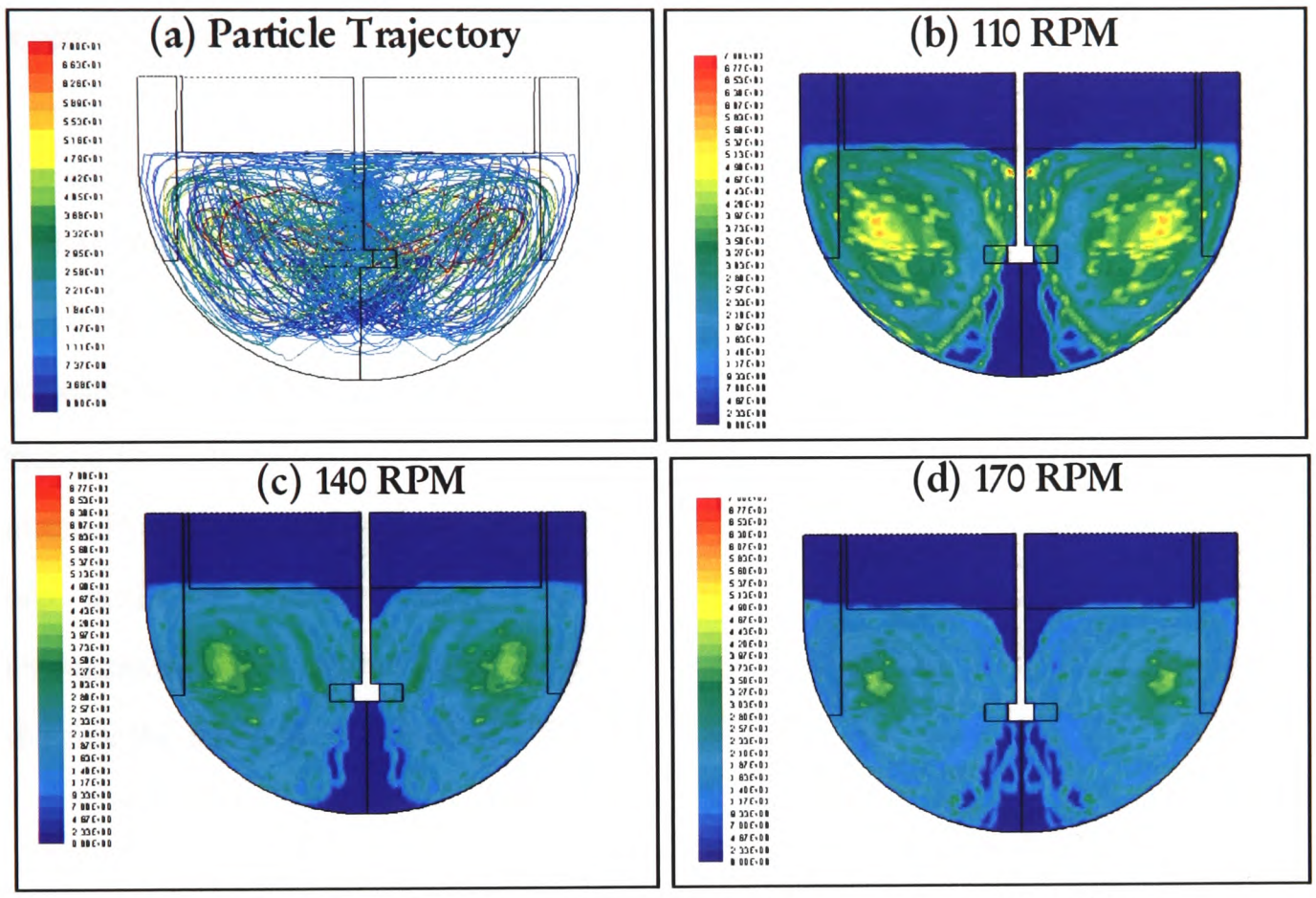

Figure 6.32: Particle Trajectory & Residence Time Distribution

The Figure-6.32 (a) shows a typical snapshot of the particle trajectory. The objective of this simulation is to quantify the residence time distribution of particles under various operating conditions. Figures 6.32 (b) – (d) give the contours for averaged residence time distribution of particles for three operating conditions (i.e. impeller rotation speed 110 RPM, 140 RPM, 170 RPM). As expected, it can clearly be seen (comparing contour colour with scale) that particles have tendency to stay longer in the bulk region near the baffles. This pattern of particle residence time is similar for all cases but, residence time decreases with increasing impeller speed. This pattern is obvious and also observed in the experimental trial. It is also evident that residence time is more uniformly distributed in the case of higher impeller

speed. It can be concluded that higher impeller speed gives more homogeneous suspension of particles. In all cases, a dead zone of negligible residence time can be found just below the impeller near the kettle bottom. Clearly, the spread of this dead zone is bigger in the case of lower impeller speed. It is interesting to note that the velocity field in this area is very small in magnitude (see Figures – 6.6, 6.8 and 6.11). Similar patterns for the distribution are also observed on the water model when polystyrene beads are used to represent the particulate second phase.

At the moment no experimental data is available to validate these results, however, it is clear that this calculation has qualitatively captured the behaviour of particle in the flow field. These features are also observed in reality. At the moment these simulations can only be regarded as exploratory in nature. However, a great deal of information, particularly the residence time distribution of the particulate second phase, about the flow structure can be obtained from these simulations. It is particularly useful in the case of lead refining process where residence time distribution of particulate phase cannot be determined experimentally. Also, a number of parametric studies can be performed using this technique to identify the most favourable operating configuration.

6.6.2 ASM Model for Particulate Second Phase

The Algebraic Slip Model (ASM) [89] is another method that can be used to predict the behaviour of second-phase in the impeller-stirred tank. For example, [23] used this method to simulate the distribution of bubbles. The momentum equations were solved using mixture properties and spatial distribution of bubbles was computed by the concentration equation. The computed results were in good agreement with experimental data. It was found that large bubbles rose directly to the surface and small bubbles followed closely the motion of the liquid and dispersed more uniformly throughout the tank.

In order to calculate the distribution of solid particles [116] applied further simplification to the standard ASM model. Here, the effects of the solid particles on the average liquid flow

were neglected and the diffusion velocity of the particles was assumed to be in the axial direction. With this assumption, the concentration of the particulate phase was computed using a mixture model. The flow field for the main fluid was calculated using FLUENT and a separate code was used for the computation of particle distribution. The turbulent diffusion of the particles was included in the model using a diffusion coefficient. The mixture model for simulating the behaviour of particulate second-phase in an impeller-stirred mixing has successful in predicting the industrial scale process too [27]. Here, mixture model was applied to simulate the impeller-stirred distribution of silicon carbide particles in liquid aluminium. The calculated result was in good agreement with experimental data

It is established from the above literature review that the ASM model has successfully been applied to predict the distribution of disperse phase in plant scale processes for some of the industrially important flow problems. With this as a motivation, the present modelling context ASM is applied to simulate the drawdown and dispersion of the floating particles. As it was pointed out in [61] (also see Figure-1.6), drawdown and dispersion of floating particle depends on the shape of the vortex generated by the rotation of the impeller. Hence, the present modelling for particulate second phase is carried out using the three-dimensional grid that also includes the vortex shape (see Figure-6.241). At the top surface a layer of particulate second-phase is introduced.

It has already been pointed out that the vortex formation provides the mechanism for the drawdown of floating particles (See Figure-1.6 & [61]). The slope of the vortex causes the particles to get into good contact with liquid and become wet and after that, particles are sheared into the main flow field. In our model the vortex shape is already part of the grid, and hence, particles are assumed to be wet already. Keeping this in mind, a fifty-percent mass fraction of floating particles is introduced on the top layer.

In the present model, the calculation for impeller rotation is carried out using the multiple-reference-frame and transient mixing of particulate phase is achieved by solving the time dependent ASM model equations. The ASM model is available only in the unstructured

grid based solver FLUENT5 [75], the structured grid (which was already generated to calculate the flow field using structured grid based solver FLUENT4.5 [75]) was exported to this unstructured solver.

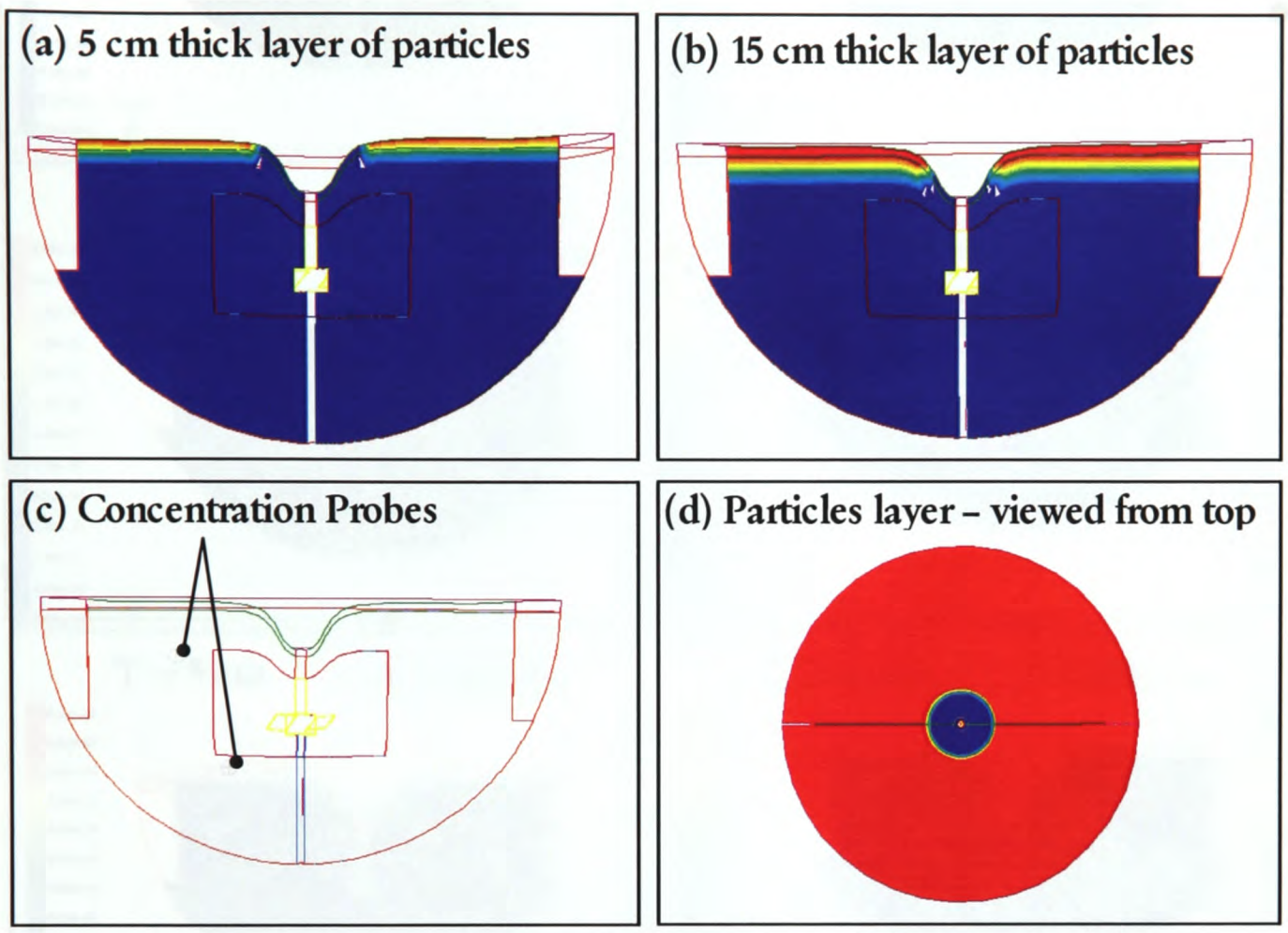

Figure 6.33: Drawdown and Dispersion of Floating Particles

Simulations are run again for water model with 140 RPM impeller rotational speed where calculations are carried out for two different thickness, 5 cm and 15 cm (Figure-6.33 (a) and (b)), of the particulate second phase. The particle properties used are that of polystyrene beads of 3×10^{-3}m diameter and 900kg/m^3 density. During the simulation the transient evolution of particle concentration is monitored at two locations: one above and one below the impeller (Figure-6.33 (c)). Figure-6.33 (d) shows the initial uniform distribution of particles on the top surface.

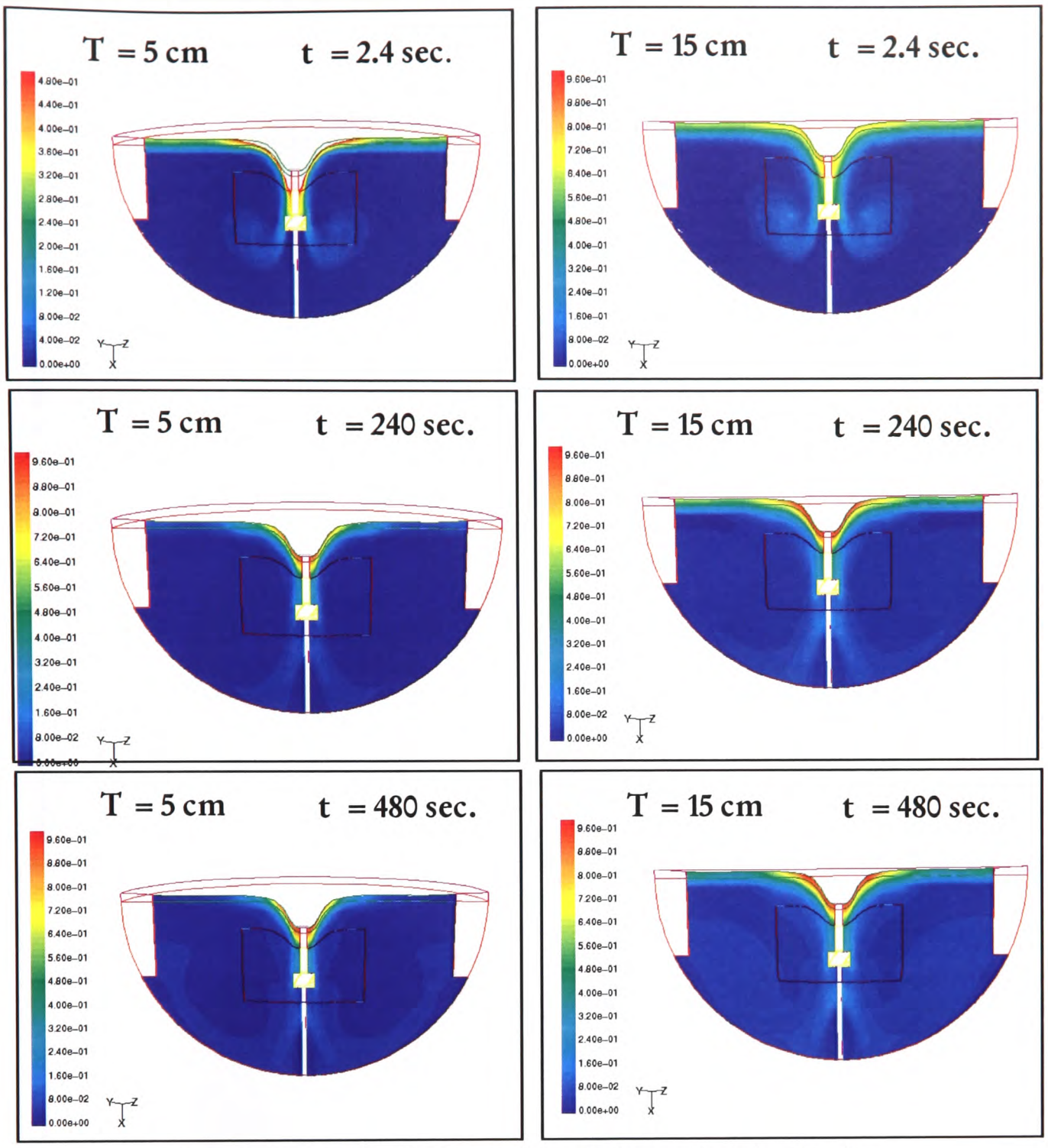

Figure 6.34: Distribution of Particle on the Top Surface

Figure-6.34 presents the contour on the vertical plane passing through the kettle representing the distribution of particle concentration at various time steps. In every panel of this figure, T represents thickness of particle layer and t represents time step. We can see from the simulation results that at the starting time (t = 2.4 sec.) the particles are just being drawn into the vortex. At a later time (t = 240 sec.) particles concentration hits the bottom and forms a re-circulation motion and move upward to occupy the bulk. At about t = 480 sec. particles have almost distributed through the whole bulk. As expected, the concentration of the particles in the bulk is higher in the case of thick layer.

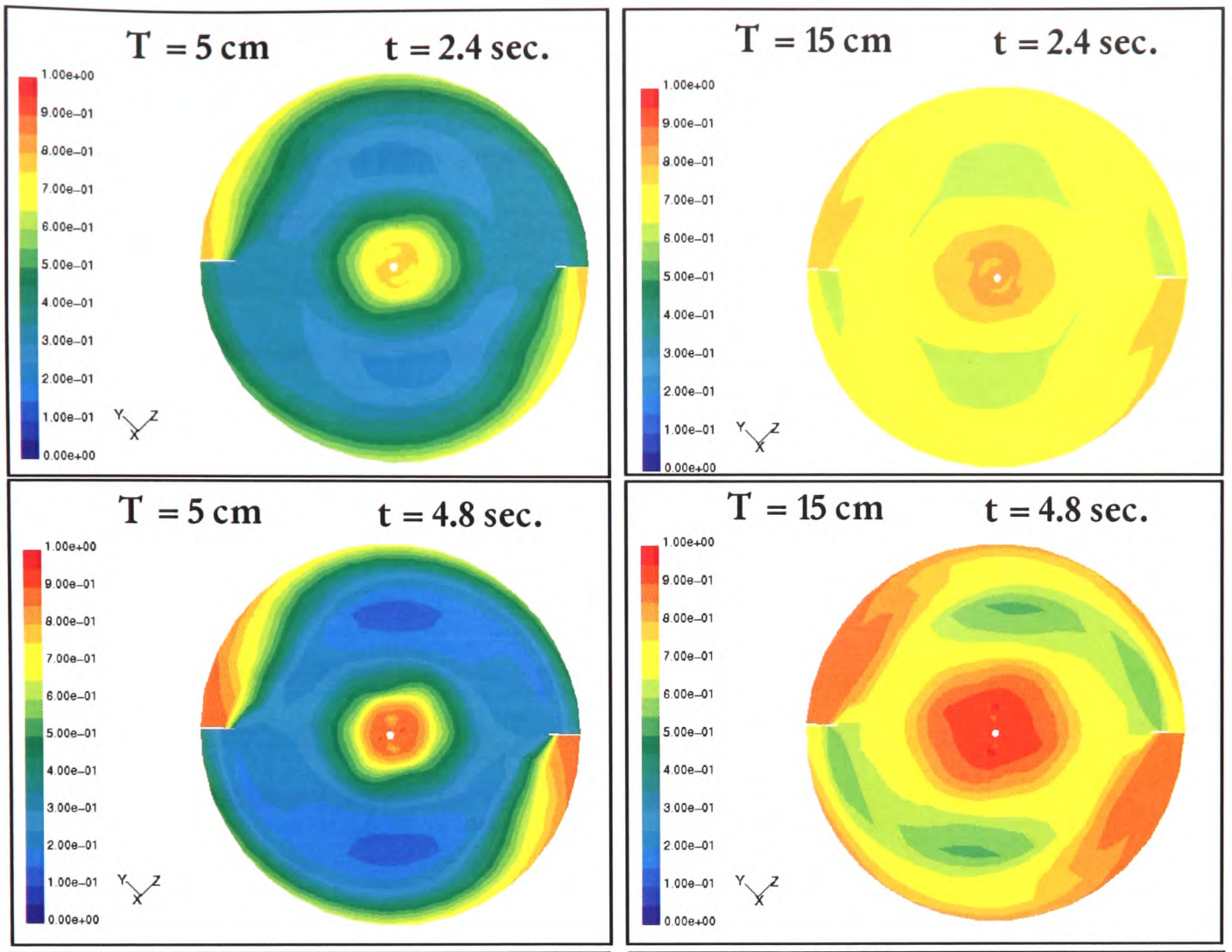

Figure 6.35: Distribution of Particle on the Top Surface

Figure-6.35 presents the contour on the top surface of the kettle representing the distribution of particle concentration at various time steps. Here also, in every panel, T represents thickness of particle layer and t represents time step. From the contour immediately after starting time (t = 2.4) it can be seen that particle concentration has dramatically increased in the vortex area and also, behind the two baffles. And this pattern of particle concentration has become more prominent at t = 4.8 where patches of low concentration zone have appeared in the middle. It is the same pattern observed during experiment too. Particles tend to accumulate in the vortex area and from there they are drawn into the bulk and enter into re-circulation zone and are thrown out towards the surface near the baffles and hence, high concentration found there. This process leaves two big patches of low concentration zone on the surface. It is obvious that at t = 192 much of the particles have been drawn into the bulk leaving a wider area of low concentration on the surface. Similar pattern follows for the later time steps too. We can clearly see that at t = 480 sec. much of the particles drawn into the bulk leaving wide clean surface. The similar pattern is also observed on the water model.

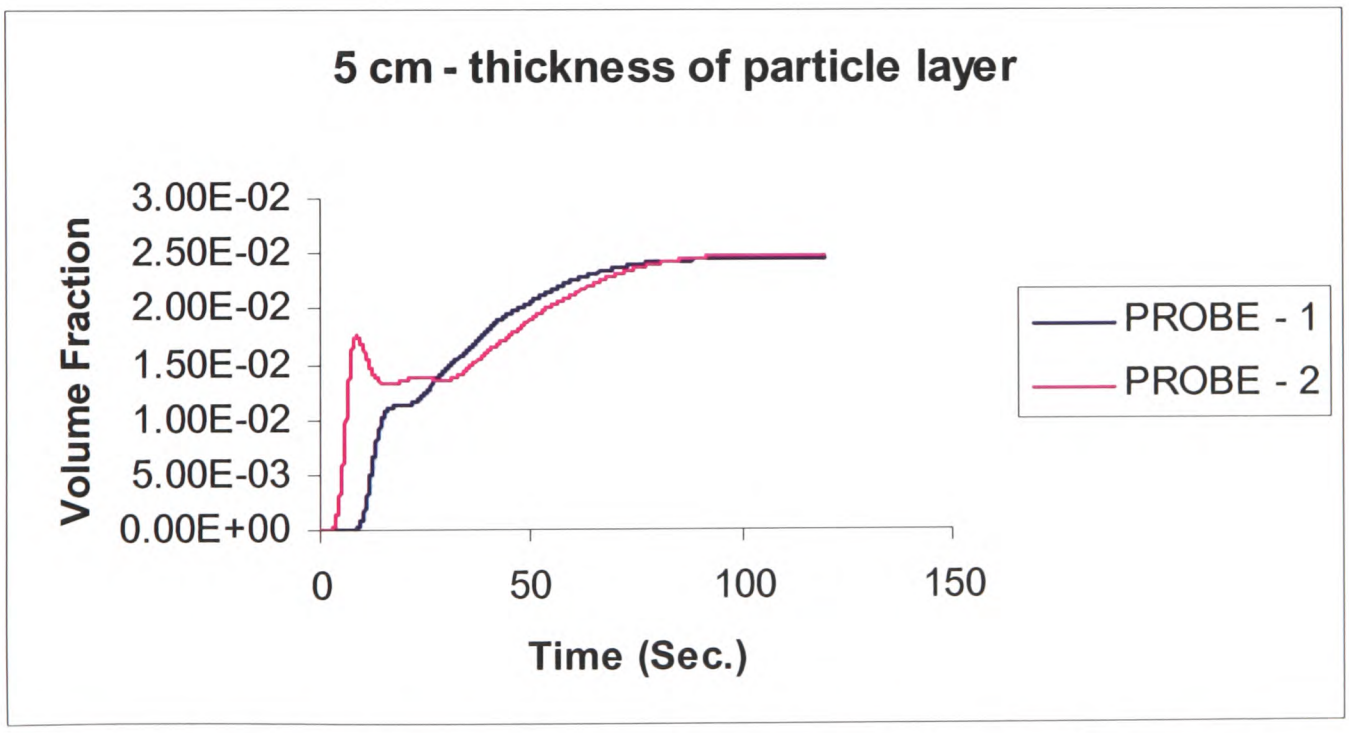

Figure 6.36: Particle Concentration for Two Probe Locations in 5cm Thick Top Layer

Figures-6.36 and 6.37 show the change in particle concentration over time at two probe locations (as shown in Figure-6.33 (c)) for two cases with 5 cm and 15 cm thick particles layers. As it is clear from the graphs that concentrations at these two locations for both the

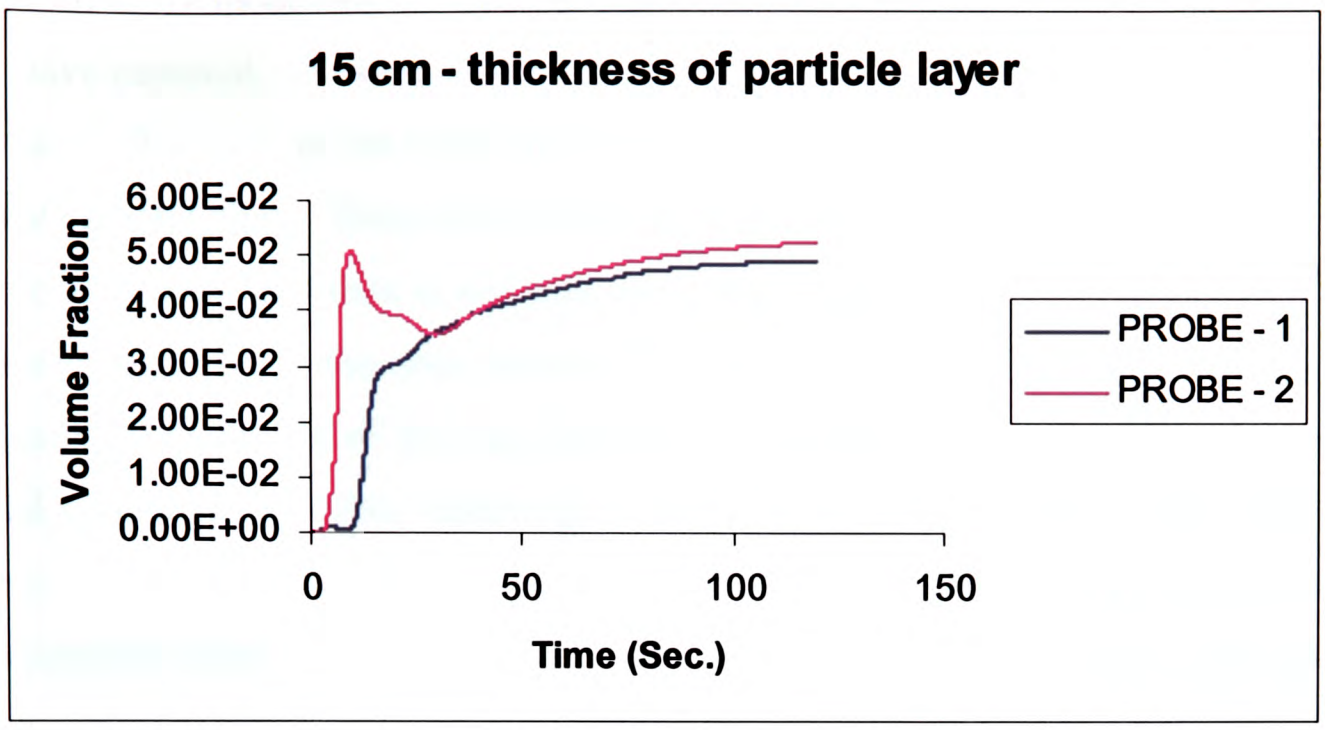

Figure 6.37: Particle concentration for Two Probe Locations in 15 cm Think Top Layer

cases become equal in about 30 sec. then further increase asymptotically till they almost become constant. These constant values represent the homogeneous spread of particles in the bulk.

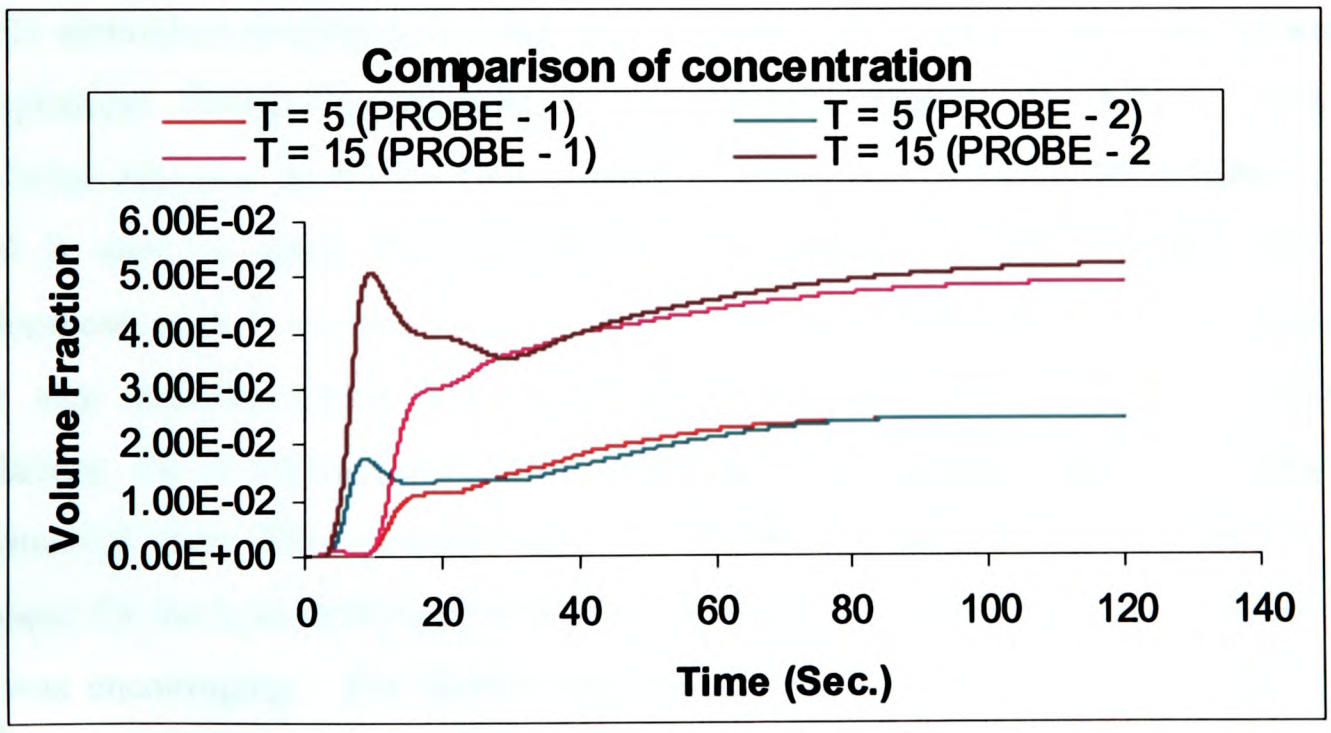

Figure 6.38: Comparative particle Concentration at Two Probe Locations Both 5 cm and 15 cm Thick Top Layer

Figure-6.38 presents the comparative plot of the pattern of transient concentrations evolution for both the cases. It is evident that the both patterns are similar except the value of concentration is higher in the case of thick layer. This fact is in qualitative agreement with the fact found in real situation. From the above discussion, about the results from

ASM based CFD modelling of floating particulate second phase, that these simulations clearly have captured the essential details of the flow features. It qualitatively agrees well with what is observed on the water model when polystyrene beads are used as a floating particulate second phase. These simulations are exploratory in nature at the moment, as no experimentally measured data is available for comparisons. However, this is probably the first attempt, available in the open literature, to use CFD model to investigate the impeller-stirred flow characteristic of floating particles. A validated model like this can easily be extended to simulate the flow behaviour of dross in the lead refining kettles. The results from these simulations can prove to be of great importance to the refining industry as it can furnish detailed information regarding the effect of various operating parameters affecting the flow characteristics. Consequently, this can be used as design decision tool for efficiency improvement.

6.7 Conclusions

A CFD simulation method is developed that models the complex flow field generated in hemispherical shaped impeller-stirred lead refining kettles. As there is only little knowledge available about the flow behaviour of the melt in the refining kettle, a water model is used to guide the development and validate the CFD model. The model development work is carried out in a number of successive stages where calculations at every step included more flow complexities into the model. Firstly, a number of simulations for a lead-refining kettle were run and validated against corresponding experimental data. This exercise was to establish to applicability of CFD modelling technique for the lead refining process. The comparison of these results with experimental data was encouraging. The further refinement and development in the CFD model, to handle a range of phenomena taking place in the lead refining process, were carried out using water models. At the next stage of model development, simulations for the water model kettle were run for a number of operating configurations, namely, unbaffled kettle using centred and off-centred shaft baffled kettle with centred shaft.

In these models the free-surface at the air-water interface was approximated as shear free flat surface. The simulation results for baffled and unbaffled cases were validated against experimental data and these were found to be in good agreement. The CFD result for off-centred case was able to capture similar vortex structure as was observed on the water model. These three-dimensional models were further extended to incorporate the shape of impeller induced central vortex. This was achieved by using a novel CFD solution strategy. In this, first of all a two-dimensional axisymmetric model, using the blade element theory to model impeller rotation, was developed that was capable of modelling the vortex shape. The calculated vortex shape was then used to regenerate the three-dimensional grid. This was subsequently used to run steady-state full three-dimensional simulations. At each stage of the simulation, results are validated against experimental data and that were found to be in good agreement. This validated model was further extended to incorporate the particulate second phase to simulate the drawdown and dispersion of floating particles.

The CFD simulation work undertaken here can be regarded as novel in many ways. The overall modelling strategy followed here was a unique attempt to solve the real life industrial scale problems using CFD. Results from these analyses clearly identified the benefit of using baffles. This has been incorporated at the industrial collaboration site.

Chapter 7

CONCLUSIONS AND FUTURE WORK

7.1 Conclusions

Impeller-stirred mixing of molten lead bullion is the main process employed in the lead refining industry. Prediction and control of the associated flow phenomena are crucial to establish an optimum process regime. This thesis presented the techniques and results from Computational Fluid Dynamics (CFD) and Physical modelling that was aimed at predicting the complex flow phenomena taking place inside the lead refining kettle.

Presentation in this thesis started with an introduction to the lead refining process. This was followed by a discussion on the motivation and method for this research. The techniques and findings from this investigation are summarised in the following sections.

7.1.1 Modelling Techniques and Results

First of all, a thorough literature survey was undertaken in order to identify the state-of-the-art methods available within CFD technology for modelling the impeller-stirred tank. It was recognised that main challenge for using CFD to predict flow field in an impeller-stirred tank was to represent the geometry and rotation of the impeller blades. To tackle this problem a number of techniques have been developed over the last two decades.

One of the traditional methods is to treat the impeller region as a black box where its action is included into the simulation using experimental data. The technique mainly relies on

experimental data and hence, is limited in its applications to some specific cases where experimental data are available. Blade-element theory based impeller model is relatively wider in scope; however, this also requires experimentally determined lift and drag coefficients and that are only available for some well known blade shapes. Recently have more general three-dimensional models become available. For example, a rotating reference frame is used around the full geometry of impeller to model its interaction with the surrounding. Further, a sliding grid method can be used to model the rotation of impeller transiently. This method is most general but also most compute intensive.

It was realised that obtaining adequate knowledge, about the flow behaviour of molten lead, directly from real refining kettle was impossible. Hence, a physical modelling (water model) technique was integrated in this research project with the objective to guide the development of CFD and also, supply data for its validation. The theoretical foundation, based on the principles of similitude, for the physical model was described in details. In addition, its applicability was illustrated for the power consumption and vortex depth prediction in an impeller-stirred tank.

The experimental results like, power consumption, vortex depth, etc., from physical model (water model) under various operating conditions were presented. Here Acoustic Doppler Velocimeter (ADV) probe was used for the velocity measurement at various locations inside the water model. From these experimental results alone, some of the valuable insight gained about the flow phenomena occurring inside the refining kettle. For example, when fluid is stirred above certain rotational speed (where Reynolds number becomes bigger than 10^5) the vortex depth becomes independent of the Reynolds number of the operation. This was a significant finding as it established the use of water model in replicating the vortex depth occurred in the real lead refining kettle. From ADV measured velocity data it was found that flow in the bulk region of the two-baffled kettle exhibited axisymmetric flow pattern. This finding was used to reduce a three-dimensional CFD model to a two-dimensional model.

In order to access applicability of CFD modelling technology for the lead refining mixing process, a number of simulations were carried out using molten lead as a working fluid. This was perhaps the first attempt to apply the CFD technology to model the impeller-stirred mixing in the lead refining industries. These were three-dimensional models that used the rotating-frame techniques for the impeller. And top surface at melt-air interface was approximated as flat shear free surface. The simulation results for the surface velocities were validated against experimental data (velocities measured by observing the movement of floating steel ball). These comparisons were encouraging and established the fact that CFD could be used as an investigation tool in the lead refining process. However, the data from experiment on lead refining kettle were not enough for conclusive validation. In addition to this, the majority of phenomena taking place in the refining kettle were not included in this CFD model. Hence, the rest of the simulations were compared with the corresponding water model where experimental data was available with relative ease.

Further development of CFD model was undertaken in a number of steps with gradual increase of complexities. First of all, three-dimensional CFD calculations were carried out for the water model with different conditions like, unbaffled, two-baffled, centred and off-centred shafts. These simulation results were validated with experimental data. Results for the two-baffled case were in close agreement with experimental data. And any discrepancies were attributed to the flat surface approximation.

After these simulations, a novel two-dimensional axisymmetric CFD model capable of predicting the vortex shape at the free surface was developed. In the open literature this was probably the first attempt to calculate the vortex shape by using the Volume of Fluid (VOF) method in combination with blade-element based impeller model. The calculated vortex depth showed similar trends as that of the experiments. These calculated vortex shapes were then used to regenerate the three-dimensional grids. Further simulations were carried out using those grids. The results from these models were further validated with the experimental data and that showed very good agreement.

In order to quantify the relative mixing performance under different operating conditions, the results from the three-dimensional model with vortex shape were used to simulate the

transient blending of neutral tracer. It was found that increasing the impeller speed reduced the blending time. These CFD models were further extended to simulate the behaviour of particulate second phase in the flow field. For this, both Lagrangian Particle Tracking (LPT) and Algebraic Slip Model (ASM) were used. The LTP was used to investigate the residence time distribution of the dross particles, whereas ASM was used to obtain a detailed picture about the transient drawdown and dispersion of the floating dross particles.

7.1.2 Methodology for Kettle Design

The main advantage of using CFD modelling is that it can provide a great deal of information (e.g. velocities, pressure distribution, turbulence etc,) about the flow field. Such detail is not possible to obtain from the experimental methods alone. However, a feasible CFD model for complex flow phenomena like impeller-stirred mixing can only be developed by applying a number of simplifying assumptions (for turbulence, geometry, etc.). That along with the approximate nature of the numerical algorithm in the CFD solver makes it essential to validate the simulation results against experimental data to ensure the accuracy of the predictions. Experiments on physical models offer the opportunity to visualise flow phenomena (e.g. vortex break up, surface swirl, etc.) in real time. The CFD modelling for this can be extremely difficult if not impossible. Also, physical modelling can be used to guide the development of a CFD model and supply data for the validation. A validated CFD model can then be used for the parametric study to identify the optimum operating conditions.

The techniques and findings from this research have established both, physical modelling and CFD modelling, as independent tools of investigation for the flow behaviour of molten lead in the refining kettle. As said before, both of these methods have their own advantages and disadvantages. However, combining these tools together opens up new opportunities of analysis that is not possible by either of the methods alone. The aim of this integration is to promote further understanding of the kettle refining process and identify suitable new designs that optimise the refining process. Figure-7.1 outlines the strategy to use these

techniques when investigating the performance of a current kettle or deciding on the design for a new one [117].

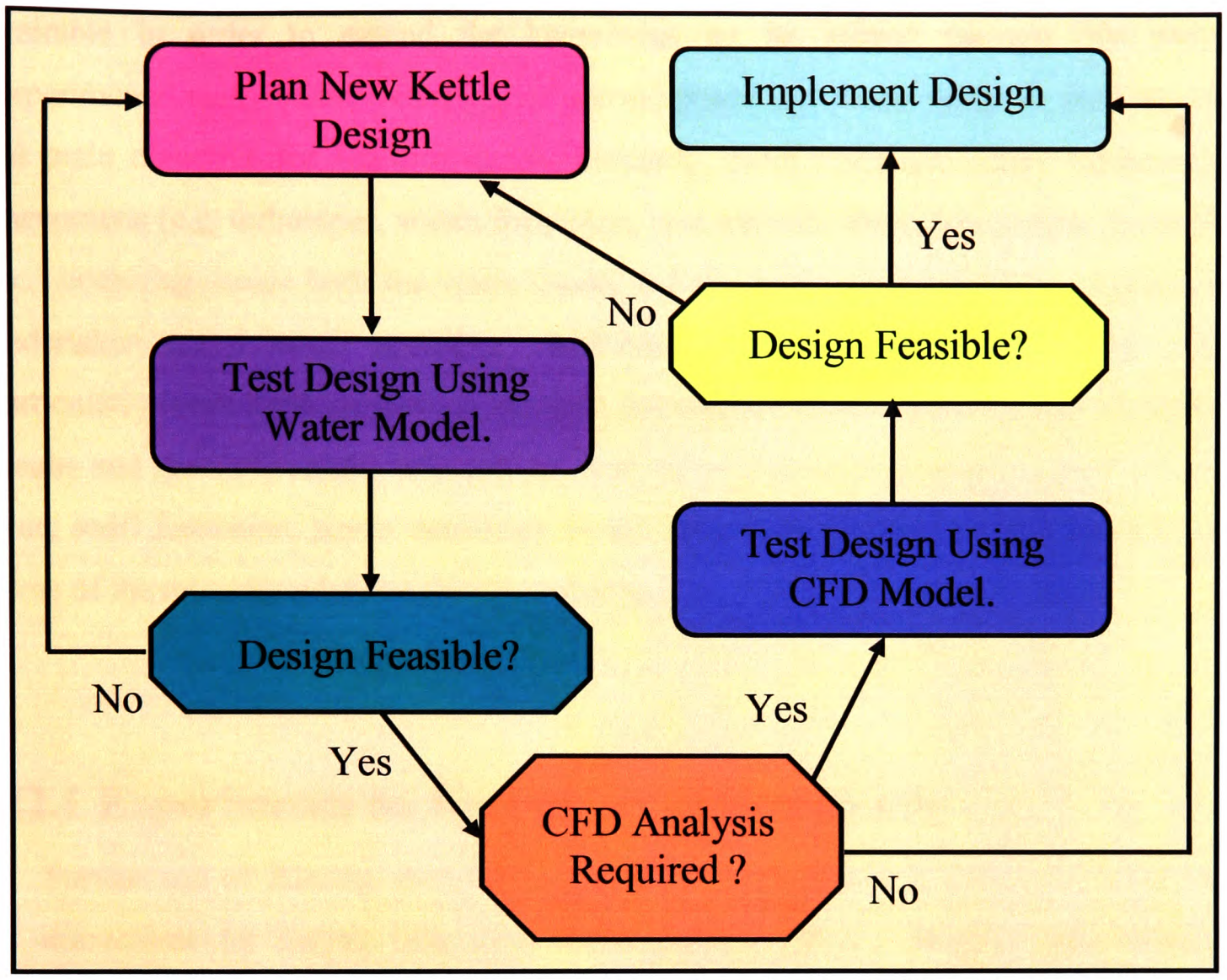

Figure 7.1: Suggested Route for Using the Modelling Tools

Full use of the water model should be made before deciding on any CFD work. The water model is a very cost effective way of quickly observing changes that may result in the mixing performance of a kettle when a design change is made. After water modelling analysis has been undertaken and the design is feasible, a decision then needs to be made on whether a CFD analysis is required. Such an extra analysis will compliment the water model analysis. Obviously, detail of data that can be obtained from the CFD simulations is much greater than that from the water modelling. The CFD simulations should only be used once a new design has been investigated using the water model. The results from a CFD analysis will help fine tune the process parameters to ensure optimum kettle performance is obtained from the new design of the kettle.

7.2 Future Work

Further experiments on both the real lead refining kettle and the water model are highly desirable in order to extend the knowledge so far gained through this research. Experimental study of the behaviour of second phase (i.e. dross, reagents, etc.) should be the main objective for future research. Similarly, more CFD simulations addressing all phenomena (e.g. turbulence, vortex formation, heat transfer, chemical reaction, dross phase, etc.) occurring inside both the water model and the lead refining kettle is required to be undertaken for a range operating conditions. And also, validation of CFD results, particularly for multiphase flow, is required. Information drawn from both the experimental results and the CFD results will then be used for process optimisation in terms of mixing time, swirl formation, power consumption and then dross yield. Following sections gives some of the recommendations for future research.

7.2.1 Experiments on Real Lead Refining Kettle

- Further use of floating steel ball as a marker to measure the surface velocity. Here, corrections for factors (lift, drag and buoyancy forces) affecting the readings are required to be considered.
- Measure time for dross lead content to reach certain low value.
- Device a method for better power consumption readings.
- Measure the effect of kettle temperature on various process variables (e.g. mixing time, dross grade, etc.).

7.2.2 Physical Modelling

- More readings for power consumption and vortex depth can be used to develop correlation equations for these variables. That will prove to be a valuable aid when any decision about new process design is taken.

- Use concentration probe to measure the time of mixing. For example, the readings from a PH probe, when a measured quantity of acid is added to the mixing tank, can be used to calculate the time taken by the system to reach homogenous concentration.

- Use a measured size distribution of polystyrene beads to give better representation of dross.

- Experimental techniques need to be developed to quantify the flow variables for multiphase flow.

7.2.3 CFD Modelling

1. Extend two-dimensional model to three-dimensional model for the vortex shape calculations.
2. Use Euler-Euler method for particulate second phase (dross) simulations.
3. Extend the model to incorporate heat transfer and chemical reactions taking place inside the real lead refining kettle.
4. Further extend the model to tackle whole range of phenomena (e.g. turbulence, vortex formation, heat transfer, chemical reaction, dross phase, etc.) simultaneously.
5. Explore the possibilities for reducing computation time while handling a range of complexity simultaneously. For this purpose methods of parallel processing can be used.

APPENDIX-A

BLADE ELEMENT THEORY BASED IMPELLER MODEL

A.1 Equations for Impeller Model

Based on the blade-element theory [118], momentum transfer from rotating impeller blades to the surrounding fluid can be given by quadratic volumetric source terms [23]. If blades are vertical then most dominant momentum term is tangential momentum; however, when blade is tilted by an angle then the axial component of momentum is also required to be considered. Following are the equations for axial and tangential momentum source terms:

$$S_u = \frac{1}{2}\rho\left[(\omega r\cos\theta)^2 - u^2\right]C_d n\overline{A}_f \tag{A.1}$$

$$S_w = \frac{1}{2}\rho\left[(\omega r\sin\theta)^2 - w^2\right]C_d n\overline{A}_f \tag{A.2}$$

where S_u, S_w are axial and tengential components of momentume source terms; u and w are the axial and tangential velocity components; θ is the blade angle with respect to vertical axis; ρ is the fluid density, C_d is the drag coefficient of the flat blade [118], n is the number of blades, and $\overline{A}_f$ is the time averaged blade area and is defined below.

The time averaged blade area $\overline{A}_f$ is the average value of blade surface sweeping through a given dicretised cell of volume V_c and given by [25]:

$$\overline{A}_f = \frac{V_c}{2\pi r} \tag{A.3}$$

A.2 Implementation

This section presents the steps in implementing the axial momentum source term for the rotating impeller. The tangential momentum source term can also be implemented in the same way. Furthermore, similar argument can be applied to model the presence of baffles. The baffles can be regarded as impeller with flat vertical blades and acting as a time averaged momentum sink (source with negative sign).

Equation (A.1) for axial momentum source term can also be written as:

$$S_u = \frac{1}{2}\rho C_d n\overline{A}_f(\omega r\cos\theta - u)\left|(\omega r\cos\theta + u)\right| \tag{A.4}$$

where $\left|(\omega r\cos\theta + u)\right|$ is calculated using u from the previous iteration. Hence, the term $1/2\,\rho C_d n\overline{A}_f\left|(\omega r\cos\theta + u)\right|$ in Eq-A.4 can be considered as constant for the current iteration. Now consider

$$K = \frac{1}{2}\rho C_d n\overline{A}_f\left|(\omega r\cos\theta + u)\right| \tag{A.5}$$

then Equation (A.4) can be written as:

$$S_u = K(\omega r\cos\theta - u) \tag{A.6}$$

It is mentioned in Section-5.5.3.2 that source term is required to be linearised and should have following form:

$$S_u = A + Bu \tag{A.7}$$

where A and B are constants and in this case, using Eq-A.6, they are given as follow:

$$A = K\omega r\cos\theta \tag{A.8}$$

$$B = -K \tag{A.9}$$

A.2.1 Pseudo Code

Following is the equivalent pseudo code that was implemented through user subroutine in FLUENT4.5 [75] to model the rotation of impeller. This code fragment implements the axial momentum source term. Similar can be obtained to model the tangential source term and also, the presence of baffles.

Start: Subroutine

Start: Comments

Cd = Drag coefficient

Rho = Fluid density

Theta = Blade angle from vertical axis

Omega = Revolution per second

N_{blade} ***= Number of blades***

$I_{impeller\_start}$ ***represents the start of the I index of impeller swept region***

$I_{impeller\_end}$ ***represents the end of the I index of impeller swept region***

$J_{impeller\_start}$ ***represents the start of the J index of impeller swept region***

$J_{impeller\_end}$ ***represents the end of the J index of impeller swept region***

$(Vel_{axial})^{n}$ ***represents the axial velocity at current (nth) iteration***

$(Vel_{axial})^{n-1}$ ***represents the axial velocity from previous, (n-1)th, iteration***

Subroutine "Get: variable" supplies the value of variable for current cell

Radius = radial distance of cell centre from the vertical axis of geometry

Area = time averaged area of impeller blade

Vol = volume of a cell

S_{axial} ***= axial momentum source***

A, B and K are constants

End: Comments

Read: Cd, Rho, Theta, Omega

Do: $I = I_{impeller\_start}$ ***to*** $I_{impeller\_end}$

Do: $J = J_{impeller\_start}$ ***to*** $J_{impeller\_end}$

Get: Vol

Get: Radius

Set: Area = Vol/2*Pi*Radius

Get: $(Vel_{axial})^{n-1}$

Set: $K = (0.5)*Rho*Cd*N_{blade}*Area*(Omega*Radius*Cos(Theta)+(Vel_{axial})^{n-1})$

Set: $A = K*Omega*Radius*Cos(Theta)$

Set: $B = -K$

Set: $S_{axial} = A+B*(Vel_{axial})^{n}$

End: Do

End: Do

End: Subroutine

APPENDIX-B

ANALYTICAL METHOD TO PREDICT VORTEX SHAPE

Vortex shape of free surface at the liquid-air interface in an unbaffled cylindrical vessel equipped with a flat blade impeller can analytically be found using Nagata model [50]. In this model it is assumed that only tangential flow is dominant in comparison with axial flow and hence, influence of axial flow is neglected. It is also assumed that there are two regions of flow fields, one with "forced vortex" and another with "free vortex", exist inside the vessel. The forced vortex is assumed to exist inside a hypothetical cylinder of fluid with

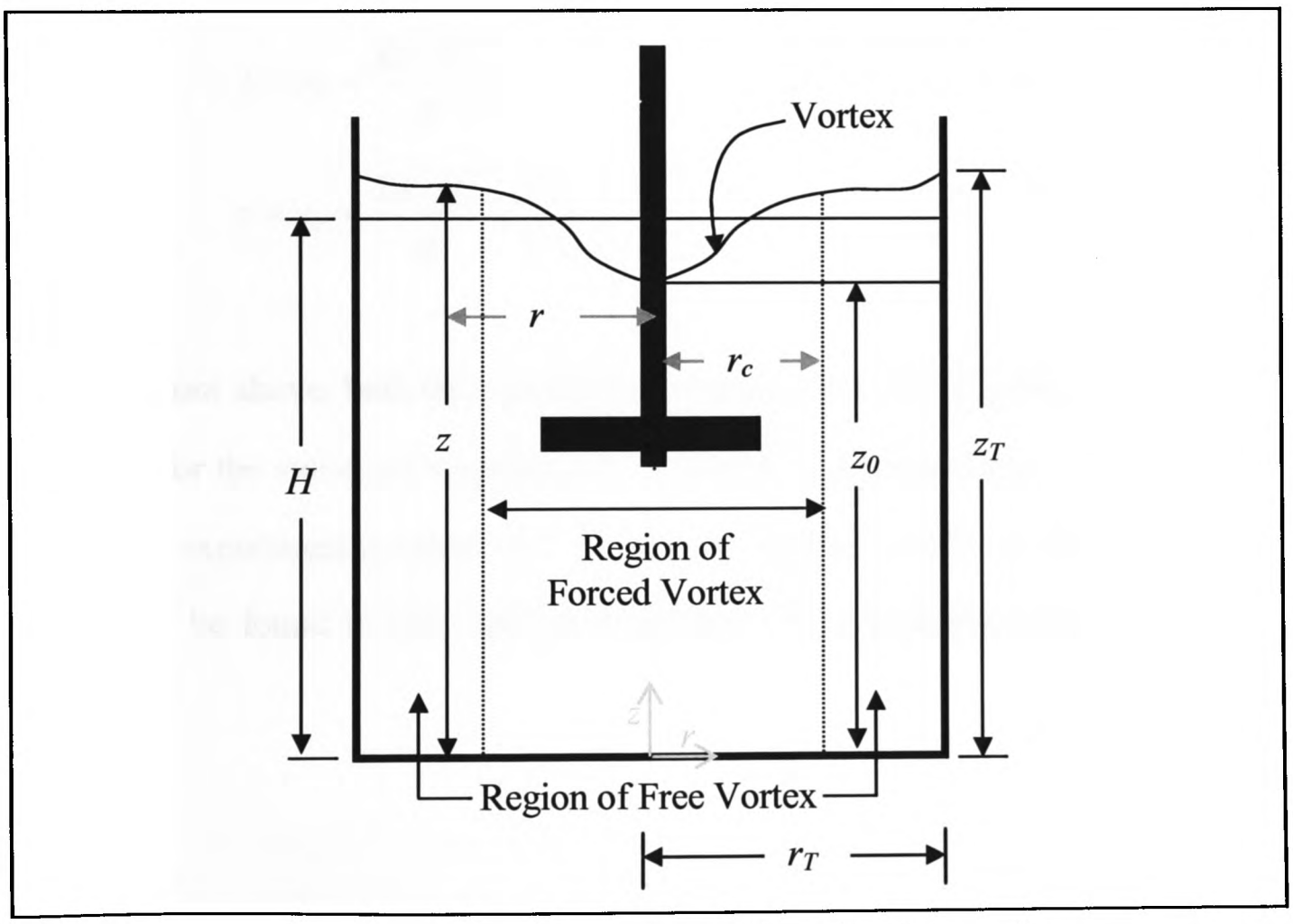

Figure B.1: Geometry of Impeller Stirred Vessel

critical radius r_c at the centre of the cylinder and undergoes solid body rotation with an angular velocity of the impeller. Outside this zone, starting from the critical radius r_c, another region of concentric fluid cylinder exists. This is the region of free vortex, where it

is assumed that flow field has a hyperbolic tangential velocity profile and no impeller generated torque acts there.

Figure-B.1 gives the schematic representation of the vortex shape. In this figure, H is the original level of the liquid, z and r are axial and radial position of a point on the free surface respectively, r_c and r_T are the critical radius and radius of the vessel respectively, z_0 and z_T are height of liquid at the centre and at the vassel wall respectively. In order to obtain an analytical expression for the vortex shape, the governing equations for fluid flow (Navier-Stokes equation) are solved in the cylindrical polar coordinate representing the impeller-vessel geometry. These equations are applied in both the forced vortex and free vortex regions saperately . Expressions for calculating vortex shape in the forced vortex and free vortex regions is respectively given as [64]:

$$z = z_0 + \frac{2\pi^2 N^2}{g} r^2 \qquad \text{for} \qquad 0 \le r \le r_c \tag{B.1}$$

$$z = z_T + \frac{2\pi^2 N^2}{g} r_c^4 \left(\frac{1}{r_T^2} - \frac{1}{r^2} \right) \qquad \text{for} \qquad r_c \le r \le r_T \tag{B.2}$$

We can see from above, both the equations hold true at the critical radius r_c hence, we can equate them for the values of variables at r_c. Therefore, critical radius r_c can be obtained by supplying experimental values for z_0 and z_T. Further details on deriving the above equations can be found in [64] and the technique for calculating critical radius can be found in [50].

APPENDIX-C

VOLUME OF FLUID (VOF) METHOD

The Volume of Fluid (VOF) method is applied to track the movement of interface between two or more immiscible fluids. In this method the fluids share a single set of conservation equations (see Chapter-5) and the volume fraction of each of the fluids is tracked throughout the domain.

The volume fraction α_q (the volume fraction of qth phase) is used as a marker function that uniquely identifies the presence of qth fluid in a given cell. A unit value of α_q represents a cell completely filled with qth fluid, whereas a zero value represents complete absence of the qth fluid. A cell with intermediate value of α_q indicates a presence of an interface between phases. The tracking of the movement of motion of the interface(s) is achieved by solving a time dependent continuity (advection) equation for the volume fraction of one (or more) of the phases. For the qth fluid this equation is given as:

$$\frac{\partial \alpha_q}{\partial t} + u_i \frac{\partial \alpha_q}{\partial x_i} = 0 \qquad \text{(C.1)}$$

The volume fraction of the phases must also satisfy the following constraint:

$$\sum_{1}^{n} \alpha_p = 1 \qquad \text{(C.2)}$$

Owing to this constraint, we do not need to solve the volume fraction equation (Eq-C.1) for the primary phase as it can be computed from Eq-C.2.

Since the flow variables and properties are shared by all the phases, these are represented as volume-averaged values. Therefore, volume-averaged density and viscosity can be given as follow:

$$\rho = \sum_{1}^{n} \alpha_p \rho_p \qquad \text{(C.3)}$$

$$\mu = \sum_{1}^{n} \alpha_p \mu_p \qquad \text{(C.4)}$$

The finite-volume discretisation of the time dependent volume fraction equation (advection equation) requires the fluxes of α_q through the cell faces. Furthermore, during the calculation α_q at the current time-step is also related to the value at the previous time steps. There are several methods available to calculate the face fluxes for the VOF. One of the most popular methods is the donor-acceptor scheme [86]. This scheme is available in FLUENT4.5 [75, 76] and used for this research.

In this scheme one cell acts as a donor of an amount of fluid from one phase and another neighbour cell acts as the acceptor of that same amount of fluid. This minimises the numerical diffusion at the cell interface. The amount of fluid from one phase that can be convected (donated) across a cell boundary is limited by the minimum of the filled volume in the donor cell or the free volume in the acceptor cell.

APPENDIX-D

EULERIAN-LAGRANGIAN METHOD

The trajectory of a spherical particle dispersed in a continuous phase is calculated by integrating the particle velocity equation in a Lagrangian frame of reference. The particle velocity is given as:

$$\frac{d\vec{x}}{dt} = \vec{u}_p(t) \tag{D.1}$$

where x is Cartesian coordinate, t is time and $\vec{u}_p$ is the particle velocity.

The particle velocity is obtained by integrating the equation for force balance as given by

$$\frac{d\vec{u}_p}{dt} = \frac{18\mu}{\rho_p d_p}\frac{C_D \mathrm{Re}_r}{24}(\vec{u} - \vec{u}_p) + \vec{g}\left(\frac{\rho_p - \rho}{\rho_p}\right) \tag{D.2}$$

In this equation gravity and drag forces are considered to be the main forces acting on particle as other forces such as lift force, Basset history force, the virtual force are negligible in comparison. Here, u is fluid velocity, $\vec{u}_p$ is the particle velocity, μ is the molecular viscosity of the fluid, ρ is the fluid density, ρ_p is the density of the particle, d_p is the diameter of the particle, C_D is the drag coefficient and Re_r is the relative Reynolds number. The drag coefficient, C_D is calculated from the function as:

$$C_D = a_1 + \frac{a_2}{\mathrm{Re}_r} + \frac{a_3}{\mathrm{Re}_r^2} \tag{D.3}$$

The relative Reynolds number, Re_r is calculated as:

$$\mathrm{Re}_r = \frac{\rho \cdot d_p \cdot |u_p - u|}{\mu} \tag{D.4}$$

The constants a's in Eq-D.3 are given for several ranges of Re_r between 0.1 to 5×10^4 in [119]. The drag coefficient for a spherical particle at a very small Reynolds number is

given as $C_D = 24/\mathrm{Re}_r$ and at a very high Reynolds number this becomes approximately 0.4.

The turbulence in the continuous phase also affects the trajectory of the disperse phase particle and hence, trajectory calculation must also incorporate the effect of the turbulence. In turbulent flow field the instantaneous velocity is a sum of mean and the fluctuating velocities. This fluctuating velocity can be calculated using a stochastic method, which employs the continuous random walk model. In this model, the instantaneous fluid phase velocity is obtained by solving Langevin equation [120] given by

$$du_i = \frac{1}{T} u_i dt + \left(\frac{2\overline{u'_i u'_i}}{T_i} \right)^{1/2} dw \qquad \text{(D.5)}$$

where T_i is the integral time, the time spent in the turbulent flow field along the path, and w is the Gaussian distributed random number. The local value of the *rms* (root mean square) fluctuation components is obtained by assuming isotropy as:

$$\sqrt{\overline{u'^2_i}} = \sqrt{\frac{2k}{3}} \qquad \text{(D.6)}$$

For a small particle that moves with the fluid, the integral time is the fluid Lagrangian integral time T_L and in k-ε turbulence model this is approximated as:

$$T_L = 0.15 \frac{k}{\varepsilon} \qquad \text{(D.7)}$$

APPENDIX-E

ALGEBRAIC SLIP MODEL (ASM)

This section presents an overview of the governing equations and technique employed in Algebraic Slip Model (ASM) for modelling multiphase flow. The similar explanation can also be found in [121] and for further details [91] is an excellent reference.

E.1 Continuity Equation for the Mixture

$$\frac{\partial \rho_m}{\partial t} + \frac{\partial}{\partial x_i}(\rho_m u_{m,i}) = 0 \tag{E.1}$$

E.2 Momentum Equation for the Mixture

The momentum equation for the mixture can be obtained by summing the individual momentum equations for both phases. It can be expressed as

$$\frac{\partial}{\partial t}(\rho_m u_{m,j}) + \frac{\partial}{\partial x_i}(\rho_m u_{m,i} u_{m,j}) = \frac{\partial}{\partial x_i}\mu_m\left(\frac{\partial u_{m,i}}{\partial x_j} + \frac{\partial u_{m,j}}{\partial x_i}\right) \tag{E.2}$$
$$-\frac{\partial p}{\partial x_j} + \rho_m g_j + V_j + \frac{\partial}{\partial x_i}\sum_{k=1}^{n}\alpha_k \rho_k u_{Dk,i} u_{Dk,j}$$

where n is the numeber of phases and ρ_m is the mixture density

$$\rho_m = \sum_{k=1}^{n}\alpha_k \rho_k \tag{E.3}$$

μ_m is the viscosity of the mixture

$$\mu_m = \sum_{k=1}^{n}\alpha_k \mu_k \tag{E.4}$$

where $\vec{u}_m$ is the mass-averaged velocity.

$$\vec{u}_m = \frac{\sum_{k=1}^{n} \alpha_k \rho_k \vec{u}_k}{\rho_m} \tag{E.5}$$

and $\vec{u}_{Dk}$ are the drift velocities.

E.3 The Relative (Slip) Velocity and Drift Velocity

The relative velocity or slip velocity is defined as the velocity of the secondary phase (p) relative to the primary-phase (q) velocity

$$\vec{u}_{pq} = \vec{u}_p - \vec{u}_q \tag{E.6}$$

The drift velocity and the relative velocity $\vec{v}_{qp}$ are connected by the following expression

$$\vec{u}_{Dp} = \vec{v}_{qp} - \sum_{i=1}^{n} \frac{\alpha_i \rho_i}{\rho_m} \vec{v}_{qi} \tag{E.7}$$

The basic assumption of the ASM model is that, to prescribe an algebraic relation for the relation for the relative velocity, a local equilibrium between the phases should be reached over short spatial length scales. The form of the relative velocity is given by

$$\vec{u}_{qp} = \tau_{qp} \vec{a} \tag{E.8}$$

where $\vec{a}$ is the secondary-phase particle's acceleration and τ_{pq} is the particulate relaxation time

$$\tau_{qp} = \frac{\rho_p d_p^2}{18 \mu_q} \tag{E.9}$$

BIBLIOGRAPHY

1. Tatterson, G. B., Brodkey, R., and Calabrese, R. V., (1991) "*Move Mixing Technology into the 21st Century*", Chemical Engineering Progress, Vol. 6, pp. 45-48.

2. Harnby, N., Edwards, M. F., Nienow, A. W., (1985) "*Mixing in the Process Industries*", 2nd ed., Butterworth-Heinmann, Boston, M. A.

3. Gill, C. B., (1980) "*Nonferrous Extractive Metallurgy*", John Wiley & Sons, New York.

4. Barrett, K. R., Knight, R. P., (1985) "*Lead bullion refining and precious metal recovery*", Extractive Metallurgy 85, London, England, 09-12 Sept. 1985, pp. 683-708.

5. Wood, J. R., Lurshay, A. M., (1990) "*The Production of Lead Cable Sheathing Alloys at Britannia Refined Metals Ltd.*", Presented by Adrian Lurshay at the LDA Seminar: "Lead Cable Sheathing – New Technologies for Improving Endurance", 8-9 Nov. 1990, Café Royal, London.

6. Smith, J. M., (1991) "*Industrial Needs for Mixing Research*" Trans. Inst. Chem. Eng., 68, Part A, pp. 3-6.

7. Zlokarnik, M., (May 1984) "*Scale-Up Process Engineering*" German Chemical Engineering, Vol. 7, No. 3, pp. 150-159.

8. Bailey, C., Patel, M. and Kumar, S., (January – April 2001) "*Computational modelling – a key component in materials processing*" Transactions of the Institute of Mining & Metallurgy, Section C, Mineral Processing & Extractive Metallurgy, Vol. 110.

9. Ranade, V. V., (Sept. 2001) "*Computational Flow Modelling for Chemical Reactor Engineering*" Academic Press.

10. Szekely, J., Evans, J. and Bimacombe, K., (1988) "*The Mathematical and Physical Modelling of Primary Metals Processing Operations*", TMS Pub.

11. Ranade, V. V., (1995) "*Computational Fluid Dynamics for Reactor Engineering*", Reviews in Chemical Engineering, Vol. 11, No. 3, pp. 229-289.

12. Daskopoulos, Ph., Harris, C. K., (1996) "*Three Dimensional CFD Simulation of Turbulent Flow in Baffled Stirred Tanks: An assessment of the Current Position*", ICHEME Symposium Series No. 140, pp. 1-8.

13. Kumar, S., (1998) "*Application of CFD in Modelling of Impeller-Stirred Vessels – MSc Dissertation*", University of Greenwich, UK.

14. Ranade, V. V., (2002) "*Computational Flow Modeling for Chemical Reactor Engineering*", PSE Vol. 5, Academic Press.

15. Ranade, V. V., Joshi, J. B., Marathe, A. G., (1989) "*Flow Generated by Pitched Blade Turbines I: Measurements Using laser Doppler Anemometer*", Chem. Eng. Comm., Vol. 81, pp. 197-224.

16. Ranade, V. V., Joshi, J. B., Marathe, A. G., (1989) "*Flow Generated by Pitched Blade Turbines II: Simulation Using k-ε Model*", Chem. Eng. Comm., Vol. 81, pp. 225-248.

17. Ranade, V. V., Bourne, J. R., Joshi, J. B., (1991) "*Fluid Mechanics and Blending in Agitated Tanks*" Chemical Engineering Science, Vol. 46, No.8, pp. 1883-1893.

18. Ranade, V. V., Mishra, V. P., Saraph, V. S., Deshpande, G. B., Joshi, J. B., (1992) "*Comparison of Axial Flow Impellers Using a Laser Doppler Anemometer*" Industrial Engineering Chemistry Research, Vol. 31; No. 10, pp. 2370-2379.

19. Sahu, A.K., Joshi, J. B., (Feb 1995) "*Simulation of flow in stirred vessels with axial flow impellers: effect of various numerical schemes and turbulence model parameters*" Industrial Engineering Chemistry Research, Washington DC, USA, Vol. 34, No. 2, pp. 626-639.

20. Fokema, M. D., Kresta, S. M., Wood, P. E., (1994) "*Importance of Using the Correct Impeller Boundary Conditions for CFD Simulations Stirred Tanks*", Can. J. Chem. Eng., 72, pp. 177-183.

21. Middleton, J. C., Pierce, F., Lynch, P. M., (1984) "*Computations of Flow Fields and Complex Reaction Yield in Turbulent Stirred Reactors, and Comparison with Experimental Data*" IChME Symposium Series No. 87, pp.239-246.

22. Ahlstedt, H., Lahtinen, M., (October/November 1996) "*Calculation of flow field in a stirred tank with Rushton turbine impeller*" The CFX International Users Conference, pp.37-54.

23. Pericleous, K. A., Patel, M. K., (1987) "*The modelling of tangential and axial agitators in chemical reactors*" PCH, Physicochem, Hydrodyn. , 8, pp.105-123.

24. Niclasen, D. A., Rudman, M., Blackburn, H. M., Wu, J., (1997) "*Flow Simulation of a Mixing Vessel Incorporating Blade Element Theory*" Inter. Conf. on CFD in Mineral & Metal Processing and Power Generation CSIRO, pp. 395-401.

25. Bui, R. T.; Ouellet, R.; Kocaefe, D., (Aug. 1994) "*Two-phase flow model of Al-SiC composite melt*", Metallurgical and Material Transactions B: Process Metallurgy and Material Processing Science, Vol. 25, No. 4, pp 607-618.

26. Kocaefe, D., Bui, R. T., (Dec. 1996) "*A One-Phase Model of the Mixing of Al-SiC Composite Melt*" Metallurgical and Material Transactions, B, Vol. 27B, pp.1015-1023.

27. Kocaefe, D., Bui, R. T., Provencher, R., Bourgeois, T., (1996) "*Simulating and Optimizing a Al-SiC Composite Mixing Tank*" The Minerals & Materials Society, pp.913-919.

28. Abid, M., Xuereb, C., Bertrand, (April 1994) "*Modelling of the 3D Hydrodynamics of 2-Blade Impellers in Stirred Tanks Filled With a Highly Viscous Fluid*" The Canadian Journal of Chemical Engineering, Vol. 72, pp. 184-193.

29. Dong, L., Johansen, S.T., Engh, T. A., (1994) "*Flow Induced by an Impeller in an Unbaffled Tank-I Experimental*" Chemical Engineering Science, Vol. 49, No. 4, pp. 549-560.

30. Dong, L., Johansen, S.T., Engh, T. A., (1994) "*Flow Induced by an Impeller in an Unbaffled Tank-II Numerical Modelling*" Chemical Engineering Science, Vol. 49, No. 20, pp. 3511-3516.

31. Hutchings, B. J., Patel, B. R, Weetman, R. J., (1989) "*Computation of Flow Fields In Mixing Tanks with Experimental Verification*" ASME Annual Winter Meeting, San Francisco, CA.

32. Harvey III, A. D., Lee, C. L., Rogers, S. E., (Oct. 1995) "*Steady-State modeling and Experimental Measurement of a Baffled Impeller Stirred Tank*" AIChE Journal, Vol. 41, No. 10, pp. 2177-2186.

33. Ranade, V. V., Dommeti, S. M. S., (May 1996) "*Computational Snapshot of Flow Generated by Axial Impellers in Baffled Stirred Vessels*" Trans IChemE, Vol. 74, Part A, pp.476-484.

34. Brucato, A., Ciofalo, M., Grsafi, F., Micale, G., (1994) "*Complete Numerical Simulation of Flow Fields in Baffled Stirred Vessels: the Inner-outer Approach*" IChemE Symposium Series No.136, pp. 155-162.

35. Luo, J. Y., Issa, R. I., Gosman, A. D., (1994) "*Prediction of Impeller Induced Flows in Mixing Vessels Using Multiple Frames of Reference*" IChemE Symposium Series No.136, pp.549-556.

36. Luo, J. Y., Gosman, A. D., Issa, R. I., Middleton, J. C., Fitzgerald, M. K., (May 1993) "*Full Flow Field Computation of Mixing in Baffled Stirred Vessels*" Trans. IChemE, Vol.71, Part A, pp. 342-344

37. Perng, C. Y., Murthy, J. Y., (1993) "*A Moving-deforming-Mesh Technique for Simulation of Flow in Mixing tanks*" AIChE Symposium Series No. 293, vol. 89, pp.37-39.

38. Rai, M. M., (1985) "*Navier-Stokes Simulations of Rotor-Stator Interaction Using Patched and Overlaid Grids*", AIAA Paper 85-0955, pp. 282-283.

39. Perng, Y. C., Murthy, J. Y., (1992) "*A Moving Mesh Technique for the Simulation of Flow in Mixing Tanks*" Proc. AIChE Ann. Meet, Miami Beach, FL, AIChE.

40. Bode, J., (1994) "*Computational Fluid Dynamics Applications in the Chemical Industry*" Computers chem. Engng, Vol. 18, Suppl., pp. S247-S251.

41. Lee, K. C., Ng, K., Yianneskis, M., Lang, F., Sanatian, R., (1996) "*Sliding Mesh Predictions of the Flows Around Rushton Impellers*" IChemE Symposium Series No. 140, pp.47-58.

42. Jaworski, Z., Wyszynski, M. L., Moore, I. P. T., Nienow, A. W., (1997) "*Sliding mesh computational fluid dynamics- a predictive tool in stirred tank design*" Proc Instn Mech Engrs, Vol 211, Part E. pp. 149-156.

43. Tabor, G., Gosman, A. D., Issa, R. I., (1996) "*Numerical Simulation of the Flow in a Mixing Vessel Stirred by a Rushton Turbine*", Fluid Mixing V, IChemE Symposium Series, No.140, pp. 25-34.

44. Lane, G. L., Koh, P. T. L., (1997) "*CFD Simulation of a Rushton Turbine in a Baffled Tank*" Inter. Conf. on CFD in Mineral & Metal Processing and Power Generation CSIRO, pp. 377-385.

45. Hervey III, A. D., Rogers, S. E., (Oct. 1996) "*Steady and unsteady computation of impeller-stirred reactors*" AIChE Journal, Vol. 42, No. 10, pp. 2701-2712.

46. Bakker, A., Laroche, R. D., Calabrese, R. V., (Jan. 1997) "*Sliding Mesh Simulation of Laminar Flow in Stirred Reactors*" Trans. IchemE, Vol.75, Part A, pp. 42-44.

47. Szekely, J., (1979) "*Fluid flow phenomena in metals processing*" New York; London (etc.), Academic Press.

48. Bird, R. B., Stewart, W. E., Lightfoot, E. N., (1960) "*Transport Phenomena*" John Wiley & Sons, Inc.

49. Markopoulos, J., Kontogeorgaki, E., (1995) "*Vortex Depth in Unbaffled Single and Multiple Impeller Agitated Vessels*" Chem. Eng. Technol.18, , pp 68-74.

50. Nagata, S., (1975) "*Mixing Theory and Applications*" Wiley, London.

51. Coulson, M., Richardson, J. F., (1998) "*Chemical Engineering - Fluid Flow, Heat Transfer & Mass Transfer*", Vol.1, 5th Ed., Butterworth-Heinemann.

52. Davey, T. R., Dance, N. J., Castle, J. F., Richards, J. H., (1963) "*Flow Characteristics of Molten Lead*" Symposium on Chem. Engng. in the Metallurgical Industries, Instn. Chem Engrs., pp.105-118.

53. Hayward, P. L. T., Harrison, D. A., "*Batch Lead Refining - A Case Study for Process Modelling*" BRM Internal Report.

54. Patel, M. J., (1982) "*Power Consumption Measurements and Surface Movement of Dross in a 0.42 scale Lead Kettle Model*" ISP Research Report 82/29.

55. Gammon, M. W., Ogborn, C. J., (1980) "*Lead Kettle Modelling*" ISP Research Report 80/23.

56. Marks, P. S., (May 1983) "*Lead Kettle Stirring Traits and Stirrer Power Consumption Characteristics*" BRM Report.

57. http://www.nortek-as.com/

58. Schafer, M., Yianneskis, M., Wachter, P., Dust, F., (June 1998) "*Trailing Vortrices around a 45^{o} Pitched-Blade Impeller*" AIChE Journal (Fluid Mechanics and Transport Phenomena), Vol. 44, No. 6, pp-1223-1246.

59. Placek, J., Tavlarides, L., (July 1985) "*Turbulent Flow in Stirred Tanks- Part I: Turbulent Flow in the Turbine Impeller Region*" AIChE Journal, Vol. 31, No. 7, pp1113-1120.

60. Bakker, A., Frijlink, J. J., (March 1989) "*The Drawdown and Dispersion of Floating Solids in Aerated and Unaerated Stirred Vessels*" Chem Eng Res Des, Vol. 67, pp.208-209.

61. Hemrajani, R. R., Smith, D. L., Koros, R. M., Tarmy, B. L., (1988) "*Suspending Floating Solids in Stirred Tank-Mixer Design, Scale-Up and Optimisation*" Proc. 6th European Conf. On Mixing, Pavia, Italy, pp. 259-265.

62. Edwards, M. F., Ellis, D. I., (1984) "*The Drawdown of Floating Solids Into Mechanically Agitated Vessels*" IChemE. Symposium Series 89, pp.1-13.

63. Takahashi, K., Sasaki, S., (1999) "*Complete Drawdown and Dispersion of Floating Solids in Agitated Vessel Equipped With Ordinary Impellers*" Journal of Chemical Engineering of Japan, 32, 1, pp. 40-44.

64. Markopoulos, J., Kontogeorgaki, E., (1995) "*Vortex Depth in Unbaffled Single and Multiple Impeller Agitated Vessels*" Chem. Eng. Technol.18, pp. 68-74.

65. Halliday, D., Resnick, R., Walker, J., (2000) "*Fundamentals of Physics*", 6th Ed., Wiley.

66. "*ADV Operation Manual*", (April 1998), NORTEK AS, Norway.

67. "*ADV Software Manual*", (1998), Ver. 2.7, NORTEK AS, Norway.

68. Launder, B. E.; Spalding, D. B. (1974) "*The Numerical Computation of Turbulent Flows*", Compt. Methods Appl. Mech. Eng., 3, pp. 269-289.

69. Smith, G. D. (1985) "*Numerical Solution of Partial Differential Equations: Finite Difference Methods*", 3rd Ed., Clarendon Press, Oxford.

70. Zienkiewicz, O. C., Taylor, R. L., (1991) "*The Finite Element Method – Vol. 2: Solid and Fluid Mechanics*", McGraw-Hill, New York.

71. Canuto, C., Hussaini, M. Y., Quarteroni, A., Zang, T. A., (1987), "*Spectral methods in fluid mechanics*", Springer, Berlin.

72. Patankar, S. V. (1980). "*Numerical Heat Transfer and Fluid Flow*", Hemishere Publishing Corporation, Taylor & Francis Group, New York.

73. Versteeg, H. K.; Malalasekera, W., (1995) "*An Introduction to Computational Fluid Dynamics – The Finite Volume Method*" Longman.

74. Ferziger, J., Peric, M., (1999) "*Computational Methods for Fluid Dynamics*", 2nd Ed., Springer.

75. http://www.fluent.com

76. "*FLUENT 4.5 USER'S MANUAL*", Vol. 1-4, (1998) Fluent Inc, Lebanon, NH (USA).

77. Patankar, S. V., (1998) "*Elliptic Systems: Finite-Difference Method I*", Handbook of Numerical Heat Transfer, Wiley, pp. 215-240.

78. Patankar, S. V., Karki, K. C., Kelkar, K. M., "*Finite Volume Method*", The Handbook of Fluid Dynamics, CRC Press, pp. 27-1 to 27-26.

79. Gourdin, A., Boumahrat, M., (1996) "*Applied Numerical Methods*", Prentice-Hall of India Private Limited, New Delhi.

80. Rhie, C. M., Chow, W. L., (1983) "*Numerical Study of the Turbulent Flow Past an Aerofoil with Trailing Edge Separation*", AIAA J., Vol. 21, No. 11, pp. 131-146.

81. Briggs, W. L., (1987) "*Multigrid Tutorials*", SIAM.

82. Thompson, J. F., Warsi, Z. U. A., Mastin, C. W., (1985) "*Numerical Grid Generation – Foundation and Applications*" Elsevier, New York.

83. Laszlo, M. J., (1999) "*Computational Geometry and Computer Graphics in C++*", Prentice-Hall of India Private Limited, New Delhi.

84. Filipiak, M., (Nov. 1996) "*Mesh Generation*", Edinburgh Parallel Computing Centre, The University of Edinburgh, Version 1.0.

85. The, J. L., Raithby, G. D., Stubley, G. D., (1994) "*Surface-Adaptive Finite-Volume Method for Solving Free Surface Flows*", Numerical Heat Transfer, Part B, 26:367-380.

86. Hirt, C., Nichols, B., (1981) "*Volume of Fluid (VOF) Method for the Dynamics of Free Boundaries*", Journal of Computational Physics, 39, pp. 201-225.

87. Darwish, M., Moukalled, F., Sekar, B., (2001) "*A Unified Formulation of the Segregated Class of Algorithms for Multifluid Flow at All Speeds*", Numerical Heat Transfer, Part B, 40:99-137.

88. Crowe, C., Sommerfield, M., Tsuji, Y., (1998) "*Multiphase flows with droplets and particles*", CRC Press, Boca Raton, Florida.

89. Pericleous, K. A., Drake, S. N., (1986) "*An Algebraic Slip Model of PHOENICS for Multi-phase Applications*", Numerical Simulation of Fluid Flow and Heat/Mass Transfer Processes, Eds.: Markatos, N. C., Tatchell, D. G., Cross, M., Rhodes, N., Lecture Notes in Engineering 18, Berlin: Springer-Verlag.

90. Johansen, S. T., Anderson, N. M., de Silva, S. R., (1990) "*A Two-Phase Model for Particle Local Equilibrium Applied to Air Classification of Powders*", Powder Technology, 63, pp. 121-132.

91. Manninen, M., Taivassalo, V., Kallio, S., (1996) "*On the Mixture Model for Multiphase Flow*", Technical Research Centre of Finland, ESPOO.

92. http://www.cham.co.uk

93. http://www.flow3d.com/Default.htm

94. http://www-waterloo.ansys.com/cfx/default.asp

95. http://physica.gre.ac.uk/physica.html

96. http://www.cd-adapco.com/products/

97. Kumar, S., Bailey, C., Patel, M., Piper, A. and Forsdick, R., (1999) "*Modelling the Mixing of Lead Bullion During the Refining Process*" (in Fluid Flow Phenomena in Metals Processing, Pub TMS).

98. Kumar, S., Bailey, C., Patel, M., (March 1999) "*Predicting the mixing of molten metal using CFD*", 7th ACHME Conference, 29-30, University of Durham, U.K., pp. 79-82.

99. Bailey, C., Kumar, S., Patel, M., Piper, A., Forsdick, R. and Hance, S., (Dec. 1999) "*Comparison Between CFD and Measured Data for the Mixing of Lead Bullion*", (Second International Conference on CFD in the Minerals and Process Industries CSIRO, Melbourne, Australia, 6-8 Dec. 1999).

100. Kumar, S., Bailey, C., Patel, M., Piper, A. and Forsdick, R., Cowling, M., (April 2000) "*Application of CFD in the Lead Refining Process*", 8th ACHME Conference, 16-19 April 2000, University of Greenwich, U.K.

101. Kumar, S., Bailey, C., Patel, M., Piper, A., Cowling, M., and Forsdick, R., (Feb. 2002) "*Computational Modelling of Vortex Formation in the Lead Refining Kettle*", 2001 TMS Fall Extraction and Process Metallurgy Meeting, (Rescheduled from Sept. 23-26, 2001 to Feb. 17-21, 2002)

102. Kirk-Othmer, (1989) "*Encyclopaedia of Chemical Technology*", 3ed., Vol. 14 (Laminated Wood-Based Composite to Mass Transfer), Wiley, pp. 98-139.

103. Rieger, F., Ditl, P., Novak, V., (1979) "*Vortex Depth in Mixed Unbaffled Vessel*", Chemical Engineering Science, Vol. 34, pp397-403.

104. Hayduk, W. and Neale, G., (Oct. 1978) "*Vortex Formation in Stirred Draining Vessels*", The Canadian Journal of Chemical Engineering, Vol. 56, pp. 544-549.

105. Ju, S., Mulvahill, T., Pike, R., (Feb. 1990) "*Three-Dimensional Turbulent Flow in Agitated Vessels with a Nonisotropic Viscosity Turbulence Model*", The Canadian Journal of Chemical Engineering, Vol. 68, pp. 3-16.

106. Ciofalo, M., Brucato, A., Grisafi, F., Torraca, N., (1996) "*Turbulent Flow in Closed and Free-Surface Unbaffled Tanks Stirred by Radial Impellers*", Chemical Engineering Science, Vol. 51, No. 14, pp. 3557-3573.

107. Smith, L., Wooddruff, S., (1998) "*Renormalization-Group Analysis of Turbulence*" Annu. Rev. Fluid Mech., 30, pp. 275-310.

108. Bakker, A., Fasano, J. B., (July 1998) " *Turbulent Mixing and Chemical Reaction in Stirred Tanks*", The Online CFM Book, http://ourworld.compuserver.com/homepages/AndreBakker/cfmbook.htm

109. Zwietering, Th. N., (1958) "*Suspending of Solid Particles in Liquid by Agitators*", Chem Eng Sci, 8, pp. 244-253.

110. Nouri, J. M., Whitelaw, J. H., (1992) "*Particle Velocity Characteristics of Dilute to Moderately Dense Suspension Flows in Stirred Reactors*", Int. J. Multiphase Flow, Vol. 18, No. 1, pp. 21-33.

111. Joosten, G. E. H., Schilder, J. G. M., Broere, A. M., (1977) "*The Suspension of Floating Solids in Stirred Vessels*", Trans. I. Chem. E., 55, pp. 220-222.

112. Thring, R. W., Edward, M. F., (1990) "*An Experimental Investigation into the Complete Suspension of Floating Solids in an Agitated Tank*", Ind. Eng. Chem. Res., 29, pp. 676-682.

113. Patterson, G. K., (1991) "*Measurements and Modelling of Flow in Gas Sparged Agitated Vessels*", Proceedings of the 7th European Congress on Mixing, Brugge, pp. 209-215.

114. Decker, S., Sommerfeld, M., (1996) "*Calculation of Particle Suspension in Agitated Vessels With the Euler-Lagrange Approach*", Icheme Symposium No. 140, pp. 71-82.

115. Barrue, H., Xuereb, C., Pitiot, P., Falk, L., Bertrand, J., (1999) "*Comparison of Experimental and Computational Particle Trajectories in a Stirred Vessel*", Chem. Eng. Technol, 22, 6, pp. 511-521.

116. Bakker, A., Fasano, J. B., Myers, K. J., (1994) "*Effects of Flow Pattern on the Solid Distribution in a Stirred Tank*", Icheme Symposium Series No. 136, pp. 1-7.

117. "*Analysis Technologies for Lead Refining Kettles – A User Guide*", (2001) BRM Internal Report.

118. Yahya, S. M., (2000) "*Turbines Compressors and Fans*", Tata McGraw-Hill, New Delhi

119. Morsi, S. A., Alexander, A. J., (1972) "*An Investigation of Particle Trajectories in Phase Flow Systems*", J. Fluid Mech., 55, pp. 193-208.

120. Thomson, D. J., (1987) "*Criteria for Selection of Stochastic Models of Particles Trajectories in Turbulent Flows*", J. Fluid Mech., 180, pp. 529-556.

121. "*FLUENT 5 USER'S MANUAL*", Vol. 1 - 4, (1998) Fluent Inc, Lebanon, NH (USA).